Multiscale Modelling of Neuronal Dynamics and Their Dysfunction in the Developing Brain

Richard Ewald Rosch
Wellcome Centre for Human Neuroimaging
UCL Queen Square Institute of Neurology
University College London

Supervisors:

Prof Karl J. Friston
Wellcome Centre for Human Neuroimaging
UCL Queen Square Institute of Neurology
University College London

&

Prof Torsten Baldeweg
Developmental Neurosciences
UCL Great Ormond Street Institute of Child Health
University College London

October 2018 | This dissertation is submitted for the degree of
Doctor of Philosophy in Theoretical Neurobiology

Yet brains are not 'like' any artificial machine. If anything, they are 'like' natural self-organizing processes such as stars or hurricanes

Walter Jackson Freeman III

The main interest in life and in work is to become someone else you were not in the beginning.

Michel Foucault

Whats [sic] going on with mycareer [sic]

@cher

Declaration

I, Richard E. Rosch, confirm that the work presented in this thesis is my own. Where information has been derived from other sources, I confirm that this has been indicated in the thesis. All of the experimental chapters (Chapters 4-7) are the product of collaborations with various scientists and clinicians. My individual contribution is highlighted at the beginning of each chapter.

Dr Richard E Rosch

Acknowledgements

First on this list are of course the dream team – Karl Friston and Torsten Baldeweg, my supervisors. Karl's improbably mix of expansive knowledge, generosity and pragmatism shaped my thinking far beyond what I have illustrated here in this thesis. The hour-long in-depth discussions with his ever-changing group of researchers left me with a broad neuroscience education no taught degree could have offered. I can only aspire to maintain some of the broad aspiration and curiosity instilled by Karl in my future work. Witnessing Torsten's ability to run a research programme with and for children with epilepsy and neurological impairments, involving such a diverse set of basic science and clinical colleagues will remain an inspiration for the years to come. His breadth of knowledge and keen eye for ways to apply it is something I hope to be able to refer back to in the future. Thanks to both of them for the support throughout the PhD.

The other benefit of working with Karl and Torsten (and at UCL more generally) is that I got to work with some incredible people across different departments. Discussion, coffee and commiserations with Gerald Cooray, Ryszard Auksztulewicz, Gerold Baier, Birgit Pimpel, Hayriye Cagnan, Peter Zeidman, Sophie Adler, Thomas Parr, Manuela Pisch, Berk Mirza, Andrew Levy, and many more really shaped my day to day experience during the PhD and made the long haul possible.

The Centre staff at the FIL have tolerated my endless outlandish requests and I cannot stress enough how lucky the fellows at the centre are/were to be working with people like Kamlyn Ramkissoon, Monica Bumbury, Peter Aston, David Bradbury, Shiv Jhala, Alphonso Reid, Marcia Bennett (even in her reduced capacity as honorary social secretary), Marina Anderson and the whole IT crew.

None of the work would be possible without the unwavering support from clinical colleagues who are committed to keep pushing the boundaries of what we know about patients with neurological conditions. Clinicians who have had a direct impact on the work presented here, as well as on myself as a clinical academic include Elaine Hughes, Deb Pal, Ming Lim, Martin Tisdall, Rachel Thornton, Friederike Moeller, and Sushma Goyal. Equally this thesis would not exist if it were not for the curiosity, generosity and openness of other scientific collaborators and fellow scientists, such as Paul Hunter, Martin Meyer,

Colin Peters, Peter Ruben, Yujiang Wang, Gabrielle Schroeder, Louise Upton, Margarita Papadopoulou, and Angela Vincent.

Throughout my time at UCL I have been fortunate to supervise driven and smart students for a part of their journeys. It may sound like a trope, but supervising always feels more like learning than teaching, so I want to thank Stasa Tumpa, George Choa, Merry Leung and Micha Heilbron for offering the opportunity to learn along with them. I'm proud of their achievements, grateful for their excitement about their various projects and curious to see where they go next.

Last but not least, I would not be here without the support of my family and friends, who despite different priorities – in the time it took me to put this PhD together, I have acquired 4 new nephews – have kept me sane(ish). Reunions with Maggie and Mike, near-daily life advice from Alasdair, restorative swims with Sarah, endless rants with Massih, forced (but appreciated) excursions into nature with Nat, delicious meals with George, doggy chats with Kirsten, and all the other ways to distract from too much neuroscience were deeply appreciated – thank you.

My time at the FIL, and this work more broadly was supported by Clinical PhD funding from the Wellcome Trust, and I am immensely grateful for the opportunities this funding has provided.

Abstract

Over the last few decades, an increasing number of neurodevelopmental disorders has been associated with molecular causes – such as genetic mutations, or autoantibodies affecting synaptic transmission. Yet understanding the pathophysiology that leads from particular molecular disruptions at the synapse to patients' signs and symptoms remains challenging, even today.

The work presented in this thesis illustrates how computational models can help bridge the explanatory gap between disruptions at the molecular scale and brain dysfunction at the level of integrated circuits. I utilise computational models at different scales of neuronal function, ranging from the neuronal membrane, to integrated cortical microcircuits and whole-brain sensory processing networks. These computational models are informed with, and further constrained by both empirical data derived from a number of model systems of neurodevelopmental disorders, and clinical patient data. The worked examples in this thesis include the biophysical characterisation of an epilepsy-causing mutation in the voltage-gated sodium channel gene *SCN1A*, calcium imaging in a larval zebrafish model of epileptic seizures in the immature brain, electrophysiological recordings from patients with NMDA receptor antibody encephalitis as well as from a mouse model of the disorder, and pharmacologically induced NMDA receptor blockade in young adults that captures features of acute psychosis and schizophrenia.

The combination of this diverse range of empirical data and different computational models offers a mechanistic, multi-scale account of how specific phenotypic features in neurodevelopmental disorders emerge. This provides novel insights both in regard to the specific conditions included here, but also concerning the link between molecular determinants and their neurodevelopmental phenotypes more broadly.

Table of contents

List of figures

List of tables

Abbreviations

Ab	Antibody
AMPA	α-amino-3-hydroxy-5-methyl-4-isoxazolepropionic acid
AMPAR	α-amino-3-hydroxy-5-methyl-4-isoxazolepropionic acid receptor (glutamate receptor)
CMC	Canonical microcircuit
DCM	Dynamic causal modelling
DS	Dravet syndrome
ECoG	Electrocorticography (type of intracranial EEG)
EEG	Electroencephalography
EIEE	Early infantile epileptic encephalopathies
ERP	Event-related potential
fMRI	Functional magnetic resonance imaging
GABA	γ-aminobutyric acid
GABAR	γ-aminobutyric acid receptor
HH	Hodgkin Huxley model
ILAE	International league against epilepsy
JR	Jansen-Rit model
KL	Kulback-Leibler
LFP	Local field potential
MMN	Mismatch negativity
NMDA	*N*-Methyl-D-aspartate
NMDAR	*N*-Methyl-D-aspartate receptor (type of glutamate receptor)
PTZ	Pentylenetetrazole (acute chemoconvulsant drug)
SPM	Statistical parametric mapping
WC	Wilson-Cowan model

Associated publications

The following publications are associated with work conducted as part of this thesis. Where there is significant overlap between published work and chapters in the thesis, this has been indicated appropriately.

Published / in press

1. **Rosch, R.E.**, Wright, S., Cooray, G., Papadopoulou, M., Goyal, S., Lim, M., Vincent, A., Upton, A.L., Baldeweg, T., Friston, K.J., 2018. NMDA-receptor antibodies alter cortical microcircuit dynamics. *Proc Natl Acad Sci*, *in press*, doi: 10.1073/pnas.1804846115
2. **Rosch, R.E.**, Auksztulewicz, R., Leung, P.D., Friston, K.J., Baldeweg, T. 2018. Selective prefrontal disinhibition in a roving auditory oddball paradigm under N-Methyl-D-Aspartate Receptor Blockade. *Biol Psychiat: Cog Neurosci Neuroimaging, in press*, doi: 10.1016/j.bpsc.2018.07.003
3. **Rosch, R.E***., Hunter, P.R*., Baldeweg, T., Friston, K.J., Meyer, M.P., 2018. Calcium imaging and dynamic causal modelling reveal brain-wide changes in effective connectivity and synaptic dynamics during epileptic seizures. *PLoS Comp Biol*, 14(8), e1006375
4. Friston, K.J., **Rosch, R.**, Parr, T., Price, C., Bowman, H. 2018. Deep temporal models and active inference. *Neurosci Biobehav Rev*, 90. 486-501.
5. Oates, S., Tang, S., **Rosch, R.**, Lear, R., Hughes, E.F., Williams, R.E., Larsen, L.H.G., Hao, Q., Dahl, H.A., Møller, R., Pal, D.K. 2018. Incorporating epilepsy genetics into clinical practice: a 360 evaluation. *npj Genomic Med*, 3(1), 13.
6. **Rosch, R.**, Baldeweg, T., Moeller, F., Baier, G. 2018. Network dynamics in the healthy and epileptic developing brain. *Netw Neurosci*. 2(1). 41-49.
7. Baier, G., **Rosch, R.**, Taylor, P.N., Wang, Y. 2018. Design principle for a population-based model of epileptic dynamics. In *Complexity Synergistics*, 333-47. Springer, New York, NY.
8. Papadopoulou, M., Cooray, G., **Rosch, R.**, Moran, R., Marinazzo, D., Friston, K.J. 2017. Dynamic causal modelling of seizure activity in a rat model. *NeuroImage*, 146. 518-532.

9. Omidvarnia, A., Pedersen, M., **Rosch, R.E.**, Friston, K.J., Jackson, G.D. 2017. Hierarchical disruption in the Bayesian brain: Focal epilepsy and networks. *NeuroImage Clin* 15, 682-8.
10. **Rosch, R.E.,** Cooray, G., Friston, K.J. 2017. Dynamic causal modelling of dynamic dysfunction in NMDAR-receptor antibody encephalitis. In *Computational Neurololgy and Psychiatry.* 121-148. Springer, New York, NY.
11. Peters, C.*, **Rosch, R.E*.**, Hughes, E., Ruben, P.C. 2016. Temperature-dependent changes in neuronal dynamics in a patient with an SCN1A mutation and hyperthermia induced seizures. *Sci Rep*, 6. 31879.

Submitted for publication

1. Hamburg, S.*, **Rosch, R.***, Startin, C.M., Friston, K.J., Strydom, A. 2018. Dynamic causal modelling of the relationship between cognition and theta-alpha oscillations in adults with Down syndrome. *revision submitted*
2. Cooray, G.K., **Rosch, R.**, Baldeweg, T., Lemieux, L., Friston, K.J., Sengupta, B. 2017. Bayesian belief updating of spatiotemporal seizure dynamics. *arXiv:* 1705.07278.

* equal contribution

1

Introduction

The explosion in genomic technologies that are now accessible to clinical medicine has recently renewed research interest in a broad range of neurodevelopmental disorders. The ability to comprehensively investigate patients with disabling neurological and neuropsychiatric conditions that have a significant impact on development has provided a whole host of break-through insights: Even just within the last five years, the Deciphering Developmental Delays (DDD) study has provided compelling evidence for the role of *de novo* mutations in >90 genes as the cause of intellectual disabilities (Deciphering Developmental Disorders Study, 2017); the Schizophrenia Working Group of the Psychiatric Genomics Consortium has provided evidence for >100 genes conferring a risk for schizophrenia, highlighting a number of biological mechanisms (Schizophrenia Working Group of the Psychiatric Genomics Consortium, 2014); the Epi4K Consortium provided similar evidence for the role of *de novo* mutations in epileptic encephalopathies (Epi4K Consortium and Epilepsy Phenome/Genome Project, 2013).

The increasing availability of genetic testing has led to a number of major broad insights regarding the molecular basis of neurodevelopmental conditions: Even genes that have been identified from well-defined clinical cohorts are often associated with a much broader phenotypic spectrum than initially anticipated (e.g. the voltage-gated sodium channel *SCN1A* was first described in a specific familial syndrome, but is now recognised as a risk factor for common epilepsies (Escayg et al., 2000; International League Against Epilepsy Consortium on Complex Epilepsies, 2014)). This broad association of individual genetic risk factors can even span disease categories – it is now becoming clear, that e.g. epilepsy

and schizophrenia share genetic risk factors despite very distinct phenotypic expressions of this shared molecular dysfunction (Vonberg and Bigdeli, 2015).

This leaves translational neuroscience (and in fact neurology and psychiatry) with the next big challenge – how do we relate molecular abnormalities that can be diagnosed with increasing precision and technological sophistication to phenotypes observed in patients. How do we identify which part of the phenotype is associated with which molecular disruption in order to make sense of the increasingly 'genomic view' on many neurodevelopmental disorders (Thomas and Berkovic, 2014)?

In this thesis, I will offer a particular strategy that may help address this question in the future. I am proposing that the use of computational models that capture some of the biophysical properties of real neuronal systems can help us link neurobiological abnormalities at the microscale with observable features of clinical phenotypes. I will illustrate this approach using a few examples and model systems where there is a known strong effect of the molecular abnormality on the phenotype. As such, these are models of the extremes of single-molecule-deficit neurodevelopmental disorders, but these models will illustrate different strategies in applying computational models to the broader questions applicable also in the more common conditions.

In Chapter 2, I review the principal stages of postnatal human brain development, in order to give context to different neurodevelopmental disorders. I then provide an overview over two distinct groups of such disorders: the epilepsies, and schizophrenia and related disorders. In contrasting these two examples, I highlight the differential impact even shared molecular abnormalities may have at different stages in brain development. I also highlight how different types of computational models may capture phenotypic features characteristic for the disorders, which leads me to the next chapter.

In Chapter 3, I provide an overview of different strategies that can link measures of neuronal (dys-)function with quantitative models of the biophysical setup of neuronal systems. For this chapter, I focus particularly on the types of models used later in this thesis, in order to illustrate the principles under which these models can operate. Here, I place particular emphasis on the mesoscale models – models that sit somewhere between a molecular representation of neuronal function, and phenotypes that are observable at the whole-brain scale – as these may help us in the future to bridge the explanatory gap between phenotypes and molecular dysfunction specified in Chapter 2.

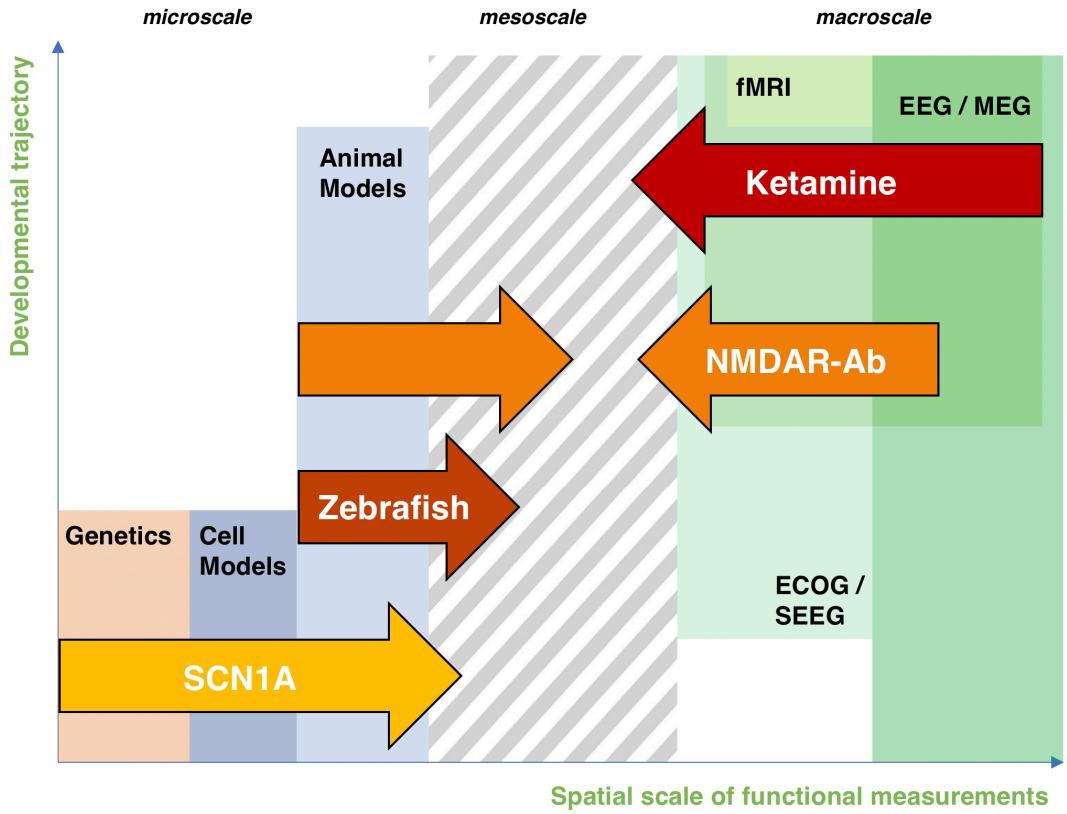

Figure 1.1 – Linking micro- and mesoscale in the empirical chapters of this thesis. This thesis contains 4 empirical chapters illustrating worked examples of using computational models at different scales to explain neuronal pathology. These integrate insights from different data modalities, each with their specific advantages and disadvantages: Whilst genetics and cell models allow detailed examination of microscale abnormalities, they do not allow examination of developmental trajectories. On the other hand, imaging and neurophysiological recordings in human subjects allows whole-brain functional evaluation at different stages in development but do not easily relate to microscale abnormalities. The arrows indicate the scale at which the different models employed in this thesis operate.

'SCN1A' refers to Chapter 4, 'Zebrafish' refers to Chapter 5, 'NMDAR-Ab' refers to Chapter 6, 'Ketamine' refers to Chapter 7 of this thesis.

The subsequent 4 chapters are worked examples of multiscale computational analysis strategies – using a diversity of empirical data in a range of model systems of neurodevelopmental disorders, I highlight the potential applications of this analysis approach. Each of the individual projects presented carries their own biological hypotheses, and in combination they reveal the power of using computational models at different explanatory scales to link our understanding of the micro- and the macroscale (Figure 1.1).

In the first of these chapters – Chapter 4 – I employ empirical estimates of channel gating behaviour from patch-clamp recordings in a cell-based model of a human epilepsy

mutation (in *SCN1A*) in a computational model of the neuronal membrane. Exploration of the dynamic behaviour of this patient-derived *in-silico* model then provides an insight into possible mechanism of how the microscale abnormalities caused by the mutation can induce the heat-induced seizures seen in the patient.

The following chapter, Chapter 5, applies network-models of neuronal population activity to light-sheet imaging data of induced epileptic seizures in the developing zebrafish brain. I use the models to infer the types of network-wide changes that occur during an epileptic seizure caused by a pharmacological intervention. The detailed imaging possible in this animal models allows an integration of insights from local coupling changes and larger between-region changes in synaptic coupling during such an induced seizure.

In Chapter 6, I focus on NMDA-receptor antibody (NMDAR-Ab) encephalitis. In this autoimmune condition, patients can show both neuropsychiatric symptoms and develop EEG abnormalities and epileptic seizures – making it an attractive model system to investigate the link between NMDAR dysfunction and a range of neurodevelopmental disorders. I combine models of neuronal population dysfunction with clinical EEG recordings of patients with NMDAR-Ab encephalitis, and local field potential recordings in a mouse model of the disorder. This approach allows me to harness the experimental control afforded by the animal model alongside clinical EEG recordings in patients to identify the sort of circuit abnormalities responsible for the observed EEG phenotypes associated with the disorder.

The last empirical chapter – Chapter 7 – focusses on a placebo-controlled experiment investigating the effects of pharmacological NMDAR-blockade (with ketamine) on neurophysiological markers typically impaired in schizophrenia. Here the combination of a pharmacological intervention and human subject EEG data, together with network models of cortical circuitry allows me to infer the localised neuronal effects of NMDAR-blockade and relate these to models of psychopathologies in schizophrenia.

Lastly, in Chapter 8, I draw overall conclusions that emerge from these thematically consistent approaches at distinctive scales – distinct, both in terms of biological insights they offer (regarding the relation of mesoscale neuronal behaviour, and the disruption of synaptic function); and in terms of the types of inference we can draw from empirical data using the multi-scale modelling approaches in future applications.

2

Dysfunction in the developing brain

During childhood and adolescence, the human brain undergoes dramatic developmental changes that affect the brain at every scale – from basic synaptic neurotransmission and neuronal membrane properties, all the way to the organisation of dynamic coordinated whole-brain oscillatory networks (Courchesne, 1990; Gogtay et al., 2004; Whitford et al., 2007). There are a number of conditions that can be characterised as neurodevelopmental disorders, in that they interact with, or disrupt some of these developmental processes (Hu et al., 2014). These conditions are often characterised by incidence peaks around well-defined age ranges, which suggests that they are associated with specific vulnerabilities of the developing brain that emerge at distinct stages in brain development.

In this chapter I discuss the neuronal dysfunction underlying two sets of neurodevelopmental disorders: epilepsy (and in particular a group of conditions known as epileptic encephalopathies) and schizophrenia and associated psychotic disorders. Whilst the epilepsies have a peak incidence in the neonatal period, early infancy and childhood (Olafsson et al., 2005), schizophrenia and psychosis are classically conditions of adolescence and young adulthood (Paus et al., 2008). In combination, these example groups of disorders allow a window on the importance of distinct developmental processes and illustrate how neuronal dysfunction unfolds in the context of very different developmental stages.

2.1 Stages of development in the human brain

Human infants are born at a comparatively early stage in their brain development, with many developmental processes taking place postnatally – full functional and structural brain 'maturity' is only achieved well into the third decade of life. Evidence of this protracted developmental trajectory can be measured both in terms of basic neuronal physiology, and in behavioural experiments (Silbereis et al., 2016). Thus, brain development in infants, children and adolescents sits at a complex and changing interface between genetic determinants, developmental trajectories, and environmental influences. Aberrations in each can contribute to neurodevelopmental disorders, with the differential contribution to overall risk changing with age of onset of the various neurodevelopmental conditions.

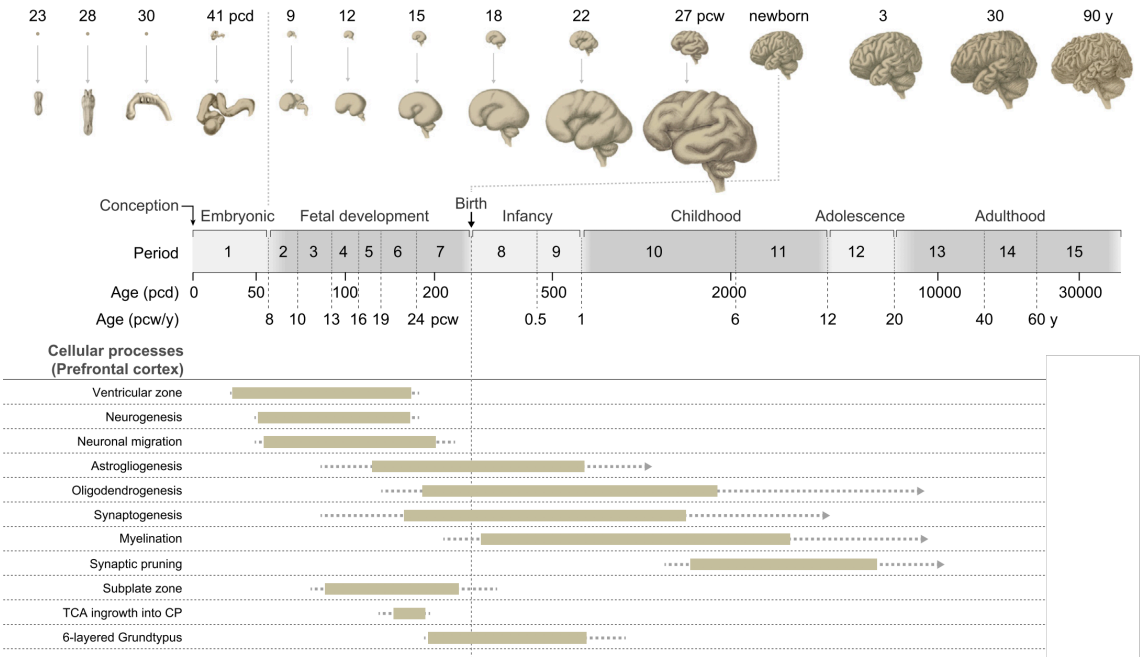

Figure 2.1 – Cellular processes during postnatal development. This figure illustrates brain morphology across the human life span (top panel) and identifies the time windows during which specific cellular processes occur (bottom panel). Infancy, childhood and adolescence are the temporal windows associated with glial growth and maturation (astrogliogenesis, oligodendrogenesis, and myelination), as well as synaptic development (synaptogenesis, and synaptic pruning), whilst most of the neurogenesis is complete at the time of delivery.

[Reproduced with permission, (Silbereis et al., 2016)*]*

In the following section, I provide a brief overview over different stages in human brain development at three different scales – ranging from cellular and synaptic development, to

circuit development, and whole brain functional architecture. By necessity, this is a focussed review, highlighting key stages in postnatal development, in particular those that are relevant to the processes under investigation throughout the rest of this thesis and those that are mechanistically implicated in the disease processes at hand.

2.1.1 Cellular changes in development

Brain function depends on the properties of individual neurons and their synaptic coupling. Whilst prenatal brain development involves a complex array of cell production, migration and functional integration, the vast majority if neurons are already in place at the time of a normal term delivery, with post-natal neurogenesis only playing a limited role in postnatal functional changes (Jiang and Nardelli, 2016).

Thus, many changes observed in brain function during human brain development are ultimately associated with maturational changes of the properties of existing neurons and alterations in their synaptic connections. Figure 2.1 highlights distinct cellular changes that occur postnatally during infancy, childhood and adolescence. I will discuss the distinct developmental profiles of two classes of changes here: changes at the synapse (i.e. synaptogenesis and synaptic pruning), and glial changes (gliogenesis and myelinsation). These illustrative examples highlight how whole-brain development is shaped by the interaction of a range of developmental trajectories of distinct, but related cellular processes.

2.1.1.1 Synaptogenesis, functional maturation, and synaptic pruning

Effective connections between individual neurons are essential for information processing and thus nervous system function. In the central nervous system, the majority of such connections are mediated through chemical synapses – allowing signalling from a presynaptic neuron via neurotransmitter release to a postsynaptic neuron. Immature neurons in the brain start the process of forming synapses approximately half-way through gestation, but the process continues until mid-childhood for some brain regions and neuronal subtypes. This initial burst of synaptogenesis appears to be an 'over-production', with only a fraction of the synaptic connections made in early infancy surviving into adulthood (Huttenlocher and Dabholkar, 1997; Silbereis et al., 2016).

The developmental drive invoking synaptogenesis appears to be genetic – with the timing and number of synapses formed being relatively experience-independent. However, the

specific morphology and function of newly formed synapses in early development is significantly shaped by experience (Bourgeois et al., 1989).

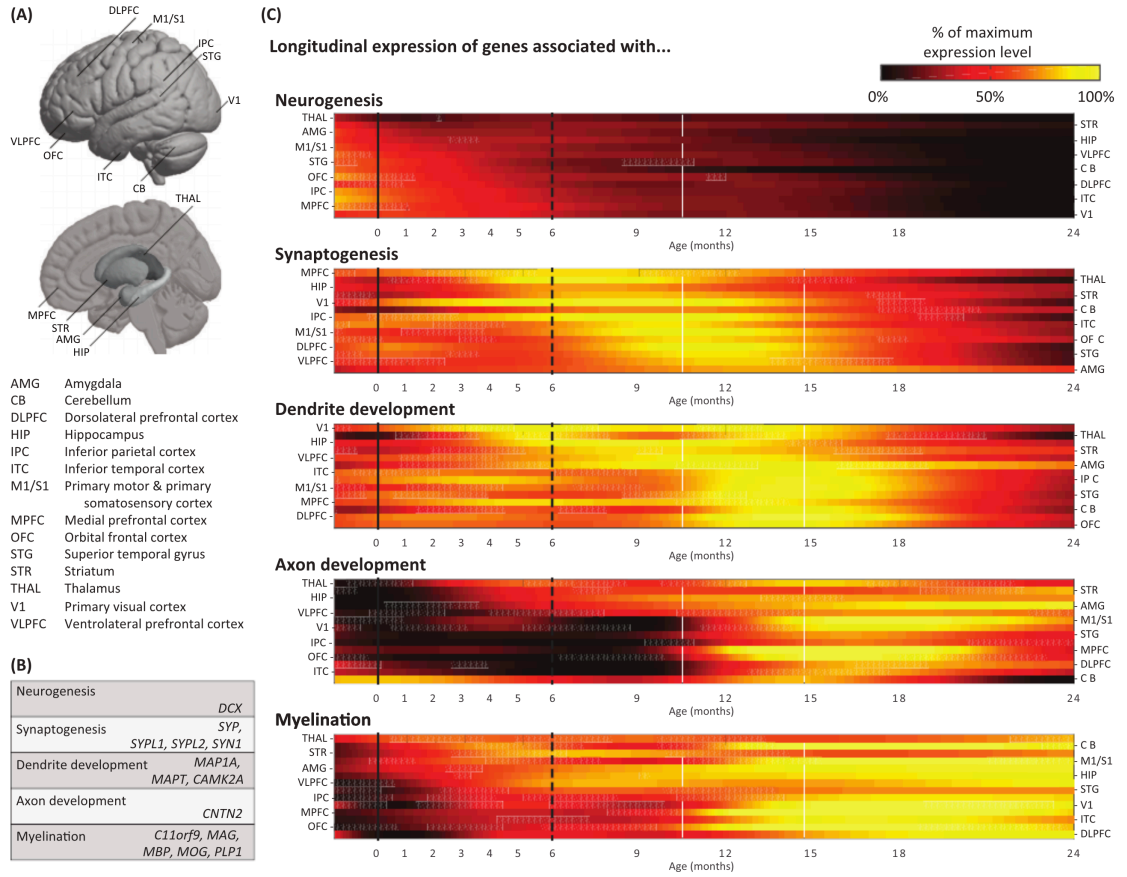

Figure 2.2 – Gene expression levels tracking developmental processes in the human brain. (A) Identifies key cortical and subcortical regions for which gene expression measures are available. (B) The selection of genes associated with specific developmental functions for which transcription levels are tracked. (C) Longitudinal expression of genes associated with these functions. Plots are ordered according to peak expression levels – with neurogenesis genes peaking first, and myelination genes peaking latest in their expression.

[Reproduced with permission from (Shultz et al., 2018)*]*

The time window of synaptogenesis can be tracked in humans through gene expression studies. Molecular markers of synapse formation peak within the first two years of life and follow a developmental trajectory that broadly resembles the cortical hierarchy – with subcortical regions and early sensory cortices peaking earlier and association cortices peaking later in terms of gene expression (Figure 2.2). Such spatiotemporal patterning of synapse formation may help direct the experience-dependent modulation of brain regional circuitry, effectively linking the experiences and learning demands of different

developmental stages with brain regions generating new synaptic connections (Silbereis et al., 2016).

In addition to synaptogenesis, the first few years of postnatal development in humans are also associated with profound functional changes of synaptic function. These functional changes at structurally already established synapses may alter the fundamental properties of a given synapse over the course of development and affect future survival of the synapse as well as long-term and experience dependent plastic changes. Functional changes may be as profound as switching the function of γ-aminobutyric acid (GABA) from excitatory to inhibitory, which is believed to occur early in postnatal development (Ben-Ari et al., 2012); or fundamentally altering the temporal integration of signals at excitatory synapses, by altering the role of glutamatergic synapses in learning (Liu, 2004).

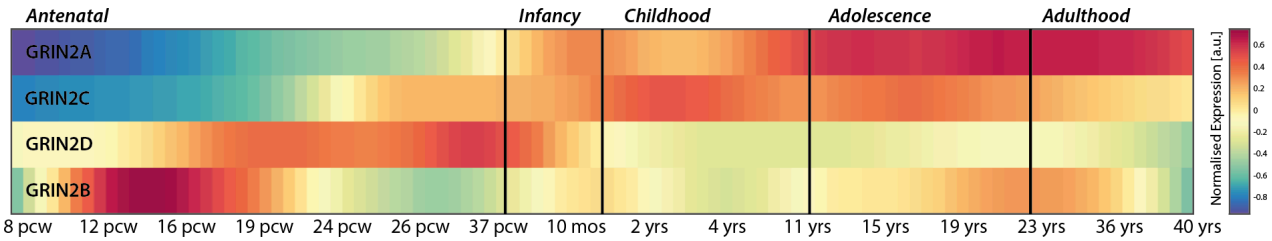

Figure 2.3 – Normalised expression of NMDA-receptor subunit-2 subtypes during development. NMDAR transmission undergoes a dramatic shift during normal development. Normalised expression levels are shown for four different subtypes of the NMDA receptor subunit 2. There is a developmental shift from GRIN2B to GRIN2A over the course of antenatal and postnatal development.

[Data from publicly available repository: Allen Developmental Transcriptome at www.brainspan.org, accessed on 24/07/2018]

Glutamate is the predominant excitatory neurotransmitter throughout the central nervous system (Pankevich et al., 2011). There are different subtypes of glutamate receptors, including both ionotropic receptors (i.e. ion channels that allow direct passage of electrically charged ions across the neuronal cell membrane), and metabotropic receptors (i.e. receptors that exert their downstream effects through an intracellular messaging cascade). Particularly the two ionotropic glutamate receptors – the α-amino-3-hydroxy-5-methyl-4-isoxazolepropionic acid (AMPA) receptor, and the N-methyl-D-aspartate (NMDA) receptor have well characterised roles in excitatory synaptic transmission: Whilst AMPAR mediates fast excitatory postsynaptic potentials mainly consisting of sodium,

NMDAR mediate slower post-synaptic currents of more unselected cations. In addition to the glutamate-gating, NDMAR are also weakly voltage-gated due to larger cations (such as Mg^{2+}) blocking the channel pore at resting membrane potentials. This renders glutamate transmission through NMDAR dependent on recent or concurrent excitatory neurotransmission, which plays a key role in mechanisms of synaptic plasticity (Malenka and Nicoll, 1993). NMDARs are heterotetrameric, usually comprising two GluN1 subunits (encoded in the *GRIN1* gene), and two GluN2A-D subunits (encoded in the *GRIN2A-D* gene family). Interestingly the subunit 2 undergoes a drastic developmental shift in expression – whilst most synaptic NMDAR antenatally contain GluN2B subunits, by around adolescence most cortical synapses will have changed to GluN2A (Monyer et al., 1992; Wenzel et al., 1997). This developmental shift can be seen in the *GRIN2* gene family expression patterns (Figure 2.3). The balance between different ionotropic glutamate receptors (AMPAR/NMDAR) and their subtypes affects most neuronal functions, from message passing (Sanchez et al., 2015), to oscillatory dynamics (Roopun et al., 2008), and synaptic plasticity (Kullmann et al., 1996; Moreau and Kullmann, 2013; Thiele, 2012).

Whilst the first two years of life are characterised by synaptogenesis and the establishment of new functional synapses, over the course of childhood and adolescence, mammalian brains lose a significant amount of their synapses. This pruning of excitatory synapses appears to occur in two distinct stages: (1) in early childhood, pruning targets predominantly functionally immature synapses – characterised by their prolonged postsynaptic responses arising from shifts AMPAR/NMDAR ratio and the NMDAR-subtype expression; (2) in the transition from adolescence to adulthood, functionally apparently mature synapses are significantly pruned: In parts of primate cortex the density of excitatory synapses decreases drastically (up to 40-50%) during this late adolescence (Gonzalez-Burgos et al., 2008).

2.1.1.2 Gliogenesis

The majority of cells in the brain is non-neuronal: glia cells make up >50% of all cells. There are two main types of CNS macroglia: astrocytes and oligodendrocytes. Glial cells (and in particular astrocytes) share embryonal progenitors with neurons, and are produced in distinct spatiotemporally defined waves of gliogenesis (Rowitch and Kriegstein, 2010).

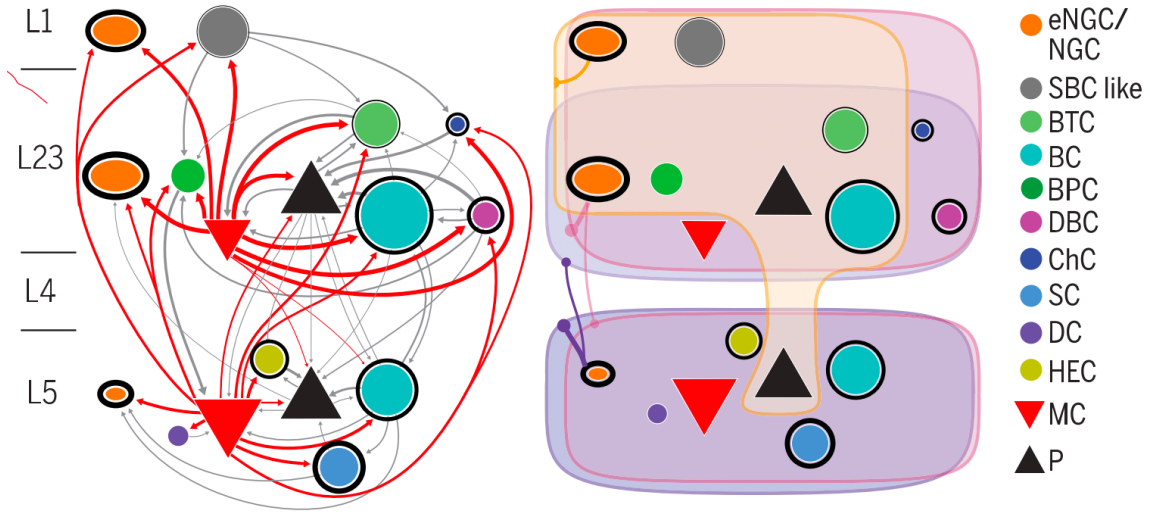

Figure 2.4 – Cortical column intrinsic connectivity structure. Mammalian neocortex shows a laminar organisation, in which different cell subtypes follow certain connectivity principles. Thalamocortical afferents mainly target cells in layer 4, whilst corticocortical output mainly derives from L2/3 pyramidal cells. Predominant synaptic connectivity patterns within a cortical column for different morphologically defined cells is are shown in the left panel. The right panel shows presumed non-synaptic (volume conduction) connectivity between neuroglia cells and other neuronal subtypes.
This connectivity follows three broad patterns: There are highly connected 'master regulator' cells that provide broad inhibitory connectivity across the cortical column (*eNGC/NGC* – elongated neurogliaform cells / neurogliaform cells; *MC* – Martinotti cells). Some interneuron subtypes selectively target other interneurons (Interneuron-selective interneurons: *BPC* – bipolar cell; DC – deep projecting cell; *SBC-like* – single-bouquet cell-like cell); Other interneuron subtypes selectively target pyramidal cells, alongside some connectivity to the same subtype (pyramidal-neuron-targeting interneurons: *BC* – basket cell; *BTC* – bitufted cell; *ChC* – chandelier cell; *DBC* – double-bouquet cell; *HEC* – horizontally elongated cell; *SC* – shrub cell)

[reproduced with permission from (Jiang et al., 2015)*]*

Astrocytes and their precursors are established soon after neurogenesis as a possible terminal differentiation for radial glia (which act as precursors to both astrocytes and cortical neurons). Committed astrocyte precursors then migrate towards their final position, and – apart from in response to injury or insult – are largely quiescent after terminal maturation there. The peak of astrocytogenesis in animal models occurs in late prenatal or early postnatal development. Mature astrocytes play an important role in glutamate metabolism and potassium homoeostasis, and they assume this role during early postnatal development. This functional maturation (unlike astrocytogenesis, and migration) is directly dependent on neuron-astrocyte interactions (Yang et al., 2013).

Oligodendrocytes are produced in three distinct waves during embryonal, foetal and postnatal development, arising from progressively more dorsal origins and unlike astrocytes continue active genesis and functional remodelling until late in life. Compared

to astrocytes, the peak of their genesis occurs later in postnatal development. In rodents (where this can be measured empirically), oligodendrocyte genesis peaks at a developmental stage comparable to mid-to-late infancy in human development (Dutta and Sengupta, 2016).

2.1.2 Maturation of micro- and macrocircuits

Alongside (and closely related to) the changes at single cells and synapses, significant changes also occur at higher organisational levels. Throughout infancy and until late in childhood, there are significant changes of functional organisation at the level of integrated neuronal microcircuits (i.e. within a brain region, at the level of a single 'cortical column'), as well as in the coupling between distinct macroscopic brain regions.

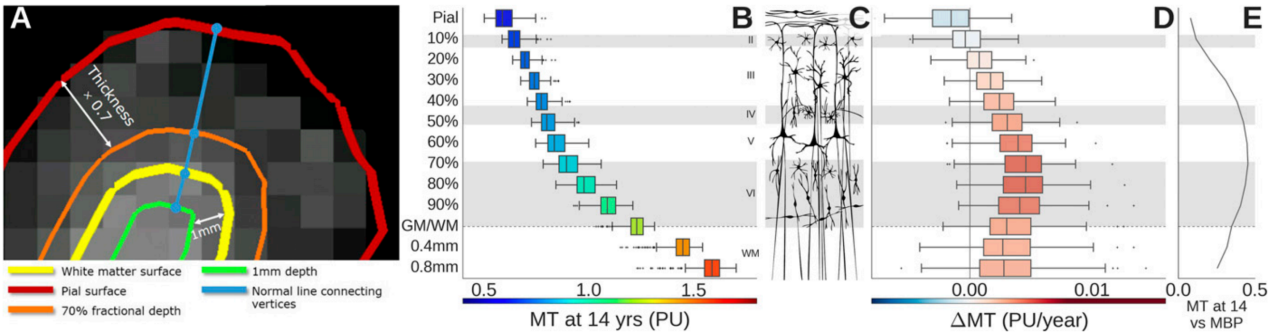

Figure 2.5 – Magnetisation transfer (MT) mapping of intracortical myelination. (A) Illustration of how fractional cortical depths are defined for MT measurement. (B) Increasing cortical depth is associated with a higher degree of cortical myelin content reflected in increased magnetisation transfer (maximum in the white matter). (B-E) However, rates of MT change show a different profile, with the largest developmental increase occuring on cortical layers IV – VI.

[reproduced with permission from (Whitaker et al., 2016)*]*

Mammalian cortex is arranged in layers that follow certain generic connectivity principles and are organised into functional units in adults (Figure 2.4). Developmental changes in the function of these microcircuits is mostly related to changes in the synaptic connectivity: synaptogenesis, synaptic pruning, and myelin maturation all contribute to the changing functional integration at these cortical columns. In experimental animal models such developmental changes can be tracked at the level of single cells. These studies give a detailed picture of neuronal integration into functional circuits that emerges at different times in development within specific functional domains (Ko et al., 2013).

In normally developing children, there is limited access to measures of microcircuit maturation empirically. Neuroimaging and non-invasive neurophysiological recordings offer one strategy to assess maturation of cortical microarchitecture. In particular, quantitative analysis of structural magnetic resonance imaging has recently provided more detailed insight into regional variations in the developmental trajectories of different areas in the cortex, with measures of cortical myelin linking macroscopic changes in cortical structure (T1/T2 signal changes, cortical thickness) with the cellular mechanism (e.g. intracortical myelinisation and oligodendrocyte homeostasis, shown to be remodelled until late in life (Deoni et al., 2012; Hill et al., 2018). Local cortical circuits achieve their mature myelination and thickness at different times in development – with primary cortices maturing earlier than association cortices, some of which may only mature in the third decade of life. Furthermore, myelination changes more within specific aspects of the cortical microcircuit (Figure 2.5). At least some of this spatiotemporal distribution is patterned through expression of myelination relevant genes. Notably, cortical regions that mature later play a more central role in cortical networks, assuming hub-like positions (Vértes et al., 2016; Whitaker et al., 2016)

This regionally patterned maturation of local circuits is further shaped through maturation of corresponding large-range white matter connections. Most of the structural modules in the human connectome are already in place and structurally connected by the age of 2 years, with subsequent developmental changes – that continue until late adolescence – including extensive changes in regional myelinisation of white matter tracts. This reshaping of existing structural connections over the course of childhood brain development leads to more efficient networks with an increasingly close correlation between functional and structural network architecture (Hagmann et al., 2010; Kaiser, 2017).

2.1.3 Functional integration of whole-brain dynamics

There are significant changes in the composition, structure, and function of neuronal networks at all levels throughout childhood – ranging from changes in the ratio of specific neurotransmitter receptors to maturation of regional brain connectivity. The combination of all these changes has a significant impact on whole-brain function at different stages of development, something that can become observable in whole-brain functional brain recordings as afforded by fMRI and EEG in healthy children and adolescents.

EEG is characterised by ongoing oscillatory activity that shows characteristic distributions over the scalp and is significantly affected by age. Overall, there is an increase of the frequency of the predominant rhythms with age – whilst in the neonate, most of the activity is in the lower frequency bands (delta to theta range), by mid-childhood, a faster predominant rhythm in the alpha range should normally have been established. Whilst EEG in the neonatal period and early infancy during sleep is often polymorphic, and transitions between different stages are relatively diffuse, throughout childhood, more discrete and recognisable sleep patterns emerge during the transition from infancy to childhood and continue to evolve until adolescence (Eisermann et al., 2013).

Electrophysiological markers of sensory processing also show distinct neurodevelopmental changes. The mismatch negativity – a stereotyped event-related potential (ERP) associated with surprising or novel sounds – starts off as a positive response in neonates (Kushnerenko et al., 2007). In later childhood, ERPs tend reduce in their amplitude and latency, usually approximating the responses seen in adults closely by puberty (Uppal et al., 2016). More complex cognitive tasks show a developmental improvement in performance that is closely correlated to increased long-range synchrony, suggestive of increased network efficiency later in development (Uhlhaas et al., 2009).

Functional networks can also be evaluated using fMRI across a broad range of children – including neonates and infants who will tolerate the scans whilst asleep (Fransson et al., 2007), and older children as young as about 6 years old (Van Essen and Glasser, 2016). Functional imaging studies of brain networks associated with specific function indicates that functional integration across a network reflects is associated with domain-specific mechanisms that increase efficient processing for those tasks (Weiss-Croft and Baldeweg, 2015). Network changes are also apparent in functional network descriptions derived from resting state recordings of children at different ages. Evaluation of these resting state network changes is methodologically challenging – resting state functional connectivity estimates are sensitive to movement artefacts, which itself is age dependent (Power et al., 2012; Tierney et al., 2016). However, measures derived from these functional connectivity studies broadly reflect the kinds of changes observed in the structural connectome: Over the course of development, functional networks organise in an architecture structure with reduced characteristic path lengths, increased global efficiency and reduced network clustering coefficients (Hulvershorn et al., 2014).

2.2 Disruptions of fundamental oscillatory rhythms: Insights from epilepsy

Epileptic seizures are defined as the occurrence of signs and/or symptoms caused by excessive, hypersynchronous activity in the brain (Fisher et al., 2005). Epilepsy is defined as the persistent tendency of a patient to experience these epileptic seizures and represents a heterogeneous mixture of aetiologically diverse neurological conditions (Thomas and Berkovic, 2014). Whilst epilepsy remains a clinical diagnosis (Fisher et al., 2014), in many cases there are associated abnormalities on EEG recordings, such as spike-and-wave discharges, or spreading fast activity at the onset of a seizure (a more detailed description of different EEG features will be given in section 2.2.2). Clinical features and EEG patterns together allow classification of different epilepsies into particular electroclinical syndromes. In childhood, these are particularly diverse reflecting both a diverse range of underlying aetiologies, and the interaction of those aetiologies with developmental processes. In the following section I discuss the features of classically recognised electroclinical epilepsy syndromes of childhood.

Despite this diversity of electroclinical epilepsy syndromes, there are some key features across them that are preserved (indeed justifying the shared diagnostic label of 'epilepsy' across these conditions). These include particular EEG features both during epileptic seizures and during interictal 'epileptiform' discharges. Some of these can be identified with relatively high reliability and are strongly suggestive of a diagnosis of epilepsy (Adachi et al., 1998; Schulz et al., 2000; Smith, 2005). Some such features can be related to basic mathematical properties of dynamic systems, which I discuss in section 2.2.2.

This section gives an insight into (1) into both the diversity of epilepsy, which in childhood unfolds across a wide range of diverse syndromes; and (2) some key dynamic features in the measurable brain signals that allow linking the diverse abnormalities within a common mathematical framework.

2.2.1 Epileptic syndromes of childhood

The diagnosis of epilepsy is constantly evolving in line with novel insights into the underlying brain pathology afforded by improvements in neuroimaging (Adler et al., 2017; Neal et al., 2018), genetic and genomic testing (Martin et al., 2014; McTague et al., 2018;

Oates et al., 2018) and increasing efforts to map features associated with different possible syndrome categories (Chowdhury et al., 2014; von Spiczak et al., 2010).

Table 2-1 – List of commonly diagnosed electroclinical epilepsy syndromes. This list contains diagnoses within particular age brackets as summarised in the ILAE 2008 terminology (Berg et al., 2010).

Neonatal Period
Early myoclonic encephalopathy (EME)[1]
Ohtahara syndrome[1]
Benign familial neonatal epilepsy (BFNE)

Infancy
Epilepsy of infancy with migrating focal seizures[1]
West syndrome[1]
Myoclonic epilepsy in infancy (MEI)[1]
Dravet syndrome[1]
Myoclonic encephalopathy in non-progressive disorders[1]
Benign infantile epilepsy
Benign familial infantile epilepsy

Childhood
Epilepsy with myoclonic atonic (previously astatic) seizures[1]
Lennox-Gastaut syndrome[1]
Epileptic encephalopathy with continuous spike-and-wave during sleep (CSWS)[1]
Landau Kleffner syndrome (LKS)[1]
Febrile seizures plus (FS+) (can start in infancy)
Panayiotopoulos syndrome
Benign epilepsy with centrotemporal spikes (BECTS)
Autosomal-dominant nocturnal frontal lobe epilepsy (ADNFLE)
Late onset childhood occipital epilepsy (Gastaut-type)
Epilepsy with myoclonic absences[2]
Childhood absence epilepsy (CAE)[2]

Adolescence-Adult
Juvenile absence epilepsy (JAE)[2]
Juvenile myoclonic epilepsy (JME)[2]
Epilepsy with generalised tonic-clonic seizures alone[2]
Progressive myoclonus epilepsy (PME)
Autosomal dominant epilepsy with auditory features (ADEAF)
Other familial temporal lobe epilepsies

Other categories
Distinctive constellations (e.g. mesial lobe epilepsy with hippocampal sclerosis)
Epilepsies attributed to structural or metabolic causes (e.g. malformations of cortical development)

[1]Diagnoses usually considered within the epileptic encephalopathy spectrum; [2]Diagnoses within the genetic/idiopathic generalised epilepsy spectrum

This is reflected in the frequently updated official classifications released by the International League Against Epilepsy (ILAE) (Commission on Classification and

Terminology of the International League Against Epilepsy, 1989; Fisher et al., 2005; Scheffer et al., 2017).

The most recent iteration of the ILAE classification does away completely with officially approved syndrome classification, instead focussing on intersections of aetiological, EEG and clinical categories to support clinical decision making (Smith, 2005). However, up to this most recent version, lists of recognised electroclinical syndromes were an integral component of the ILAE classification. The ones included in the 2010 ILAE classification (Berg et al., 2010) are summarised and grouped according to their age-of-onset in Table 2-1 .

This list focusses on syndromic diagnosis where epilepsy is the primary feature. There are many other conditions of childhood that are associated with epilepsy, which generally classified according to the overall diagnosis, rather than the particular features of patients' epilepsies. Examples for this are the various epileptic phenotypes that can be associated with cerebral palsy (Bruck et al., 2001), complex neurodevelopmental syndromes such as Angelman's syndrome (Pelc et al., 2008), or epilepsies that are associated with a clear structural cause, such as focal cortical dysplasia (Thornton et al., 2011), or polymicrogyria (Perucca et al., 2014).

This list of syndromes where epilepsy is the primary pathology, does however allow a number of observations:

1. Most electroclinical epilepsy syndromes are very age specific – the majority of the diagnostic labels listed start within a clearly defined age range, which fall into distinct developmental stages (broadly categorised here into neonatal period, infancy, childhood, and adolescence).
2. The most severe epilepsy syndromes appear to cluster earlier in life – this is particularly true for the epileptic encephalopathies, which make up a majority of primary electroclinical epilepsy syndrome diagnoses in the neonatal and infantile age categories (Berg and Rychlik, 2015).
3. On the whole, the majority of electroclinical syndromes (that are not attributed to structural or metabolic causes) are diagnoses made in the paediatric age ranges, with only a smaller number of epilepsy syndromes seen in older patients, typically with an onset in the young adult (e.g. juvenile myoclonic epilepsy).

The close relationship between development and epilepsy will be discussed in the following sections using three broad groups of conditions to map out the distinct patterns observed: (1) Epilepsies that are attributed to structural or metabolic causes, which are some of the most common epilepsies across different age groups; (2) Epileptic encephalopathies, which is a group of devastating epileptic disorders that occur mostly in early childhood and infancy; and (3) Idiopathic generalised epilepsies (more recently relabelled genetic generalised epilepsies), which are highly heritably epilepsy syndromes that can have an onset in late adolescence and young adults. These categories are presented here as pragmatic tools for thinking through issues associated with epilepsies and are not perfectly discrete conceptual entities – for example, some patients with a diagnosis of an early epileptic encephalopathy have an identifiable underlying structural abnormality. Yet this selection will illustrate some of the breadth of the clinical reality when considering the epilepsies in childhood.

2.2.1.1 Epilepsies attributed to structural or metabolic causes

The particularly high incidence of epilepsies in the first decade of life is a reflection both of the inherent susceptibilities of the developing brain, particularly in infancy (Rakhade and Jensen, 2009), but also the comparatively high incidence of acquired brain injuries, developmental structural abnormalities and inborn errors of metabolisms in this age group.

Acquired brain lesions: Epilepsy on the background of perinatally acquired brain lesions (e.g. haemorrhages, congenital infections, hypoxic-ischaemic encephalopathy) account for a large proportion of epilepsy-associated disease burden globally (World Health Organization, 2005). Patients with perinatally acquired brain lesions and epilepsy are also often affected by additional impairment and disability, such as the motor and cognitive impairments in the context of cerebral palsy (Ignjatovic, 2009).

Structural abnormalities in brain development: Epileptogenic abnormalities in structural brain development range from those that are highly epileptogenic, usually presenting with devastating epilepsies in early childhood (e.g. polymicrogyria, tuberous sclerosis (Leventer et al., 2008), to those that may present with focal onset epilepsies later in life (e.g. focal cortical dysplasias (Kabat and Król, 2012)).

Neurometabolic conditions: Seizures can be the manifestation of inborn errors of metabolism in infants and children. The mechanisms by which neurometabolic disorders

cause seizures ranges from resultant energy deficiency (e.g. Glucose transporter-1 deficiency), neurotoxicity (e.g. organic acidurias), specific impairment of neuronal inhibition (e.g. pyridoxine dependent epilepsy) and many more (Dhamija et al., 2012; Lado et al., 2013).

More recently, a range of autoimmune conditions have emerged that can cause seizures because of direct antibody mediated disruptions of neuronal circuits – most notable are the autoimmune encephalitides, such as NMDA-receptor encephalitis, or MOG-antibody encephalitis (Ogawa et al., 2017; Wandinger et al., 2011).

As a group, epilepsies associated with structural or metabolic causes, despite being aetiologically diverse, have particular clinical significance because of their treatment implications:

1) *Primary prevention:* Perinatally acquired brain lesions are often preventable with appropriate obstetric and neonatal care, making them the single biggest preventable cause of epilepsy (Newton and Garcia, 2012).
2) *Secondary prevention:* For a number of inborn errors of metabolism, the neuronal dysfunction (and over time lasting brain damage) can be halted by circumventing the impaired metabolic pathway (e.g. ketogenic diet in GLUT-1 deficiency, (Kass et al., 2016)). This can stop seizures and prevent further acquired brain damage.
3) *Effective treatment:* Where epilepsy is the clear product of a structural brain lesion, or associated with the presence of neuronally-specific autoimmune antibodies, removing this underlying cause can lead to complete seizure freedom, and effectively cure a patient of their epilepsy (Spencer and Huh, 2008).

2.2.1.2 Epileptic encephalopathies

In some early onset epilepsy syndromes, it is believed that the burden of abnormal, epileptic activity in and of itself causes more widespread disruption of brain dysfunction and impacts on the development of patients. These syndromes are commonly referred to as epileptic encephalopathies, and sometimes (in reference to their peak incidence) as early infantile epileptic encephalopathies (EIEE).

The EIEEs are characterised by (1) widespread and often pervasive electrographic paroxysmal abnormal activity, (2) mixed and multiple seizure types in individual patients, (3) and cognitive, behavioural and neurological deficits associated with the burden of EEG

abnormalities (Khan and Al Baradie, 2012). Many patients with EIEEs can be classified into recognisable syndromes that are clustered around typical ages of onset (cf. Table 2-1). One of the most common EIEEs is West syndrome. It is classically defined as the triad of infantile spasm (a particular seizure type), hypsarrhythmia (an interictal EEG abnormality pattern), and associated developmental delay or even regression with an onset in infancy (Pavone et al., 2013). West syndrome is closely associate with a set of genetic and neurodevelopmental syndromes, such as Down syndrome, tuberous sclerosis or Aicardi syndrome, but West syndrome is also recognised in children without any underlying, causative diagnosis.

Where identified, the range of underlying causes may be either very focal lesions (Chugani et al., 2010), or widespread neurodevelopmental abnormalities as part of a genetic syndrome (Paciorkowski et al., 2011). Yet the age and developmental stage at which these underlying causes find their expression in the triad of signs and symptoms that defines West syndrome are very specific. For the majority of patients this particular constellation of signs and symptoms does not start before the age of three months, and evolves by the age of two years (Kurokawa et al., 1980).

Individual patients with a diagnosis of an EIEE are classically thought to transition between different age-specific phenotypes during their development, which often means that they will change diagnostic labels in terms of their electroclinical epilepsy syndromes. One classic example is the relationship between Ohtahara syndrome (an EIEE of the neonatal period), West syndrome and Lennox-Gastaut Syndrome (an epileptic encephalopathy of childhood). In one classic description of the natural history of patients with Ohtahara syndrome, a majority of surviving patients would go on to develop West syndrome and subsequently Lennox Gastaut syndrome.

Taken together, this suggests that the individual diagnostic categories that have been established for the different age-of-onset epileptic encephalopathy syndromes, are not necessarily identifying aetiologically distinct pathologies. The diversity of underlying causes that can converge to the same EIEE phenotype suggests that the EIEE syndromes reflect a common pathway of how severe, and epileptogenic abnormalities in brain function can express themselves in the developing brain. Within certain limits, differences between clinical syndromes are more likely to result from the particular developmental

context in which the epileptogenic dysfunction unfolds than underlying aetiology differences between patients.

2.2.1.3 Idiopathic/Genetic Generalised epilepsies (IGE / GGE)

A contrasting group of epileptic syndromes that stands out from the ILAE classifications in Table 2-1 are 'idiopathic' (now termed 'genetic') generalised epilepsy syndromes of childhood and adolescence: Childhood absence epilepsy, epilepsy with myoclonic absences, juvenile absence epilepsy, juvenile myoclonic epilepsy, and epilepsy with generalised tonic-clonic seizures alone. These epilepsies are typically 'isolated' epilepsy syndromes – unlike the epileptic encephalopathies, they usually occur in patients without additional severe neurodevelopmental issues and are often effectively treatable with anti-epileptic medication.

This group of conditions has long been recognised to show a high heritability with a likely high presumed genetic burden (Berkovic et al., 1998). Yet despite the transformative effect of genomic technologies on epilepsy-gene identification in the EIEEs, the molecular and genetic basis for these 'genetic' generalised epilepsies have remained elusive to date.

However, despite the lack of an age of 'genetic generalised epilepsy gene discovery', several insights have been made from genetic studies in these patient cohorts:

- Copy number variations (duplications or deletions of segments of the genome) are more common in patients with GGEs than controls (a possible genetic risk factor burden shared with a range of neurodevelopmental syndromes) (Helbig et al., 2013; Mullen et al., 2013)
- Multi-gene approaches reveal that some of the risk of developing GGE syndromes can be explained through mutations in a number of genes that share a physiological mechanism (e.g. GABA transmission) (May et al., 2018)
- A recent review of genome-wide association studies revealed a single signal with genome-wide significance as risk allele for genetic generalised epilepsies near the vaccinia-related kinase 2 (VRK2) gene, and the Fanconi anaemia, complementation group L (FANCL) gene (International League Against Epilepsy Consortium on Complex Epilepsies, 2014). Interestingly, a nearby locus has previously been described as the location of a schizophrenia risk allele (Donnelly et al., 2012).

Having briefly reviewed the nosology of epilepsy from a clinical perspective, I will now turn to phenotyping in terms of dynamic in the setting of dynamical systems.

2.2.2 A dynamic systems perspective on epilepsy and epileptic seizures

As illustrated above, the term 'epilepsy' encompasses a broad range of distinct phenotypes, with an even greater range of sometimes overlapping genetic and pathophysiological mechanisms. How then can this multitude of mechanisms and phenotypes be recognised as a common entity (or indeed a group of related entities). Mathematics and theoretical physics may offer helpful perspectives here: In understanding the brain as a time varying, dynamical system, we can identify some general principles that emerge from the manifold molecular disruptions that appear to give rise to clinical epilepsy in patients.

Mathematical dynamic systems can be defined through differential equations that define the evolution of the system states over time. Where there are non-trivial relationships (e.g. nonlinear relationships) between the system states, they become difficult to predict and can show non-intuitive relationships between changes in the parameters of the system, and the dynamic behaviour in time (Rabinovich et al., 2006).

One of the key insights we can draw from these mathematical dynamical systems, is that the 'switch' between, e.g. noisy low-amplitude activity, and high amplitude regular oscillations as seen in the transition into an epileptic seizure, can be thought of in terms of 'bifurcations' of a dynamical system. Bifurcations occur when a small, smooth change in a model parameter qualitatively changes the behaviour of the model. They can be classified according to the sort of changes that can be observed in the data on approaching and transitioning the bifurcation point (Izhikevich, 2007).

This has become an attractive perspective for understanding and classifying epileptic seizures. The amplitude and frequency changes recorded in ictal EEG just before and just after the onset (or offset) of a seizure can be used to identify the kind of bifurcation that best captures the paroxysmal dynamics that occur (Jirsa et al., 2014).

Figure 2.6 illustrates features of some of the different bifurcation types that can arise from just changing a single parameter in a dynamical system (Codimension-1 bifurcations). These vary in the signal changes that become visible as the bifurcation point is approached (e.g. gradual increase in amplitude in the supercritical Hopf bifurcation). And somewhat surprisingly, the vast majority of seizure onset- and offset patterns as observed on the EEG

can be classified as corresponding to a set of these mathematical forms – highlighting some universal and invariant properties of seizure dynamics (Friston, 2014).

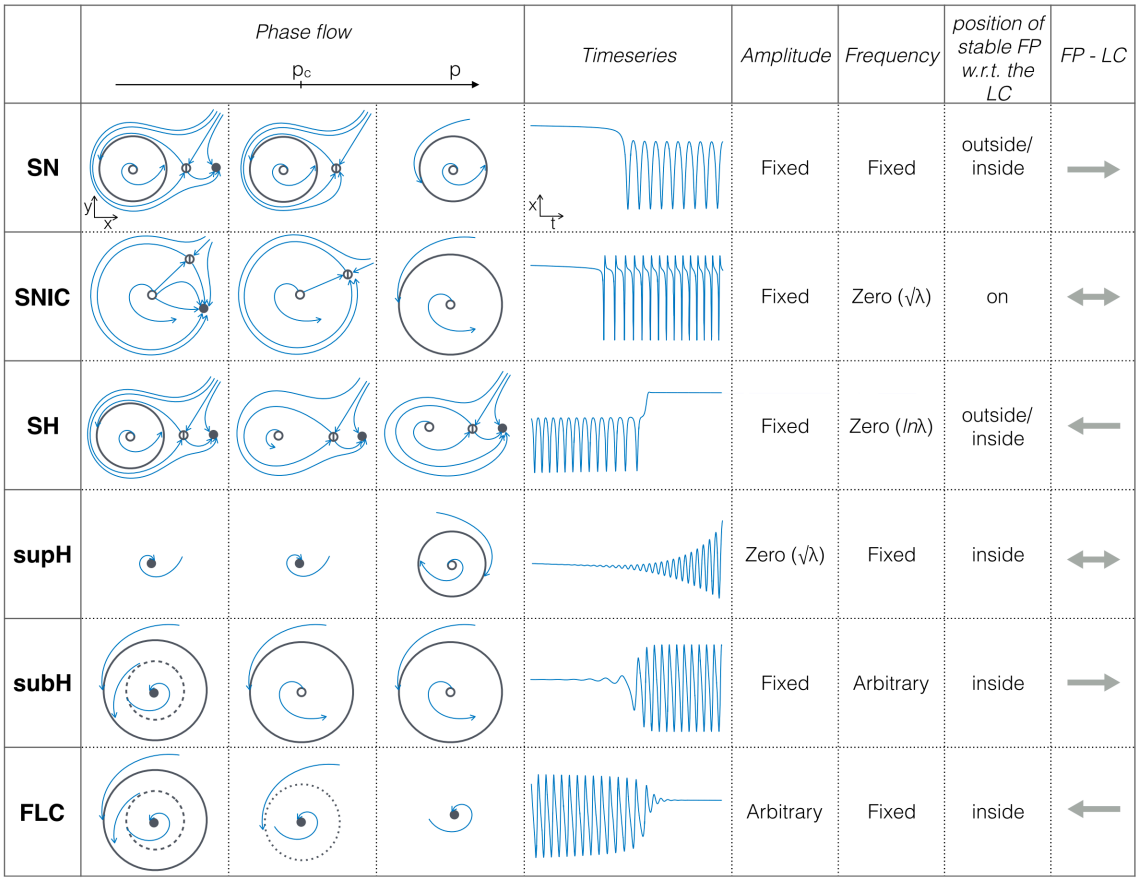

Figure 2.6 – Codimension-1 bifurcation types. This figure illustrates the different bifurcations types that link fixed points (where the system does not change over time) and oscillatory regimes. In the oscillatory states, the system moves around a so-called limit cycle, a closed trajectory in state space that acts as an attractor.
The phase flow columns illustrate the change of the dynamic landscape as relevant parameters of the system are changed. These are represented in a two-dimensional representation of the system's state (e.g. excitatory, and inhibitory neuronal activity), with blue lines illustrating individual trajectory as the system evolves in time. Small circles indicate fixed points, large circles indicate limit cycles; solid lines are stable FP/LC, dashed lines are unstable FP/LC. The timeseries column illustrates how the bifurcation would appear if only one state is recorded over time. The remaining columns show amplitude-frequency behaviour, where λ signifies the distance from the critical transition point. The penultimate column indicates whether the FP is inside or outside the stable LC. The last column indicates the possible directions the bifurcation can be crossed – i.e. whether it is an onset bifurcation, offset bifurcation, or both.

FLC – Fold Limit Cycle, FP – fixed point, LC – limit cycle, SH – saddle homoclinic bifurcation; SN – saddle node bifurcation; SNIC – saddle node on invariant circle bifurcation; subH – subcritical Hopf bifurcation, supH – supercritical Hopf bifurcation;

[reproduced with permission from (Saggio et al., 2016)*]*

These descriptions of invariance and universality stand in stark contrast to both observations of phenotypic diversity at the whole-brain level (as highlighted in the sections above), and the particulars of interacting cellular dynamics and spatiotemporal

organisation of individual neurons during an epileptic seizure (Liou et al., 2018; Smith et al., 2016). Yet the particular perspective offered by these dynamical systems approaches may help us to organise our understanding of these multi-level system particularities along conceptually relevant categories. Similar approaches has already helped integrating observations at different spatial and temporal scales (Proix et al., 2018; Richardson, 2011). In the following chapters of this thesis, I will use a range of different computational models of neuronal function (discussed in more detail in Chapter 3), each of which (1) is a mathematical formulation of a dynamical system, and (2) describes biophysical properties of neuronal systems at a particular scale (e.g. neuronal membrane, single neuron, or neuronal population / circuit). It is through the inherently universal representation of abnormal dynamics within the context of a dynamical system, that these models may help us to link apparently diverse underlying biological mechanisms into coherent categories of disease.

2.3 Disruptions of cognitive function in adolescence: Lessons from schizophrenia

Whilst some of the most severe neurological conditions emerge during the earliest developmental stages of infancy and childhood (as discussed for, e.g., the epileptic encephalopathies above), there is a separate group of conditions whose incidence peaks later in development: Many neuropsychiatric disorders, such as obsessive-compulsive disorder, mood disorders, and schizophrenia are diagnosed most commonly in older teenagers or in young adults. Despite this comparatively late onset, these conditions can significantly impact and alter a previously healthy young person's life (Erskine et al., 2015), and are associated with significant morbidity and mortality (Boys et al., 2003; Patton et al., 2009; Wittchen et al., 1998).

Schizophrenia is a cardinal example of one such condition. The most commonly reported onset of symptoms is at approx. 20-25 years, depending on gender and cohort (Häfner et al., 1993; Sham et al., 1994). Prior to this the child or young person may have been developing normally, with no reported symptoms. Yet despite the apparently later onset, many cognitive processes are altered profoundly in patients: perception, decision making, social cognition are all impaired in patients with the diagnosis – often to the point where independent living becomes impossible and the patient may become a danger to himself

or others if left untreated (Porcelli et al., 2018; Strauss and Cohen, 2017; Takeda et al., 2018). And even with the best currently available treatment, a diagnosis of schizophrenia is associated with a reduction in life expectancy of approximately 20 years (Laursen et al., 2014).

Like many epilepsies, schizophrenia has long been recognised as a heritable neurodevelopmental disorder with a likely high genetic burden (Cardno et al., 1999; Sullivan et al., 2003). Yet – and again like e.g. idiopathic/genetic generalised epilepsies – whilst many candidate and risk factor genes have been identified (Freedman et al., 1997; Greenwood et al., 2012; Schizophrenia Working Group of the Psychiatric Genomics Consortium, 2014), almost none of these insights about the genetic background have been translated into an immediate clinical benefit for patients yet.

On the other hand, the combined insights from neuroscience and molecular genetics do give us biological insights into the development of different neuropsychiatric conditions, including schizophrenia. In the following section of this chapter, I discuss the particular vulnerabilities of the adolescent brain that may predispose patients to developing particular neuropsychiatric conditions in this crucial time period. I then illustrate how molecular and computational perspectives give us complementary insights into the pathophysiological mechanisms underlying the disorder.

2.3.1 Adolescence as a sensitive period during brain development

Many neuropsychiatric syndromes have their peak onset during adolescence (Paus et al., 2008) – including substance abuse disorders, mood disorders, anxiety disorders, and schizophrenia (Figure 2.7). This particular developmental timescale suggests that the contemporaneous developmental changes in neurobiology confer particular vulnerabilities to disruptions in brain functions that manifest in neuropsychiatric conditions (as opposed to e.g. the early infantile epileptic encephalopathy, that seem to disrupt more fundamental neuronal processes that are established earlier in neurodevelopment).

There are a broad range of key developmental changes occurring in the human brain around the time of puberty and later adolescence (Asato et al., 2010; Blakemore and Choudhury, 2006; Uhlhaas et al., 2009). The most widely accepted global brain changes during adolescence include synaptic pruning, and intracortical and white-matter tract myelination (cf. earlier sections of this chapter, Figure 2.1).

Figure 2.7 – Peak onset of different neuropsychiatric conditions in adolescence. Many neuropsychiatric disorders have their peak onset during adolescence.

[Reproduced with permission from (Paus et al., 2008)*]*

Evidence of a reduction of the number of synapses (i.e. synaptic pruning) after childhood has been provided by detailed, opportunistic studies on post-mortem human brain specimens (Huttenlocher and Dabholkar, 1997; Huttenlocher and de Courten, 1987). Quantitative experiments in non-human primates then confirmed that the loss of these synapses is likely accelerated around puberty (Bourgeois and Rakic, 1993). Furthermore, putative electrophysiological markers of intracortical connectivity (i.e. low-frequency band power during sleep on EEG, (Tononi and Cirelli, 2006)) also show their largest developmental change during adolescence and can be assessed across large, representative samples in normally developing human participants (Feinberg and Campbell, 2010). This developmental change in electrophysiological measures of cortical function also appears to be correlated with MRI-measurable, structural markers of cortical structural maturation during childhood and adolescence (Buchmann et al., 2011).

In terms of neuronal function, there seems to be an optimum amount of intracortical 'connectedness' for network-level computations. In a simple neural net trained to recognise words from phonetic input, pruning initially improves performance, before there is a decline in further performance (Figure 2.9). Notably in the case of 'over-pruning', the model starts 'recognising' words in periods of no input – a notion that is relevant for computational models of schizophrenia, suggesting that an 'excess' of certain brain changes can confer a behaviour consistent with e.g. a psychotic phenotype.

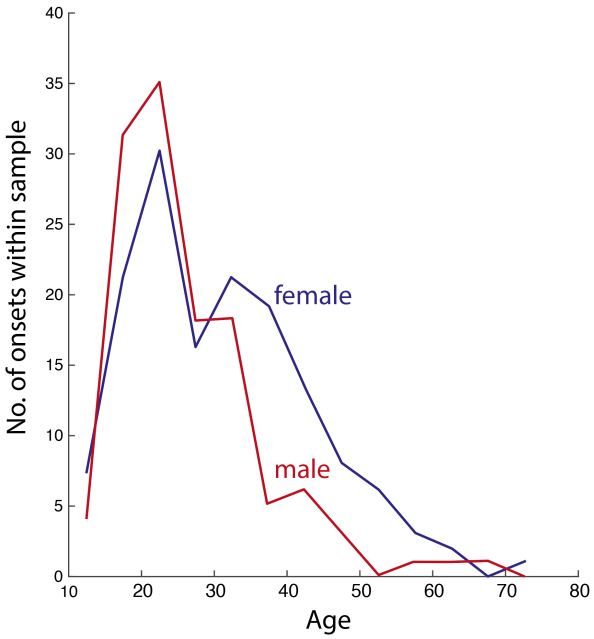

Figure 2.8 - Age of onset distribution in schizophrenia.

This figure shows the age of onset of schizophrenia for male and female patients identified as part of a Swedish family study of schizophrenia.
Both male and female patients show a peak incidence during adolescent brain development at around 15-25 years of age.

[Figure adapted from (Sham et al. 1994)]

Whilst these general principles of synaptic pruning are observable across the whole brain, maturation does not unfold evenly across the cortex. Many of the structural measures of brain development in adolescence that we can derive through neuroimaging methods point towards protracted maturational profiles particular in higher order association cortices (Gogtay et al., 2004). Thus, adolescence may be a particularly sensitive period during brain development, during which higher order cognitive processes (that rely on the high-level association cortices) can be selectively impaired (Fuhrmann et al., 2015).

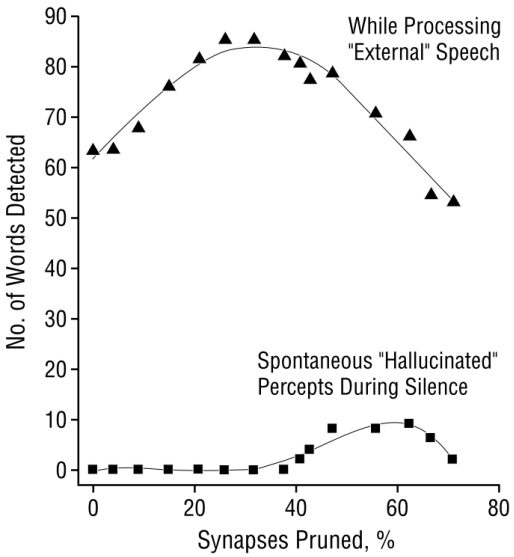

Figure 2.9 – Effects of synaptic pruning on computational performance. The plot shows performance of neural net against gradual reductions of synaptic connectivity. This neural net recognises words from degraded phonetic input. Gradual 'Darwinian' pruning of synaptic connections (where the strongest synapses survive) initially increases performance, with a clear optimum at around 30% pruning.
At higher rates of pruning, the performance drops, and the model starts increasingly recognising words even during periods of complete silence.

[Figure reproduced with permission from (McGlashan and Hoffman, 2000)*]*

Changes in cortical myelination can give quantitative insights into brain maturation during adolescence. When assessed with structural MRI across a broad adolescent age

range, Whitaker et al. have reported evidence of locally patterned changes in cortical thickness and intracortical myelination during adolescence. Interestingly, the topology of these structural markers of brain maturation was associated with regional expression of myelination-related genes, as well as schizophrenia risk genes (Whitaker et al., 2016).

2.3.2 Features of schizophrenia

Schizophrenia is a chronic psychiatric condition with a peak onset during adolescence (Figure 2.8). A clinical diagnosis made on the basis of a mixture of positive and negative psychiatric symptoms, summarised in Table 2-2. The diagnosis can be made based on symptoms present for a significant portion of at least a one month period (unless treatment is initiated earlier), and a significant portion of patients experience chronic ongoing symptoms throughout their lives (Lewis and Lieberman, 2000).

Table 2-2 - DSM-5 Criteria for the diagnosis of schizophrenia.
[Adapted from: (Tandon et al., 2013)*]*

Two or more of the following must be present for a significant portion of the time during a 1-month period (or less if sufficiently treated). At least one of these should include symptoms 1-3

1) Delusions
2) Hallucinations
3) Disorganised speech
4) Grossly disorganised or catatonic behaviour
5) Negative symptoms (i.e. diminished emotional expression or avolition)

Schizophrenia is related to a number of syndromes that share some symptomatology (particularly psychosis-related symptoms) but differ in their long-term outcomes and associated other psychiatric symptoms (such disorders include acute psychotic disorders, schizoaffective disorders, and schizophreniform disorders).

Cohort studies of genetically at-risk individuals, and retrospective reviews of patient data revealed that clinically diagnostic symptoms can be preceded by more subtle abnormalities at a younger age, including infancy, and pre-diagnosis adolescence (Jones, 1997). Children who later developed schizophrenia were more likely to have abnormal gross motor development in infancy (Fish and Kendler, 2005), as well as more likely to have overt psychotic symptoms by the age of 11 (Fisher et al., 2013).

Whilst positive symptoms (e.g. delusions, hallucinations, etc.) most commonly lead to diagnosis, the presence or absence of negative symptoms (e.g. social withdrawal,

diminished emotional expression) is more predictive of future outcomes for individual patients (Fenton, 1991). Presence of significant negative symptoms indicates more severe disease of likely insidious onset with potentially longer periods of untreated symptomatology. Early treatment with antipsychotic medication appears to have a small but significant beneficial longer-term effect, but both recurrent positive and persistent negative symptoms are present in a majority of patients even >10 years after initial presentation (Hegelstad et al., 2012), irrespective of early treatment status.

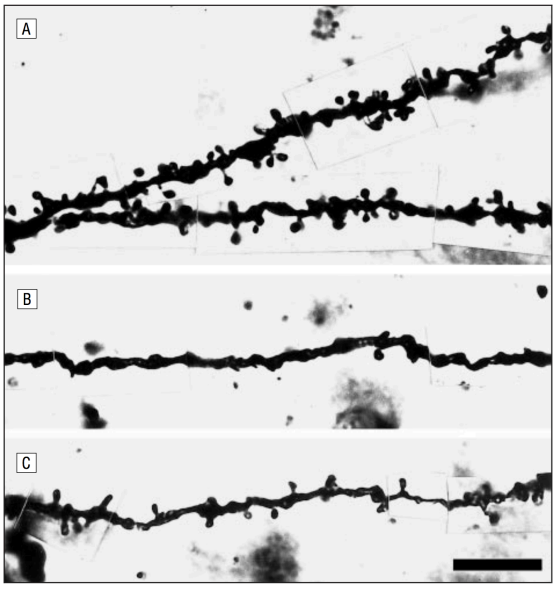

Figure 2.10 – Dendritic spine reduction in patients with schizophrenia. Golgi-stained widefield microscopy images are shown for dendritic processes of human post-mortem specimens from (A) a control subject, and (B-C) patients with schizophrenia, illustrating the reduction in the number of dendritic spines in patients.

[Figure reproduced with permission from (Glantz and Lewis, 2000)*]*

Whilst the psychiatric symptoms are diagnostic in schizophrenia, it has long been recognised that neurological signs, structural brain abnormalities and electrophysiological markers of dysfunction exist in patients. The most frequently reported neurological impairments include sensory dysfunction and motor coordination deficits (Schröder et al., 1991).

Structural brain imaging has further provided insights into potential anatomical correlates of schizophrenia. A number of studies showed that schizophrenia is associated with progressive volume loss, with the earliest involved brain areas consistently reported to be prefrontal cortex, temporal pole and mesial temporal lobe (DeLisi, 2008). Those brain areas showing the most severe volume loss are also affected by microscale changes in cellular organisation – including those indicative of reduced intracortical connectivity, such as reduced number of dendritic spines (Figure 2.10).

There is a number of well recognised electrophysiological markers frequently observed in patients with schizophrenia, even EEG recordings have not (yet) been included in routine clinical practice (Owens et al., 2016). A number of these are changes in event-related potentials evoked during particular sensory paradigms (e.g. P50, P300, Mismatch Negativity /MMN), whilst changes in stimulus-induced gamma frequency power. Furthermore sleep spindles and slow waves during sleep have been reported to be reduced in patients with schizophrenia (D'Agostino et al., 2018). Specific electrophysiological markers have been the point of much theoretical discussion in regard to their underlying mechanisms, some of which will be reviewed in Chapter 7 of this thesis. Recent genetic and genome-wide association studies have aimed to relate these electrophysiological 'endophenotypes' to risk alleles in schizophrenia and have identified a dosage effect – where increased schizophrenia risk allele burden is broadly associated with more severe electrophysiological deficits (Hall et al., 2015).

Over the last couple of decades, some of these observations in schizophrenia have been re-contextualised through insights gained from genetics. Amongst a range of studies applying different approaches, we have gained the following three key insights:

- Population-wide *common* variants – such as specific catechol-O-methyltransferase (COMT – a catecholamine degrading enzyme) associated haplotypes – can be associated with an increased risk of developing schizophrenia (Shifman et al., 2002).
- Individually *rare* genetic variants (including copy number variations (Malhotra and Sebat, 2012)) account for a large proportion of the genetic risk in schizophrenia (Donnelly et al., 2012; Purcell et al., 2009; Walsh et al., 2008) – this is now believed to be a contributing factor to many common neurodevelopmental disorders (Gibson, 2012).
- Genes affected by *rare, de novo* mutations that confer a high risk of schizophrenia disproportionally affect postsynaptic density formation, and more specifically the NMDA-receptor complex, and the activity-related cytoskeleton-associated protein (ARC) complex (Figure 2.11).

2.3.3 A computational neuroanatomy of schizophrenia

The picture of schizophrenia that emerges is complex, as outlined above: Schizophrenia is associated with cardinal psychiatric symptomatology, as well as a wide range of associated neuroanatomical, neurophysiological and synaptic/genetic abnormalities. Several theories have been developed to bring together some of these apparently disparate features of the wider syndrome and relate them to one another.

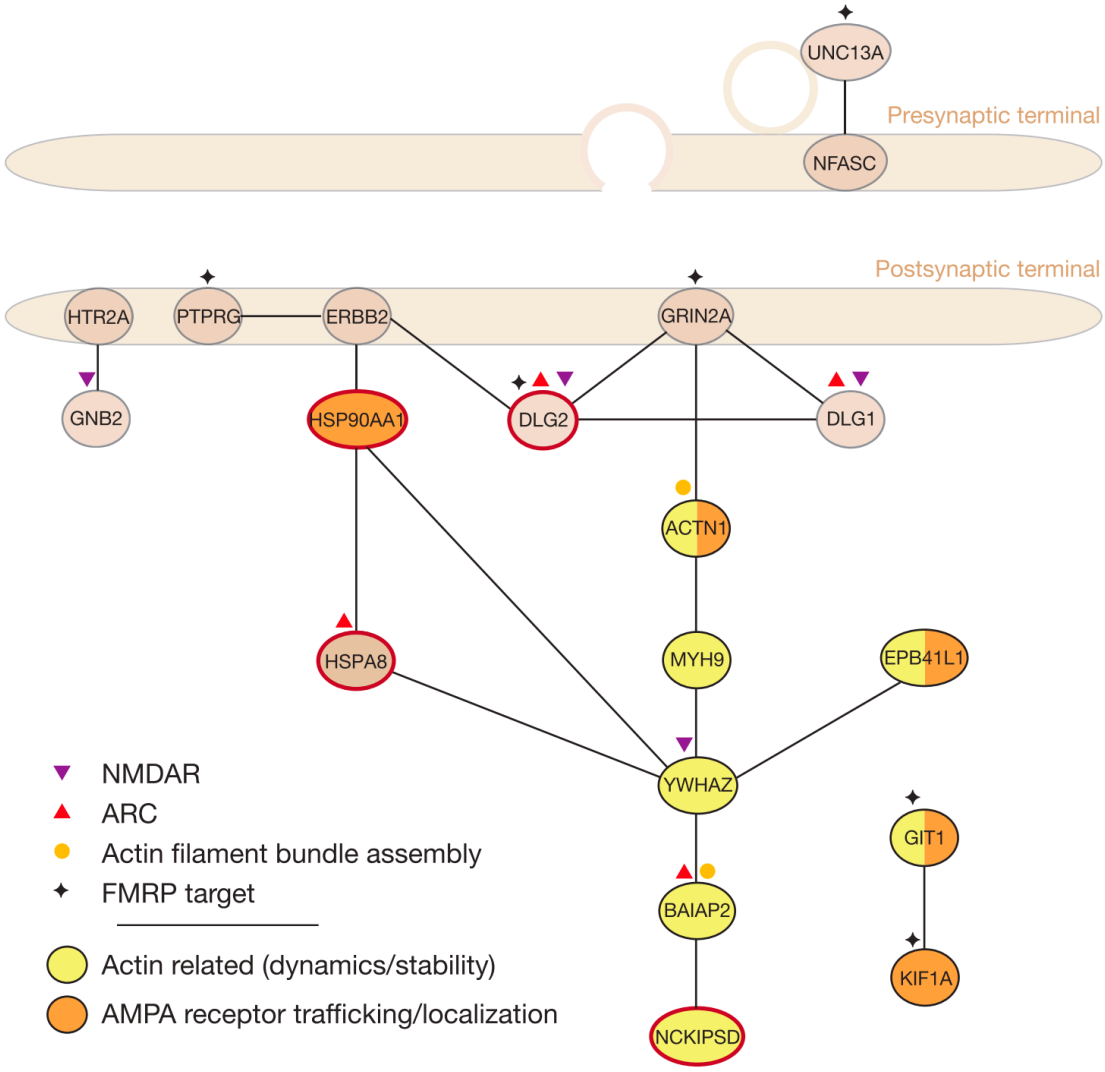

Figure 2.11 – Postsynaptic gene network affected by *de novo* mutations in schizophrenia. The figure indicates the roles of genes affected by *de novo* mutations in schizophrenia. Different functional groups are marked; red outlines indicate loss of function; black outlines indicate non-synonymous mutations.
NMDAR – N-methyl-D-aspartate receptor; ARC – activity-related cytoskeleton-associated protein complex; FMRP – fragile X mental retardation protein.

[Figure reproduced with permission from (Fromer et al., 2014)*]*

One such perspective is offered by the so called 'dysconnection hypothesis' (Friston et al., 2016a) / 'disconnection hypothesis' (Friston, 1998; Weinberger, 1993). Crucially this hypothesis integrates observations from molecular genetics and pharmacology (principally the central role of NMDAR transmission and its modulation by neuromodulatory systems), and features of psychopathology and neurophysiology in schizophrenia. The central proposition is that the physiological effects of abnormal modulations of NMDAR-mediated plasticity (e.g. the context sensitive modulation of gain in cortical pyramidal cells) cause impairments in local (i.e. intrinsic) and between-region (i.e. extrinsic) coupling, which in turn explain the related phenotypes.

Providing evidence for this hypothesis critically rests on linking abnormal synaptic coupling and psychopathology. In order to make this link, there needs to be a mapping between the different components of cortical neuronal circuitry, and the specific normal and abnormal computations conducted that are completed by this circuitry. Predictive coding offers one framework in which this link is possible (Friston and Kiebel, 2009): According to this framework, higher cortical areas generate predictions of future sensory states and attempts to minimise the error between these predictions and actual sensory evidence that is encoded in prediction errors in lower cortical areas. This process requires the brain to learn a generative model of the world and infer the setup of this model from (degenerate) sensory input. This Bayesian account of normal cognitive function (particularly in reference to normal sensory processing) provides quantitative predictions of different types of signals used for processing: top-down/backward predictions, bottom-up/forward prediction errors and a precision term that describes the uncertainty around them (Friston, 2012; Shipp, 2016). This Bayesian computation can be related directly to different aspects of neurobiology: the stereotyped, or 'canonical' connectivity between cortical layers and between cortical regions is believed to be closely associated with different processes and quantities in predictive coding. This link can be formalised through quantitative dynamic models of cortical circuitry that are formally related to simpler representations of neural population dynamics (which will be introduced in more detail in the following Chapter 3), but relate more closely to the presumed predictive coding processes in the human brain: The 'canonical microcircuit' (Bastos et al., 2012).

This quantitative link between neurobiology and computational processes has allowed the testing of a range of hypotheses in regards to normal brain function (Bhatt et al., 2016;

Brown and Friston, 2013; Garrido et al., 2008), as well as dysfunction in human neurological and psychiatric disorders (Breakspear et al., 2015; Friston, 2005; Lawson et al., 2015; Ranlund et al., 2016).

In specific regard to schizophrenia, the dysconnection hypothesis – contextualised through the predictive coding paradigm and its quantitative links between neurobiological processes and neuronal computation – has led to a number of key insights. First, the psychopathology observed in schizophrenia is consistent with an abnormal encoding of precision of the sensory evidence – i.e. because of abnormally high precision weighting of incoming sensory evidence, the brain is unable to discount random variations and considers everything as meaningful (Adams et al., 2013). Second there are a number of synaptic mechanisms that could result in the downstream failure to control the gain on cortical superficial pyramidal cells – which corresponds to the abnormally high precision in the predictive coding scheme. These synaptic mechanisms include NMDAR dysfunction, GABAergic abnormalities and excitation-inhibition imbalance, all of which have been described in schizophrenia (Friston et al., 2016a). Third, a range of macroscopic structural and functional connectivity measures indicates that there is indeed an apparent reduction in connectivity (Pettersson-Yeo et al., 2011), with the patterns broadly consistent with predictions made on the basis of the dysconnection hypothesis – indicating a particular disruption of prefrontal circuits, where NMDAR hypofunction has long been implicated in schizophrenia phenotypes (Akbarian et al., 1996).

2.4 Conclusion

Considering the breadth of the topics discussed in this chapter, the above illustrations are not meant to represent a fully comprehensive manual on dysfunction in the developing brain. Rather, by focussing on laying out key stages in (particularly postnatal) human brain development, and temporally relating them to quite contrasting neurodevelopmental disorders – epilepsy, and schizophrenia – this chapter illustrates a number of insights and questions that the rest of this thesis will build on.

Different neurodevelopmental disorders reveal distinct vulnerabilities of the developing brain. Both the epilepsies and schizophrenia carry significant morbidity for affected patients. The way in which they disrupt normal brain function appears to be associated with the particular vulnerabilities of the developmental stage in which they most

commonly emerge. For example, in the early infantile epileptic encephalopathies (EIEEs), the fundamental oscillatory activity of the brain is continuously disrupted to the extent that the implicit dysconnection causes global delay across all developmental domains. In contrast, whilst schizophrenia can be disabling, the cardinal symptoms are recognisable as affecting particular cognitive and affective domains and are associated with a relatively localised dysfunction (or dysconnection) in specific neuronal circuits. And crucially these circuits also appear to be the ones that undergo the biggest changes later in development, suggesting that adolescence is a neurobiologically predestined time of vulnerability for the development of schizophrenia.

Molecular mechanisms reveal distinct but overlapping mechanisms in neurodevelopmental disorders. The examples discussed above highlight the diversity of causes in neurodevelopmental disorders. The disorders described in this chapter capture two ends of a likely spectrum: Whilst in the very early onset epilepsies, up to 75% of patients may have a single gene mutation detected by clinical testing (Oates et al., 2018), such single gene diagnostics play no role in schizophrenia to date. However, even at these two extremes of how molecular / genetic mechanisms are expressed in the individual, they also share key features in terms of their molecular pathologies.

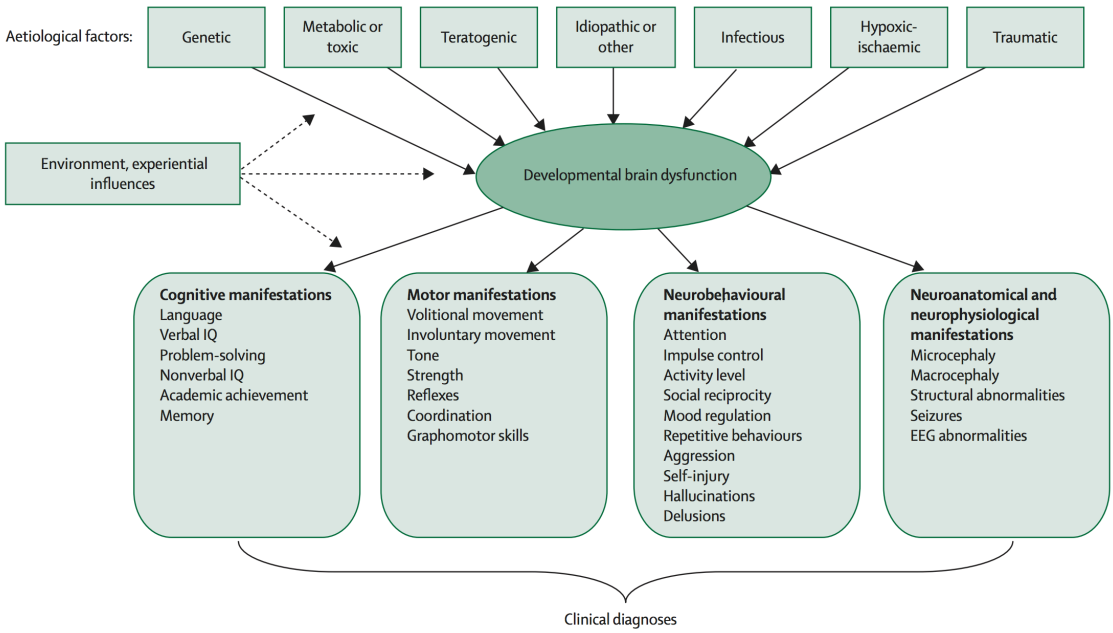

Figure 2.12 – Model of developmental brain dysfunction.

[Reproduced with permission from (Moreno-De-Luca et al., 2013)*]*

The genetics of both epilepsy, and schizophrenia indicate that both could be considered 'synaptopathies' – pathologies whose main mechanism is dysfunction at the synapse (Luo et al., 2018). In terms of the genetics underlying this functional disruptions, the study of neurodevelopmental disorders has revealed novel mechanisms of human disease inheritance (e.g. the surprising role of copy number variations in a broad range of neurodevelopmental disorders (Grayton et al., 2012; Magri et al., 2010; Mulley and Mefford, 2011). Lastly and in many ways surprisingly, disruptions of similar mechanisms apparently can produce different phenotypes within the broad set of neurodevelopmental disorders: NDMAR dysfunction is now a well described cause of both epileptic encephalopathies (Lemke et al., 2014; Lesca et al., 2013), and schizophrenia (Demontis et al., 2011). In fact autoimmune disruption of NMDAR transmission in NMDAR-antibody encephalitis (the focus of Chapter 6 of this thesis) causes both neuropsychiatric symptoms and epileptic seizures at different stages of the disease (Crisp et al., 2016; Wandinger et al., 2011). In fact, the recent wave of discoveries indicating the shared molecular basis for a broad range of neurodevelopmental disorders has brought with it a revival of the idea that these conditions are differential expressions of mixed risk factors (Figure 2.12).

Microscale mechanisms and phenotypic observations need to be linked to understand dysfunction in the developing brain. Both within the epilepsies, and for neurodevelopmental disorders more broadly, there is a gap between our understanding of molecular background, and the range of phenotypes observed. In the remainder of this thesis I outline with empirical examples, how quantitative models of neuronal function and dynamics may offer an approach to close this gap – both those reproducing dynamic signatures of epileptic seizures, and those recapitulating some of the computational deficits in schizophrenia. In most of neuronal dysfunction there is no one-to-one mapping between molecular determinants of neurobiology and system function as a whole. Using quantitative models to identify a set of key mechanisms that underpin specific aspects of a diverse set of phenotypes will mediate the mapping between molecular mechanisms and patient phenotypes and allow us to reduce the complexity of this challenge.

An approach like this is necessary if we want to reconcile the phenotypic specificity of the neurodevelopmental disorders under consideration with the apparent continuum of genetic and molecular causes that underlie them. In the following chapter, I indicate how specific sets of models can be utilised this approach. I then test a range of such approaches

across a number of model systems of neurodevelopmental disorders – ranging from heterologous expression systems to identify the dynamic effects of an epilepsy-related *SCN1A*-mutation (Chapter 4), to human pharmacological experiments reproducing key features of the psychopathology in schizophrenia (Chapter 7).

3

Computational modelling of neuronal dynamics §

3.1 Empirical data for computational neurology

3.1.1 EEG as quantitative measurements of whole-brain function

The invention of electroencephalography (EEG) in the early 20th century facilitated a revolutionary insight into the dynamic behaviour of the human brain. For the first time, clinicians and researchers were able to examine direct evidence of brain function, in both normal human participants and patients with neurological conditions (Jung and Berger, 1979). Clinically this new way of assessing brain function has had significant impact on our understanding of a number of neurological and psychiatric conditions, but none more so than epileptic seizure disorders.

EEG measures potential differences across the scalp: through electrodes placed on different locations on the scalp surface, one can record sub-millisecond fluctuations in electric potentials that can be shown empirically to correspond to brain function. Electrical signals measured on the scalp depend on potential changes that are generated locally in the

§ Parts of this chapter have been published as part of the following book chapter:

Rosch, R.E., Cooray, G., Friston, K.J. 2017. Dynamic causal modelling of dynamic dysfunction in NMDA-Receptor Antibody Encephalitis. In Erdí, P., et al. (eds.), Computational Neurology and Psychiatry. Springer Publishing, Cham, Switzerland.

The review included here was conceived by me, Gerald Cooray and Karl Friston. All theoretical work and review of computational modelling included in this chapter was completed by myself.

cortical extracellular space by neuronal activity. Post-synaptic potentials and action potentials cause changes in permeability of neuronal membranes which allows for transmembrane flow of charges ions to and from the extracellular space. This space, however, is limited to only small inter-cellular clefts because of the high number of neuron-to-neuron connections and a densely packed variety of glial cells. Glial cells therefore play an important role in regulating extra-neuronal ion concentrations and influence actively the distribution of charges ions across the extra-neuronal domains.

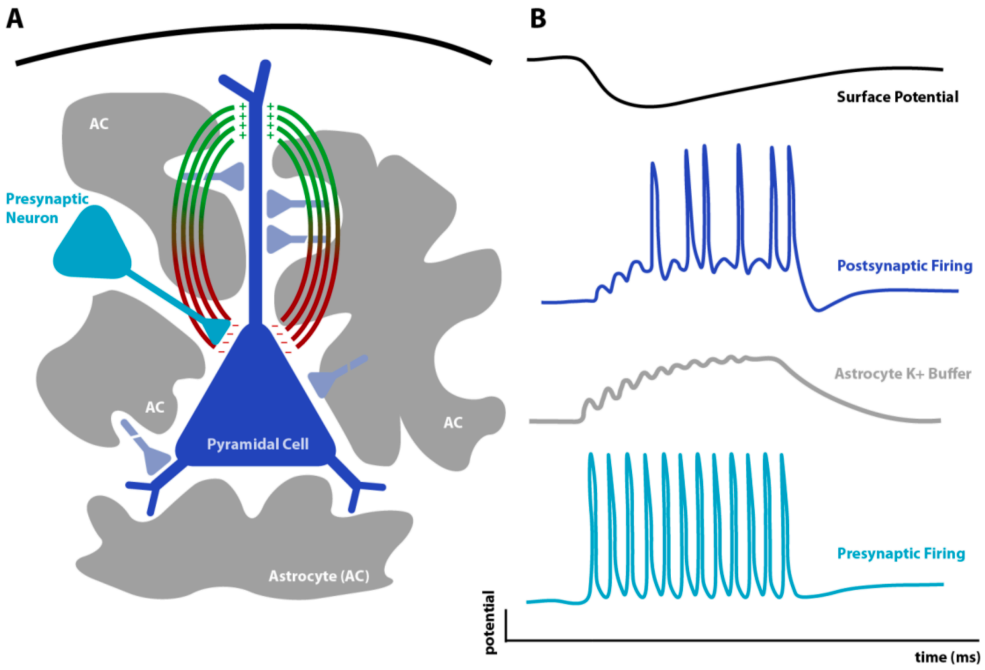

Figure 3.1 – Cortical contributors to the EEG signal. (A) Potentials as measured by EEG electrodes are generated by local dipoles that originate from spatially separate differences in extracellular potentials. These are generated for example through synaptic transmission as illustrated here. (B) A presynaptic neuron fires and causes local excitatory post synaptic potentials (EPSPs) and possible postsynaptic action potentials. These are associated with an extracellular ionic shift, leading to a locally more negative extracellular potential. This extracellular space is tightly regulated by astrocytes, which buffer and distribute ion concentration changes through a gap-junction coupled network. The difference between negatively charged membrane patches, and other parts of the membrane generates a dipole, along which microcurrents equilibrate the differences. These slower changes in dipoles along the postsynaptic membrane (rather than fast, self-limiting action potentials) are reflected in the composite potential measured at the scalp (top panel). The direction (positive or negative) of the surface potential depends on the direction of the dipole.

[Figure adapted from (Speckmann and Elger, 2005)*]*

Where changes in the extracellular potentials are spatially segregated, they will invoke an electromagnetic field along which current flows, i.e. a dipole. All of the excitable

membranes that permit transmembrane currents contribute to this extracellular field, generating a composite, indirect measure of neuronal function. However, there are certain characteristics of neuronal potential changes that cause it to have a higher impact on the electrical activity at the scalp: (1) proximity to the surface means less information is lost through volume conduction and noise effects, (2) signals with longer time constants (i.e. slower decay) such as post-synaptic potentials are more likely to summate over time and have sufficient synchrony to produce a large enough 'populations shift' to be measurable, (3) channel opening that does not generate a significant ionic current does not contribute much to the overall signal (e.g. GABA channels opening at rest, where the Cl^- reversal potential is similar to the existing membrane potential, (Buzsáki et al., 2012)). These characteristics are best met by the dendrites of pyramidal cells: superficially located, these are long apical dendrites summating many post-synaptic potentials, a large proportion of which are excitatory (Figure 3.1).

Whilst the concept that abnormal electrical activity causes epileptic seizures predates the invention of EEG, much of our current physiological understanding and clinical decision making is based on EEG recordings from patients suffering from epilepsy (Eadie and Bladin, 2001). Descriptions and analyses of EEG recordings have remained virtually unchanged since its original conception. Its clinical use largely rests on the description of visually recognisable features and their phenomenological categorisation, with the exception of some recently adopted advanced source localisation algorithms (Zschocke and Hansen, 2012). But relying just on these visually apparent pathological patterns does not capture the entire breadth of information that is available in an EEG recording.

One of the main advantages of EEG (that is shared with magnetoencephalography, MEG) is its temporal resolution, which still remains unparalleled when it comes to investigating the human brain *in-vivo*. This results in rich datasets that capture interacting fluctuations of electric activity across frequencies that may be two or three orders of magnitude apart. Whilst surface EEG recorded non-invasively from the scalp has a limited spatial resolution, it does allow for the simultaneous recording of neuronal activity across almost the entirety of the cortical surface. Furthermore, the spatial resolution limitations can be addressed where clinically necessary by using invasive EEG recordings from neurosurgically placed electrodes.

Much of the information contained within these datasets is not accessible through visual inspection alone, but rather needs to be elicited utilising more quantitative analysis methods (Tong and Thakor, 2009). Applying such quantitative analysis methods has led to the description of a wide variety of novel electrophysiological findings. For example, analysing the correlation between the time series of individual EEG channels will yield a matrix of channel-to-channel correlation measures. These can be read as indicators of functional connectivity, with the results interpreted in a graph theory framework as functional network analysis (Bullmore and Sporns, 2009). Another example can be found in the recent emergence of cross-frequency coupling as a potentially important mechanism for neuronal computation: Quantitative analysis of power at different EEG frequencies in humans has shown that amplitude fluctuations are measurably modulated and time-locked to the phase of concurrent slower frequency oscillation, known as phase-amplitude cross-frequency coupling (Canolty and Knight, 2010).

3.1.2 Microscale neurophysiological recordings

Dynamic changes in permeability of neuronal membranes can be measured through a number of cellular neurophysiology techniques referred to collectively as patch-clamp recordings. In principle the concept is based on two steps: (1) isolating small membrane compartments (i.e. a *patch*) from influences of surrounding ion concentrations by establishing a tight seal with a glass pipette; (2) enforcing specific electrical conditions, e.g. at a set voltage (known as voltage-*clamp*), mediated via the electrolyte in the clamping pipette (Kornreich, 2007). This set up, together with pharmacological regulation of specific channels or receptors allows the direct measurement of membrane permeability to specific ions under specified electrical conditions. The technique builds on classical voltage-clamp designs, where electrical properties are measured and clamped through a pair of intra- and extracellular microelectrodes (rather than the pipette). The novel pipette approach first established in 1976 (Neher and Sakmann, 1976), however, allows more experimental control, and resolves to the dynamics of even a single channel.

Patch clamp experiments are usually performed in cell / tissue culture, with some successful applications of voltage-clamp paradigms on individual neurons *in-vivo* in animal models (Kitamura et al., 2008). This means that its use to make inference regarding human neuronal function is limited to a specific set of experimental designs:

Human pathology in animal or cell culture models: Where a causative gene mutation for a human condition is known, inference on the disease mechanism can sometimes be made by expressing the mutant gene product in an animal organism or cell line and assessing its functional effects in the model using patch clamp (the focus of Chapter 4 in this thesis). Examples of this include patch-clamp characterisation of gating abnormalities in epileptic conditions associated with calcium-sensitive potassium channels (Du et al., 2005). This approach makes strong assumptions regarding the monogenic cause underlying the respective conditions, and rests on reliably identified molecular causes.

Biopsy-derived tissue culture: Access to neuronal tissue from human probands is rare, but possible in conditions where surgical treatment is an option, or from acute post-mortem specimens. Patch clamp techniques have been applied in cultured slices of tissue from such specimens, resected for temporal lobe epilepsy. Patch-clamp studies in sclerotic mesial temporal lobe tissue from human patients, for example, have identified abnormalities in potassium current dynamics in astrocytes (Schröder et al., 2000).

Patient-derived induced pluripotent stem cells: One of the more recent advances has been the possibility to develop neuronal cultures directly from patient-derived stem cells. These carry the entire genetic make of specific patients and are therefore better models for complex gene-gene interactions. This approach has been applied for example to investigate human epilepsy causing mutations in the voltage-gated sodium channel gene, *SCN1A* and for the first time identify single cell mechanisms through which loss-of-function mutations could produce hyperexcitable cellular phenotypes (Chen et al., 2015).

3.1.3 Molecular determinants of neuronal function

Alongside advances in the detailed quantitative analysis of macroscopic EEG signals in health and disease, there has been an exponential increase in our understanding of the molecular, and to some extent cellular basis of many of the epilepsies and other neurodevelopmental conditions (Helbig et al., 2008; Thomas and Berkovic, 2014). Increasingly, knowledge of associated molecular abnormalities such as the presence of relevant gene mutations or specific autoantibodies against synaptic targets influences prognosis, clinical management, and specific treatment decisions for affected patients. Features of disease-associated molecular abnormalities have also led to a putative understanding of the pathophysiological mechanisms underlying different epileptic seizure disorders. For example, the frequency of mutations in ion channel genes has led to

the concept of epilepsies and other paroxysmal neurological disorders being channelopathies, i.e. disorders in neuronal ion channel function, which can be further investigated in appropriate animal model systems.

However, with the increase in knowledge, new challenges arise. The availability and increased clinical use of testing for specific mutations and autoantibodies has quickly led to the realisation that even apparently specific molecular abnormalities are associated with a wide variety of disease constellations – both in terms of recognisable syndromes and diseases, and some less specific changes (McTague et al., 2018, 2016; C. F. Wright et al., 2015) – in human patients. The same mutation in the voltage gated sodium channel gene *SCN1A* for example can cause a diverse selection of phenotypes within the same family: ranging from comparatively mild phenotypes consisting of childhood febrile seizures, to a severe epileptic disorder characterised by difficult to control frequent daily seizures associated with global developmental delay (Miller and Sotero de Menezes, 2014). Similarly, mutations in the *GRIN2A* gene, coding for a subunit of the N-methyl-D-aspartate receptor (NMDAR) can cause a range of electroclinical syndromes, even within the same family (Lesca et al., 2013).

With the advent of increased genetic and molecular diagnostics, we can thus now empirically identify the molecular context in which the paroxysmal neurological disorders unfold: The available diagnostic tools are focussing us on the persistent and detectable abnormalities at the microscale – such as genetic mutations – that allow for intermittent pathological dynamics to emerge at the whole brain scale.

3.2 The explanatory gap

3.2.1 Different scales in experimental neuroscience

The different empirical perspectives illustrated above open an explanatory gap: On one side there is an increased understanding of the putative molecular and cellular causes of dynamic disorders of the brain; on the other there are macroscale measures of abnormal brain function that, whilst loosely associated with some microscale abnormalities do not allow a direct one-to-one mapping. Bridging this gap is likely to require an intermediate step – a conceptual bridge that can link information about molecular dysfunction with its expression in neuronal function at an intermediate level, the *mesco*scale, in order to

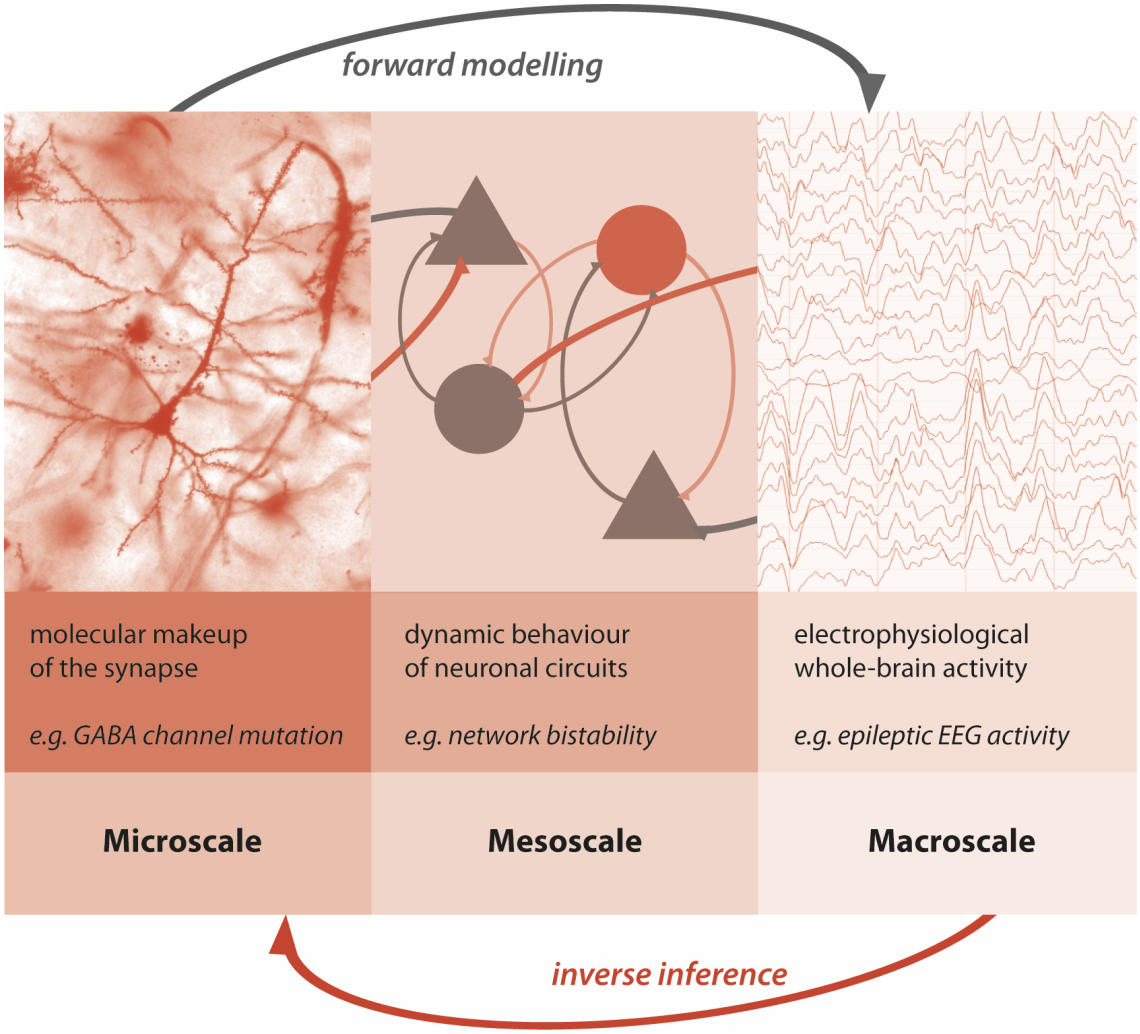

Figure 3.2– Understanding epileptic dynamics at different scales. Different lines of evidence lead to descriptions of pathology on different scales. Clinical syndromes often rely on the description of recognisable phenotypes at the macroscale. Recent advances in understanding associated molecular abnormalities have improved our pathophysiological understanding of many diverse epilepsy and other neurodevelopmental syndromes, but robustly linking clinical phenotypes with microscale abnormalities has proven difficult. Including an intermediate consideration of network dynamics may aid both prediction and allow for addressing the inverse problem of inferring pathophysiology from whole-brain electrophysiological measure.

understand the emergence of phenotypic variability observed in human patients (Freeman, 2000a).

In other areas within the neurosciences, similar approaches are emerging as a necessary step for linking observations at the microscale (e.g. cellular neuronal circuits) with the observation at the macroscale (e.g. organism behaviour). Whilst descriptions of the cellular circuitry may include too many particular details to understand their functional contributions to overall behaviour, evaluating only behaviour of the whole organism may

not sufficiently represent the complexity and the constraints of the underlying neuronal processes. Bridging this gap requires the identification of recurrent themes at an intermediate functional level – such as that of neuronal circuits – that may be implemented through differing neuronal circuits, but produce similar overall effects (Carandini, 2012).
In the context of clinical neurology, a similar approach would suggest that in order to link putative molecular causes (microscale) with diverse disease phenotypes observed in patients (macroscale), the intermediate step needs to be considered: Dysfunction at the level of integrated, neuronal microcircuits (mesoscale, Figure 3.2). Linking molecular abnormalities to *in-vivo* neuronal dysfunction is now a standard component of identifying disease mechanisms in emerging genetics and autoimmune conditions (Pal and Helbig, 2015). Attempts in relating macroscale findings to models of mesoscale neuronal dynamics have been less forthcoming but will be the focus of this chapter. An introduction of population models of neuronal function will be followed by an in-depth discussion of how such models can be used to make inference on the mechanisms underlying specific electrophysiological changes.

3.2.2 Linking phenotype and pathophysiology: An ill-posed problem

The functional validation of possible molecular causes of neurological disease is an essential step in any description of new pathophysiological mechanisms. A candidate genetic mutation that is epidemiologically linked with a specific phenotype may or may not play a causative role in the pathogenesis of the associated condition. In order to increase confidence that a direct biologically causative link exists, evidence that the molecular/cellular pathway affected is involved in neuronal function is considered a standard requirement (Quintáns et al., 2014).
Providing this evidence usually relies on replicating the molecular abnormality in an experimental model organism or cellular system and evaluating the model for any resultant deficits, particularly regarding neuronal function. For example, to provide evidence for the direct pathogenicity of NMDAR-antibodies in the recently described NMDAR-antibody associated encephalitis (Dalmau et al., 2008), the antibody-rich patient cerebrospinal fluid was applied to murine hippocampal slices prepared for voltage-clamp recordings in order to measure the effects of antibody exposure on glutamate transmission. This provided evidence both for acute antagonism of NMDAR by the antibody, as well as chronic reduction of NMDAR associated with antibody exposure (Hughes et al., 2010).

Whilst this approach is powerful, and necessary in order to evaluate candidate molecular causes of neurological disorders in the context of neuronal function, several problems remain unsolved when relying on this approach alone:

- Animal models for human disease: Model systems used to assess the pathological effects of molecular abnormalities are usually non-human organisms or tissues, leaving uncertainty as to whether similar effects would be evident in the human brain.
- Emergent properties at different scales: There may be a gap between individual cell and small circuit abnormalities assessable in an experimental model system, and the inference drawn on larger networks and systems. These models are particularly prone to neglecting emergent properties at different scales (e.g. bistability of a network), and the effects of unknown modulators in the whole system that may enhance or suppress the observed microscale abnormality.
- Human phenotypic variability: An unexpected result of the recent increase in molecular diagnoses in neurology is the discovery of large phenotypic variability even where a molecular cause has been identified and well characterised (Hildebrand et al., 2013). Functional investigations in homogeneous model systems alone do not address the mechanisms underlying phenotypic diversity.

Issues of disease pathology in humans, understanding whole-organism, and delineating relevant categories within phenotypically diverse groups are essential for translating basic neuroscientific findings into clinically relevant advances. In order to start addressing these issues, the inverse problem has to be addressed: How do macroscale abnormalities relate to underlying pathophysiology?

The EEG signal despite containing a lot of rich information is a poor measure of neuronal function at the cellular, or synaptic level: because of the spatial inaccuracies and the summation of many million individual neurons' activity into a composite signal, there are an infinite number of possible neuronal constellations that could cause the same measurable EEG signatures. Attempting to relate this composite, diffuse signal to underlying neuronal dysfunction is thus an ill-posed problem, where no unique solution exists.

Ill-posed problems are common in neuroscience, both in terms of problems researchers encounter when investigating nervous systems (e.g. the source localisation problem for EEG signals (Friston et al., 2008)), and the problems that nervous systems themselves have to address (e.g. the feature binding problem (Di Lollo, 2012)). Pragmatically, these problems are not impossible to solve, as is evident in the successful application of source-reconstruction algorithms in identifying epileptogenic brain areas for surgery (Lantz et al., 2011), and the brain's successful and reliable decoding of visual information (Kawato et al., 1993).

With underdetermined ill-posed problems, providing constraints to the range of possible solutions is crucial (Friston, 2005b). Constraining the problem reduces the space of possible solutions and makes finding a possible, good solution more tractable. These constraints also help in keeping inverse solutions more interpretable and relevant to the scientific question at hand, where applied to inference on neurobiological data.

One way to constrain such inverse problems in neuroscientific research is the use of computational models of neuronal populations as a mesoscale representation of neuronal dynamics. This casts the inverse problem of attempting to infer microscale causes of macroscopic phenomena into a more restricted problem: Assuming basic mechanisms of neuronal function and organisation are met (i.e. the neuronal model applies), which setup of the known circuitry could produce an observed effect (i.e. which specific set of model parameters can produce the observed macroscale response?).

In the following sections, I discuss mesoscale models of neuronal function and how they can be used to link observable measurements of neuronal function across multiple different scales. I introduce the basic concepts underlying neuronal population modelling and focus on methods that will be applied in later chapters of this thesis.

3.3 Biophysical models for empirical neuroscience

Neuronal systems are highly nonlinear coupled systems (Werner, 2007). This means that predicting input-output relationships is challenging and often counterintuitive. One of the great strengths of computational models is that they can be used to explore input-output relationships systematically and help identify some of the otherwise difficult to anticipate effects produced by nonlinear interactions.

The pioneering work by Hodgkin and Huxley (Catterall et al., 2012; Hodgkin and Huxley, 1952) produced one of the first such computational explanations for the observable behaviour of neuronal systems – and by some measures this remains the most successful approach to link empirical observations and underlying neurobiology through the use of computational models. Using empirical voltage clamp measurements from the giant squid axon, they elegantly developed a model of neuronal membrane dynamics based entirely on voltage dependent ion channels that could predict many patterns of neuronal behaviours observed empirically.

Since then, a range of models have been developed across a multitude of different spatial and temporal scales. These range from models describing subcellular compartment dynamics to models describing the output of whole neuronal populations and networks. Because of the spatial scales of measurement, those models that represent whole neuronal populations are particularly informative when relating them EEG measurements.

One of the earliest such models was the Wilson and Cowan neural mass model (Wilson and Cowan, 1972) – they describe the behaviour of a whole set of interconnected neurons not individually but as whole aggregates, based on similar approaches in particle physics. They also provide a justification for this method based, interestingly, not just on its computational tractability, but rather the conceptually different inference this approach enables:

> *It is probably true that studies if primitive nervous systems should be focussed on individual nerve cells and their precise, genetically determined interaction with other cells […] [S]ince pattern recognition is in some sense a global process, it is unlikely that approaches which emphasize only local properties will provide much insight. Finally, it is at least a reasonable hypothesis that local interactions between nerve cells are largely random, but that this randomness gives rise to quite precise long-range interactions.*
>
> (Wilson and Cowan, 1972)

Using this approach, they arrive at a system of two ordinary differential equations, describing a neuronal oscillator consisting of two different populations, one excitatory, one inhibitory:

$$\tau_e \frac{dE}{dt} = -E + (k_e - r_e E) S_e (c_1 E - c_s I + P) \tag{3.1}$$

$$\tau_i \frac{dI}{dt} = -I + (k_i - r_i I) S_i (c_3 E - c_4 I + Q) \tag{3.2}$$

This system describes two neuronal populations, whose current states (E , I : proportion of cells in the population firing) influence each other through weighted connections (c_{1-4} weights of population connections, see Figure 3.3 A. This coupling is mediated through a sigmoid activation function $S_{e/i}$, which acts like a switch integrating all incoming synaptic influences and translating them into a postsynaptic state change within a defined dynamic range (i.e. 0-1). The sigmoid functions are population specific (and can therefore be parameterised independently) and are the source of non-linearity in the model.

Even despite the extreme simplification of these models of neuronal function, a whole range of dynamic behaviours can be reproduced with WC-type models at the scale of neuronal populations or cortical patches (Heitmann et al., 2012; Meijer et al., 2015; Wang et al., 2014). Because of the coupled nonlinearities, however, 'forward' predictions of model behaviour given specific parameters is often non-intuitive and usually requires simulation of the model responses. Repeat simulations for varying parameter values can then be used to establish a link between model parameterisation and overall dynamic responses Figure 3.3 B.

These parameter/response relationships can be exploited in order to make inference on model parameters underlying a given observation. Faced for example with noisy measurements of a population oscillation (Figure 3.3 C), one can use systematic variations of a model parameter to identify the specific parameter value that best fits the data (Figure 3.3 D, illustrated for the stimulating current parameter *P*). However, even adding a single additional free parameter (e.g. the connection parameter c_1) creates a complex model prediction error landscape that is much more difficult to optimise (Figure 3.3 E) – an important problem that I will return to later.

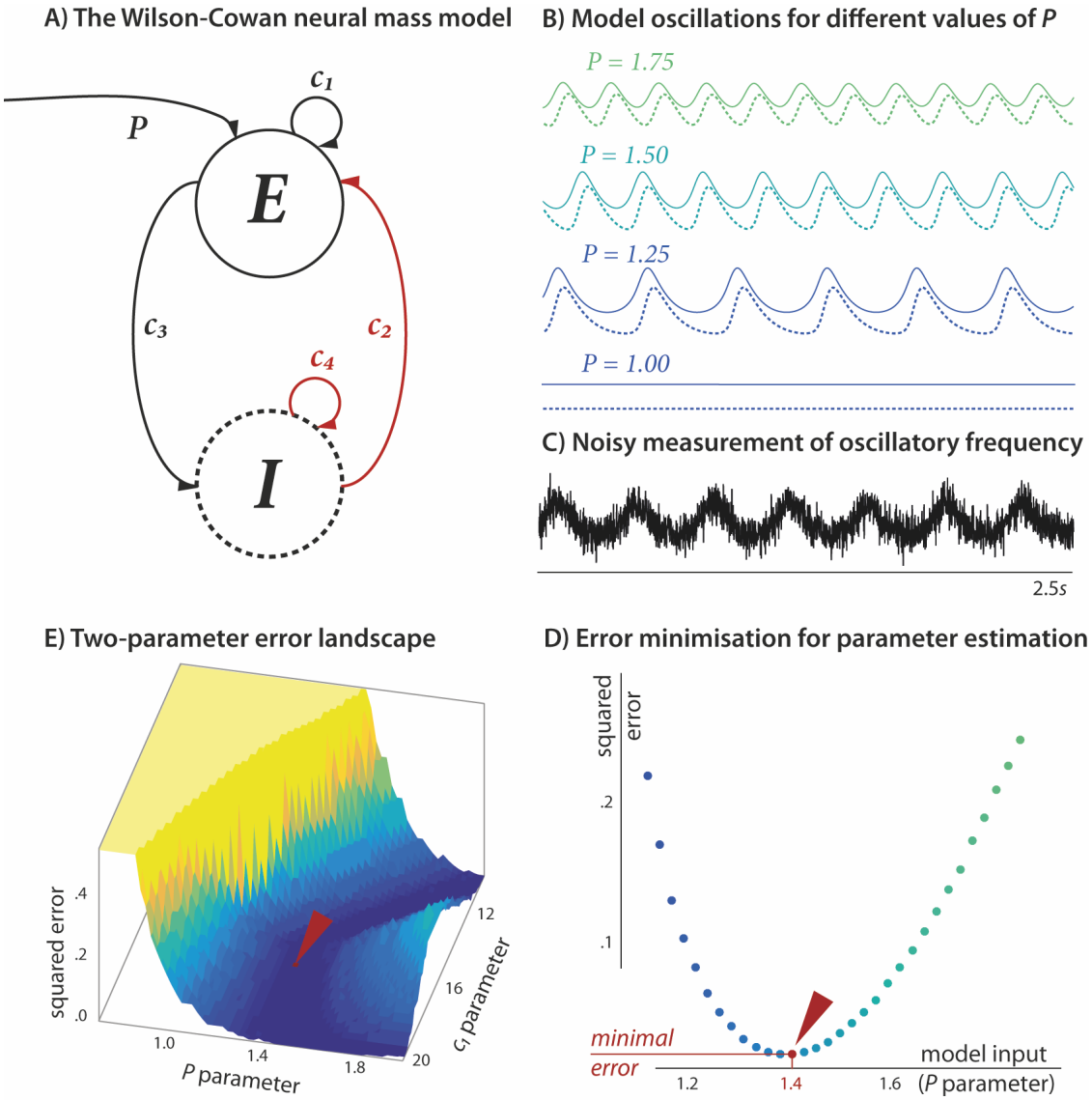

Figure 3.3 – The Wilson-Cowan neural mass model. (A) The model consists of one inhibitory and one excitatory neuronal population, coupled through synaptic connections of a specific connection strength (c_i parameters). These can be excitatory (*black*) or inhibitory (*red*). The system receives external stimulating current input (*P* parameter) and acts as a neuronal oscillator. (B) The model generates particular oscillation patterns for different parameter constellations – this figure illustrates steady state oscillatory responses with decreasing values for the input parameter *P*. Excitatory populations are represented by the *solid lines*, inhibitory populations by the *dashed lines*. (C) Synthetic data illustrating a noisy measurement of neuronal population oscillation driven with *P = 1.4*. *Oscillatory frequency* alone can be used to derive the *P*-parameter from noisy measurements such as this: (D) Estimates of steady state oscillatory frequency can be derived from the model for a range of different values for *P*. Plotting the squared difference between estimated frequencies and that derived from the noisy synthetic signal, the *P* value that produces the minimal error can be identified. This approach identifies *P* = 1.4 as the value producing the minimal error (indicated by the *red arrow*). (E) If more than one parameter is allowed to vary (e.g. input *P* and self-excitation strength c_1), the error landscape becomes more complex and error minimisation alone does not produce unambiguous results – the *red arrow* indicates the same parameter constellation identified in panel (D) of this figure. The model specifications were taken directly from the model's original description (Wilson and Cowan, 1972). Parameters for the modelling were taken from one of the known oscillatory states and unless otherwise stated were: $c_1 = 16$, $c_2 = 12$, $c_3 = 15$, $c_4 = 3$, $P = 1.25$

WC models allow for generation of complex dynamics that remain computationally tractable enough to explore different parameter compositions and attempt inference on parameter combinations producing a certain dynamic response. However, in the original formulation consisting of a single excitatory and inhibitory population they are limited in how well they can represent the range and complexity of cortical dynamics observed in the laminate cortex.

A major extension of the WC model was introduced by Jansen and Rit (Jansen and Rit, 1995) building on an extant literature of adaptations of WC-type models (Lopes da Silva et al., 1974). The Jansen and Rit (JR) model explicitly models dynamics of a local cortical circuit by ascribing different neuronal populations to specific cortical lamina and describing their dynamics in terms of differential equations. In this model, an additional excitatory neuronal population is added allowing separate parameterisation for two excitatory neuronal populations.

$$\tau_e \frac{dx_1}{dt} = H_e(P + S_1(v_2)) - 2x_1 - \frac{v_1}{\tau_e} \tag{3.3}$$

$$\frac{dv_1}{dt} = x_1 \tag{3.4}$$

$$\tau_i \frac{dx_2}{dt} = H_i S_2(v_3) - 2x_2 - \frac{v_2}{\tau_i} \tag{3.5}$$

$$\frac{dv_2}{dt} = x_2 \tag{3.6}$$

$$\tau_e \frac{dx_3}{dt} = H_e S_3(v_1 - v_2) - 2x_3 - \frac{v_3}{\tau_e} \tag{3.7}$$

$$\frac{dv_3}{dt} = x_3 \tag{3.8}$$

This constellation of neuronal populations allows a diverse spectrum of frequency mixtures to be modelled, and is capable of producing a host of response dynamic also observed in empirical measurements of cortical potential fluctuations (Aburn et al., 2012; Goodfellow et al., 2012; Jansen and Rit, 1995). An additional benefit that emerges from the laminar specificity of the JR model is that it relates naturally to commonly available brain recordings in humans – specifically MEG and EEG. The electromagnetic activity measurable at the scalp is thought to mainly reflect postsynaptic currents in the apical

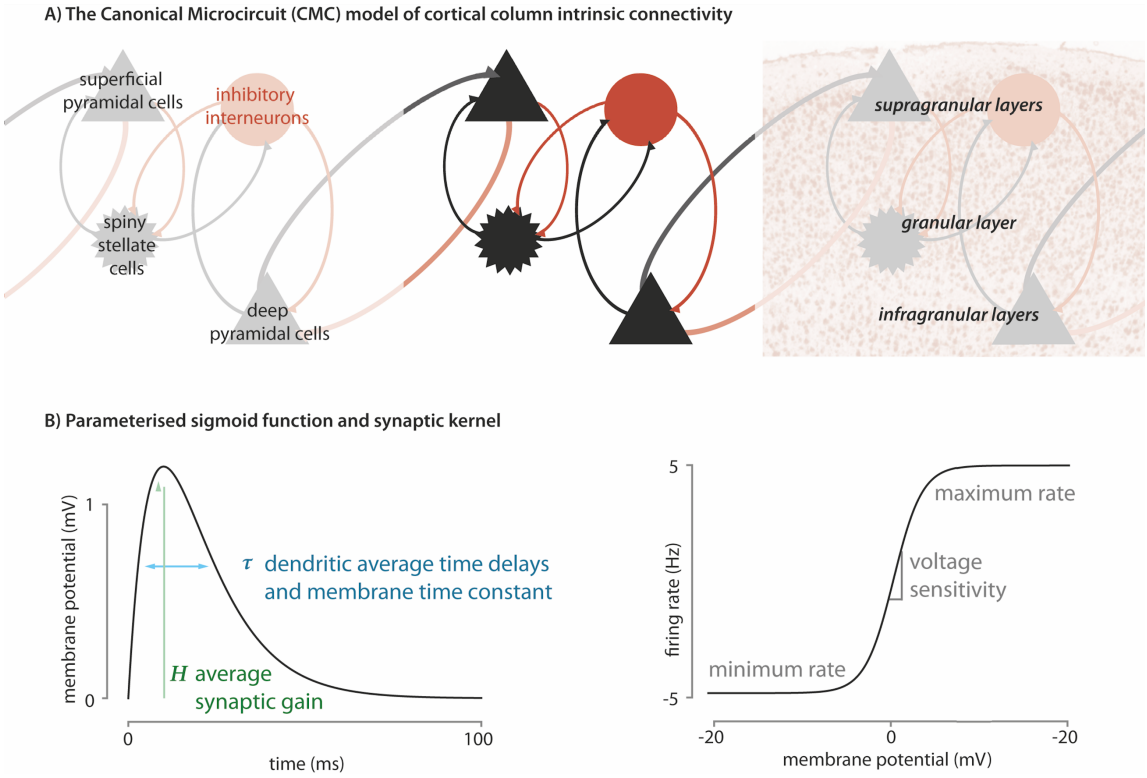

Figure 3.4 – The canonical microcircuit (CMC) model. (A) This extension of the Jansen-Rit model consists of four neuronal populations (*left panel*) mapping onto different cortical laminae (*right panel*). The *middle panel* shows the intrinsic excitatory (*black*) and inhibitory (*red*) connections contained in the model (for simplicity, recurrent self-inhibition present for each population is not shown here). (B) Two operators define the evolution of population dynamics: First, a synaptic kernel performs a linear transformation of presynaptic input into an average postsynaptic potential, dispersed over time (*left panel*). This is parameterised by synaptic gain parameters and averaged time constants. Second there is a nonlinear transformation of average membrane potential into population firing rates, described as a parameterised, population-specific sigmoid function (*right panel*).

dendrites of populations of pyramidal cells (Lopes da Silva, 2010). These are explicitly modelled in the JR model, so that their selective contributions to EEG/MEG measurements can be separated from the activity of other cell populations.

The laminar specificity and the wide range of physiological frequencies that can be modelled mean that JR-type models are commonly employed in computational neuroscience as models of cortical function. They currently form one of the model-based approaches for the analysis of large scale brain dynamics, such as the dynamic causal modelling (DCM) framework, which will be discussed in more detail later (David and Friston, 2003). Because they aim to represent the biophysical connectivity patterns found in actual cortical microcircuits, their architecture is also congruent with computational motifs thought to be the basis of cortical processing (e.g. predictive coding, (Bastos et al., 2012)).

Within the DCM framework, several extensions of existing neuronal models have been developed to address specific hypotheses regarding neuronal function (Moran et al., 2013). One of the extensions to the classical JR model employed in DCM is the so-called 'canonical microcircuit', or CMC (Figure 3.4).

The model consists of a simple extension of the differential equations given in equations Eq (3.3) to Eq (3.8). Using the mean-field approximation, the model can also be reconceptualised in terms of average membrane potentials and firing rates interacting through specific kernels that summarise the activity-dependent integration of input at the postsynaptic membrane, and the nonlinear transformation of all input into an output firing rate (Figure 3.4 B).

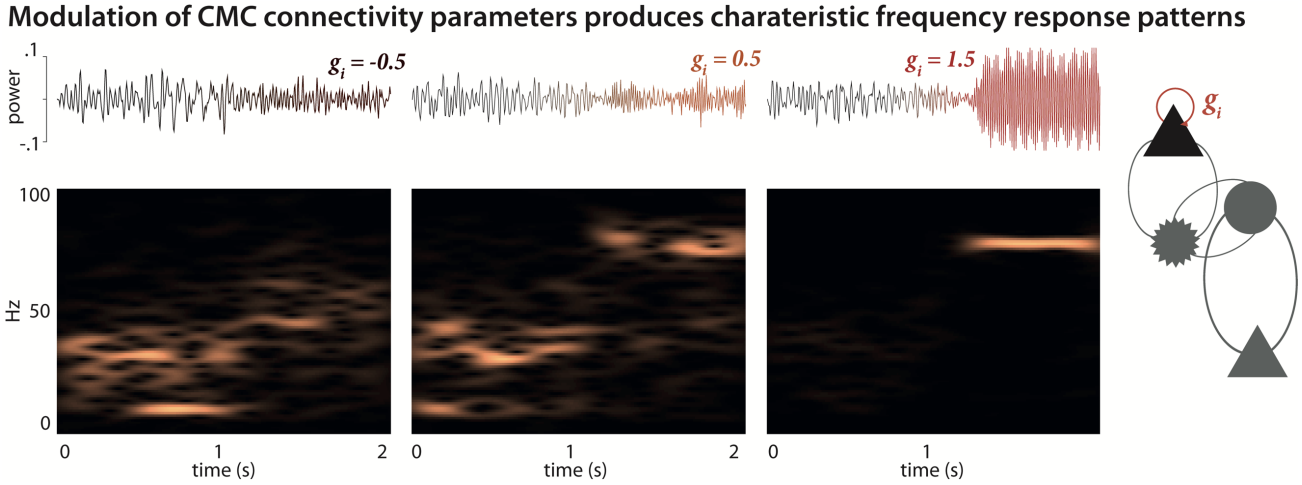

Figure 3.5 – Changes in intrinsic connectivity produce characteristic spectral responses. Gradual changes to the recurrent self-inhibition gain parameter g_i are introduced to a CMC model of the cortical column at around 1s, changing the intrinsic modulation from 0 to -0.5, 0.5, and 1.5 respectively (*left, middle,* and *right panels*). These changes produce characteristic signatures in the spectral output, apparent in botht he time traces (*top panels*), and the spectral densities (*bottom panels*) with increases in self-inhibition leading to high power high frequency oscillations.

Because the architecture of the CMC model represents neuroanatomical features of the cortex, most of the modelling parameters are neurophysiologically meaningful and thus easily interpretable. The model parameters can be directly manipulated to reproduce many different dynamic behaviours – increasing the degree of self-inhibition in superficial pyramidal cells for example will produce high frequency oscillations (Figure 3.5, (Papadopoulou et al., 2015)).

Clearly the more intriguing question is whether inference on the model parameters can be made from empirical measurements, in order to identify which functional abnormality in

the microcircuitry produced an abnormal measurement. This problem usually has more than one possible solution – meaning that many different possible constellations of parameters may cause apparently identical measurements, particularly where only some of the system's states are measurable, or observable (e.g. local field potentials), whilst many remain hidden (e.g. fluctuations of intracellular ion concentrations); i.e. the problem is ill-posed. This becomes particularly problematic where many different parameters can be used to explain a limited set of observed states. Even for the WC models with very few free parameters, simple optimisation routines, as indicated in Figure 3.3, quickly become intractable with complex multidimensional error landscapes that cannot be comprehensively mapped. The flexibility afforded by the increased number of free parameters in the CMC model comes at the cost of increased complexity of the space of possible solutions, making it difficult to evaluate which one best explains observed behaviours.

There are several possible approaches to addressing such ill-posed problems, many of which have been employed in the computational modelling of epileptic seizures and EEG abnormalities. In the following sections, I introduce a few of these approaches, with a focus on highlighting the genealogy of dynamic causal modelling, which will be one of the key methods employed in the remaining chapters of this thesis.

3.4 Model inversions as applied to EEG abnormalities

One of the most intuitive strategies to inversely link observed EEG features to changes in the parameters of an underlying generative model – i.e. to inverting models – is to systematically vary the parameters and evaluate how well the model simulations then fit the observed measurements. This can be done 'by hand', choosing individual parameter ranges independently of one another, and assessing the individual modelling outcomes (illustrated in Figure 3.3 (D-E) for the simple case of estimating input currents producing a specific frequency output in the WC model). Such an approach can be informative, even in complex models of laminar cortical connectivity (Du et al., 2012), but is limited to small numbers of varying parameters if comprehensive parameter mapping is attempted.

3.4.1 Optimisation algorithms

Optimisation algorithms describe computational strategies to identify parameter constellations within a range of possible values that produce a model output that best matches the observed results. There is a large literature regarding competing optimisation methods in a whole host of different areas of science and engineering. Thus, in this section I focus on only a few algorithms applied in fitting neuronal models to EEG data.

One of the most commonly applied group of algorithms are gradient descent (or ascent, depending on whether one is attempting to find minima or maxima of the function that is to be optimised) algorithms. The basic idea is that from a random starting point, in order to find a minimum, one could iteratively take steps following the direction of the steepest downward gradient until no more changes are made at each step, i.e. the algorithm converges. Because the local gradient is defined by the first derivative of the cost function (discussed further below), this cost function will have to be locally differentiable and smooth for gradient descent to be applicable. This approach is intuitive and easy to apply to a range of optimisation problems, such as seizure classification (Thomas et al., 2008), or to refine aspects of EEG source reconstruction (Hansen and Hansen, 2015).

There are two major limitations to this approach, however, which apply to the problem at hand – namely inverting complex, multi-parameter neural mass models to fit EEG data:

1. The gradient descent approach relies on the cost function to be smooth and continuous in order to be able to calculate the derivatives. Furthermore, in systems where there are unobserved variables in addition to unknown parameters that need to be inferred, calculating the derivatives directly is often not possible because of recursive dependencies between variables and parameters.
2. The algorithm by design identified local optimum, not necessarily the global optimum. Where the cost function is complex and has multiple local extrema, the local optimum identified in this approach may be far from the global optimum possible in the parameter ranges. Yet this global optimum may remain 'invisible' to the algorithm

There are several alternative optimisation algorithms that address these problems. Genetic algorithms for example resemble the process of natural selection by producing random

parameter variations and propagating the most 'successful' ones. After iteratively varying some of the parameters (introducing mutations) and then choosing the best variant (selection), the algorithm will converge to the best global solution, without requiring estimation of local gradients for its progression. This has been applied to fitting parameters of a detailed phenomenological model of individual EEG abnormalities in clinical EEG recordings, identifying patient-specific differences in the transition through parameter space (Nevado-Holgado et al., 2012). Similarly, algorithms such as particle swarm optimization or simulated annealing use direct search strategies that do not rely on knowledge of the gradients. These algorithms converge to a global maximum without getting stuck in local optima. A variety of these have been used in model based analyses of EEG signals (Gollas and Tetzlaff, 2005; Shirvany et al., 2012; van Dellen et al., 2012).

These examples illustrate two broad classes of algorithms: (1) global direct search strategies that yield robust convergence to global optima, but come at a high computational cost, and (2) gradient descent algorithms that are more computationally efficient but may get stuck in local optima and not yield a global resolution. The balance of these competing limitations dictates which optimisation algorithm is the most appropriate in a given situation.

When making inference on models with relatively few parameters, it is often possible to use one of the global algorithms for a model inversion, as the computational requirement for inverting a model of only a few parameters are often manageable. However, in models such as the CMC, where there are many free parameters that need to be fitted, the computational expense of these stochastic algorithms can be prohibitive and more efficient gradient descent algorithms are called upon. In this setting, prior constraints are used to ensure model inversion is less susceptible to arresting in local optima. Paradoxically the local minima problem can also be finessed by having many free parameters (as 'escape routes' are more likely to be present where there are many different dimensions of parameter space).

The gradient descent approach can be further finessed to address some of the remaining problems: local linearization can be used to estimate gradient where the underlying cost function is expensive to calculate; expectation-maximisation (EM) algorithms can be employed to invert probabilistic models where not all variables are observed (Do and Batzoglou, 2008), hierarchical model inversion can help to avoid local extrema (Friston et

al., 2016). Each of these strategies is employed within the DCM framework – but all crucially hinge on the type of function that is being optimised – often referred to as the cost function, which will be discussed below.

3.4.2 Cost Functions

In order to apply optimisation routines and improve how well a model represents data, we need to define which measure should be optimised. Often the most intuitive approach is to calculate the difference between the numerical predictions of the squared errors between model prediction and empirical measurement. This approach has been successfully applied to EEG in a variety of ways (Babajani-Feremi and Soltanian-Zadeh, 2010; Sitnikova et al., 2008).

If closeness of the model fits is the only criterion for the optimisation function, all free parameters within the models will be adjusted in order to produce the best model fit. Especially in models with many free parameters, this can lead to idiosyncratic results that resemble specific features of a given dataset, but show poor generalisability across different, similar datasets – a problem that has been termed *overfitting*. Seevral strategies can be employed to avoid overfitting and ensure generalisability of the modelling results.

One such approach has emerged naturally from reformulating the cost function not in terms of an absolute error that needs to be reduced, but rather in terms of the Bayesian model evidence (also known as the marginal likelihood) that needs to be maximised. The evidence is simply the probability of getting some data under a model of how those data were caused. This is generally evaluated by trying to estimate the underlying parameters of a model. In more detail: within the Bayesian framework, one estimates the probability of a given parameterisation θ, given a set of observations, or data y, by assuming that these were produced from a model m as follows:

$$p(\theta \mid y,m) = \frac{p(y \mid \theta,m)\,p(\theta,m)}{p(y \mid m)} \tag{3.9}$$

This posterior probability is not easy to estimate directly, but various approaches can be used to approximate it. Variational Bayes is a generic approach to the analysis of posterior probability densities. In this approach, the *free energy* represents a bound on the log of the model evidence and can therefore be used in optimization routines to identify optima in the model evidence distribution (Friston et al., 2007). The (log-) evidence of marginal

likelihood is defined as follows (where D (||) denotes the Kulback-Leibler, or KL divergence – a measure of the difference between two probability distributions; y denotes data; m denotes the model; θ denotes a set of model parameters; $q(\theta)$ denotes the variational density, i.e. the approximating posterior density that is being optimized. Thus, $-\langle \ln q(\theta) \rangle_q$ denotes the entropy and $\langle L(\theta) \rangle_q$ denotes the expected energy; F denotes the free energy):

$$\ln p(y \mid m) = F + D(q(\theta) \,||\, p(\theta \mid y, m)) \tag{3.10}$$

$$F = \langle L(\theta) \rangle_q - \langle \ln q(\theta) \rangle_q \tag{3.11}$$

The log evidence itself can be split into an accuracy and a complexity term, and thus automatically contains a penalty for overly complex models that are prone to overfitting. In the context of DCM, the complexity of the model is established on the basis of how far parameters deviate from their prior values. Therefore, maximising this Bayesian estimate of model evidence provides a compromise between goodness of model fit, and the generalisability of the model.

Specifically, in regard to epilepsy there are further specific problems that need to be addressed: Often the change of parameters that vary with time are of interest (for example whilst trying to track network changes during the transition into a seizure). If no account were taken of the temporal contiguity between individual time steps, the already computationally expensive model inversion needs to be fully repeated at each time step, treating each window as independent sample.

For dynamic systems, where there is a temporal dissociation between fast varying states and more slowly changes in underlying model parameters, this problem can be addressed through optimisation approaches that take into account the temporal dependencies between parameter values at preceding time points. One of the most successful of these approaches is the Kalman filter. This was originally developed for linear systems, but soon extended to nonlinear systems (Julier and Uhlmann, 2004). The Kalman approach has been used very successfully to estimate parameters underlying transitions into seizure state, where it has proven to benefit from its ability to estimate unobserved (hidden) states (Freestone et al., 2014).

A similar (and mathematically equivalent) approach can be implemented within the DCM framework, where each time step receives the preceding model inversion posteriors as prior expectations, resulting in evidence accumulation (also known as Bayesian belief updating)

across all of the modelled temporal windows (Cooray et al., 2016). More recently, a generic approach to estimating parameters at two modelling levels has allowed to accommodate arbitrary relationships between individual model inversion steps in a computationally efficient way (parametric empirical Bayes, (Friston et al., 2016)).

In summary, a Bayesian framework for the cost function allows incorporating constraints that can help solve the inverse problem when trying to fit neurobiological models to explain observations made in electrophysiological recordings. These constraints are formally incorporated as *prior beliefs* regarding certain parameters, which are specified as densities with an expected value, and an uncertainty measure around that value. The use of priors furthermore allows the model evidence to be cast directly in terms of a balance between model accuracy and model complexity, preventing overfitting of excessively complex models, ensuring higher generalisability of the models derived with this approach. Furthermore, several computationally efficient techniques are available to accommodate modelling of time series data.

3.5 Models in clinical neurosciences.

This chapter offers an introduction to using empirical electrophysiological data to inform the parameterisation of advanced mesoscale neuronal models. This approach is particularly suited to link conditions where long-lasting, or even permanent pathologies (such as a lesion, or a molecular abnormality) find their pathophysiological expression only transiently in abnormal neuronal dynamics. Either during discrete, paroxysmal events, such as in epilepsy, or from a transient expression at longer, developmental time scales.

Linking macroscopic, and often transient observations – such as variably apparent clinical features, or EEG measurements – to underlying causes, even where they are understood in some detail remains far from intuitive. This is rooted in the nature of the system that the models are trying to describe – which due to the inherent nonlinearities does not respond with easily intuitable linear additive responses to perturbation and external influences. Whilst the discoveries of more and more specific molecular mechanisms underlying some neurological and neuropsychiatric conditions suggest converging pathological mechanisms, understanding how these mechanisms affect synaptic connectivity and normal neuronal function requires more work in linking underlying pathology and phenotypic expression – for example through the sort of modelling approaches introduced

here. This gap in understanding – specifically how molecular abnormalities impact on whole brain phenotypes – limits our ability to make patient specific predictions and prognoses both based on the molecular cause of their disease, and on the neurophysiological measures (such as EEG) that clinicians routinely access.

In this chapter I introduced mesoscale computational modelling as a possible link between molecular, or microstructural pathology and macroscale phenotypes. Exploiting recent advances in both neuronal models of cortical function, and the fitting of parameters to empirical data within the well-established dynamic causal modelling (DCM) framework allows for the testing of mechanistic hypotheses. The approach presented here allows researchers to directly address specific questions emerging from other disease models and evaluate whether evidence for similar mechanisms can be identified in human patients.
These computational models can facilitate a thorough understanding of the dynamic effects of apparently static abnormalities within an organism. Whilst they are not set up to reproduce the complexity of whole organisms, they allow the mapping of changes in the model parameters and dynamic outputs of the model. They are therefore an ideal tool to further explore hypotheses derived from newly identified genetic mutations, other molecular causes, or animal models of specific conditions.
The use of computational models should not be seen in isolation, but instead provides a novel and necessary perspective on existing scientific questions emerging from clinical neurosciences. When attempting to identify causative mechanisms for human neurological disorders, neither clinical observations, computational approaches, nor animal based studies alone will provide conclusive evidence in favour or against specific mechanisms. Rather the strength of the evidence provided by the models (and in the remainder of this thesis) lies in the use of existing evidence across model systems and human patient observations to constrain computational analyses to address specific, competing hypotheses with quantitative information. This 'evidence accumulation' is most productive, where all lines of evidence refer to related neurophysiological concepts (e.g. connection strengths, time constants, gain parameters). Indeed, one can foresee the application of dynamic causal modelling to data from animal models to provide a formal integration of animal and human measurements.

4

SCN1A-associated changes in neuronal excitability §

4.1 Introduction

A diagnosis of epilepsy is established when a patient shows continued susceptibility for recurrent epileptic seizures. Although in some patients this susceptibility is conferred by structural brain abnormalities (such as tumours, previous strokes, or congenital malformations), for a majority the suspected – or indeed the confirmed - cause is genetic (Thomas and Berkovic, 2014).

Mutations in a wide variety of synaptically relevant genes – coding for ion channels, structural proteins, or regulatory proteins – have been implicated in epilepsy. For a number of these, a clear causative link has been established, which means that now several familial as well as apparently sporadic epilepsies can be explained by pathogenic mutations in synaptic genes (Spillane et al., 2016). Somewhat surprisingly, a large proportion of genes where direct causation could be established were identified not from common, familial

§ The work reported here has also been described in the following publication:

Peters, C.*, **Rosch, R.E.***, Hughes, E., Ruben, P.C. 2016. Temperature-dependent changes in neuronal dynamics in a patient with an *SCN1A* mutation and hyperthermia induced seizures. Sci Rep, 6:31879. ***equal contribution**.

As part of this work, I proposed the study design, designed the experiments together with collaborators, independently performed the computational modelling and wrote the report. I was not directly involved in the patch-clamp recordings of the neuronal channels, which are reported here for completeness.

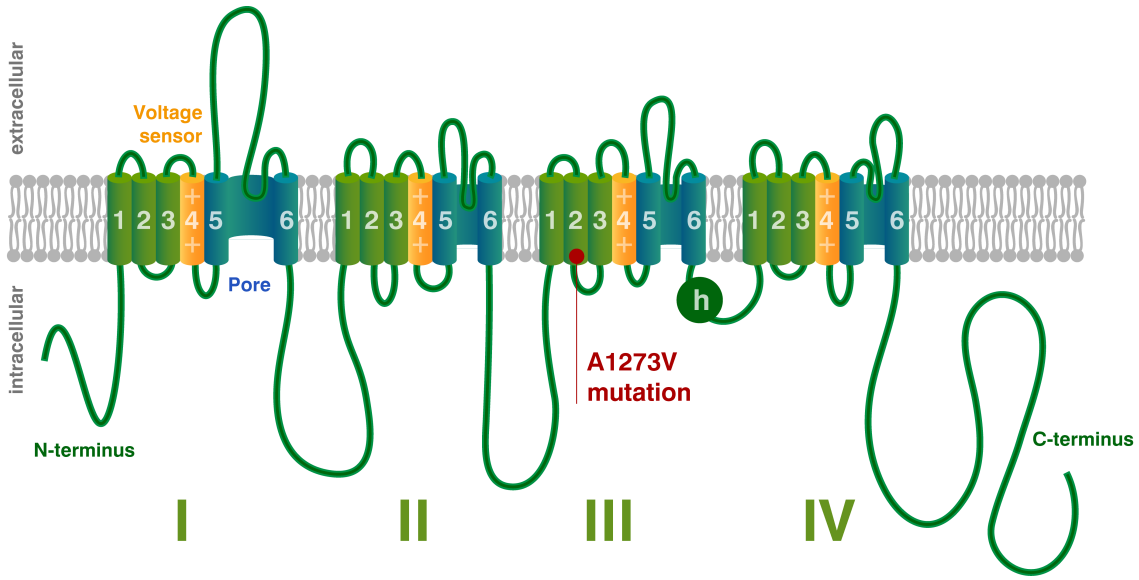

Figure 4.1 – Schematic sodium channel topology. The figure shows the domain and segment structure of the mammalian voltage-gated sodium channel and its relationship to the neuronal cell membrane. Pore forming regions of each domain are shown in blue (segments S5 and S6), while the positively charged S4 segment S4 of the voltage-sensors are shown in yellow. Locations of fast inactivation particle (*h*-gate, linking Domains DIII and DIV) and the A1273V mutant (in segment S2 of Domain III) are also shown.

epilepsies (which have recently been reclassified as genetic generalised epilepsies as discussed in Chapter 2 in this thesis) (Helbig, 2015), but from epileptic encephalopathies (Mulley and Mefford, 2011) – sporadic severe epilepsies occurring mainly in childhood. Genomic diagnostics in patients with neonatal onset, severe epilepsies can have a diagnostic yield of up to 75% (Oates et al., 2018) - meaning that genomic testing can identify specific genetic mutations responsible for up to three quarters of patients with previously 'idiopathic' epilepsy in this age group.

One of the first ion channel 'epilepsy gene' implicated in epilepsy was *SCN1A* which encodes the neuronal voltage-gated sodium channel $Na_V1.1$. It was initially described in patients with Generalised Epilepsy with Febrile Seizures plus Type 2 (Escayg et al., 2000), but quickly became recognised as the cause for – and is indeed most strongly associated with – Dravet syndrome (DS). DS was previously described as severe myoclonic epilepsy of infancy (Claes et al., 2001), an early onset epileptic encephalopathy. The link between the two conditions was made because of the shared susceptibility to recurrent, prolonged febrile seizures; patients living with Dravet syndrome in particular experience seizures in response to increases in environmental temperatures such as hot baths or other hot environments (Wolff et al., 2006).

Mammalian voltage-gated sodium channels are comprised of 4 domains (DI to DIV), encoded by a single transcript. Each domain constrains 6 transmembrane segments (S1 to S6) (Noda et al., 1984). The segments S1 to S4 constitute the voltage sensors, whilst S5 and S6 form the channel's central pore. The protein structure of the channel is shown in further detail in Figure 4.1 . Movement of the positively charged S4 segments towards the extracellular side of the membrane leads to opening of the channel pore and an influx of sodium (Chanda, 2002; Kontis et al., 1997). Following channel activation, the current ceases due to a process called fast inactivation: the linking segment between DIII and DIV moves to occlude the channel pore (illustrated as fast inactivation particle *h* in Figure 4.1) (West et al., 1992). Channel missense mutations which lead to channels with altered rates and voltage dependence of gating can impair electrical signalling at the synapse, and in the case of neuronal channels lead to different epilepsy syndromes.

SCN1A mutations related to Dravet syndrome include severe disruptions of channel integrity (e.g. frameshift mutations, deletions) and, albeit less commonly, missense mutations leading to either channel impairment, or gain of function. The prevalence of complete loss-of-function mutations in clinical cohorts of patients with epilepsy is counterintuitively high (Zuberi et al., 2011) – voltage-gated sodium channels are integral to action potential generation and neuronal excitability, so the link between a loss of this excitability and an epilepsy phenotype is non-trivial. The paradoxical link between loss of sodium-channel mediated excitability and increased seizure susceptibility may be explained by the observation that $Na_V1.1$ channels are predominantly found on GABAergic interneurons. Thus loss of function in $Na_V1.1$ may cause overall cortical disinhibition, which itself would be permissive of epileptic seizure activity (Ogiwara et al., 2007; Yu et al., 2006). This also explains the paradoxical exacerbation of seizures in response to sodium channel blocking antiepileptic drugs observed in many Dravet patients (Ceulemans et al., 2004).

This $Na_V1.1$ haploinsufficiency account of epileptogenesis in Dravet and associated epilepsies does not fully explain all clinical observations. A significant number of patients with gain of function mutations show severe epilepsy phenotypes considered more typical of deletion or frameshift mutations (Catterall et al., 2010; Scheffer, 2011; Zuberi et al., 2011). Indeed, one of the recently described *SCN1A* mutations with the one of the most severe associated clinical phenotypes is a missense mutation resulting in a single

substituted amino acid (Sadleir et al., 2017). Mapping possible direct mechanistic link s between sodium channel mutations and increased seizure susceptibility may help improve our understanding of genotype-phenotype correlations – and indeed has produced promising results for a separate group of neurodevelopmental disorders caused by mutations in the *SCN2A* gene (Ben-Shalom et al., 2017). Here I will show how integrating experimental measurements into a computational model can allow contextualisation of what effects mutation-related changes of channel biophysics may have on neuronal function. Using a clinical case with a novel *SCN1A* mutation as illustrative example, I will highlight how a single mutation may result in a mixture of effects at an *in-silico* neuronal model – thus deriving candidate mechanisms of epileptogenesis. This work, in future, may help categorise diverse sets of biophysical effects at the single channel into functionally relevant groups of mechanistically related phenotypes at the level of integrated neuronal circuits (Catterall et al., 2012; Strohman, 2002).

Here I report on a patient with an early-onset, temperature-sensitive epilepsy phenotype and a not previously characterised *de novo* heterozygous *SCN1A* mutation (*c.3818C>T*, ClinVar Accession: RCV000180969.1) coding for an amino acid exchange in DIII S2 of the $Na_V1.1$ channel (*p.Ala1273Val*; will be referred to as *AV* from here on). Using patch-clamp characterisation of channel properties, my collaborators on this project have identified dynamic, temperature-dependent differences from wild-type (*WT*) channels. I then integrate the empirical results into computational models of action potential dynamics at the membrane of a cortical neuron, specifying the functional effects of the mutation and describing a mechanism that can explain the temperature-sensitive epilepsy observed in this patient.

4.2 Methods

4.2.1 Patient selection

The patient was identified by a clinical collaborator (Dr Elaine Hughes, King's College Hospital) on the basis of their phenotype and previously uncharacterised *SCN1A* mutation. The patient's mutation was identified through bidirectional Sanger sequencing by the West of Scotland Genetics Service laboratories as part of routine clinical workup. The use of genetic and clinical information for the study and all experimental protocols were approved by the UK National Research Ethics Service (NRES). Written consent was

given by the patient's parents prior to the experiments described below. Use of all clinical and genetic information was carried out in accordance with relevant guidelines (including university and hospital data protection guidelines as well as the principles laid out in the Good Clinical Practice framework).

4.2.2 Bacterial transformations and mutagenesis

All bacterial transformations for this project were performed by collaborators (Prof Peter Ruben and Dr Colin Peters, Simon Frasor University, Burnaby, Canada) in TOP10/P3 *E. coli* bacteria (Invitrogen). As *SCN1A* is known to spontaneously mutate in bacterial cultures, the entire length of the sodium channel was sequenced following every transformation. The original *SCN1A* DNA in the PCDM8 vector was generously provided by Dr Lori Isom (University of Michigan, Ann Arbor, USA). All transformants from the original *SCN1A* vector were found to express the T1967A and G6923T mutations (compared to NM_006920.4), which encode the V650E and A1969 mutants in $Na_V1.1$, respectively. A QuikChange Lightning Mutagenesis kit (Agilent Technologies, USA) with primers shown in Table 4-1 was used to get the WT and mutant DNA.

Table 4-1 – Primers used for mutagenesis for wild type, and pathological variant.

A1967T	5' – CACTGTGGATTGCAATGGTG**T**GGTTTCCTTGGTTGGTGGAC – 3'
	5' – GTCCACCAACCAAGGAAACC**A**CACCATTGCAATCCACAGTG – 3'
T5923G	5' – CTGATCTGACCATGTCCACT**G**CAGCTTGTCCACCTTCC – 3'
	5' – GGAAGGTGGACAAGCTG**C**AGTGGACATGGTCAGATCAG – 3'
C3818T	5' – CTGGAAATGCTTCTAAAATGGGTGG**T**ATATGGCTATCAAAC – 3'
	5' – GTTTGATAGCCATAT**A**CCACCCATTTTAGAAGCATTTCCAG – 3'

4.2.3 Electrophysiology

Chinese Hamster Ovary (CHO-K1) cells were acquired and used to measure channel biophysics in a heterologous expression system by the collaborators Prof Peter Ruben and Dr Colin Peters. CHO-K1 (Sigma-Aldrich, MO, USA) were grown in Ham's F12 medium supplement with 10% Foetal Bovine Serum at 37°C in 5% CO_2. At about 24-48h prior to the experiment, cells were transfected with 1μg of the *SCN1A*, 1μg of the eGFP (enhanced green fluorescent protein), and 0.5μg of the β1 subunit using Polyfect transfection reagents

and associated protocols (Qiagen, Venlo, NL). At approximately 8-12h post transfection, the cells were plated on sterile glass coverslips.

Whole cell patch clamp experiments were then performed at 32°C, 37°C (normal human body temperature), and 40°C (febrile temperature) using borosilicate glass pipettes pulled with a P-1000 puller (Sutter Instruments, USA), dipped in dental wax and polished to a resistance of 1.0-1.5 MΩ. Extracellular solutions contained: NaCl (140mM), KCl (4mM), $CaCl_2$ (2mM), $MgCl_2$, 4-(2-hydroxyethyl)-1-piperazineethanesulfonic acid (HEPES, 10mM), and Ethylene glycol-bis(2-aminoethylether)-*N,N,N',N'*-tetraacetic acid (EGTA, 10mM). Extracellular solutions and intracellular solutions were titrated to pH 7.4 with Caesium hydroxide (CsOH) solution.

All experiments were performed using an EPC9 patch-clamp amplifier digitised using an ITC-16 interface (HEKA Elektronik, Lamprecht, Germany). For data collection and analyses, the Patchmaster/Fitmaster (HEKA Eletronik) and Igor Pro (Wavemetrics, USA) were used on an iMac (Apple Inc., USA). Temperature was maintained using a TC-10 temperature controller (Degan Corporation, USA). The data were low-pass filtered at 5kHz, and a P/4 leak subtraction procedure for all recordings was applied. The holding potential between protocols was set at -90mV.

4.2.4 Pulse protocols and analysis

Macroscopic currents were elicited with 20ms depolarizations to membrane potentials between -100mV and +60mV. Conductance was determined by dividing peak current by the experimentally observed reversal potential subtracted from the membrane potential. Normalised conductance plotted against voltage was fit by a single Boltzman equation. The decay of current was fitted by a single exponential equation to determine the time constant of open state inactivation at a given voltage.

Steady state fast inactivation was measured as the proportion of current remaining in a test pulse of 0mV following 200ms pulses to voltages between -130mV. The normalised current plotted against voltage was fitted by a single Boltzman equation. The time course of fast inactivation recovery at -90mV was measured as the proportion of current after a 200ms depolarisation to 0mV and a recovery pulse of varying lengths to -90mV. The normalised current was plotted versus recovery time and fitted with a double exponential equation.

4.2.5 Statistical analysis

I used a two-factor completely random design analysis of variance (ANOVA) to test first for evidence that the AV mutant has differential temperature sensitivity compared to the WT channel. The mutant effect was evaluated as a nominal independent variable and temperature as a continuous independent variable. The distribution of residuals from the statistical model were approximately normally distributed. In this analysis the interaction between temperature (continuous variable) vs. mutant (nominal variable), was used as a predictor variable. A significant difference in the interaction term was taken as evidence of a difference in temperature sensitivity between the AV mutant and WT channels. If this was not the case, the analysis was repeated without the interaction term to test for main effects of mutant and temperature. All statistical analyses were performed using the JMP software package (SAS Institute, USA). Statistical significance was evaluated at $p < 0.05$, and measurements of error are reported as standard error of the mean. Means, standard error of the mean and number of recordings for experimental data are reported in full in the Results section in Table 4-3. Inference drawn from the statistical tests are reported in the Results where appropriate.

4.2.6 Computational modelling

I modelled the mutation's effects on action potential generation by implementing the empirically derived biophysical parameters of channel function in a Hodgkin Huxley (HH) model adapted specifically to fit the dynamics of responses seen in regular spiking cortical pyramidal cells (Pospischil et al., 2008). The full model has been made publicly available online (https://github.com/roschkoenig/SCN1A_HodgkinHuxley) and custom code is included in the appendix to this thesis, section A.4. The online repository includes a detailed description of how to reproduce figures pertaining to the modelling results that is also included in the appendix of this thesis.

The HH model estimates changes in membrane potential from non-linear, voltage-dependent changes on ion-specific membrane conductances using the following set of differential equations, Eq. (4.1)-(4.10).

$$C\frac{dV_m}{dt} = -\bar{g}_{Na}m^3h(V_m - E_{Na}) - \bar{g}_K n^4(V_m - E_K) - \bar{g}_l(V_m - E_l) + I_{stim} \quad (4.1)$$

$$\frac{dx}{dt} = \frac{x_\infty(V) - x}{\tau_x(V)} \tag{4.2}$$

$$x_\infty(V) = \frac{\alpha_x(V)}{\alpha_x(V) + \beta_x(V)} \tag{4.3}$$

$$\tau_x(V) = \frac{1}{\alpha_x(V) + \beta_x(V)}, \text{ where x is } m, n, \text{ or } h \tag{4.4}$$

$$\alpha_n(V) = -0.032 * \frac{V - V_t - 15}{\exp(-\frac{V - V_t - 15}{5}) - 1} \tag{4.5}$$

$$\alpha_m(V) = -0.32 * \frac{V - V_t - 13}{\exp(-\frac{V - V_t - 13}{4}) - 1} \tag{4.6}$$

$$\alpha_h(V) = 0.128 * \exp(-\frac{V - V_t - 17}{18}) \tag{4.7}$$

$$\beta_n(V) = 0.5 * \exp(-\frac{V - V_t - 10}{40}) \tag{4.8}$$

$$\beta_m(V) = 0.28 * \frac{V - V_t - 40}{\exp(\frac{V - V_t - 40}{5}) - 1} \tag{4.9}$$

$$\beta_h(V) = \frac{4}{1 + \exp(-\frac{V - V_t - 40}{5})} \tag{4.10}$$

These equations are a system of coupled ordinary differential equations, describing the changes of membrane voltage – Eq.(4.1) – and ion channel gating parameters – Eq. (4.2) over time. In this formulation, there are only two specified ion channels: voltage-gated potassium channels, and voltage-gated sodium channels. The latter of these is of particular interest, as I will use changes in the specifications of the voltage-gated sodium channels in order to implement the experimentally derived changes in gating parameters *m* and *h* in this computational model. This allows me to identify the effects of biophysical channel properties on dynamics at the neuronal membrane.

At steady state, the gating parameters are described by Eq. (4.3) (Gurney, 2006). This represents a sigmoid function, which can also be parameterised using the generic Boltzmann formulation (Willms et al., 1999) as follows:

$$x_{\infty}(V) = \frac{1}{1+\exp(\frac{V-V_{2x}}{s_x})} \tag{4.11}$$

Experimental measurements taken from voltage clamp experiments include measures of midpoints (V_{2x}) and slope (s_x) of conductance and fast inactivation of sodium channels, representative of steady state gating parameters *m* and *h* respectively, and thus speak naturally to the Boltzmann formulation of these gating parameters in the HH model. However, because the experimental design did not fully replicate physiological states in cortical neurons (as a heterologous expression model was used (CHO-K1 cell line), and non-physiological additives such as fluoride are used to stabilise cell membranes during the experimental procedure, I first normalised the empirical results to a formulation of the HH model that captures physiological cortical dynamics (Pospischil et al., 2008) using the following computational steps, which can also be identified in the custom code provided in the Appendix section A.4:

1. Simulate cortical neurons using the parameterisation given in Pospischil et al. 2008
2. Fit Boltzmann equation parameters to these simulations and derive midpoint voltages and slope of steady state gating parameters for the Pospischil parameterisation
3. For the WT simulations at 37°C, the parameters (V_{2m}, s_m, V_{2h}, s_h) were set to the baseline values identified from the HH model described in Pospischil et al. 2008
4. For all remaining simulations, parameters were adjusted using the original parameterisation as baseline – preserving the absolute offset compared to WT (V_{2m}, V_{2h}), or the relative difference compared to the WT (s_m, s_h)
5. An additional offset parameter was introduced for fast inactivation gating equations Eq (4.7) and Eq (4.10) to account for temperature-dependent differences in time constants (note that with the Boltzman formulation for equation 3, only time constants – Eq (4.4) – depend on equations Eq (4.5) - (4.10). This is specified as follows:

$$\alpha_h(V) = 0.128 * \exp(-\frac{V-V_t-17+T_{offset}}{18}) \tag{4.12}$$

$$\beta_h(V) = \frac{4}{1+\exp(-\frac{V - V_t - 40 + T_{offset}}{5})} \quad (4.13)$$

This process yields four parametrisations of the same HH model, which represent different degrees of deviations from a standard model of regular spiking pyramidal cells. This normalisation was introduced to ensure that the experimental values are translated into physiologically plausible section of parameter space, whilst also preserving the relative differences in parameterisation between different experimental conditions. Parameter values used for capacitance, channel conductances and Nernst (reversal) potentials are summarised in Table 4-2 below.

Parameter	Units	**WT37**	**WT40**	**AV37**	**AV40**
C	$\mu A/mm^2$	0.010	0.010	0.010	0.010
g_L	$\mu S/cm^2$	0.0205	0.0205	0.0205	0.0205
g_K	mS/cm^2	5	5	5	5
g_{Na}	mS/cm^2	56	56	56	56
E_L	*mV*	-70.3	-70.3	-70.3	-70.3
E_K	*mV*	-90	-90	-90	-90
E_{Na}	*mV*	50	50	50	50
I_{stim}	$\mu A/mm^2$	0.20	0.20	0.20	0.20
V_t	*mV*	-55	-55	-55	-55
s_m	**-**	**7.4**	**6.6**	**6.1**	**7.6**
s_h	**-**	**-4.0**	**-3.4**	**-3.4**	**3.8**
V_{2m}	***mV***	**-39.0**	**-32.5**	**-33.1**	**-29.1**
V_{2h}	***mV***	**-43.3**	**-45.2**	**-41.0**	**-31.6**
T_{off}	***mV***	**0**	**1.9**	**-2.4**	**-11.7**

Table 4-2 - Parameter values for the computational model in the four different conditions evaluated. All parameters were normalized to an existing model of cortical Hodgkin-Huxley dynamics, and empirical differences represented as appropriate shifts in the model parameters. Parameters that change between conditions are indicated in bold.

Based on these model specification, I investigated the four conditions included in further analysis (i.e. WT at 37°C and 40°C; AV at 37°C and 40°C) in regards to their response to different levels of stimulation (included as the I_{stim} parameter in Eq(4.1)). I first explored the changes of model dynamics qualitatively, observing the changing nature of responses at different input states, and then addressed this more comprehensively using systematic variations in the input currents in order to perform a bifurcation analysis, which is reported on in detail in the Results section.

Table 4-3 – Empirical parameters of biophysical channel properties. This table summarises key parameters derived from patch clamp experiments with wild type (WT) and A1273V mutant (AV) at three different temperatures. *A* – amplitude, *G* – conductance, *SEM* – standard error of the mean, τ – time constant, *z* – apparent valence

(A) Conductance *G* and steady state fast inactivation (SSFI): Boltzman parameters

	WT at 32°C			***AV at 32°C***		
parameter	*mean*	*SEM*	*N*	*mean*	*SEM*	*N*
G V½ (mV)	-12.6	2.1	11	-16.4	1.9	8
G z	3.73	0.28	11	3.62	0.18	8
SSFI V½ (mV)	-50.2	2.6	9	-58.9	1.6	9
SSFI z	-4.07	0.30	9	-3.12	0.37	9

	WT at 37°C			***AV at 37°C***		
parameter	*mean*	*SEM*	*N*	*mean*	*SEM*	*N*
G V½ (mV)	-14.1	3.1	9	-12.0	1.5	5
G z	3.43	0.24	9	4.08	0.21	5
SSFI V½ (mV)	-57.2	1.1	5	-54.8	3.7	5
SSFI z	-3.14	0.11	5	-3.73	0.63	5

	WT at 40°C			***AV at 40°C***		
parameter	*mean*	*SEM*	*N*	*mean*	*SEM*	*N*
G V½ (mV)	-10.0	2.0	7	-4.2	2.0	11
G z	3.39	0.19	7	3.07	0.19	11
SSFI V½ (mV)	-59.1	3.4	5	-45.5	3.1	6
SSFI z	-3.79	0.17	5	-3.38	0.49	6

(B) Activation: Time in ms to 50% maximal activation

	WT at 32°C			***AV at 32°C***		
membrane potential	*mean*	*SEM*	*N*	*mean*	*SEM*	*N*
-20mV	0.303	0.011	11	0.304	0.016	9
-10mV	0.290	0.010	12	0.300	0.013	9
0mV	0.274	0.010	12	0.277	0.013	9
10mV	0.256	0.011	12	0.261	0.013	9
20mV	0.238	0.011	12	0.244	0.012	9
30mV	0.224	0.010	12	0.228	0.013	8
40mV	0.219	0.014	10	0.214	0.012	9
50mV	0.211	0.013	10	0.210	0.013	9

	WT at 37°C			***AV at 37°C***		
membrane potential	*mean*	*SEM*	*N*	*mean*	*SEM*	*N*
-20mV	0.269	0.057	9	0.267	0.011	5
-10mV	0.250	0.008	9	0.266	0.008	5
0mV	0.227	0.006	9	0.257	0.012	5
10mV	0.211	0.005	9	0.237	0.012	5
20mV	0.199	0.004	9	0.218	0.011	5
30mV	0.191	0.004	9	0.204	0.010	5
40mV	0.185	0.004	9	0.194	0.009	5
50mV	0.181	0.006	6	0.187	0.008	5
60mV	0.182	0.006	6	0.180	0.010	5

	WT at 40°C			***AV at 40°C***		
membrane potential	*mean*	*SEM*	*N*	*mean*	*SEM*	*N*
-20mV	0.260	0.023	4	0.263	0.009	9
-10mV	0.261	0.019	7	0.270	0.010	10
0mV	0.238	0.016	7	0.256	0.011	10

10mV	0.222	0.015	7	0.239	0.012	10
20mV	0.206	0.013	7	0.225	0.010	10
30mV	0.196	0.011	7	0.211	0.009	10
40mV	0.189	0.010	7	0.200	0.005	10
50mV	0.182	0.008	7	0.183	0.006	8
60mV	0.181	0.013	6	0.186	0.007	8

(C) Fast inactivation recovery curves: Double exponential fits

	WT at 32°C			***AV at 32°C***		
parameter	*mean*	*SEM*	*N*	*mean*	*SEM*	*N*
Flrec τ1 (ms)	2.18	0.29	9	2.55	0.70	5
Flrec A1	0.597	0.030	9	0.508	0.046	5
Flrec τ2 (ms)	97	20	9	125	34	5
Flrec A2	0.357	0.024	9	0.400	0.025	5

	WT at 37°C			***AV at 37°C***		
parameter	*mean*	*SEM*	*N*	*mean*	*SEM*	*N*
Flrec τ1 (ms)	1.62	0.44	5	1.42	0.23	5
Flrec A1	0.542	0.087	5	0.536	0.041	5
Flrec τ2 (ms)	81	16	5	141	56	5
Flrec A2	0.418	0.022	5	0.337	0.023	5

	WT at 40°C			***AV at 40°C***		
parameter	*mean*	*SEM*	*N*	*mean*	*SEM*	*N*
Flrec τ1 (ms)	1.27	0.21	6	1.24	0.13	5
Flrec A1	0.396	0.030	6	0.623	0.033	5
Flrec τ2 (ms)	72	22	6	138	57	5
Flrec A2	0.503	0.034	6	0.285	0.033	5

(D) Open state fast inactivation time constants: Single exponential fit (τ in ms)

	WT at 32°C			**AV at 32°C**		
membrane potential	*mean*	*SEM*	*N*	*mean*	*SEM*	*N*
-10mV	0.641	0.097	12	0.571	0.104	7
0mV	0.364	0.043	12	0.327	0.030	7
10mV	0.256	0.026	12	0.246	0.028	7
20mV	0.181	0.014	12	0.178	0.027	7
30mV	0.163	0.015	12	0.176	0.028	6
40mV	0.154	0.016	11	0.140	0.015	5

	WT at 37°C			**AV at 37°C**		
parameter	*mean*	*SEM*	*N*	*mean*	*SEM*	*N*
-10mV	0.369	0.040	6	0.809	0.102	5
0mV	0.249	0.024	6	0.429	0.017	5
10mV	0.181	0.017	6	0.273	0.013	5
20mV	0.188	0.022	6	0.209	0.017	5
30mV	0.168	0.023	6	0.165	0.026	5
40mV	0.134	0.010	5	0.158	0.033	5

	WT at 40°C			**AV at 40°C**		
parameter	*mean*	*SEM*	*N*	*mean*	*SEM*	*N*
-10mV	0.494	0.100	7	0.686	0.117	9
0mV	0.259	0.042	7	0.487	0.104	9
10mV	0.170	0.026	7	0.245	0.037	9
20mV	0.159	0.025	7	0.174	0.025	9
30mV	0.127	0.016	7	0.150	0.014	9
40mV	0.124	0.017	7	0.116	0.010	6

4.3 Results

4.3.1 Clinical case report

The child whose mutation is investigated here was highlighted by clinical collaborators due to their phenotype and miss-sense mutation in *SCN1A*. The child was first admitted to hospital at the age of 6 months with a brief, self-terminating febrile seizure with a right-sided predominance in his twitching movements. He subsequently presented with prolonged recurrent seizures, both with and without fever. Some of these lasted 30 minutes or more. These seizures required emergency treatment with benzodiazepines, and one intensive care unit admission related to respiratory depression following treatment. After the intensive care admission, treatment with phenytoin was started, which reduced the duration of his seizures to less than 5 minutes at a time. Interestingly, a proportion of these seizures were apparently provoked by a hot bath, or whilst playing on a very warm environment.

There was no evidence of focal neurological impairment after recovery from seizures during any of his hospital admissions, nor was any focal impairment reported by the parents. He was born at term and had an uncomplicated perinatal course. There was no family history of epilepsy, neurodevelopmental or psychiatric conditions and he was the first child of non-consanguineous parents. No abnormalities were found on systemic examination, nor during extensive cardiology review – clinical examination, echocardiogram, and electrocardiogram were unremarkable.

Because of the clinical phenotype he underwent genetic sequencing of the *SCN1A* gene at 12 months of age. This showed a *de novo* heterozygous missense mutation (*c.3818C>T*) causing changes in a functionally significant and highly conserved region of the *SCN1A* protein (*p.Ala1273Val* – referred to as AV in this chapter). This genetic mutation together with the clinical context suggest a diagnosis of a seizure disorder within the wider Dravet syndrome (DS) spectrum.

Following his genetic diagnosis, his treatment was changed to sodium valproate, which he tolerated well, and which has markedly reduced the number and duration of seizures. At the time of writing he continues to make age appropriate developmental progress, and only experiences a small number of seizures, mostly in the context of febrile illnesses.

4.3.2 Results from the patch-clamp recordings

Data from patch-clamp recordings of both WT and AV channels expressed in CHO-K1 cells and recorded at 32°C (standard preparation), 37°C (physiological temperature), and 40°C (febrile temperature) are reported in full in Table 4-3. I will discuss the result in terms of different aspects of sodium channel gating behaviour below.

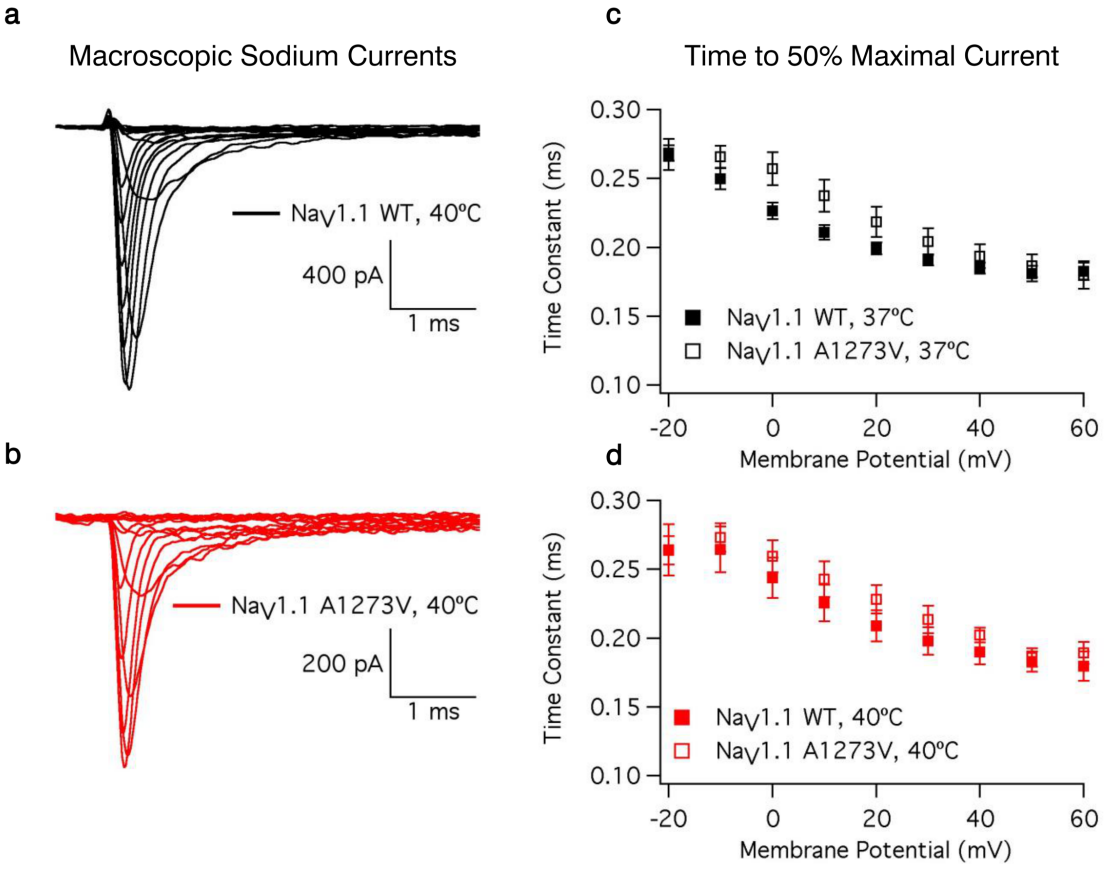

Figure 4.2 – Macroscopic $Na_V1.1$ currents. Sample WT (a) and AV (b) currents elicited at potentials between -100mV and +50mV at 40°C. Time to 50% maximal current is plotted versus voltage for WT and AV $Na_V1.1$ channels at 37°C (c) and 40°C (d). Source data for all experimental conditions is also shown in **Table** 4-3 (B).

4.3.2.1 $Na_V1.1$ activation

Sample macroscopic sodium currents from WT and AV channels are shown in Figure 4.2 (a), and (b) respectively. There is no significant difference in the time to 50% maximal current between WT and AV channels (from -20mV to +60mV in 10mV intervals: *p*-values = 0.7681, 0.1564, 0.0803, 0.0896, 0.0749, 0.1743, 0.4456, 0.2645, 0.5020), nor is there a difference in temperature sensitivity (from -20mB to +60mV in 10mV intervals: *p*-values

= 0.8318, 0.8101, 0.3128, 0.3882, 0.3936, 0.4212, 0.3160, 0.5845, 0.2824). This is shown in Figure 4.2 (c), and (d).

Increasing the temperature significantly accelerates the time to 50% maximal current at potentials between -20mV and +50mV in both WT and AV (from -20mV to +60mV in 10mV intervals: p = 0.0006, 0.0046, 0.0047, 0.0061, 0.0077, 0.0127, 0.0149, 0.0215, 0.1239). There is also a significant difference in temperature sensitivity of the conductance-voltage relationship between WT and AV (p = 0.0235), as illustrated in Figure 4.3 (a) and (b). At 37°C the AV curve is depolarised by only 2.1mV compared to WT, whilst at 40°C this difference is increased to 5.8mV.

4.3.2.2 $Na_V1.1$ fast inactivation

There is a significant difference in the temperature sensitivity of the midpoint of steady-state fast inactivation between WT and AV (p<0.0001), as illustrated in Figure 4.3 (c) and (d). At 37°C the AV steady-state fast inactivation midpoint is depolarised by 1mV

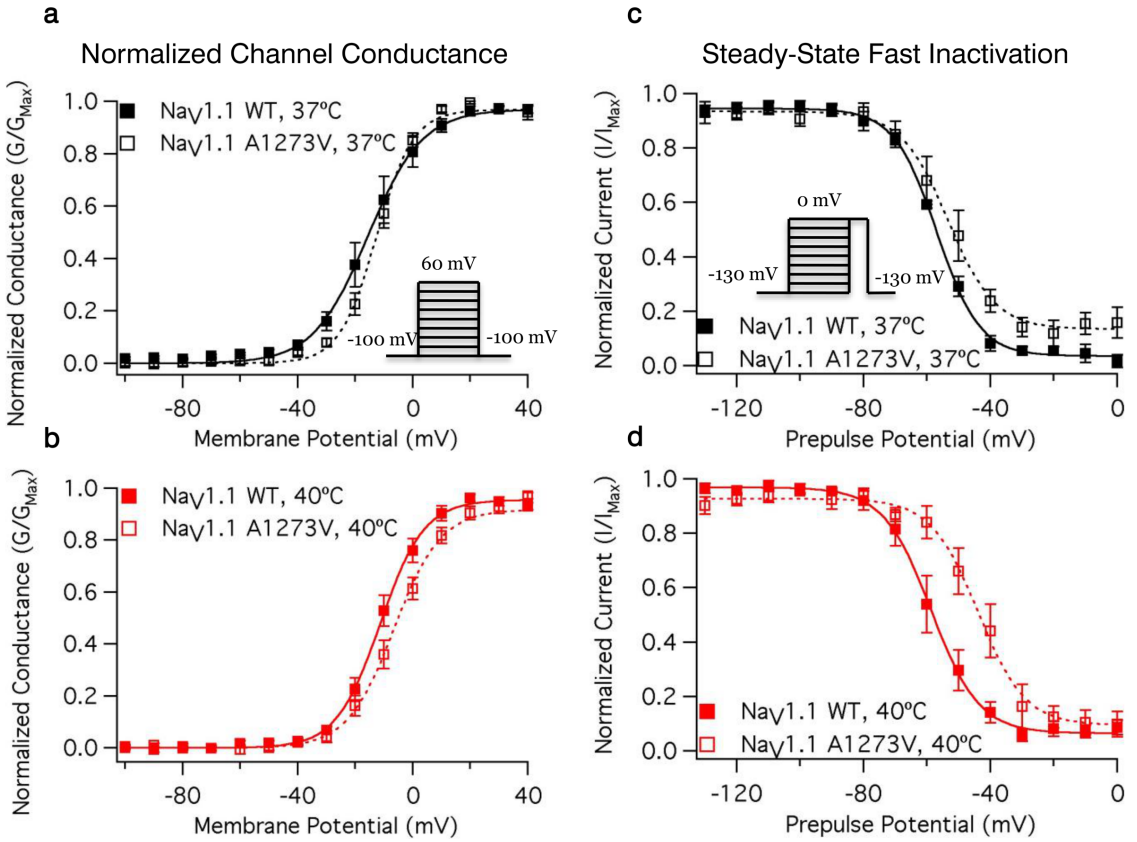

Figure 4.3 – Voltage dependence of $Na_V1.1$ conductance and fast inactivation. Normalised conductance curves for WT and AV $Na_V1.1$ channels (a) at 37°C and (b) at 40°C. Conductance was determined from macroscopic current recordings using Ohm's law, corrected for the experimentally observed equilibrium potential. Normalised current during a test pulse following a 200ms pre-pulse is plotted versus pre-pulse potential for WT and AV NaV1.1 channels (c) at 37°C and (d) at 40°C.

compared to WT (Figure 4.3 c). This difference increased to 14mV at 40°C (Figure 4.3 d). The fast time constant of recovery is significantly accelerated by increases in temperature (p = 0.0028); whilst the slow time constant of recovery is not (p = 0.8631). Neither the fast nor slow time constant of recovery are altered by the mutation (p = 0.8229, 0.0828, respectively).

There is a significant difference in the temperature sensitivity of the recovery component amplitudes in the AV mutant compared to WT (p = 0.0021). Increasing temperature decreases the fast component amplitude and increases the slow component amplitude in WT, whilst the opposite occurs in AV. The overall results are thus an increased recovery in AV channels at 40°C compared to WT channels (Figure 4.4). Open state fast inactivation time constants are shown for WT and AV channels in Figure 4.4 (c) and (d) respectively. A significant mutant effect on fast inactivation onset only occurs at 0mV (from -10mV to +40mV in 10mV intervals: p = 0.1066, 0.0366, 0.0734, 0.6507, 0.4492, 0.5990) As I tested for effects at 6 voltages, and only found difference at a single voltage point, I concluded that AV has minimal impact on $Na_V1.1$ fast inactivation onset.

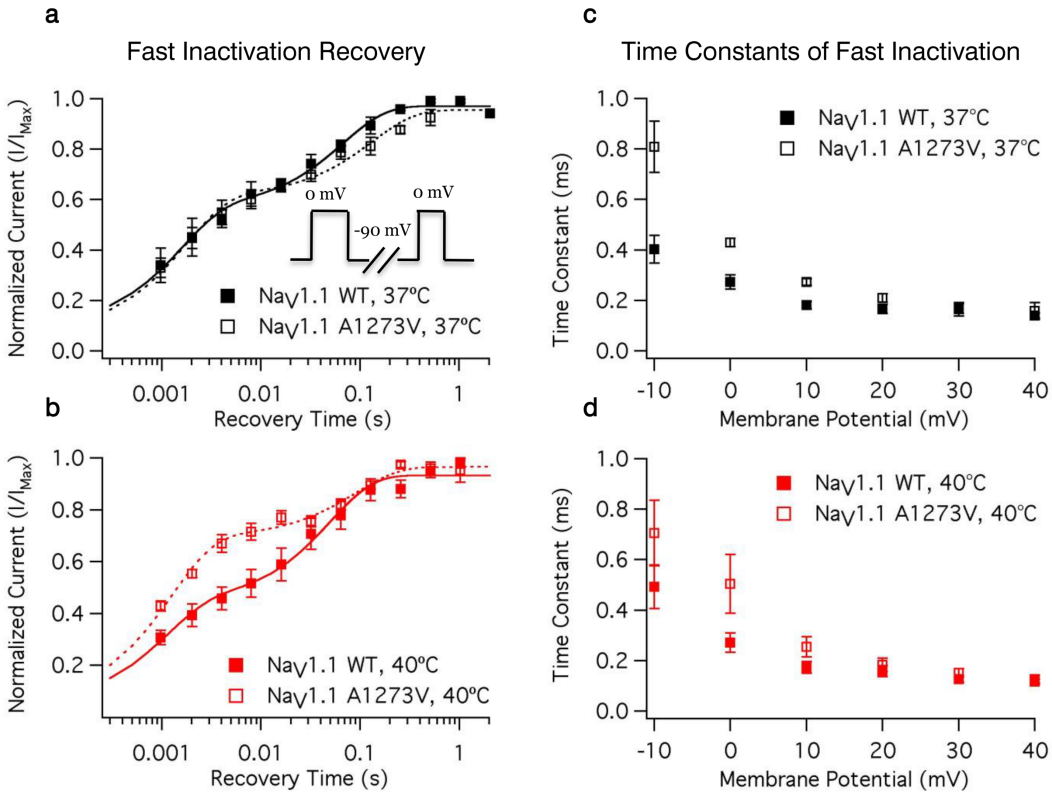

Figure 4.4 – Time course of fast inactivation. Open-state fast inactivation time constants are plotted versus voltage for WT and AV $Na_V1.1$ (a) at 37°C and (b) at 40°C. Thje time course of fast inactivation recovery versus recovery is plotted for WT and AV NaV1.1 (c) at 37°C, and (d) at 40°C respectively. The double-pulse protocol used to measure fast inactivation recovery is shown in the inset of (a).

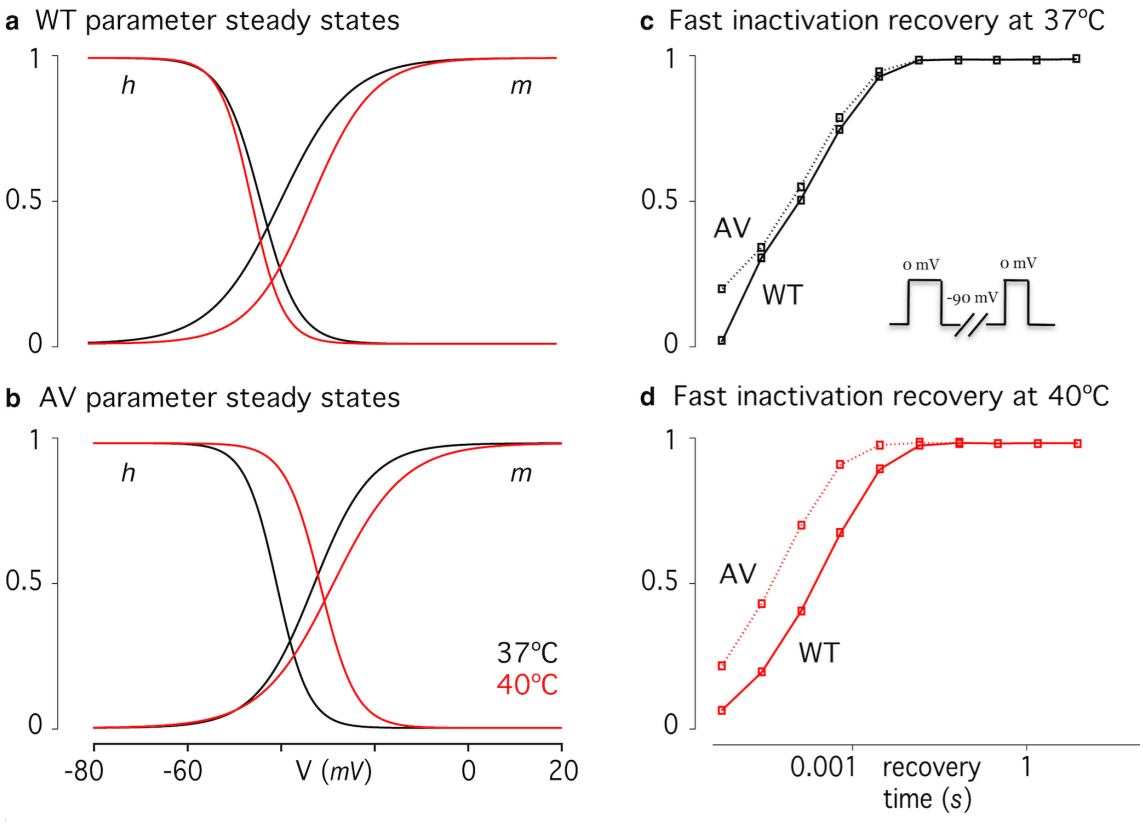

Figure 4.5 – Steady-state parameter changes implemented in a Hodgkin-Huxley model. Steady state values for different voltages were estimated for both the *m* and the *h* parameters based on values from cortical Hodgkin-Huxley type neuronal simulations. A Boltzman formulation of the steady state equation was then fitted to the estimates to derive baseline parameter values for the slopes (s_m, s_h) and half-peak voltages (V_{2m}, V_{2h}). Experimental results from the voltage clamp experiments were then translated into changes from these baseline parameters to produce steady state curves for (a) the WT and (b) the AV mutant gating parameters at different temperatures. Forward and revere rates of the fast inactivation gate ($\alpha_h(V)$, $\beta_h(V)$) were shifted along the voltage axis to correspond to the shifts in half-peak voltage of steady-state fast inactivation. The resultant recovery time courses for fast inactivation are shown for WT and the mutant at 37°C and 40°C (c-d).

4.3.2.3 Cortical Neuron Modelling

Results from the empirical measurement of channel function at different environmental temperatures was implemented in cortical neuronal models, representing WT and AV channels at 37 and 40°C each. The cortical neuronal model was parameterised to specifically incorporate the observed shifts activation and fast inactivation through changes in gating parameters *m* and *h* (Figure 4.5 a-b), as well as the AV mutant effect in fast inactivation dynamics (Figure 4.5 c-d). Simulations with minimal input strengths (I_{stim} = *0.2*, Eq (4.1)) reveal little difference in firing frequency or amplitude between WT and AV as a result of these shifts in model parameters for either temperature condition Figure 4.6 a).

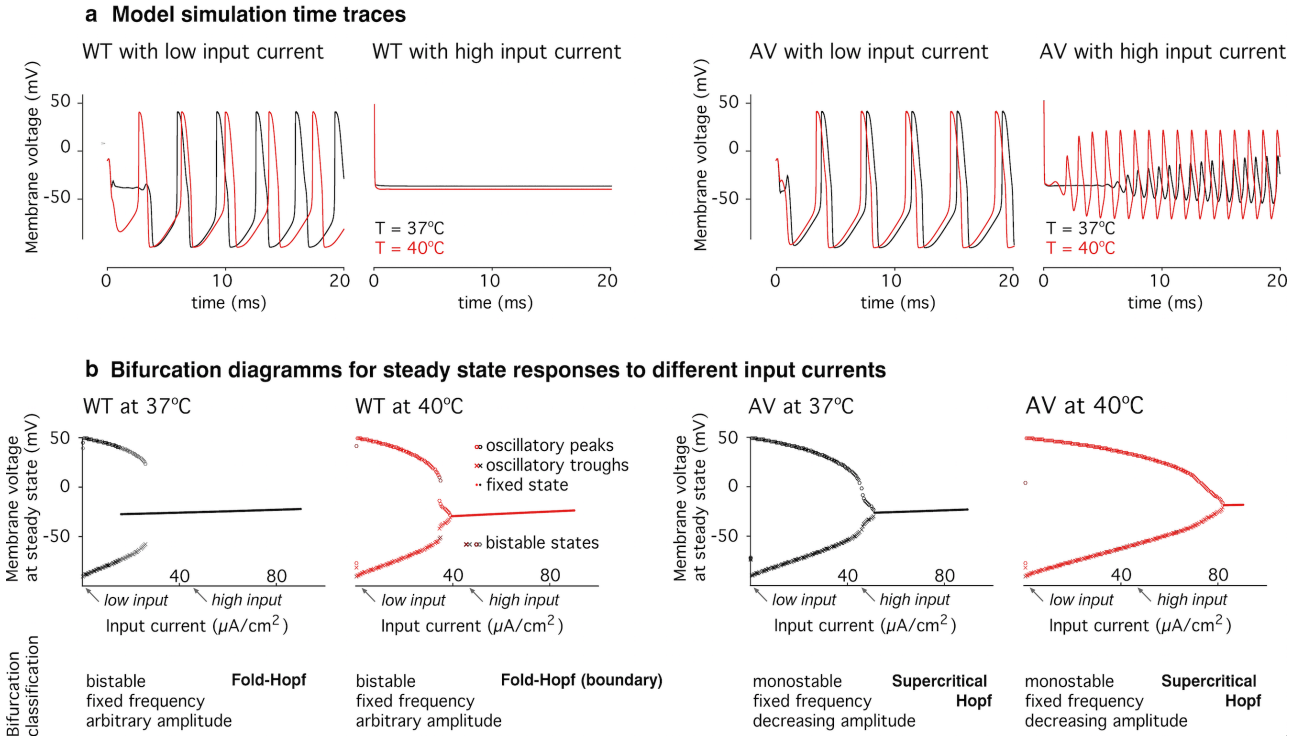

Figure 4.6 – Computational modelling of membrane dynamics. Experimental voltage clamp measurements for four experimental conditions (WT and AV at 37 and 40°C) were implemented in a Hodgkin-Huxley model of cortical neurons and normalised to the WT measurements at 37°C. (a) Simulations of the membrane response at different input current levels revealed absent action potential generation at high currents, even when the *in-silico* AV neuronal model continues to fire. (b) Bifurcation analysis shows differences in the transition from oscillation to fixed steady states at high input currents (i.e. depolarisation block), both qualitatively in terms of the bifurcation type, and quantitatively in terms of the input currents required to achieve depolarisation block. Of all experimental conditions modelled, AV neurons permit the highest input currents to elicit continuous action potentials.

Model parameters: $g_L = 2.5*10^{-5} S/cm^2$, $E_L = -70.3$, $g_{Na} = 0.056\ S/cm^2$, $E_{Na} = 50\ –mV$, $g_K = 0.005\ S/cm^2$, $E_K = -90\ mV$, $V_t = -60\ mV$, $C_m = 0.01\ \mu F/mm^2$, (Pospischil et al., 2008).

High input current: $I_{stim} = 45 \mu A/mm^2$, low input current $I_{stim} = 0.2\ \mu A/mm^2$. Remaining parameters were condition specific and defined as described in the Methods section.

Simulations with high input currents ($I_{stim} = 45$, Eq (4.1)) reveal a significant divergence in the dynamic behaviours of different model neurons. Although there is no response from the WT neurons at either temperature (due to depolarisation block), there is continued action potential firing in AV neurons at both temperatures, with higher amplitude firing at the febrile temperature condition at 40°C.

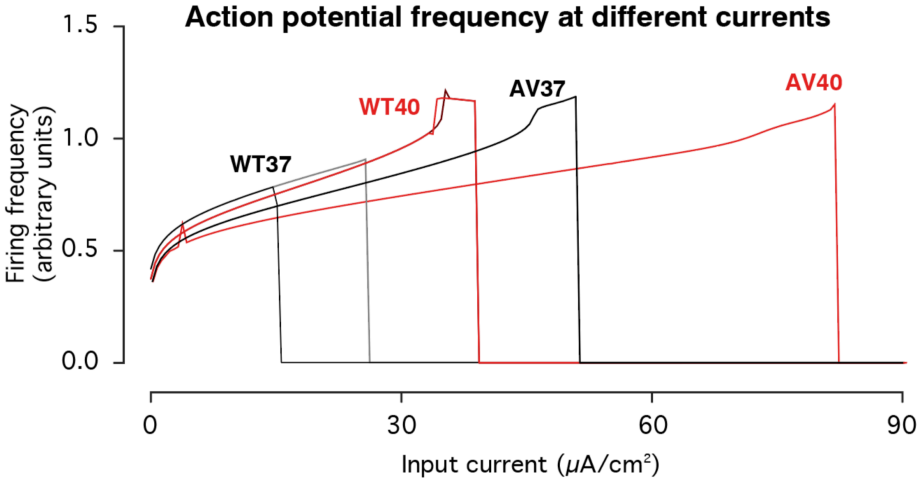

Figure 4.7 – Action potential frequency at different input currents. Action potential frequency is shown for the adapted Hodgkin-Huxley models for each of the four experimental conditions included in the modelling (i.e. WT and AV at 37 and 40°C respectively). Modelling for all conditions was performed in two directions (i.e. increasing and decreasing values for the input current with each successive simulation). This revealed hysteresis in the WT at 37°C only (grey: successive increases in stimulation current; black: successive decreases in stimulation current). The plot shows the temperature-sensitive increase in stimulation tolerance across conditions also seen in the bifurcation analysis as shown in Figure 4.6. However, for any given stimulation current, the predicted action potential frequency is lower for the low temperature vs high temperature conditions.

The dynamic behaviour of neuronal oscillators are characterised by transitions between fixed steady states and oscillations (bifurcations) (Jirsa et al., 2014). Here I am comparing WT and AV in terms of the bifurcation behaviour identified along variations of the stimulating current magnitude. There is a shift of this oscillation offset bifurcation towards higher input current values, particularly at 40°C (Figure 4.6 b). This means AB neurons in the hyperthermic condition continue to produce action potentials at very high input currents, where WT neurons will have already ceased firing. The model also shows differences in firing frequency, with slower firing in the AV neurons for any given input (Figure 4.7).

4.4 Discussion

This study highlights the value of characterising *SCN1A* variants at elevated temperatures both using a combination of empirical measurements and *in-silico* models. At the time of writing, only one previous study identified a temperature-sensitive loss-of-function mutant, R865G in the $Na_V1.1$ channel (Volkers et al., 2013).

R865G leads to primarily gain-of-function properties in channel gating at 37°C with depolarisation of steady-state fast inactivation, hyperpolarisation of channel conductance and increased window current. At 40°C the mutant also leads to a decrease in channel current during repetitive depolarisations. Most functional studies of sodium channel function in Dravet syndrome and related epileptic disorders has focussed on animal models of human *SCN1A* mutations (including fruit flies (Sun et al., 2012), zebrafish (Dinday and Baraban, 2015), and mice (Oakley et al., 2011)). These models are very flexible in that they can be used to investigate a range of genetic changes (including, e.g. heterozygous knockouts), and produce whole-organism phenotypes (including neuronal microcircuitry abnormalities, excitation-inhibition imbalance, and behavioural febrile seizure phenotypes) – giving both insights into whole-brain pathophysiological mechanisms and allowing targeted therapy development *in-vivo*. However, it is often not possible to fully characterise sodium channel gating parameters and their temperature dependence in these experimental models, where high quality temperature-specific electrophysiology is technically difficult or impossible to perform. Furthermore, the isolated contributions of channel-, cell- and network-level abnormalities as possible routes from genotype to phenotype cannot be disentangled with whole-organism models alone but requires detailed insights from basic channel biophysics.

Recently, models of patient-derived induced pluripotent stem cells (iPSCs) have also been developed. These suggest that patient derived pyramidal cells show evidence of hyperexcitability in isolation (i.e. even in the absence of faulty GABAergic control) (Liu et al., 2013). Building on this background this study further suggests that a single mutation can confer both temperature-sensitive gain-of-function (i.e. action potential generation at higher input currents) and loss-of-function (i.e. lower action potential frequency) in Dravet syndrome and related epileptic disorders.

The A1273V (AV) mutant investigated here occurs in the domain III voltage-sensor, specifically near the intracellular side of S2. Movement of the DIII voltage-sensor is part of the activation of the sodium channel (Kontis et al., 1997). Furthermore, DIII may play a role in channel fast inactivation. Previous work suggests that the primary determinant of channel inactivation is the movement of DIV, S4 followed by the binding of the DIII-DIV linker to the intracellular side of the channel (Capes et al., 2013; West et al., 1992). However, as the movements of DIII are immobilised by channel inactivation, it may also

play a role in the binding of the DIII-DIV linker (Cha et al., 1999). Thus, mutants which impact the movement of DIII, S4 may affect both channel activation and fast inactivation. In the case of the AV mutant discussed here, the empirical work on biophysical channel properties shows destabilisation of both channel activation and fast inactivation at elevated temperatures. As the temperature is elevated to 40°C, the WT channels show relatively little temperature dependence with shifts of *+4.1* and *-1.9mV* in the conductance-voltage relationship and steady-state fast inactivation, respectively. In contrast, the AV mutant is shifted by *+8.0* and *+9.3mV* in the conductance-voltage relationship and steady-state fast inactivation, respectively. These data suggest that the mutant DIII voltage sensing domain may be stabilised in the inward conformation. This stabilisation is unmasked at elevated temperatures. Crystal structures are not available for the voltage-sensing domains of mammalian sodium channels, limiting the ability to identify a molecular mechanism for the impacts of AV on $Na_V1.1$. However, one hypothesis is that the presence of a bulkier valine near the intracellular side of the DIII voltage sensor impedes and slows the outward rate of DIII, S4. This slowing becomes more apparent at elevated temperatures when presumably the rates of the other three voltage sensors are accelerated. It is also possible that the mutant alters the balance of inward and outward rates of DIII, S4 – which in turn may lead to a decreased probability of activation at elevated temperatures. This may explain why at 40°C a more depolarised voltage could be required to activate the DIII, S4 – which in turn would depolarise the opening of the channel pore.

The data reported here provide further support that DIII is part of the fast inactivation machinery in the channel. The WT channels undergo a small hyperpolarising shift in fast inactivation as temperature is increased from 37°C to 40°C (Table 4-3). This suggests that a destabilisation of the outward state in DIII, S4 can destabilise fast inactivation possibly through either decreased availability of a DIII binding site for the fast inactivation particle, or inter-domain interactions of the voltage sensor which have been previously shown (Chanda, 2004). In conjunction with the increased rate of channel recovery, the increased availability of sodium channels in the mutant at 40°C may allow for higher neuronal firing rates, consistent with the decrease in depolarisation block in my models. I found evidence of an effect on the rate of open-state inactivation at only one voltage (*0mV*). As this was one of the least positive potentials at which I measured open state inactivation, I conclude

that at more depolarised voltages the mutant does not exert large effects on the rate of inactivation, but this may not be true at more negative voltages.

The results show functional impairments of AV are temperature-specific, suggesting a direct link between the disease phenotype observed in the patient the mutation was identified in, and the genetic mutation itself at the level of channel function. My embedding these functional abnormalities at the channel level into a computational neuronal model suggests that, while low input stimulation leads to decreased action potential firing, the maximum stimulus current which results in oscillations is higher in the mutant at 40°C.

The modelling results are directly correlated to the empirical measurements. The decreased rate of action potential firing is consistent with an increased threshold for firing, which can be predicted from the depolarised conductance-voltage relationship (a loss-of-function change) in the AV mutant channel. The lack of depolarisation block, in contrast, is consistent with the depolarisation in the fast inactivation relationship – a gain-of-function leading to increased channel availability at a given resting membrane potential. Depolarisation block describes the observation that neurons stop responding at high levels of stimulation despite being depolarised beyond the firing threshold. There is evidence that it might play a role in seizure termination (Bragin et al., 1997; Ullah and Schiff, 2010). The difference in depolarisation block thresholds for the different models corresponds to the empirically measured changes in channel gating parameters: Specifically, in AV at 40°C, both channel gates are shifted to more depolarised potentials, allowing oscillations to occur, where in the WT they would not.

The model I implemented here also suggests that there are more subtle differences between WT and AV. In the WT, there are bistable bifurcations in which neurons that enter depolarisation block are subsequently more likely to remain at a fixed (i.e. blocked) steady state when stimulating currents decrease. In models incorporating the mutant channel dynamics, bifurcations are monostable: Neurons which enter depolarisation block return to oscillatory behaviour when stimulation falls even just below the bifurcation threshold. These findings suggest a pathophysiological mechanism in which neurons recover their excitability more readily after high frequency stimulation – allowing pathological participation in high activity states (such as epileptic seizures) to persist.

The change between different oscillation-offset bifurcation types occurs gradually and the bistability can be seen to collapse into a monostable bifurcation across the different conditions Figure 4.6 b. This observation likely relates to interactions between dynamic behaviours of the different voltage-sensitive parameters in the full Hodgkin Huxley model (i.e. including other channel types than just sodium channels): Through changes in the sodium channel gating parameters, the bifurcation point may be shifted to a location in the combined space that does not allow for bistability. This dynamic behaviour is an emergent property of the system as a whole and would not have easily been predicted from the gating behaviour of sodium channels alone.

Combining empirical measurements of impairments in molecular function with computational neuronal modelling integrates different scales of evidence. A similar approach identified novel pathological mechanisms resulting in abnormally increased persistent sodium currents through mutant channels in other *SCN1A* mutations (Kahlig et al., 2006). Computational models have helped identify a common mechanisms of epilepsy pathophysiology: apparently functionally different mutations affecting different sodium channels can result in neuronal hyperexcitability (Spampanato et al., 2004).

This has implications for further improvements of antiepileptic drug choices in Dravet syndrome and related epileptic disorders. The clinical effectiveness of valproate in the patient reported here is in keeping with my results, and valproate's effect on inducing use-dependent limitations of fast action potential firing reported in the literature (McLean and Macdonald, 1986). However, valproate can have significant adverse effects and is not effective in all patients. Currently, sodium channel blockers such as carbamazepine are avoided in standard clinical practice because of frequent reports of associated paradoxical worsening seizures (Chiron and Dulac, 2011). Detailed knowledge of mutation locus and associated gating abnormalities may help stratify the risk of adverse effects and permit the addition of an anti-epileptic drug with direct sodium channel blocking action for some patients. One example is lidocaine, which is already used in some centres for the treatment of status epilepticus (Hattori et al., 2008). It may therefore be a valuable addition to treatment protocols specifically for patients with similar dynamic gating abnormalities in a high-frequency firing state (e.g. status epilepticus) and may warrant further detailed study in whole organism models of such *SCN1A* mutations. This study design allows for comprehensive assessment of the molecular functional effects of the mutation under

different, controlled experimental conditions. Describing the dynamic effects caused directly by the mutation through a computational model yielded a novel mechanism of seizure susceptibility for this epilepsy patient, consistent with his phenotype.

Using such functional evaluations to achieve clinical improvements will require further study. Functional neurophysiological studies combined with computational modelling, as illustratred in this case, show that rich information can be derived about abnormal nueronla firing dynamics for individual patients. Conducting these experiments on a larger scale will confirm whether mechanisms observed in individual patients or will converge to common mechanisms that correlate to phenotypes – something that has already been pioneered in other voltage-gated sodium channel associated conditions (Ben-Shalom et al., 2017).

5

Brain-wide synaptic changes during epileptic seizures in zebrafish §

5.1 Introduction

Epileptic seizures are transient disturbances in the brain's electrical activity causing changes of patients' behaviours or perceptions. Seizure have different causes, from gene mutations to acquired brain injuries, as discussed in chapter 2 of this thesis (Thomas and Berkovic, 2014). The effects of particular pathologies on neuronal dynamics have been studied using animal models, where different interventions (e.g. chemoconvulsant exposure) can be evaluated *in-vivo* (Depaulis et al., 2015; Parker et al., 2011; Seo and Leitch, 2014). Zebrafish in particular have been of recent interest for epilepsy research because they (1) are a vertebrate organism, (2) allow the relatively quick introduction of genetic mutations (Dhindsa and Goldstein, 2015) and large-scale drug screening (Baraban et al., 2013; Griffin et al., 2017), and (3) allow recording of neuronal function at high resolution across distributed brain networks (Ahrens et al., 2013; Kibat et al., 2016). There are now several studies of epileptic seizure in zebrafish (Afrikanova et al., 2013; Hong et al., 2016; Meyer et al., 2016; Winter et al., 2008) and recent imaging studies have captured

§ The work reported here has also been described in the following published article:

Rosch, R.E*., Hunter, P.R*., Baldeweg, T., Friston, K.J., Meyer, M.P. 2018. Calcium imaging and dynamic causal modelling reveal brain-wide changes in effective connectivity and synaptic dynamics during epileptic seizures. *PLoS Comp Biol*, 14(8), e1006375 ***equal contribution**

As part of this work, I designed the experiments together with collaborators, independently performed the computational modelling and wrote the manuscript.

network-wide changes in zebrafish activity during seizures (Turrini et al., 2017; Winter et al., 2017). However, a detailed mapping of how localised activity is integrated across the brain as a functional network during seizures is still missing.

Insights into seizure dynamics have largely been derived from computational modelling of EEG and other electrophysiological signals (Jansen and Rit, 1995; Lopes da Silva et al., 1974; Lytton, 2008). Using population models of neuronal activity allows the systematic description of the relationship between local brain circuit function and neuronal dynamics (Jirsa et al., 2014). Combining novel empirical data and *in-silico* models in this way has the potential to lead to an in-depth understanding of how specific disruptions at the microscale lead to whole-brain phenotypes recognisable as epilepsy.

One strategy to combine computational modelling with imaging is dynamic causal modelling (DCM, (Friston et al., 2003)). Here, Bayesian model inversion is used to fit neuronal models to empirical data (as discussed in Chapter 3 of this thesis). This approach combines (1) widely-used neural mass models, and (2) Bayesian model inversion algorithms. It is formally related to existing work on neural mass models in epilepsy (Blenkinsop et al., 2012; Goodfellow et al., 2012; Kameneva et al., 2017; Wang et al., 2012); as well as Bayesian inference approaches (Lie and van Mierlo, 2017; Schiff and Sauer, 2008). DCM has been widely applied to scalp EEG (Cooray et al., 2016), invasive recordings in patients (Papadopoulou et al., 2015), and invasive recordings from *in-vivo* animal models (Papadopoulou et al., 2017).

Both EEG and LFP recordings are spatially sparse samples of distributed neuronal activity. Yet most modelling approaches assume measurable oscillations to represent homogeneous averages of population activity. Such averages can now be accessed more directly using light sheet microscopy, providing summaries of neuronal population activity that closely adhere to the modelling assumptions.

In this chapter, I will model empirical recordings of epileptic seizures in zebrafish across spatial and temporal scales using hierarchical DCM analysis: Spatial scales range from regional microcircuit neural mass models (mesoscale) to dynamic whole-brain networks (macroscale). Neuronal states of the underlying biophysical models capture fast oscillatory neuronal dynamics (millisecond temporal scale), whilst slowly carrying model parameters capture the slow changes in dynamic behaviour that occur over time (seconds to minutes temporal scale).

Seizures in the *in-vivo* zebrafish larval model were induced with pentylenetetrazole (PTZ) in healthy larval zebrafish and recorded *in-vivo* with light sheet microscopy of a single slice through the zebrafish brain capturing five main bilateral brain regions. PTZ is a well-characterised chemoconvulsant and acts as a GABA antagonist, thus disrupting inhibitory synaptic transmission. Acute seizures are believed to be associated with changes in (1) local microcircuit dynamics that allow for a (phase) transition between resting and seizure activity (Breakspear, 2005; Jirsa et al., 2014), and (2) changes in whole brain connectivity (Nehlig, 1998; Omidvarnia et al., 2017; Sinha et al., 2017). DCM allows concurrent testing of the following emerging hypotheses across these different spatial scales: (a) seizures lead to a measurable reorganisation of effective connectivity between regions (Burns et al., 2014), (b) local excitation-inhibition imbalance explains associated regional spectral changes (Netoff et al., 2004), (c) in addition to changes in connection strengths, seizures are also associated with changes in synaptic transmission dynamics (Papadopoulou et al., 2017).

5.2 Methods

5.2.1 Zebrafish maintenance

Zebrafish were maintained at 28.5°C in a 14/10 light/dark cycle. The transgenic line that was used was Tg(elavl3bL:GCaMP6f) (Dunn et al., 2016). Sex of individual larval animal included in the study is not known. The work was approved by the local animal care and use committee (King's College London) and was performed in accordance with the Animals (Scientific Procedures) Act, 1986; under license from the United Kingdom Home Office.

5.2.2 Construction of light-sheet microscope

The light-sheet design was based on that described in (Wolf et al., 2015). Briefly, excitation was provided by a 488nm laser (488 OBIS, Coherent) which was scanned over 800μm in the y-direction of the illumination plane by a galvanometer mirror (6215H/8315K, Cambridge Technology) creating an illumination sheet in the XY-plane. The sheet was associated with two pairs of scan and tube lenses, scanned along the z-axis using a second galvanometer mirror (6215H/8315K, Cambridge Technology) and focussed onto the specimen via a low NA illumination objective (5 x 0.16NA, Zeiss EC Plan-Neofluar). The

detection arm consisted of water immersion objective (20 x 1 NA, XLUMPlanFL, Olympus) mounted vertically onto a piezo nanopositioner (Piezosystem Jena MIPOS 500) allowing alignment of the focus plane with the light sheet. The fluorescence light was collected by a tube lens (150mm focal length, Thorslabs AC254-150-A) and passed through a notch filter (NF488-15, Thorlabs) to eliminate 488 nm photons. The image was formed on an sCMOS sensor (PCO.edge 4.2, PCO). The 20x magnification yielded a field of view of 0.8 x 0.8 mm2 with a pixel dimension of 0.39µm2. The detection arm and specimen chamber were mounted on two independent XY translation stages to allow precise alignment of the specimen, detection axis and light sheet.

5.2.3 Imaging

Nonanaesthetised *Tg(elavl3b:GCaMP6f)* larvae, 5 days post-fertilisation were immobilised in 2.5% low melting point agarose (Sigma-Aldrich) prepared in *Danieau* solution and mounted dorsal side up on a raised glass platform that was placed in a custom-made *Danieau*-filled chamber. Pentylenetetrazole (Sigma-Aldrich) was added to the *Danieau*-filled chamber after 30 minutes of baseline imaging to a final concentration of 20mM. Functional time series were acquired at a rate of 20Hz, 4x4 pixel binning (1.6µm x 1.6µm resolution). In order to achieve the maximum temporal resolution in these recordings, they were restricted to a single plane, allowing for a sampling frequency of 20Hz. The light sheet displays a hyperbolic profile along the light propagation axis. The diffraction-limited minimum (z-dimension) thickness iof the light sheet (characterised by imaging 100nm diameter florescent beads) was ~2.5µm at the focal plane of the illumination objective. This value increases to ~9µm at a distance of 80µm from the waist. This yields single neuron resolution over a field of view of ≃160 x 1000µm centred on the midline of the larval fish – a region which contains the majority of neuronal cell bodies. At the extreme lateral margins of the fish the illumination sheet spans >1 neuronal cell body diameter and therefore does not provide single neuron solution in these regions.

Time-series of the images were aligned to a Mean image in the functional imaging data for each fish (rigid body transformation as implemented in SPM12 (http://www.fil.ion.ucl.ac.uk/spm/software/spm12). Mean fluorescence traces were then extracted from ten anatomically defined regions of interest for further analyses. Analogous to other calcium-based connectivity in model organisms (Mann et al., 2017), anatomical regions were selected according to well-defined landmarks corresponding to the following

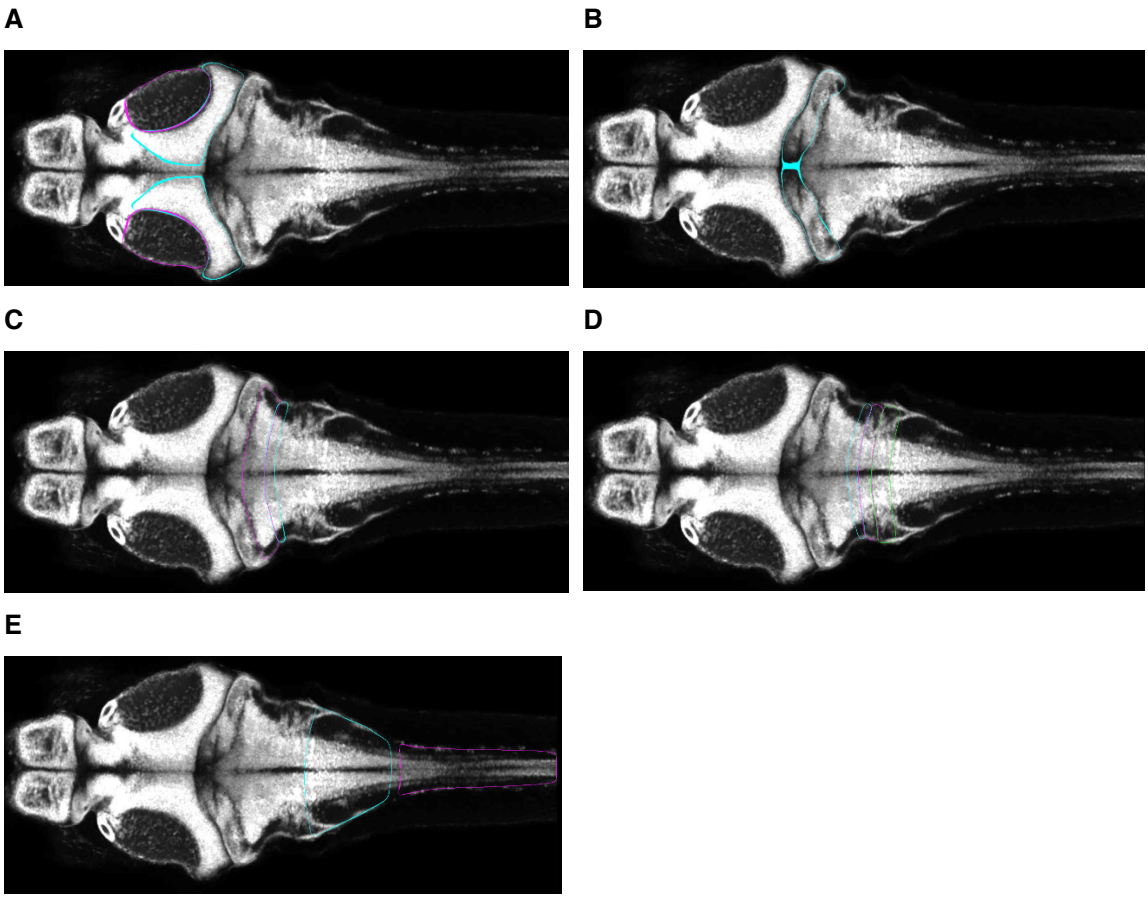

Figure 5.1- Atlas regions corresponding to the anatomical segmentation. (A) 'Tectum' corresponds to Z-Brain regions Tectum Stratum Periventriculare and Tectum Neuropil. (B) 'Cerebellum' corresponds to Z-Brain region Cerebellum. (C) 'Rostral Hindbrain' corresponds to Z-Brain regions Rhombomere 2 and Rhombomere 3. (D) 'Mid Hindbrain' corresponds to Z-Brain regions Rhombomere 4-6. (E) 'Caudal Hindbrain / Rostral Spinal Cord' corresponds to Z-Brain regions Rhombomere 7 and Spinal Cord. Images are taken from https://engertlab.fas.harvard.edu/Z-Brain [accessed 187/05/2018, all images at z = -90].

regions in a publicly available standard zebrafish atlas (Z-Brain Atlas, https://engertlab.fas.harvard.edu/Z-Brain (Randlett et al., 2015)). Cross-sectional images from the atlas corresponding to the srtructures included below are provided in Figure 5.1.

- *Tectum*: Tectum Stratum Periventriculare, Tectum Neuropil
- *Cerebellum*: Cerebellum
- *Rostral Hindbrain*: Rhombomere 2, Rhombomere 3
- *Mid Hindbrain*: Rhombomere 4, Rhombomere 5, Rhombomere 6
- *Caudal Hindbrain / Rostral Spinal Cord*: Rhombomere 7, Spinal Cord

5.2.4 Quantification and statistical analysis

Analysis was performed using custom scripts written for Matlab, as well as dynamic causal modelling packages available as part of SPM. Custom code is available online (https://osf.io/q7kth/wiki/home/) and are included in the appendix in Section A.5.

5.2.4.1 Estimation of spectral features

Mean fluorescence traces from the regions of interest were treated as multichannel time series for subsequent analysis. Short segments derived from a sliding window (length: 60s, step size: 10s) were used to estimate time-varying changes in the spectral composition of the time series: For each step of the sliding window, the real component of the Fourier spectrum was calculated. A correlation matrix of region-specific mean Fourier amplitude across all time points was used to visualise slow fluctuations in distributed activity (Betzel et al., 2012; Rosch et al., 2018). To estimate between time-window correlation, I calculated a vector containing the average power of the 0-10Hz frequency band of all channels, separately for each time window. I then calculated the full correlation matrix of each such power-distribution vector with the vectors at each other time point, yielding a k x k correlation matrix, where k is the total number of time steps. Averages of the windowed Fourier spectra and the power correlation matrix across the studied animals are shown in the results section.

5.2.4.2 Simulated calcium imaging traces

To test the construct validity of the inversion approach, I used a neural mass model with known parameterisation to generate an LFP output, convolved this output with a calcium-imaging kernel and inverted a DCM on those synthetic calcium-imaging traces to test whether the original parameterisation can be reconstructed.

The model was a three-population neural mass model already implemented as standard as 'LFP' model in the SPM12 model library (Moran et al., 2013). I generated 6 segments of LFP-like model output with linear variation of a single parameter (H_1) with values ranging from *-1* to *+1*. The convolution kernel was constructed from a fast, inverted quadratic rise lasting $t_{up} = 250ms$ of the form: $y(t) = 2t * t_{up} - t^2$. This is followed by an exponential decay function of the form: $y(t) = e^{-\frac{1}{1000}t}$. Both functions were normalised so that $y(t_{up}) = 1$.

Parameters of these functions were chosen to approximate GCaMP6f dynamics reported elsewhere (Chen et al., 2013).

5.2.4.3 Inversion of simulated calcium imaging traces

Each individual synthetic calcium imaging trace was inverted using a DCM for cross-spectral formulation with a single three-population neural mass model as the generative model (Moran et al., 2011a). The DCM analysis relies on spectral features, which are estimated using a multivariate autoregressive model that provides (complex) cross-spectral densities for each time window separately. Each of these full cross spectra is then approximated during the Bayesian model inversion.

Using a parametric empirical Bayes approach, I then compared the evidence for models where changes in a single one of the parameters explains the difference between segments (Friston et al., 2016; Rosch et al., 2017b). Parameter estimates for the winning parameter are then compared to the 'ground truth' parameter changes originally introduced into the generative model, therefore providing evidence for which parameter is changed, and how that parameter is changed to achieve the spectral changes contained in the time series.

5.2.4.4 Dynamic causal modelling of empirical calcium imaging traces

Baseline architecture: To characterise functional network architecture at rest in an initial step only. Baseline data were analysed using a DCM approach. Specifically, 4-minute segments prior to PTZ exposure were inverted using a single fully connected DCM containing 10 standard prior ('LFP' type) sources – comprising three neuronal populations each (Moran et al., 2013). DCM estimated parameter values for each of the directed, extrinsic (between region) coupling parameters, each of the intrinsic (within region) coupling parameters, regionally specific time constants, as well as a free energy approximation for the model evidence for the full model in each individual fish.

Based on this full model inversion, smaller subsets of models were then compared using Bayesian model reduction, which allows Bayesian model selection for the network architecture that best explains the baseline data with computational efficiency (Friston et al., 2016). The model space was designed as a full factorial design around three main features: The presence or absence of homologous connections between bilateral brain regions (2 model families); the presence or absence of homologous connections between bilateral brain regions (2 model families); and the presence or absence of hub-like connections from one set of brain regions to all other regions (6 model families). Thus, the

model evidence was estimated across *2* x *2* x *6* = *24* model types and evaluated using family-wise Bayesian model comparison across sections of this full model space to yield inference about hub-type connections (comparing 6 model families) and short-range connections (comparing *2* x *2* = *4* model families). The null model (Model 0) is a model where no between-region (i.e. extrinsic connectivity) exists and is included for completeness. In this model, each node is equipped with its own steady state input (a parameterised pink noise function), simulating background local activity, and has several free intrinsic connectivity parameters (local connection strengths $H_{1\text{-}5}$, and time constants of local connectivity T_E and T_I). This model space was chosen to emulate some basic features of brain connectivity found across many species and systems, specifically rich-club organisation (modelled as hub-like connectivity), hierarchical message passing (modelled as forward/backward connections along neighbouring nodes), and typically seen homotopic connections between symmetrical structures.

Seizure data inversion: Based on the dynamic network architecture identified in the step above, an additional DCM analysis was performed to identify slow fluctuations of synaptic parameters within this architecture that could explain seizure activity. For this, data were again divided into segments using a sliding window approach (60s, 50s steps) for each animal separately. DCMs with the architecture derived from the step above were inverted separately for each individual time window.

I then constructed a second level model to estimate between-time window variations in parameters using a parametric empirical Bayesian approach (Friston et al., 2016; Papadopoulou et al., 2016a). This contained several temporal basis functions that in combination can explain a majority of possible parameter trajectories: (1) an 'on/off' tonic seizure effect step function with onset at PTZ injection; (2) a monophasic seizure effect function with onset at PTZ injection; (3) a linear increase with onset at PTZ injection; (4) a set of three discrete cosine basis functions to model parameter drifts at different temporal frequencies; (5) a set of three regressors modelling random between-fish effects.

This approach provides estimates for how between-time window parameter changes can be modelled as a linear combination of the basis sets provided, as well as free energy estimate for the model evidence. I can thus perform Bayesian model reduction and selection at the second level, comparing competing model families where only subsets of parameters are free to vary between time windows, and thus select a subset of parameters

that best explain the observed changes over time. I broadly divided the model space of these between time-window (i.e. between individual DCM) effects into (a) models with variations in hierarchical coupling, (b) models with variations in hub coupling, and (c) models with variations in intrinsic synaptic coupling parameters. Family-wise Bayesian model selection was used to select relevant parameters, which were freed in a single model to provide parameter estimates at time windows with the estimated maximum PTZ effect. Forward modelling: To further explore the effects of specific parameter changes, the optic tectum with its hub-like position in the network was analysed further. Posterior parameter estimates for each time window derived from the PEB-DCM analysis above were grouped into time constant and connection strength changes. In order to allow a low dimensional projection of the multiple parameters of interest, I performed a principal component analysis separately on the intrinsic connectivity parameters ($H_{1\text{-}5}$), and the time constant parameters (T_E and T_I). The first principal component of each of these categories was then used to project the parameter changes into a two-dimensional plane. Because the DCM provides a fully generative model, I can not only plot the parameter estimates, but also generate a predicted spectral output for each point across this plane, by adding the respective principal component values to the baseline parameterisation of the model and simulating its output. I then plotted the resultant low frequency (delta-range), and high frequency (gamma-range) power across the parameter space to indicate how movement in parameter space affects the spectral output.

5.3 Results

5.3.1 Simulations

In the analysis presented here, I used electromagnetic neural mass models originally designed to explain data features observed in LFP recordings. First, I confirmed the construct validity of this approach – i.e. applying DCM for local field potentials to time traces derived from light sheet imaging – by applying the analysis to synthetic data, where the 'ground truth' is known. These were derived from a neural mass undergoing predefined parameter changes: Using a single 'source' consisting of three coupled neuronal populations, I generated noisy LFP-like data. These were then convolved with a composite exponential decay kernel modelling calcium probe dynamics (Chen et al., 2013). These

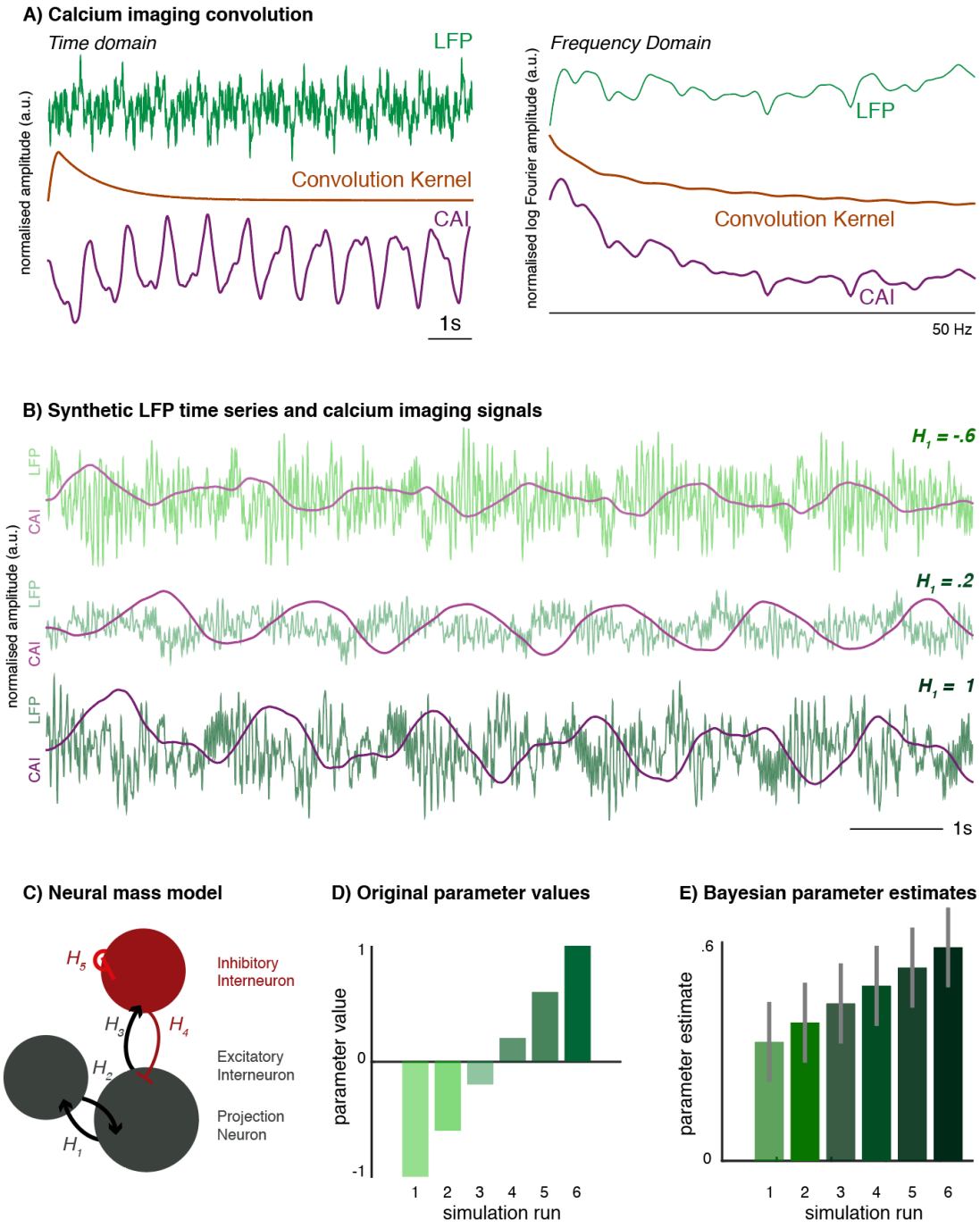

Figure 5.2 – Dynamic causal modelling of simulated calcium imaging time traces. (A) Left-hand side time series show signal amplitude over time in arbitrary units. Calcium imaging dynamics were modelled by convolving LFP-traces (top) with calcium imaging kernel (middle), resulting in a calcium imaging (CAI) time trace (bottom). The CAI trace follows slow LFP dynamics whilst attenuating faster components of the transform of the original signal. Right hand side frequency plots show normalised log-amplituds derived from a Fourier transform of respective time series over a range of frequencies (1-50Hz). In frequency space, the convolution differentially scales low and high frequency components, but preserves most frequency features (B). LFP-like time-series plotted in arbitrary amplitude units over 10s. These are derived from a three-population neural mass model with increasing values of a single parameter, H_1 – also shown in panel (C).

Example CAI traces after convolution are shown in darker colours. (C) A three-population neural mass model is used for generating LFP traces and is subsequently fitted to the convolution-derived CAI traces. (D) Bayesian model comparison (Bayes factor 2.6) between repeated model inversions identifies correctly that differences between simulated CAI traces were caused by the effects of variations in the H_1 parameter on the synthetic LFP traces. The parameter values included in the generative model are shown in the bar chart. (E) The DCM analysis provides estimates of the generative model parameters (shown in the bar chart). These results correctly infer the increase of H_1 across the six model inversions from the CAI traces. Parameter estimates are shown here with a Bayesian 95% confidence interval (grey bars). Whilst the group mean parameter value and the effect size are different, this inversion correctly identifies the linear increase in the parameter from the simulated CAI dataset.

LFP – local field potential, *CAI* – calcium imaging, *DCM* – dynamic causal model, *PEB* – parametric empirical Bayes.

surrogate fluorescence time traces are then down sampled to the sampling frequency achieved in the single-slice light sheet imaging (20Hz). This linear convolution equates to a simple addition of the signals in (log) frequency space. Because of the simple frequency composition of the calcium imaging kernel, this linear transformation preserves much of the spectral features in the underlying LFP-like signal Figure 5.2 A.

The variations in the single neural mass model parameter introduces spectral changes in both the surrogate LFP and fluorescence time traces Figure 5.2 B. I fitted a three-population neural mass model (of the kind used to generate the synthetic LFP traces, Figure 5.2 C) separately to each of the fluorescence time traces. This yielded six separate dynamic causal models (DCMs), one each fitted to the six time series generated using variations in a single parameter as shown in Figure 5.2 D. Using a hierarchical parametric empirical Bayesian model, I then identified which parameter could best explain the differences in these DCMs (fitted to fluorescence signals). This approach successfully identified variations in the correct parameter (the intrinsic connectivity parameter H_1) as the most likely cause for the differences in time series. Furthermore, the estimated between-DCM differences in H_1 values also captured the direction of the linear change introduced in the original simulated LFP.

5.3.2 Seizure recordings

In order to elicit epileptic seizures, PTZ was infuse in the bath of $n = 3$ zebrafish larvae. Resultant seizure activity was recorded with light-sheet imaging utilising somatically expressed GCaMP6f genetically encoded calcium probes. Neural activity was recorded *in-vivo* in agarose immobilised larvae capturing a single slice of the intact brain. The changes

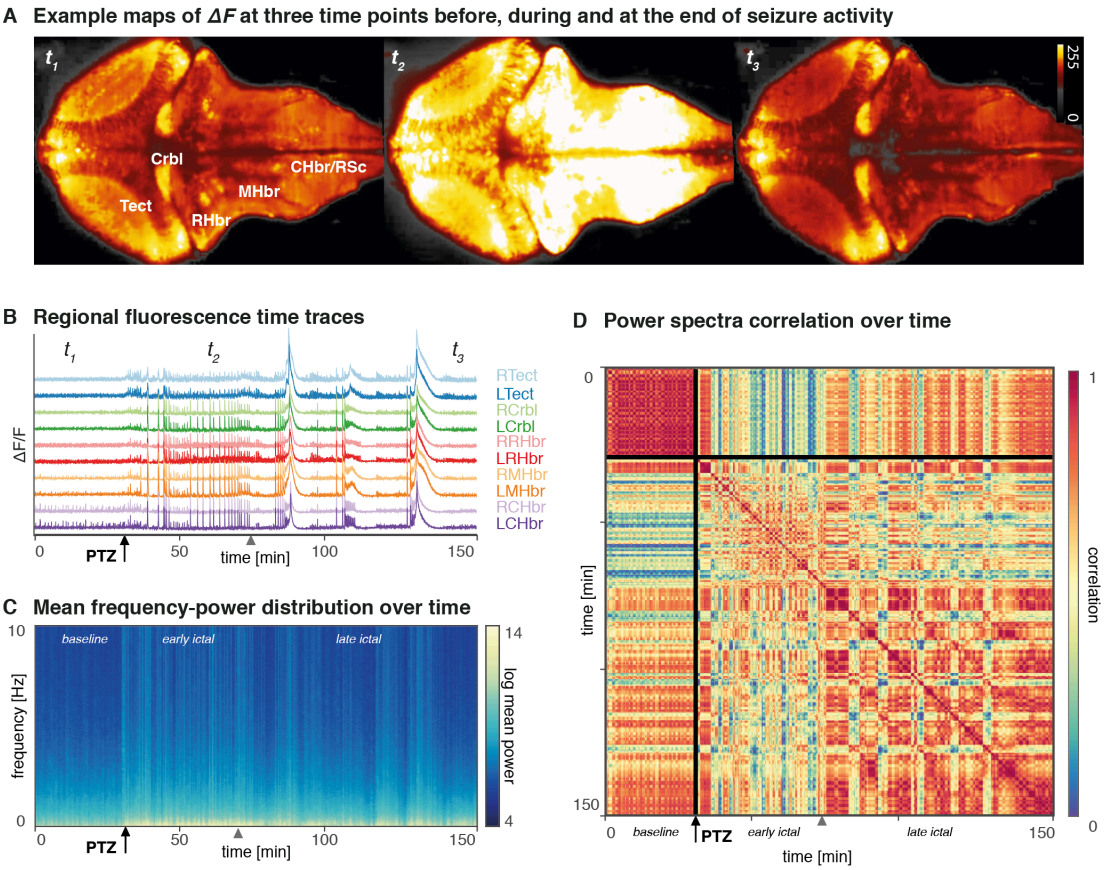

Figure 5.3 – PTZ induced seizures recorded in the zebrafish larvae using light-sheet imaging. (A) This image shows heat maps of fluorescence in a single slice of the intact larval zebrafish brain in the *xy* plane at different time points during the experiment (also marked in panel (B)). Seizure activity at t_2 is visually apparent as an overall increase in neuronal activity compared to the baseline state at t_1. (B) Regionally averaged time traces of the fluorescence signal across 5 bilateral anatomically defined regions are shown for the whole duration of the experiment in a single animal (150 minutes). Seizures are readily apparent as an increase in generalised and apparently synchronous high amplitude activity. (C) Average Fourier power spectra across fish and across all brain regions are plotted against time for the duration of the experiment, using a sliding window estimator (length: 60s, step 10s), with colours indicating log-power. The graph is the average over *n*=3 fish. (D) A correlation matrix showing correlation indices of the power-distribution patterns across different time points (delay-delay matrix). This reveals three distinct time periods, corresponding to baseline (<30min), ictal (30-70min) and late ictal (>70min) phases with distinct spectral signatures and temporal dynamics.

in activity within the whole imaged slice was readily apparent in the fluorescence images (Figure 5.3 A). The slice was divided into 5 bilateral regions of interest to extract fluorescence time series from the recording. These showed distinctive features consistent with highly correlated epileptic seizure activity (Figure 5.3 B). Using a sliding window (length: *60s*, step: *10s*) I was able to estimate the time changing frequency content using a Fourier transform, which demonstrate a particular increase in low frequency power after PTZ infusion (Figure 5.3 C), with additional intermittent bursts of broadband activity

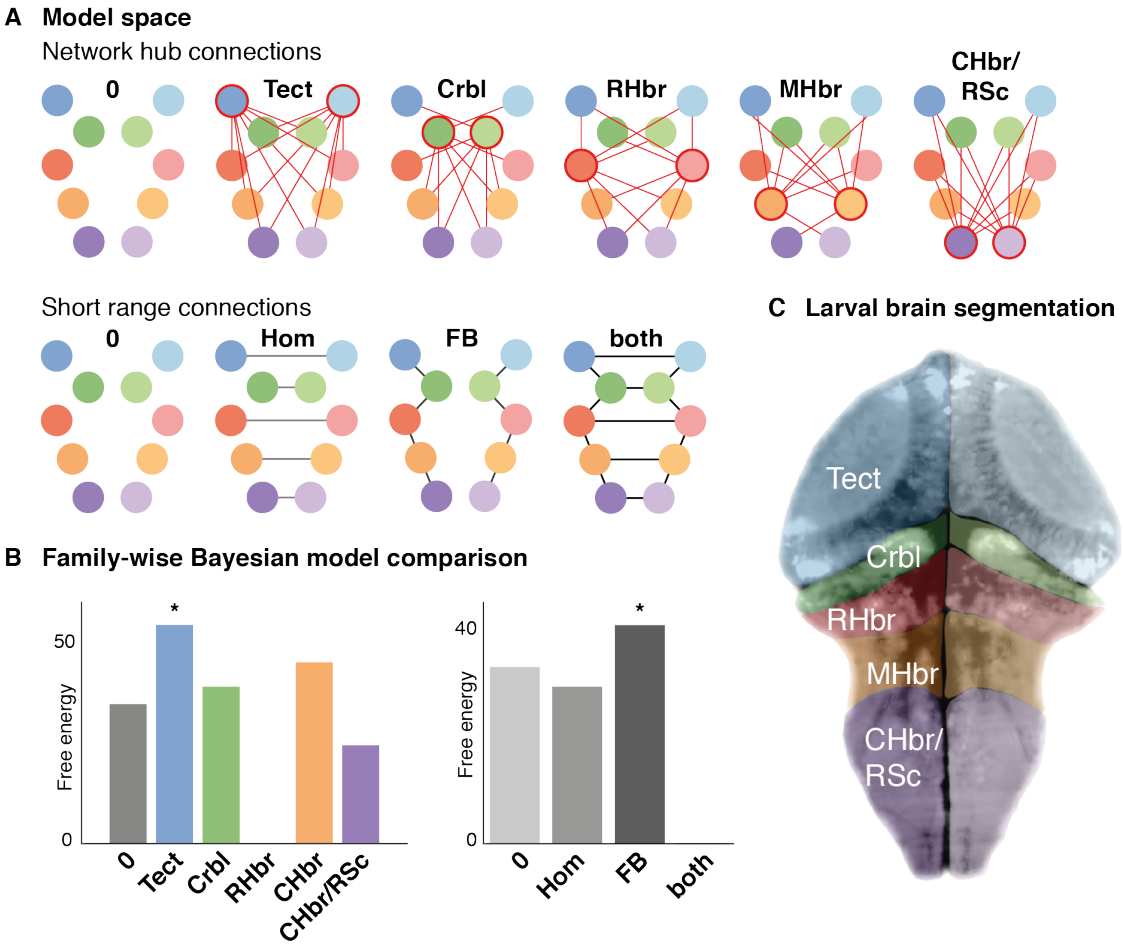

Figure 5.4 – Network model architecture during interictal background activity. (A) Two aspects of a factorial model space are shown: extrinsic connectivity of putative network hubs (yielding 6 types of models), and short-range connections between neighbouring and homotopic nodes (yielding 4 different types of models); a total of 6 * 4 = 24 models were evaluated, where any one model combines one of the network hub connectivity architectures with a short-range connectivity setup. Bayesian model reduction was used to estimate the model evidence across this model space characterised by the presence, or absence of these defined sets of between-region reciprocal connections (neighbouring, homotopic, and hub connections). (B) For each model family (corresponding to the factorial model space), the free energy difference to the worst-performing model is shown. In DCM, the free energy difference is used to approximate model log-likelihood differences: Asterisks indicate the winning model family identified from Bayesian model selection. These results indicate that the model with neighbouring, and homotopic connections as well as the optic tectum with hub-like connectivity best explain the observed spontaneous activity at baseline. (C) Mapping of the ROIs for this analysis is illustrated as overlay on a single fluorescence image taken from one of the animals included in this study. Areas were identified based on visible neuroanatomical landmarks and correspond to the nodes of the same colour in the network representations of the model space.

seen. Estimating correlations between the regional power-frequency distributions across different time windows reveals apparently distinct phases of PTZ induced seizures (Figure 5.3 D): A baseline (pre-seizure) that is stable over time (0-30min), an initial ictal period that differs the most from the baseline state (30-70min) and a late ictal period where time

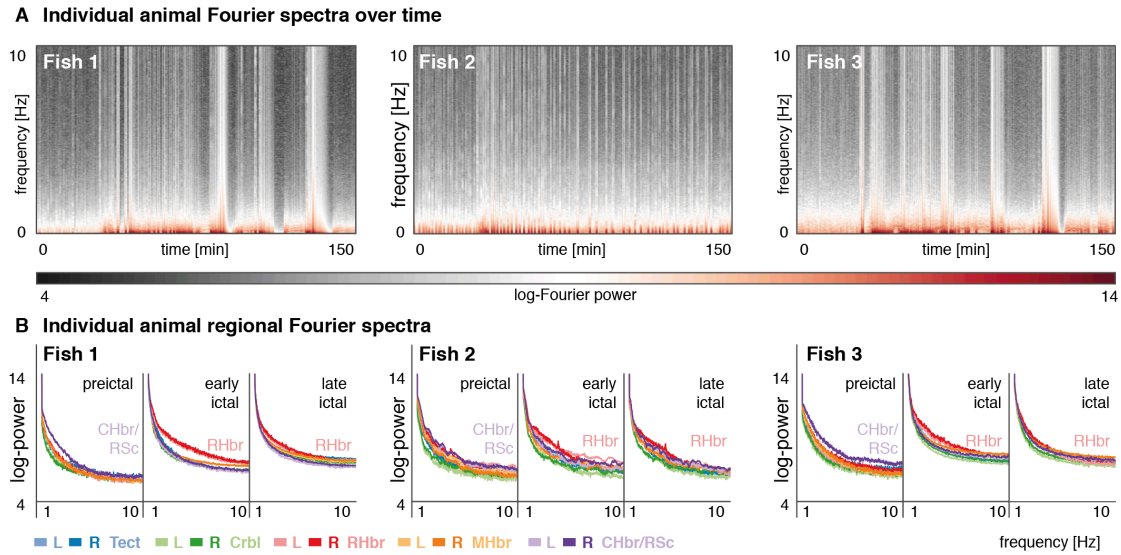

Figure 5.5 – Individual fish spectral changes during induced epileptic seizures. (A) Fourier spectra are shown for light sheet recordings of individual animal recording sessions. Using a sliding window (size 60s, step 10s), windowed estimates are made of the frequency composition of the mean time fluorescence time series across all regions and plotted over time with colour-coding indicating the (log) power at particular frequencies. Seizure onset is associated with frequency bursts, which become less frequent but more prolonged in the late ictal state. (B) Frequency power plots are shown for individual regions at preictal, early ictal and late ictal intervals for each fish. Colours indicate the brain region as indicated by the key. Individual fish show reproducible patterns of localised frequency power distribution changes at seizure onset – in the preictal state the caudal hindbrain / rostral spinal cord (CHbr/RSc) show highest overall activity; during early and late seizure activity in the rostral hindbrain (RHbr) has the highest broadband power.

periods of apparent similarity (i.e. high correlation) to the baseline are interrupted by intermittent different (i.e. low correlation) segments (70-150min).

5.3.3 Functional network architecture at baseline

I employed Bayesian model comparison to identify the effective connectivity network that best explains the observed baseline data. In brief, baseline activity was modelled as spontaneous activity arising from a coupled network of neuronal sources. Each source is made of up of a three-population neuronal microcircuit (excitatory and inhibitory interneuron populations) that is fitted to a cross-spectral density summary of the fluorescence signal at baseline. A single fully connected network was fitted to an average of the baseline activity by inverting a single fully connected dynamic causal model (DCM). Using Bayesian model reduction and Bayesian model selection I then compared models, where specific sets of between-region reciprocal effective connections were either present or absent. These sets of connections were (1) hub-like connectivity between any one region and all other regions; and (2) short range connections between neighbouring, and

homotopic brain regions (Figure 5.4 A). Bayesian model comparison across the reduced models in this model space provided evidence that the baseline configuration can best be described as a network of neighbouring connected nodes with the tectum acting as a network-wide hub (Figure 5.4 B). Notably in this mesoscale modelling, such directed connectivity is understood to be the average influence one region has over another – this may be mediated monosynaptically or through additional (hidden) network nodes. In the model each source contains a simply parameterised steady state noise input function that is updated as part of the model inversion – therefore synchronous oscillations between different nodes could possibly be explained away during the inversion by fitting identical inout functions to each source. Where more complex models with specific connectivity patterns are identified as the most parsimonious explanations for the particular spontaneous activity, this suggests that not all aspects of the complex cross-spectral densities (which include phase differences between sources) can be explained by common input alone.

5.3.4 Hierarchical dynamic models of seizure activity

Using the model architecture identified above, I then fitted individual DCMs to the sequence of sliding window derived cross-spectral density summaries of the original data. Spectral changes were found to be consistent across the fish used for this study (Figure 5.5). All seizure effects are subsequently assumed to arise from variations in the model parameters that are present in the baseline model architecture and are shared between individual fish. Thus, seizure activity may 'switch off' connections (through reduction of the particular parameter), or silence a node in the network (through increases in self-inhibition), but no new connections or nodes are added to explain data features that arise during the seizure. At this stage (i.e. first level models), each time window is modelled as an independent DCM. The model fits show that these independently inverted models recreate the dynamic fluctuations of spectral composition observed during a seizure very well and thus provide a good representation of the original data features (Figure 5.6). Across all complex cross-spectra (for all time windows and all animals), the model fits explain 74.6% of the variance in the original data ($R^2 = 0.746$).

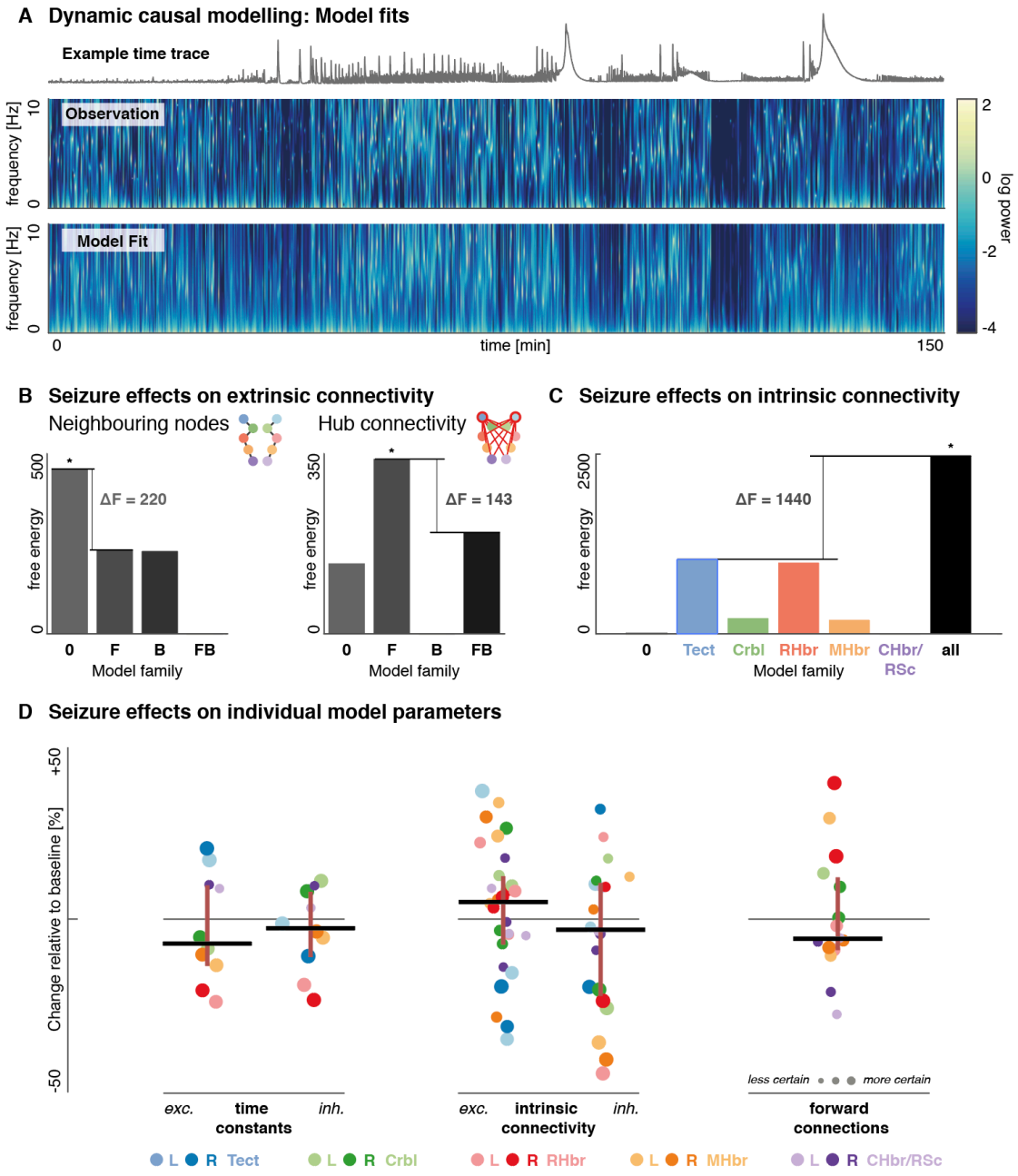

Figure 5.6 - Group level effects of PTZ-induced seizures on synaptic coupling. (A) Here (1) an example fluorescence time trace from a single region, (2) an example eigenmode summary of the cross-spectral density changes over time observed across all region in a single fish (this is derived from a multivariate autoregressive model and constitutes the primary data features in DCM), and (3) the model fits of windowed DCMs to that same animal are shown. The middle and bottom panel both plot frequency power distribution across the time of the experiment, where the log-power for any given frequency is represented by colours corresponding to the same colourbar (range -4 to 2). DCMs fitted to these individual time windows capture the spectral changes measured well for the duration of the experiment. (B) Free energy approximation for the model-family evidence for reduced models where PTZ-induced changes were restricted to a subset of coupling parameters is shown. Bayesian model comparison at this second (between time-window) level was performed to compare reduced models with PTZ-induced changes in *F* forward, *B* backward, *FB* both, *0* or neither type of regional connectivity. Asterisks indicate the winning models.

Only changes in connections from other brain regions to the hub region show evidence of being modulated by the seizure activity. (C) Similarly, free energies for model families that allow for intrinsic connectivity parameter changes in none of the brain regions, single brain regions, or all brain regions are shown. The asterisk indicates the winning model. There was strong evidence for intrinsic connection changes in all brain regions. (D) Estimates of the PTZ-effect on DCM model parameters are shown, corresponding to the expected change relative to baseline that was induced by PTZ. Each dot represents a posterior density, centred around the expected value, and its size inversely correlated to the covariance (or uncertainty), i.e. the larger the dot, the more precise the estimate. Dots are colour-coded by region as shown in the legend. Lines indicate the median of the expected values with whiskers showing 25th and 75th centiles respectively – but note that individual parameter estimates are not random samples from an underlying distribution but themselves represent more or less precise model parameters fitted to the observed data.

Model families (extrinsic): 0 – no extrinsic connectivity changes; F – extrinsic connectivity changes in forward connections only; B – extrinsic connectivity changes in backward connections only; FB – extrinsic connectivity changes in both forward and backward connections. ***Model families (intrinsic):*** 0 – no intrinsic connectivity changes; Tect – intrinsic connectivity changes only in the bilateral optic tectum; Crbl – intrinsic connectivity changes only in the bilateral cerebellum; RHbr – intrinsic connectivity changes only in the rostral hindbrain; MHbr – intrinsic connectivity changes only in the mid-hindbrain; CHbr/RSc – intrinsic connectivity changes only in the caudal hindbrain/rostral spinal cord; all – intrinsic connectivity changes across all areas.

Parametric empirical Bayes (PEB) can be employed to identify parameters across individual DCMs that vary systematically with specified experimental variables. In brief, PEB allows one to invert hierarchical models where, in this instance, the first level of the model corresponds to a sequence of time windows. The second level of the model then uses the posterior densities over the first level parameters to model changes (here fluctuations) in the first level parameters. I modelled PTZ induced changes in a mixture of four effects: (1) a simple model of PTZ bioavailability as first order pharmacokinetics with a maximum effect at 30 minutes, (2) a tonic effect switched on for the duration of the PTZ exposure, (3) a monotonically increasing effect representing the influence of prolonged seizure activity, (4) oscillatory effects at different slow frequencies represented by a set of discrete cosine transforms (Cooray et al., 2015). This approach provides a single model at the group level (i.e. across all time windows and all individual fish) and parameter changes are modelled as a mixture of experimental and random effects. The estimated mixture of parameter effects yielded consistent spectral changes across the individual fish used for the study (Figure 5.7). This type of modelling assumes that discrete oscillatory neuronal states (e.g. apparently distinct states during the seizure with very different neuronal signatures arise from mostly smooth fluctuations in the underlying parameters. This is indeed a

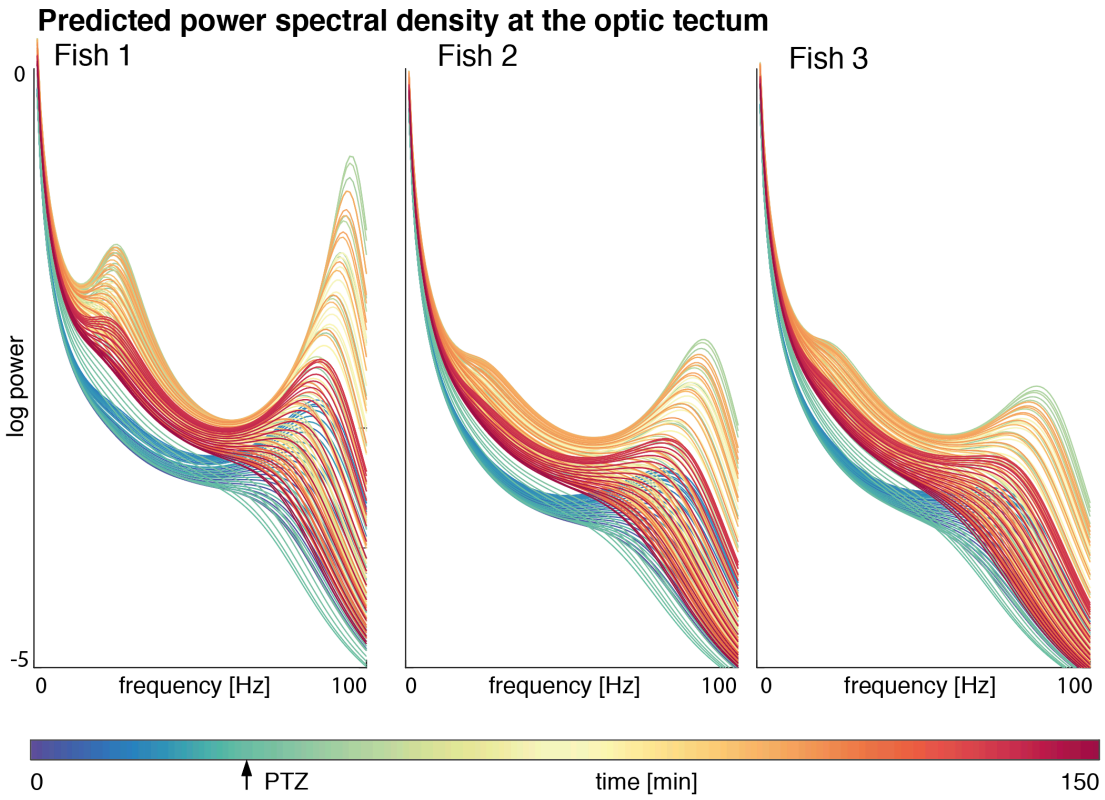

Figure 5.7 – Predicted full-spectrum power densities for individual fish. Graphs show the full spectral densities predicted by the fitted dynamic causal models derived from the hierarchical model inversion across all time windows and fish. Each graph shows time-windowed power spectral density estimates for the optic tectum, with colours indicating the time-window (see colourbar). Each fish showed recognisable frequency peaks at approximately 20Hz, and 90Hz, which differ quantitatively between fish. Note that the high frequency peak is predicted to achieve its maximum just after PTZ injection for each of the fish.

feature of the types of models at the heart of dynamic causal modelling (i.e. neural mass models) and their nonlinear mapping between parameters and states.

This has been exploited extensively in the past to link apparently sudden transitions in neuronal dynamics to slow synaptic or neurochemical changes that could cause them (Jirsa et al., 2014). These second level inversions also provide an estimate of the model evidence so that different models can be tested against each other.

In the first instance, I compared models where only subsets of between region connections were allowed to vary between time points. Bayesian model comparison shows that only changes in the forward connections to the network hub (i.e. bilateral tectum) are required to explain the spectral changes during seizure activity (Figure 5.6 B). Model comparison was also used to test for PTZ-induced changes in the intrinsic coupling parameters in

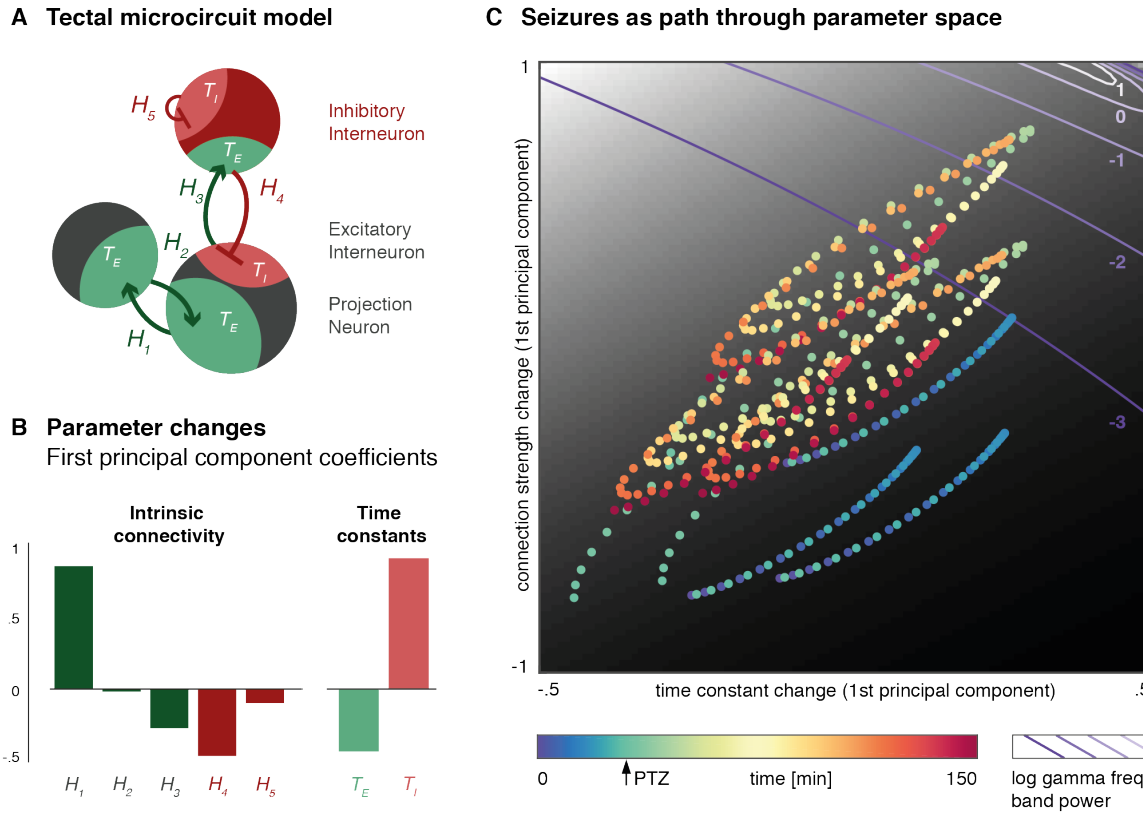

Figure 5.8 - Temporal evolution of intrinsic coupling parameter changes in the optic tectum throughout the seizure. (A) A single source 3-population model is shown, indicating the seven parameters that are fitted as part of the dynamic causal modelling: 5 intrinsic connectivity parameters (H_1 – H_3 excitatory connections, to H_4 – H_5 inhibitory connections), and 2 time constants (T_I and T_E). (B) A principal component analysis was performed separately across the posterior estimates of intrinsic connectivity, and time-constant parameters for the optic tectum across all time windows of the experiment. The coefficients for the first principal component of intrinsic connections (left) and time constants (right) are shown here. (C) Using these two principal components, parameter estimates of intrinsic coupling within the optic tectum for each individual time window are projected onto a two-dimensional parameter space. Each point of this projection is colour coded according to its time in the experiment from which the estimate was derived. In order to relate location in parameter space to spectral output at the optic tectum, for each point in this parameter space, I ran a dynamic causal model of the optic tectum in simulation mode to yield an yield an estimate of power spectral densities at that particular parameter combination. Here I map the predicted mean log-power in the delta- (black and white heat map) and gamma-band (purple isoclines) respectively. Thus the figure shows the temporal evolution of intrinsic coupling parameter estimates within the optic tectum during the seizures on a map of the spectral energy for different frequency bands for the specific parameter combinations.
Time points just after PTZ injection occupy the most extreme top-right corner of this parameter space. This indicates both slower inhibitory connectivity (time constant component) and stronger excitatory / weaker inhibitory connectivity (connectivity time constant component). These paramete changes are associated with high powers in both the gamma and the delta band.

individual regions. There was strong evidence for an involvement of all measured brain regions.

Note that among the models where seizure activity only affects intrinsic connections of a single node, the tectum and rostral hind brain emerge as the most likely models – suggesting that variations in both have a particular impact on the seizure dynamics. The estimated parameter changes induced by PTZ were varied between different brain regions, but overall showed a relative reduction in excitatory time constants (suggesting faster responses), reduction in inhibitory intrinsic connections, and a reduction of the influence of other brain regions on the optic tectum (i.e. a reduction in forward connections; estimates of the time varying parameters shown here summarise effects at the assumed peak PTZ-effect time window early in the seizure, Figure 5.6 D). Most of the larger effects in terms of intrinsic model parameters affect the rostral hind brain and the optic tectum, with at times apparently opposing effects (e.g. opposing changes in excitatory time constant changes).

Note that each value on the parameter plot (Figure 5.6 D) represents a posterior density that consists of both the estimated parameter value for the particular parameter and a posterior covariance that represents the uncertainty around that parameter estimate. In dynamic causal modelling, inferences are made via model comparison (i.e., log evidence or odds ratios provided). Thus, the plot shown in Figure 5.6 D provides a quantitative characterisation of the underlying effect sizes in terms of posterior densities, under the best model. The values show the effects and between-region differences (the scatter of the dots reflects precise and systemic inter-regional differences, not random effects). Whilst similar parameters are grouped in the scatter plot for visualisation purposes, they represent different aspects of the same model inversion and thus the optimal fit, given the data. As such their mean or median value is only informative to provide an intuition as to the overall direction of the effect. The intuition of how individual parameter changes relate to spectral output is characterised in more detail for one region (the optic tectum), below.

In the next step, I quantified the temporal evolution of the parameter changes in one example region so as to map (smooth) parameter changes against associated changes in the spectra over time. For this, I collated all the parameters intrinsic to that region (i.e. intrinsic coupling parameters H and time constants T) and simulated the associated spectral output from a single three-population source. This was done for a range of different parameter values informed by the empirically-derived posterior parameter estimates from the PEB analysis above (Figure 5.8 A).

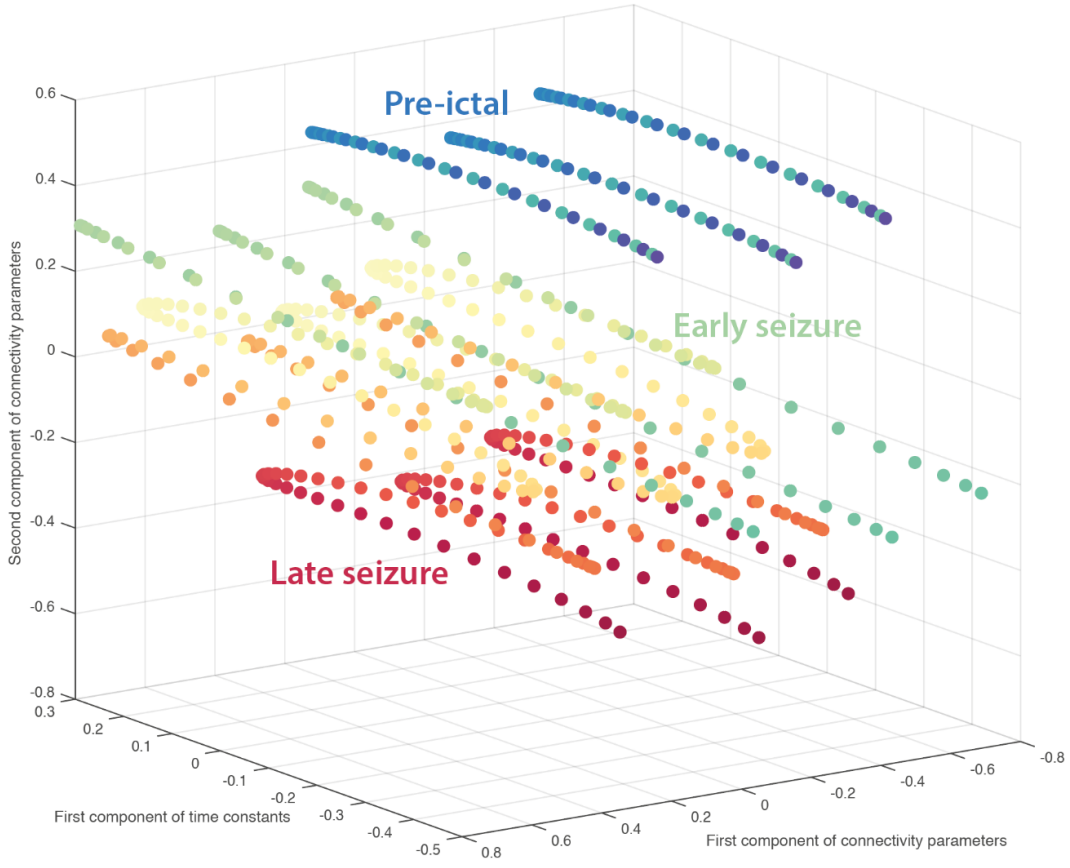

Figure 5.9 – Three-dimensional projection of seizure trajectories. Analogous to Figure 5.8 C this figure shows a low-dimensional projection of the parameter values for each individual time window as estimated for the optic tectum. Here I am plotting an additional third dimension (the second component of the PCA over intrinsic connectivity strengths), revealing a clearer separation of the different seizure phases, indicating the transition from pre-ictal, to early seizure, to late seizure phases.

I then extracted parameter estimates for time constants and intrinsic connectivity within the right tectum over time across all components of the PEB model (i.e. tonic seizure effects, monophasic PTZ effect, prolonged seizure effect, discrete cosine transforms, random between-animal effects). In order to visualise the parameter changes over time, I derived a low-dimensional representation of the data: I extracted the first principal component of the posterior estimates of the intrinsic connectivity parameters, and the time constants across time windows (Figure 5.8 B). The first principal component of the time constant changes explains 70.9% of their variance; the principal component of the intrinsic connection changes explains 49.2% of their variance (which can be increased by including an additional component to 80.0%).

Plotting each time window onto this reduced parameter space containing most of the variance in coupling parameters represents the seizure as a spiral path through parameter space. Because this parameter space specifies a fully generative model, I can apply parameter combinations at each point in the space to a microcircuit model and predict the spectral output. Here I show these predictions of log-delta band power as a heatmap, and log-gamma band power superimposed as isoclines (Figure 5.8 C). This forward modelling approach shows that during the seizure, the model enters a section of parameter space characterised by both high delta and high gamma power components, which is also seen in LFP recordings during seizures in zebrafish reported in previous studies (Baraban et al., 2013). Adding a second intrinsic connectivity component further separates out the distinct seizure phases in a three-dimensional parameter space (Figure 5.9).

5.4 Discussion

Even well studies pharmacological interventions, such as PTZ show multi-scale effects across the nervous system (Baraban et al., 2005; Huang et al., 2001; Kalueff, 2007; Nehlig, 1998). Thus, linking membrane-level changes with a whole brain seizure phenotype remains challenging. Here I combined zebrafish light-sheet imaging data during PTZ-induced seizures with dynamic causal modelling in order to identify network-wide connectivity changes.

5.4.1 Validity of DCM for calcium imaging traces of seizure activity

Calcium imaging time series are highly correlated with concurrent LFP recordings (Chan et al., 2015). Whilst LFP generally allows measurement of neuronal population activity at a higher temporal resolution (including activity > 100Hz), calcium imaging is more limited due to both the sampling frequency (Keller et al., 2014), and the fluorescence decay dynamics of the calcium-sensitive probe (Chen et al., 2013).

The predominant frequency components of both resting brain activity and seizure activity in the larval zebrafish brain are in the delta (<4Hz) and theta (4-8Hz) band (Afrikanova et al., 2013). Neuronal fluctuations in these frequency bands are largely preserved in calcium imaging, and apparent even at sampling frequencies as low as 20Hz,. The simulations here illustrate the construct validity of using neural mass models that generate electrophysiological responses to explain calcium imaging data: DCM allows correct causal

inference from calcium fluorescence time series to underlying coupling parameters. This approach provides deeper neurobiological insights than functional connectivity approaches alone. Furthermore, the hierarchical models I have applied here allow tracking of slowly varying model parameters (Papadopoulou et al., 2017), offering explanations for qualitatively very sudden changes in oscillatory behaviour (represented by the output of individual DCM models) emerging from gradual changes in model parameters (represented in across-DCM parameter changes estimated in the PEB approach).

The DCM analysis of simulated data here only recovered the trend of the activity (not the actual value). I used a convolution kernel to simulate the effects of calcium imaging on a time series but inverted the models with a DCM that lacks such a kernel – therefore some difference in the results is anticipated. However, in the time resolved analysis of connectivity changes during a seizure, I was particularly interested in the relative change of model parameters over time more than the background setup (which I account for as an additional group-mean effect in the hierarchical modelling with PEB-DCM).

This analysis harnesses specific advantages of regionally averaged calcium imaging: Light-sheet microscopy samples in a spatially unbiased fashion, thus providing a closer approximation to the assumptions underlying neural mass models (Moran et al., 2013). Heuristically, this spatial averaging suppresses local fluctuations in the same way that averaging over time in event related potential studies (in electrophysiology) reveals dynamics that are conserved over multiple realisations. Furthermore, epileptic seizures are an emergent property at the level of neuronal populations, and computational models specifically addressing this 'mesoscale' may yield important insights about emergent population-wide features less readily apparent from microscale modelling of individual neurons (Kuhlmann et al., 2015). Furthermore, this analysis allows inferences to be linked back to established knowledge about the anatomical regions included in the study. However, I do not fully exploit the spatial resolution offered by the calcium imaging data, which will need to be addressed in the future with scalable custom approaches to modelling of individual neurons (Chen et al., 2018; Rahmati et al., 2016). One strategy to exploit the resolution of light sheet images is through definition of 'regions' based on microscale neuronal properties (e.g. correlated activity, distribution of neurotransmitter receptors (Lovett-Barron et al., 2017)) – whilst the same model inversion technology illustrated here remains applicable, the data features selected for DCM inversion would be informed by

the neuroanatomical and neurophysiological information in the light-sheet imaging data and thus exploit the spatial resolution available.

5.4.2 Network organisation in the larval zebrafish brain

DCM allows for the estimation of network coupling parameters that underlie and 'cause' features observable through neurophysiological recordings, within the constraints of the available data and the hypothesises model space. The first step of my analysis thus aims to explain the pre-ictal baseline fluctuations in 5 bilateral brain regions of the zebrafish brain through any one of the proposed model architectures. Both changes in the data used for further analysis (e.g. changes in the regional divisions, or extension beyond a single imaging plane) and changes in model space (e.g. inclusion of another possible hypothesis) may therefore impact on the inference drawn. However, both the data included in this study and the model space explored reflect the types of hypotheses I sought to explore.

Early during zebrafish development, retinotectal connections develop and stereotyped but effective visuomotor behaviour is established (Meyer, 2006; Niell et al., 2004; Niell and Smith, 2005; Portugues and Engert, 2009). This is associated with distributed network activity involving information flow from the optic tectum to other brain areas. This visually-dominated early network activity is also apparent in the DCM analysis, where the tectum has been identified as a hub with widespread connectivity to the rest of the larval zebrafish brain from resting state light sheet recordings at baseline.

This network organisation is modulated during seizure activity, where my modelling identifies a reduction of the effective forward connections from other brain areas to the optic tectum. This asymmetric shift in connectivity (with only forward, but not backward connections affected), may be indicative of a key role of the optic tectum – as a central network hub at baseline – in driving network-wide synchronisation during an epileptic seizure. The selective reduction in effective connectivity corresponds to previously reported seizure-related changes in functional connectivity estimated from human EEG recordings, where increased clustering during a seizure has been described (Schindler et al., 2008).

Fluctuations in effective connectivity between regions is usually thought of as resulting from changes in direct synaptic connectivity (Nam et al., 2004). Where all connections towards a single brain region are involved, this may be due to (1) specific synaptic mechanisms affecting synaptic receptors at this particular region, or (2) changes in local

excitability. However, the asymmetric involvement of a single brain region – where only effective connectivity to (and not from) the optic tectum is reduced suggests that local microcircuitry changes may underlie the macroscale observable changes. The relationship between local and macroscale network changes in epilepsy in the context of hierarchically coupled brain areas is discussed elsewhere (Omidvarnia et al., 2017). This phenomenon has been formally described in other modelling work through a slow local permittivity variable that governs synchronisation between different brain regions and represents different slowly unfolding changes in local energy and metabolic milieu (Proix et al., 2014).

5.4.3 Intrinsic coupling changes disrupt excitation-inhibition dynamics

PTZ acts as an acute chemoconvulsant in a range of different model organisms, likely due to allosteric inhibition of GABA-A receptors (Huang et al., 2001). Previous work on a PTZ rat model showed dose-dependent regionally specific cellular activation (Nehlig, 1998), suggesting differential susceptibility of different brain regions to PTZ effects. Bayesian model comparison of seizures recorded from the zebrafish in this report indicate that PTZ-induced changes of intrinsic neuronal population coupling were required in each of the brain regions. From the free energy distribution across models with different single regions affected by seizure changes, I found relatively high model evidence for models comprising seizure-related parameter changes in the optic tectum, or in the rostral hindbrain, suggesting that there is heterogeneity in the contribution of individual brain regions to the evidence for the winning model.

PTZ-related seizure effects are modelled under the assumption that they arise from changes in the existing extrinsic (between-region) connections and intrinsic coupling parameters. I expected most of the interesting effects to occur on the coupling parameters within regions (as most of the PTZ effect will affect local inhibitory interneuron connectivity (Lee and Maguire, 2014)). Whilst epileptogenesis in the brain (i.e. developing the propensity for recurrent seizures) may require the establishment of novel, pathological connectivity, acute seizure activity most likely will not. Thus, this modelling approach has the ability to account for most neurobiologically plausible mechanisms underlying acute seizures.

However, these effects varied widely between regions. This in part reflects different baseline configurations of the regional source models, which in turn required different shifts in coupling parameters. Yet, overall the PTZ-related changes are broadly consistent

with the current understanding of its effects at the neuronal membrane. Specifically, PTZ is expected to cause a relative decrease of inhibitory connectivity compared to excitatory connectivity; and preferential blockade of fast GABA-A (and not GABA-B) mediated transmission would be expected to cause an increase in the relative inhibitory transmission time constants (i.e. slowing down), compared to excitatory synaptic dynamics – both of these effects are observed in the parameters estimated across the whole brain slice here (noting that population-level time constants are likely a product of several convergent synaptic effects (Chaudhuri et al., 2014; Huang et al., 2001; Koch et al., 1996)). Left-right asymmetries in the intrinsic estimated connectivity in the optic tectum is most likely secondary to differences in light stimulation received by either eye during the imaging process and the light sheet excitation in the visible light range.

Further exploration of individual parameter effects at a single brain region supports the notion that seizure dynamics in this recording are largely caused by two main effects: a relative disturbance in excitation / inhibition balance with increased excitation and decreased inhibition, and a reciprocal disturbance in the dynamics of excitatory and inhibitory connectivity with slower inhibition and faster excitation. Because I have fitted fully generative neural mass models, I can also make predictions about the spectral output caused by particular parameter combinations beyond the measured ≤10Hz frequency range. This approach reveals that particularly the time points where both connectivity and time constant effects changes reach their respective extremes, the typical seizure spectral output containing high amplitudes in both low (i.e. delta) and high (i.e. gamma) frequency components emerges. The addition of PTZ causes an increase in broadband activity, with particularly high predicted power in the gamma band early after PTZ administration, and more pronounced increases in slow frequency power as the seizures evolve. This is consistent with previous studies that have separately recorded LFP traces during seizures in zebrafish (Baraban et al., 2013; Turrini et al., 2017).

Recurrent neuronal loops with a close balance of overall excitation and inhibition underlie spontaneous brain activity. The brain is believed to operate near a transitional state from which both subcritical, random dynamics and supercritical, ordered dynamics can emerge (i.e. self organised criticality (Rubinov et al., 2011)). Blocking of the largely GABA-A mediated local recurrent inhibition shifts this balance and allows ordered, seizure-like activity to occur (Shu et al., 2003). In my model the emergence of seizure dynamics

requires changes in both connection strengths and their temporal dynamics. Future research will address how different pathologies may converge on the mechanisms that underlie observable seizure dynamics.

5.4.4 Limitations

Like all Bayesian modelling approaches, DCM only provides estimates of the likelihood of individual models in direct comparison to a larger model space. As the model space evolves, and other plausible hypotheses are being tested, a new model may offer an overall better solution to the inverse problem. Furthermore, as our understanding about the underlying neurophysiology progresses, prior knowledge can be incorporated into the model inversion (quantitatively in terms of changes in the prior parameter expectations) and thereby nuance Bayesian model comparison.

It is also worth noting that the DCM results are 'true' in that they represent the mathematically simplest approximation of a given dataset under specific assumptions – a more complex model may be biologically implemented but not emerge as the winning model because the added complexity is not required to explain the particular data features at hand.

The approach presented here illustrates how light-sheet imaging in zebrafish larvae can offer an insight into the kind of mesoscale dynamics that are also observable (and of interest to the modelling communities) in electrophysiological recordings. The type of modelling and inversion scheme used here is flexible enough to ultimately accommodate data that contain some of the microscale information about the neuronal ensemble (e.g. by defining 'regions' through molecular markers present on individual neurons rather than gross anatomy), however this was beyond the scope of the current – proof of concept – study presented here. Furthermore, the imaging protocol here was optimised to capture widespread activity changes at high sampling frequencies (e.g. by only imaging a single plane), assuming that activity in this plane reflects the dynamics of the whole region, whilst excluding non-imaged regions (that are situated above or below the plane) from the analysis.

Whilst only a small number of fish were included in this analysis, the effects at the level of the recordings are large and consistent between fish. For future studies on more subtle effects and observations (e.g. the topological organisation of spontaneous seizures), a higher number of fish is likely to be required.

5.4.5 Conclusion

The analysis presented here illustrates the use of computational modelling to explain neuronal dynamics in the larval zebrafish brain during acutely induced seizures. This approach exploits the spatial independence of single plane *in-vivo* light-sheet recordings of brain regions and uses dynamic causal modelling to identify the mechanisms underlying seizure dynamics. The Bayesian model inversion scheme allows translating observations from whole-network novel light sheet imaging to the concepts and models used to explain electrophysiological abnormalities observed during seizures.

Seizures in this model are associated with an asymmetric decoupling of the network hub, and changes in excitation/inhibition balance that crucially also involve temporal dynamics of excitatory and inhibitory synaptic transmission. Mapping the expected spectral changes along both the connection strength and time constant domains of the model within the pathophysiological range estimated from acute seizures allows me to delineate the independent contribution of changes in either type of parameter to the overall dynamics. This is the first step to establishing network-wide mechanisms that underlie seizures and may be targeted with novel treatments for epilepsy.

6

NMDA-receptor antibodies alter cortical microcircuit dynamics §

6.1 Introduction

The recent incorporation of novel molecular diagnostics into clinical practice has transformed our ability to identify specific molecular disruptions of synaptic functions as the cause for a diverse range of neurological disorders in patients (Crisp et al., 2016). For example, antibodies to N-methyl-D-aspartate receptors (NMDAR-Ab) have been identified as an important and treatable cause of autoimmune encephalitis (Dalmau et al., 2007), with a particularly high incidence in children, who make up approximately 40% of patients. Patients with NMDAR-Ab encephalitis show a diverse range of associated symptoms; including behavioural changes, movement disorders and seizures (Florance et al., 2009; S. Wright et al., 2015a). Important aspects of the clinical presentation are electroencephalography (EEG) abnormalities, which have been reported in up to 90% of patients undergoing EG monitoring; between 20-60% of patients also have overt epileptiform discharges or electrographic seizures (Dalmau et al., 2008; Schmitt et al.,

§ The work reported here has also been described in the following forthcoming publication:

Rosch, R.E., Wright, S., Cooray, G., Papadopoulou, M., Goyal, S., Lim, M., Vincent, A., Upton, A.L., Baldeweg, T., Friston, K.J. 2018. NMDA-receptor antibodies alter cortical microcircuit dynamics. *Proc Natl Acad Sci, in press*. doi:10.1073/pnas.1804846115

As part of this work, I proposed the computational analysis, independently performed the computational modelling, analysed clinical reports and EEG data, and wrote the manuscript. I was not directly involved in the acquisition of the rodent recordings, which are reported here for completeness.

2012). While there are EEG features that are thought to be relatively specific for NMDAR-Ab encephalitis (e.g. extreme delta brush) (Schmitt et al., 2012), the more common EEG abnormalities are non-specific, with the more global abnormalities broadly associated with more severe disease (Gitiaux et al., 2013; Nosadini et al., 2015).

At the whole organism level, NMDAR-Ab cause an increased seizure susceptibility: Passive transfer of patient immunoglobulin (IgG) containing NMDAR-Ab into a mouse model causes increased susceptibility to chemically induced seizures (S. Wright et al., 2015b). NMDAR-Ab directly affect glutamate transmission through reversible loss of NMDARs, resulting in a reduction of miniature excitatory post-synaptic currents (mEPSCs) in brain slices (Hughes et al., 2010; Moscato et al., 2014). NMDAR hypofunction is also a hallmark of psychiatric conditions, such as schizophrenia and acute psychosis (Cohen et al., 2015; Nakazawa et al., 2017) – whose clinical features resemble the neuropsychiatric and behavioural symptoms also seen in the early phases of NMDAR-Ab encephalitis.

Linking NMDAR hypofunction at the cellular level and a predisposition to seizures at the systemic scale is challenging. In the simplified view of epileptic seizures as a consequence of excitation-inhibition imbalance (Pinto, 2005), one would expect NMDAR hypofunction to be associated with a reduction of excitation, thus a decrease in seizure susceptibility. Whilst NMDAR are ubiquitous across central synapses, there is differential expression of NMDAR in different neuronal populations (Baude et al., 1993; Landwehrmeyer et al., 1995). Therefore, when considering integrated neuronal ensembles, changes in NMDAR function at the level of a single synapse may have a multitude of different emergent effects depending on the combined influence on both excitatory and inhibitory components of the neuronal circuit. In relation to NMDAR, observations in a range of experimental models motivate several mechanistic hypotheses explaining the effects of NMDAR hypofunction: These include (1) altered excitatory dynamics with a reduction in late excitatory post-synaptic potential components (Hughes et al., 2010); (2) secondary neurotoxicity, reducing the number of functional excitatory connections (Farber et al., 2002); and (3) a reduction of cortical inhibitory interneuron activity (Homayoun and Moghaddam, 2007). Furthermore, paradoxical changes in excitatory and inhibitory transmission – resulting from maladaptive homeostatic changes – have been proposed as underlying NMDAR-Ab associated abnormalities at different temporal scales (Moscato et al., 2014).

Relating observations of pathological brain dynamics to these specific hypotheses is challenging. In a highly non-linear dynamic system, such as the brain, the link between synaptic abnormalities and whole brain responses is seldom intuitive or predictable. Neuronal systems are hierarchically structured and each observational scale constrained by larger scale processes, as well as interacting with emergent properties arising from smaller scales (Freeman, 2000b). Some of these multi-scale dynamics can be successfully captured in computational models of neuronal populations, which have been integrated into validated analytical frameworks, such as dynamic causal modelling (DCM) (Friston et al., 2003; Kiebel et al., 2009; Moran et al., 2011a).

DCM rests on mesoscale neural mass models that capture the average behaviours of neural populations at roughly the scale of a cortical column – the model used here is representative of generic features of layered cortical architectures referred to as the canonical microcircuit or CMC (Moran et al., 2013). The parameters of the CMC (which describes features such as synaptic connection strengths and population response dynamics) can be fitted to macroscale neurophysiological recordings such as EEG or LFP recordings and competing models can be ranked according to their Bayesian model evidence.

I have chosen this specific model here for two reasons: (1) The CMC directly builds on models that have a long history in linking neurobiology to the dynamics of EEG during epileptic seizures and other abnormal oscillatory activity in the cortex (Jansen and Rit, 1995; Moran et al., 2013; Wilson and Cowan, 1972). These neural mass models (originally comprising 2 or 3 neuronal populations) constitute neuronal oscillators (i.e. reciprocally coupled inhibitory and excitatory populations), as well as incorporating some key inter-laminar connectivity patterns observed across a range of different cortical areas (Gilbert and Wiesel, 1983; Jiang et al., 2015; Thomson, 2003). (2) The addition of a second pyramidal cell population in this particular model affords a greater diversity of neuronal dynamics. Crucially, this addition allows for a separation in time scales between superficial and deep neuronal oscillators, which recapitulates laminar-specific dynamics observed in empirical laminar recordings in experimental animals (Bastos et al., 2015). In addition to the microcircuit structure, the prior values for the parameters are based on empirical measurements accessible in the literature, where possible (Bastos et al., 2012).

The themes of cortical laminar organisation recapitulated in the CMC are conserved across many mammalian species (Harris and Shepherd, 2015). This underpins the use of these models in a range of different experimental systems, ranging from local field potential recordings in rodents to invasive recordings in non-human primates and EEG/MEG recordings in human subjects (Cooray et al., 2016; Papadopoulou et al., 2017; Pinotsis et al., 2014). In the study presented in this chapter, I exploit this by combining measurements from invasive recordings in a rodent model of NMDAR-Ab encephalitis and human patient EEG recordings at the level of CMC parameters.

I report the results of a DCM analysis of (a) changes in spontaneous (resting state) activity in a subacute mouse model of NMDAR-Ab encephalitis, and (b) abnormal EEG paroxysms observed in a series of paediatric patients with established NMDAR-Ab encephalitis. I first model the NMDAR-Ab effect in the mouse model; using DCM to identify a minimal set of synaptic parameters required to produce the NMDAR-Ab effects on ongoing neuronal oscillations. Based on patient EEG data I then estimate fluctuations in the parameters that explain the patient recordings. I am especially interested here in how changes in the different neuronal coupling parameters *in combination* yield intermittent abnormalities typically recorded in patients. For this, I leverage experimental control (afforded by the animal model) to characterise spontaneous paroxysmal abnormalities (observed in patient recordings): Operationally I reproduce the parameter changes that best explain human EEG paroxysms in the *in-silico* models of experimental effects in mice. This allows me to identify the specific conditions that are necessary for EEG paroxysms to emerge. Understanding the neuronal context in which EEG abnormalities can appear may in future be used to improve targeted therapeutic approaches.

6.2 Methods

The analysis presented here uses DCM to infer the neurobiological parameters that underlie electrophysiological changes in patients with NDMAR-Ab encephalitis and a corresponding mouse model. Once these changes have been identified, I use the fully parameterised *in-silico* models in simulation mode to integrate the findings and explore hypotheses about how NMDAR-Ab induced changes in the neurobiology cause the EEG abnormalities observed in patients. For this, the analysis was broadly divided into three stages – explained in detail below: (a) using DCM of LFP recordings in the mouse model

(exploiting the factorial experimental design), I estimate neuronal population coupling changes in the cortical microcolumn induced by NMDAR (Figure 6.1 A-D); (2) in a corresponding DCM analysis of spontaneous EEG paroxysms recorded in human patients, I estimate fluctuations in microcircuit coupling (Figure 6.2); and (3) I implement these patient EEG derived parameter fluctuations in the *in-silico* representations of microcircuits derived from control and NMDAR-Ab conditions in the mouse experiment. This allows us to investigate the dynamics of the microcircuits with and without NMDAR-Ab effects, testing whether the association between certain model parameters shifts and paroxysmal spectral abnormalities (as observed in the human patients) depend on specific dynamic contexts (i.e. conditions in the mouse experiments) (Figure 6.1 E-H).

6.2.1 Collection and classical analysis of mouse LFP

The mouse model and associated procedures have been previously described (S. Wright et al., 2015b). Briefly, plasma with NMDAR-Ab (Immunoglobulin G, IgG) was obtained with informed consent from three female NMDAR-Ab positive patients with neuropsychiatric features, movement disorder and reduced level of consciousness, samples were de-identified before research use. Control IgG was purified from serum from two healthy individuals. C57BL/6 female mice aged 8-10 weeks were housed and examined according to ARRIVE guidelines and all analyses were performed with the observer blinded to injected antibody group.

Wireless telemetry transmitters (subcutaneous transmitter A3028B-CC from Open Source Instruments Inc) were implanted in a subcutaneous pocket over the right flank. Two craniotomies were performed at 1mm lateral and 1mm caudal from bregma. Electrode screws were fixed into the drilled holes with dental cement. After a five-day monitored recovery period, eight microliters of purified IgG (patient, or control) was injected slowly into the left lateral ventricle through a single additional craniotomy made 1mm left lateral and 0.45mm caudal from bregma.

Mice were housed in a Faraday cage during wireless LFP data collection. To test seizure susceptibility, 40mg/kg of PTZ was given intra-peritoneally and the mice were observed for 45 minutes following injection. The 45-minute time period immediately preceding PTZ injection was used as control segment.

Raw LF data was analysed in Matlab. Sliding-window (30s windows, 15s steps) Fourier estimates of power over frequency were used to statistically compare the different

conditions. ANOVA over mean delta-band power (1-4Hz) was used to estimate the effects of the two main interventions (NMDAR-Ab, PTZ) and their interaction on LFP signal composition.

6.2.2 Modelling cortical activity with the canonical microcircuit model

For the purposes of this analysis, cortical activity is assumed to arise from a cortical microcolumn that consists of four coupled neuronal populations: Two main output populations (superficial and deep pyramidal cells), and local inhibitory and excitatory populations (inhibitory interneurons, and spiny stellate cells respectively). These populations are based both on established models of cortical function (Jansen and Rit, 1995; Lopes da Silva, 1991), and empirically observed connectivity patterns (Bastos et al., 2012; Schubert et al., 2003; Thomson, 2003). These populations are organised into two oscillator pairs: one superficial (consisting of superficial pyramidal cells and spiny stellate cells); and one deep (consisting of deep pyramidal cells, and inhibitory interneurons). This architecture recapitulates generic themes in cortical organisation, whilst allowing for a diverse range of dynamics enabled by the two coupled oscillator pairs (Moran et al., 2013). Intralaminar connectivity is largely represented within neuronal populations: Each population is parameterised by recurrent inhibitory self-connection parameters, population time constants, and a parameterised sigmoid function that models the dispersion of population responses (Marreiros et al., 2008). Interlaminar coupling is modelled explicitly through population-level connectivity between the different populations. Each oscillator pair has reciprocal excitatory and inhibitory connectivity. Note that indirect inhibition from superficial pyramidal cells to excitatory interneurons – mediates via assumed intralaminar inhibitory interneurons – is absorbed into a direct inhibitory connection in this model.

6.2.3 DCM analysis of mouse LFPs

Modelling of the mouse LFP recordings can be divided into the following steps (as summarised in Figure 6.1; dynamic causal modelling was performed using SPM12, an academic software package and analysis code as well as raw data are available online - https://github.com/roschkoenig/NMDAR-Ab_Encephalitis - these require Matlab 2014b or later and SPM12 to run). Code is also included in the appendix section A.6.

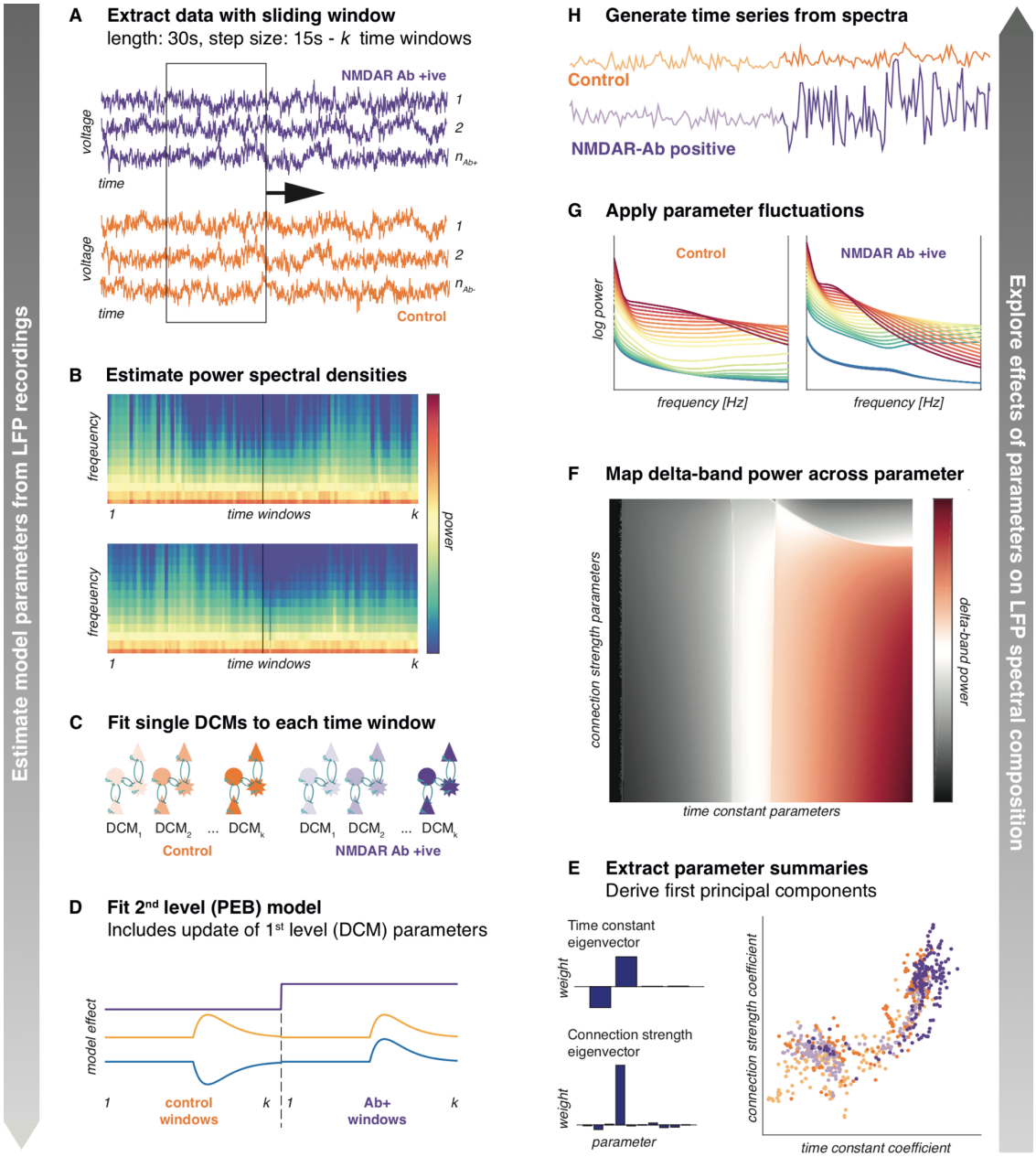

Figure 6.1 – Modelling approach to mouse LFP recordings. Modelling was designed to extract relevant parameters (left hand panels), and then explore the effects of those on delta power (right hand panels). (A) For both pre- and post PTZ injections, 45 minutes of LFP recordings were extracted for each mouse. A sliding window was used to extract a sequence of time windows for further analysis. (B) Power spectral densities were estimated for each time window, which are the basis for the DCM model fit. (C) Single-source DCMs comprising a single CMC model were fitted to each time window separately. (D) Using a parametric empirical Bayesian approach to fit a second level between-DCM general linear model I extracted parameter variations explained by specific experimental effects and updated first level DCM parameters.
(E) From the updated first level DCMs, I extracted all parameters and summarised them in two principal components over time constants and connection strengths, retaining the first component summaries of the fitted DCMs. (F) Starting from the baseline model specification, I applied the reduced (i.e. first principal component) summaries of the parameter changes to simulating cross spectral outputs of the neural populations, yielding a map of delta-power across the ensuing two-dimensional parameter space. (G) I then applied quantitative parameter changes observed in patient EEGs (summarised as their first

principal component) to the control, and NMDAR-Ab baseline model specifications *in-silico* to explore the effects of parametric fluctuations on spectral output. (H) To further illustrate the effects of parametric fluctuations, I applied an inverse Fourier transform to generate substitute time series – illustrating the nature of the changes in a time trace.

1) Inversion of separate single-source DCM for each time window (performed on group-average data)
2) Second level (PEB) model to explain parameter changes over time, based on experimental interventions
3) Forward modelling to explore effects of parameter changes on specific output measures (e.g. delta power)

Individual time windows were assumed to be relatively stationary within the 20s sliding time window in line with previous DCM analyses of EEG seizure activity (Cooray et al., 2016; Papadopoulou et al., 2017). Each time window was modelled as originating from a single cortical source comprising four coupled neuronal populations (i.e. a single cortical column modelled as single CMC). DCM employs a standard variational Laplace scheme to fit the parameters of a specified neural mass model to empirical data (Friston et al., 2003), whilst also providing a (free energy) measure of the Bayesian model evidence. The combination of posterior parameter estimates and free energy subsequently allows for computationally efficient modelling of group effects across individual DCMs, further exploited with the PEB analysis (Friston et al., 2016).

A second level model (PEB) was used to estimate parameter changes associated with the experimental modulations. Specifically, each time window was associated with a numerical value representing the absence or presence of NMDAR-Ab (0 or 1), the estimated PTZ concentration (range 0 to 1, modelled as first order kinetics after intraperitoneal injection), and an interaction term (range -1 to 1). PEB employs Bayesian model reduction based on the specified model parameters, effectively modelling between-window changes in parameters as a mixture of random effects and systematic modulation of each parameter by the main effects provided in the PEB models specification. Thus, inversion at the second (between-window) level provides posterior parameter estimates for first level model parameters (i.e. neuronal physiology) that are associated with second level parameters (i.e. experimental modulation) across the whole series of individual DCMs.

Comparison between models is based on the free energy approximation of the Bayesian model evidence. I use a Bayesian model reduction approach that is computationally efficient and provides model evidence estimates for a range of different models that differ in terms of the parameters that are free to vary to explain between-window variation in the PEB analysis (Friston et al., 2018; Friston et al., 2016). This approach provides a ranking of how well different combinations of free parameters explain a given dataset (here consisting of between-window changes in power spectral densities) and allows me to identify the most parsimonious model for the observed EEG, or LFP effects. Note that models with the highest evidence are those that generalise; in virtue of the fact that model evidence is the difference between accuracy and complexity.

The DCMs are fully specified models of spontaneous neuronal activity and can therefore be used to explore individual parametric effects on overall spectral output. Here, I utilise the parameter estimates derived as the group mean in the PEB analysis as baseline. I then extract the first principal component of the time constant, and connection strength variations across all individual time window DCMs (Figure 6.1 E). This provides a summary of covarying changes in parameters that explain most of the variance across

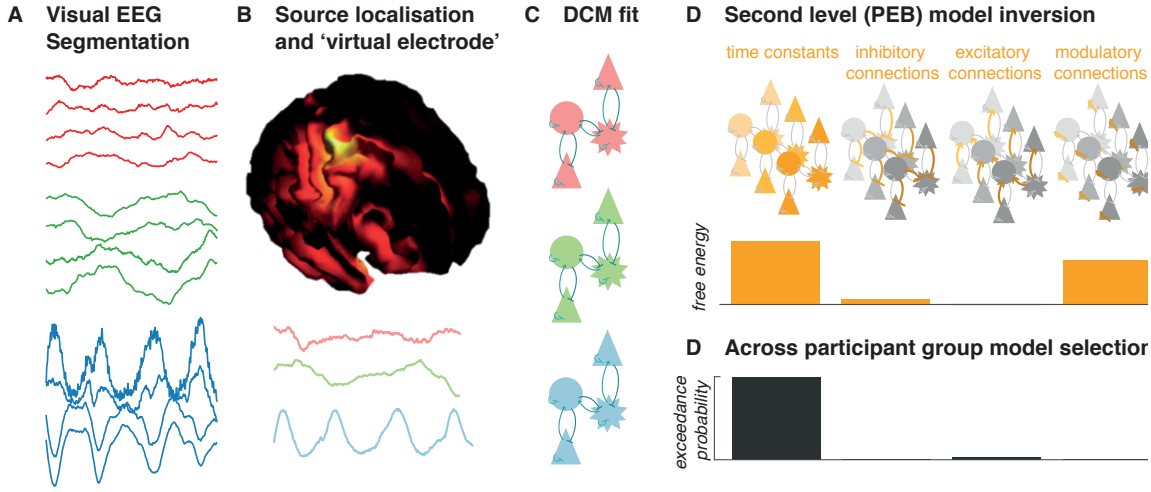

Figure 6.2 – DCM analysis approach for patient EEG recordings. (A) Visual analysis was performed to identify segments of artefact free background EEG, as well as visually apparent paroxysms of abnormal activity (which were further separated into isolated and rhythmic abnormal activity). (B) This activity was source localised using an IID approach. Subsequent modelling was performed using a virtual electrode estimate of LFP activity at the identified source (bottom of this panel). (C) Single source DCMs comprising a single CMC were fitted separately to power spectral density averages of background, and paroxysmal activities (D) PEB was employed to reduce within subject differences between individual DCMs to specific subsets of parameters. The model space was designed to distinguish between sets of models where time constant, inhibitory connections, excitatory connections, or modulatory connections explained variations among conditions. (D) A random effects Bayesian model comparison between these alternative PEB models helped identify which parameters best explain the fluctuations across the whole group of subjects.

samples. I then systematically vary the contribution of each of these two components in 300 discrete steps each around the baseline estimates. This yields 300 * 300 = 90,000 parameterisations for a single source DCM, and for each of these the spectral output can be estimated. I can then use these estimates to visualise scalar output measures (e.g. log mean delta band power) across a section of this two-dimensional parameter space (Figure 6.1 F). This combines the benefits of fitting generative models to empirical data, and exploring the effects of specific parameters on model output through forward modelling (Lytton, 2008; Wendling et al., 2002).

In the last step, I implement the microcircuit parameter fluctuations estimated from paroxysmal EEGs in patients in different conditions of the *in-silico* mouse model. Specifically, I

1) Estimate parameter changes that underlie paroxysmal EEG responses in patients (discussed in further detail below)
2) Take the first principal component of the variations of time constants across all participants and EEG states to capture most of the variance of the time constant changes
3) Implement corresponding parameter changes across the range estimated from human EEG in mouse-derived *in-silico* microcircuit models

This allows me to simulate the kind of spectral changes that would be induced if the mouse-derived *in-silico* microcircuits experienced the same (spontaneous) fluctuations in model parameters that I estimated from observed human EEG paroxysms. I then use an inverse Fourier analysis to illustrate the sort of paroxysmal responses that would be expected based on the spectral prediction under specific parameter combinations (Figure 6.1 H).

6.2.4 Patient selection and EEG recording

Patients were selected from routine clinical service at a tertiary paediatric specialist hospital that is a regional referral centre for patients with presumed autoimmune encephalitis. Patients were selected based on (1) symptoms consistent with autoimmune encephalitis, (2) positive laboratory testing for NMDAR-Ab at some point during their clinical course, (3) availability of routine clinical EEG recording during the acute phase of their illness, (4) presence of visually apparent EEG abnormalities. Anonymised clinical

information was provided by the patients' care team with written, informed consent provided by the patients' legal guardians. All patients met the Graus criteria for a clinical diagnosis of NMDAR-Ab encephalitis (Graus et al., 2016). Use of anonymised data was approved by the UK Health Regulatory Authority (Appendix A.1-A.3).

All EEGs used in this analysis were standard clinical recordings (21 electrodes, international 10-20 electrode layout, 30-minute recording time, 256 Hz sampling frequency, 1-70 Hz digital Butterworth bandpass filter). EEGs were visually analysed by two clinicians with expertise in EEG interpretation (myself, and clinical collaborator Gerald Cooray), identifying paroxysmal abnormalities, as well as segments of artefact free awake background EEG that were used for further analysis.

6.2.5 DCM analysis of patient EEG paroxysms

EEG analysis was designed to identify mechanisms underlying the frequently observed paroxysmal abnormalities in patients with NMDAR-Ab encephalitis. The purpose of this modelling approach is to identify a small set of parameters that can explain the transition between background activity and EEG paroxysms for each individual patient. The analysis can broadly be summarised as follows (also shown in Figure 6.2).

1) Visual identification of paroxysmal and background EEG activity source localisation and 'virtual electrode' source wave form extraction
2) Fitting of single source DCM to each 'virtual electrode' summary of paroxysmal and background data
3) Inversion of hierarchical (PEB) model explaining all within-subject parameter changes that lead to different EEG patterns and Bayesian model comparison between sets of reduced models at the group level (random effects analysis)

Patients were selected on the basis of the availability of clinical EEG with reported dynamic abnormalities (ranging from evidence of mild encephalopathy to overt epileptiform activity). EEGs were reviewed by two clinicians with EEG experience (RER, GC) and segments containing normal awake background, as well as paroxysmal abnormalities (isolated slow waves, intermittent rhythmic slow activity, and overt epileptiform activity) identified.

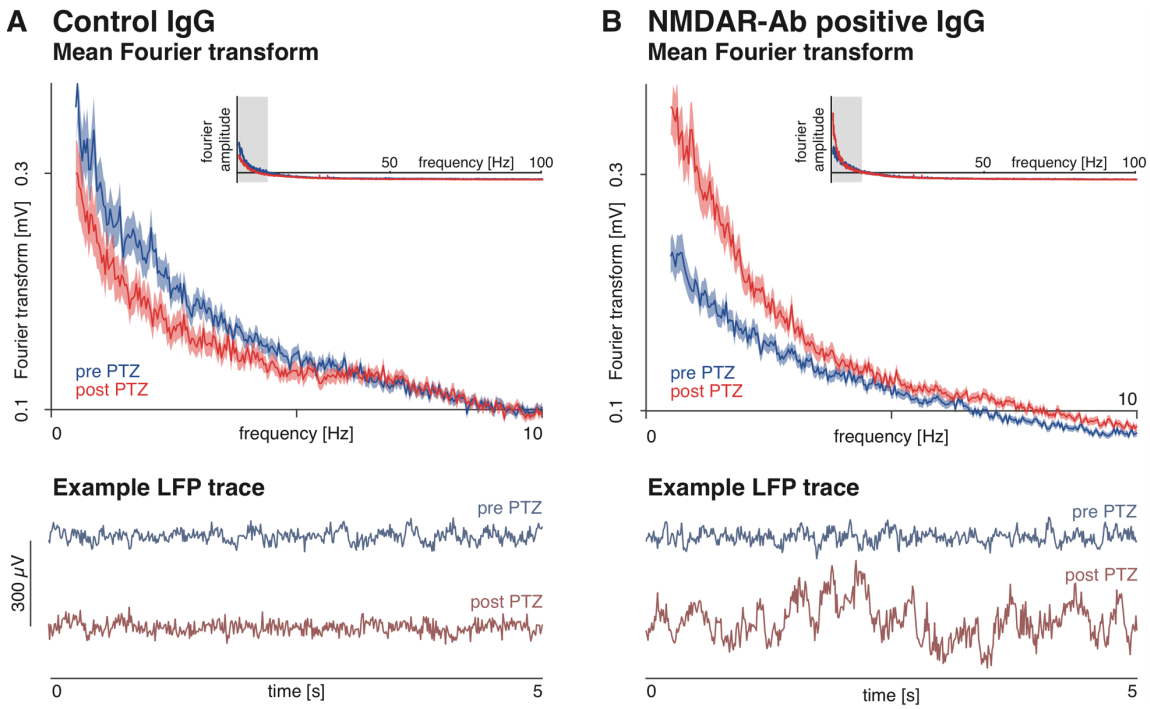

Figure 6.3 – NMDAR-Ab alter the spectral composition of resting state activity following PTZ. Average Fourier spectra of LFP recordings of endogenous activity in mice are shown (A) In control animals, PTZ injections cause a small decrease in low frequency power. (B) In NMDAR-Ab positive IgG treated animals, PTZ causes a profound increase in low frequency power, which is also visible as high power slow waves in segments; largely without overt epileptiform activity (examples shown). Average Fourier spectra across animals are shown for 45-minute recordings pre- and post-PTZ injections, shading indicates the 95% confidence interval. Insets show Fourier spectra for a broadband frequency range. Example 5s LFP segments are also shown for individual animals pre- and post-PTZ injections.

Paroxysmal activity was averaged across visually identified 2s windows and source localised using an IID (independent and identically distributed) approach in SPM12 (Litvak et al., 2011). At the cortical location with maximal activity, a single virtual electrode trace was extracted for each of the paroxysmal and background activity windows and used for further DCM analysis (Cooray et al., 2016).

This 'virtual LFP' activity was modelled using a single CMC source. An average of all paroxysm time windows, and all background time windows was inverted separately, producing 2-3 fully specified DCMs per subject. These were subsequently combined into a single hierarchical (PEB) model for each patient, in which only a subset of specific parameters was allowed to vary. A model space was created at the level of these second level models where either time constants, inhibitory between population connections, excitatory between population connections, or inhibitory self-modulatory connections were allowed to vary to explain the difference between paroxysms, and background activity.

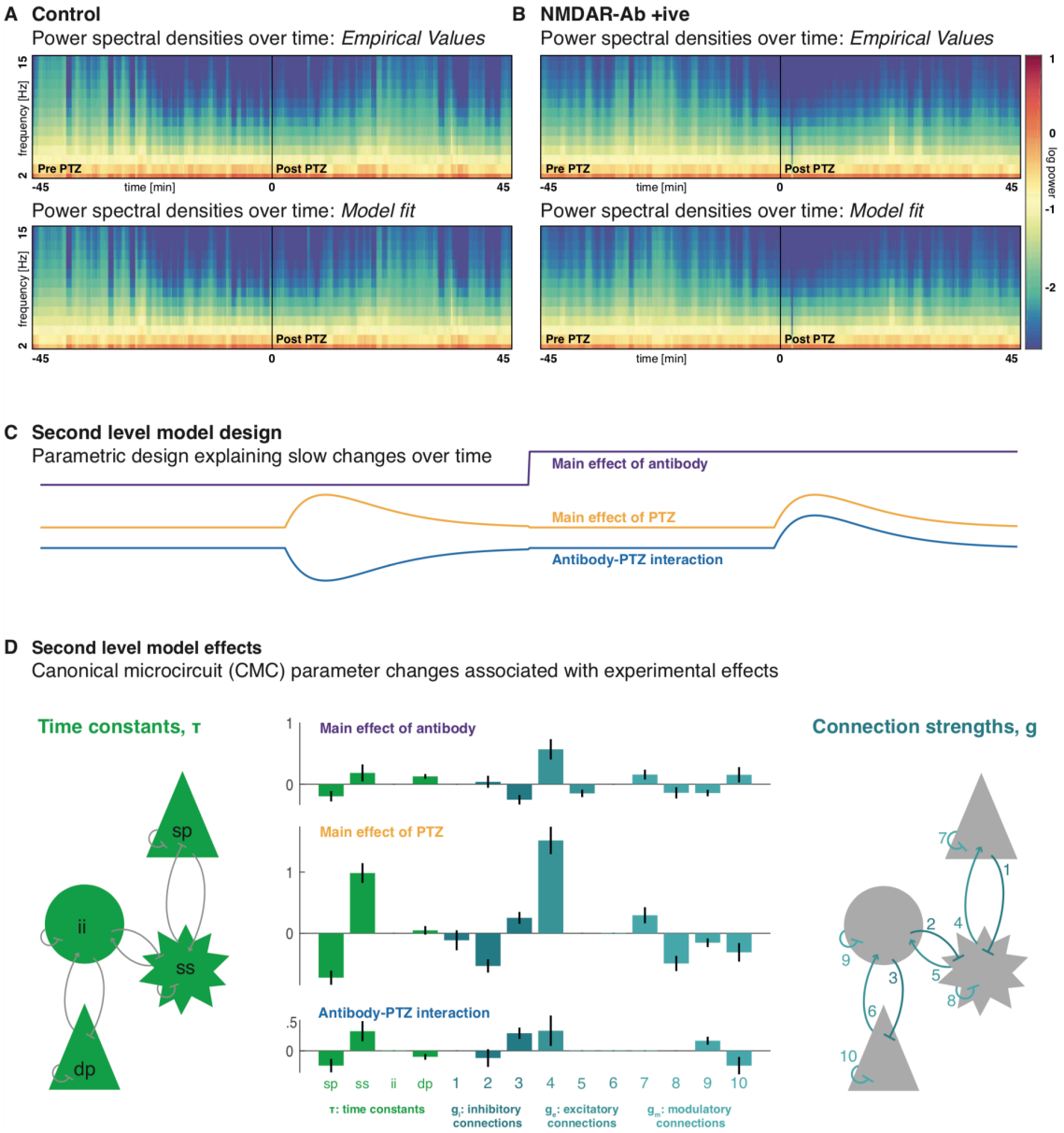

Figure 6.4 – Synergistic changes in synaptic coupling explain the effects of PTZ and NMDAR-Ab. (A,B) DCMs were fitted to sliding window power spectral density summaries of LFP recordings separately for control, and NMDAR-Ab positive animals. Top panels show the observed power spectra over time, with model fits shown in the lower panels. (C) A second level general linear model was used to estimate parameter changes associated with NMDAR-Ab exposure, PTZ, and their interaction. The regressors for the three main effects are shown. (D) These experimental effects are associated with parameter changes across all populations of the canonical microcircuit (CMC) neural mass model. The left panel illustrates the population-specific synaptic time constants that parameterise the temporal dynamics of post-synaptic responses within that population. The right panel indicates the connections between populations, which are excitatory / inhibitory connections between populations, or self-inhibitory connections. The centre panel shows how each of the parameters is modulated by each of the experimental effects. The strongest effects are caused by PTZ, with the biggest associated changes in *sp* and *ss* time constants and excitatory connection strength 4. These changes are further potentiated by NMDAR-Ab exposure. Error bars indicate Bayesian 95% confidence intervals.

sp: superficial pyramidal cells, *ss*: spiny stellate cells, *ii*: inhibitory interneurons, *dp*: deep pyramidal cells.

Random effects Bayesian model comparison across these second level models uses the approximation to model evidence from the variational Laplace model inversion (i.e. the free energy) to compare the evidence for any given model parameterisation, given the empirical data (Kiebel et al., 2009).

6.3 Results

6.3.1 NMDAR-Ab alter the dynamic response to acute chemoconvulsants in mice

Cortical dysfunction associated with NMDAR-Ab was tested in C57BL/6 mice using a two-by-two design. This design tested for the effects of NMDAR-Ab (delivered via intracerebroventricular injection), the acute chemoconvulsant pentylenetetrazol (PTZ, delivered via a later intraperitoneal injection), and their interaction. LFPs were recorded wirelessly in freely behaving animals and 45 minutes of recordings pre- and post-PTZ injection of 8 NMDAR-Ab positive and 5 control animals were included for the analysis reported here.

Antibodies alone caused a moderate suppression of the LFP signal across low frequency bands (delta and theta range) in the NDMAR-Ab positive mice. However, additional exposure to PTZ revealed a marked difference between NMDAR-Ab positive and control mice, with a large increase of low frequency (delta-band, 1-4Hz) power in the antibody positive treated mice only (Figure 6.3). Analysis of variance (ANOVA) revealed a significant main effect of NMDAR-Ab on log-delta-band power [$F(1,4601) = 9.67$; $p = 0.002$]; and a significant interaction between NMDAR-Ab and PTZ exposure [$F(1,4061) = 85.05$; $p < 0.001$]. A PTZ-induced increase in paroxysmal fast activity consistent with epileptic seizures was observed in the NMDAR-Ab positive IgG treated mice compared to

Table 6-1 – Free parameters fitted by the DCM

τ_1 (superficial pyramidal cell time constant)	g_1 (*sp* to *ss* inhibition)
τ_2 (spiny stellate time constant)	g_2 (*ii* to *ss* inhibition)
τ_3 (inhibitory interneuron time constant)	g_3 (*ii* to *ip* inhibition)
τ_4 (deep pyramidal cell time constant)	g_4 (*ss* to *sp* excitation)
	g_5 (*ss* to *ii* excitation)
	g_6 (*dp* to *ii* excitation)
	g_7 (*sp* self-modulation)
	g_8 (*ss* self-modulation)
	g_9 (*ii* self-modulation)
	g_{10} (*dp* self-modulation)

control animals, which has previously been reported elsewhere (S. Wright et al., 2015b), but this did not produce a spectral difference in the frequency bands analysed here. An example of induced, non-epileptiform slow activity is seen in the bottom panel of Figure 6.3 B. These slow wave cortical dynamic abnormalities were further analysed in the dynamic causal modelling approach reported below.

6.3.2 NMDAR-Ab potentiate PTZ-induced effects in cortical microcircuitry in mice

To explain the observed differences in spontaneous activity, a hierarchical dynamic causal model was used to infer parameter changes associated with the experimental variables over time (i.e. NMDAR-Ab exposure, PTZ infusion, and an Antibody-PTZ interaction). In brief, a sliding window (length = 30s, step size = 15s) was used to estimate the mean power spectra over successive time points. Each time window was then modelled as the steady tate output of a canonical microcircuit (CMC) model (Moran et al., 2013) with – for the duration of a single time window – fixed synaptic parameters. By repeating this analysis over windows, I identified fluctuations in synaptic parameters that corresponded to the experimental interventions. Across windows, the evolution of spectral patterns was captured well for all experimental conditions (Figure 6.4 A,B). To infer experimental effects on DCM parameters, the sequence of parameter estimates was then modelled using a parametric empirical Bayesian (PEB) approach (Friston et al., 2016b). Here, slow fluctuations of cortical coupling were modelled as between-window changes in the synaptic parameters estimated within-window (see (Papadopoulou et al., 2017) for a worked example). I included three main experimental effects of interest: (a) NMDAR-Ab, (b) PTZ, and (c) an NMDAR-Ab x PTZ interaction term (Figure 6.4 C).

The neuronal parameters that affect the spectral composition of spontaneous neuronal activity correspond roughly to the mechanistic hypotheses outlined above: (1) time constants of the neuronal populations τ describe the dynamics of neuronal population responses; (2) excitatory coupling parameters g_e describe the strength of excitatory between-population connections; (3) inhibitory coupling parameters g_i represent the strength of inhibitory between-population connections, whilst modulatory coupling parameters gm represent the strength of inhibitory self-connections (Moran et al., 2013) (Table 6-1).

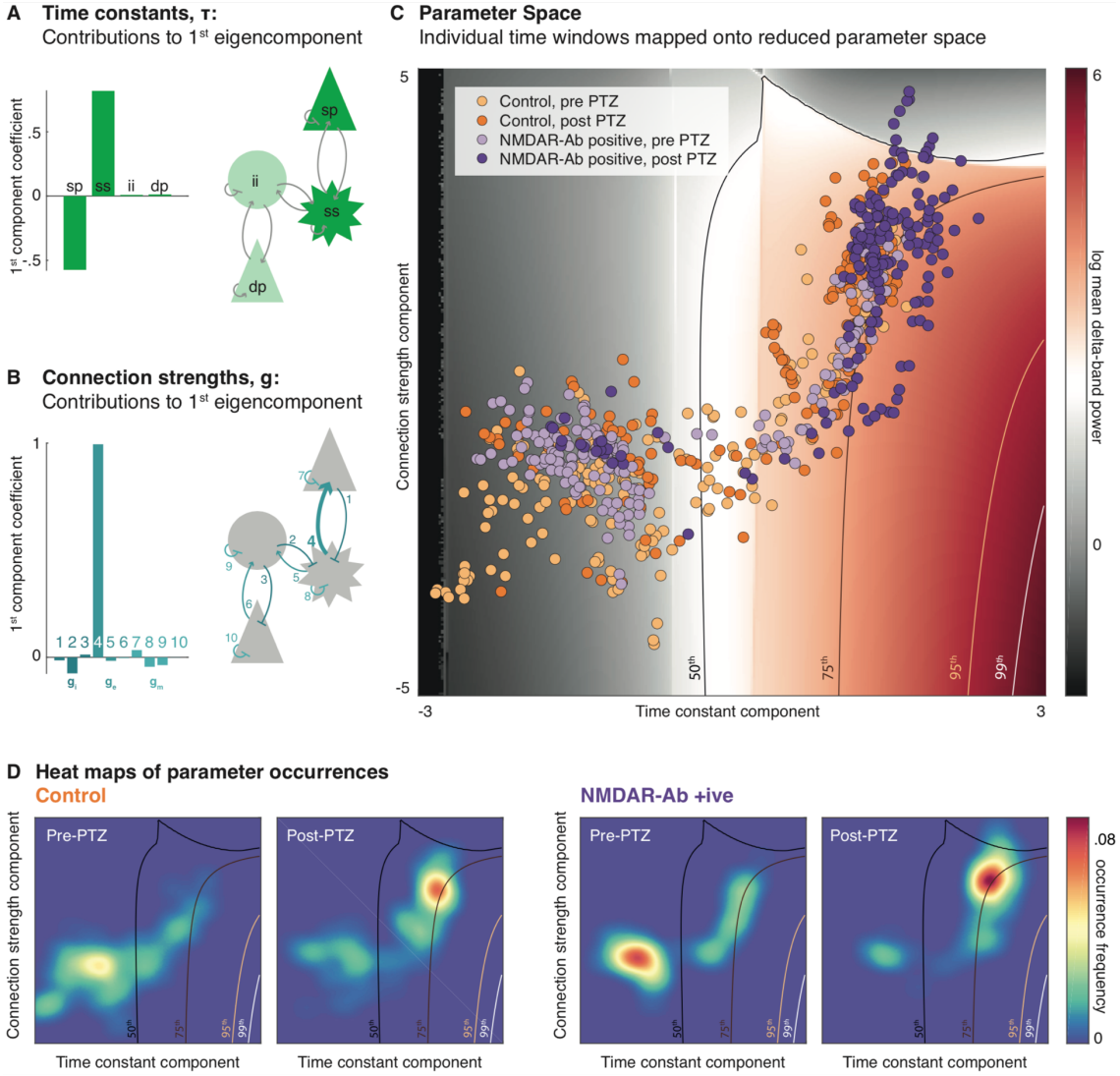

Figure 6.5 – NMDAR-Ab push the neuronal ensemble into high delta-band power regions of reduced parameter space. Parameter variations between time windows are projected onto the first principal component of (A) time constant changes consisting predominantly of superficial pyramidal cell, and spiny stellate cell changes, and (B) of connectivity strength changes consisting predominantly of spiny stellate to superficial pyramidal cell coupling changes. (C) Across this parameter space, simulations can predict spectral densities, of which log-mean delta power is shown here as background colouring (with selected centile isoclines also plotted). Individual time windows across the four conditions are then projected into the same reduced parameter space, showing an accumulation of NMDAR-Ab positive, post-PTZ time window estimates in high delta-ranges. (D) The distribution of time windows in parameter space is further illustrated with smoothed heat maps of parameter combination occurrence frequencies over the same section of parameter space for control animals (left) and NMDAR-Ab positive animals (right). Estimates in NMDAR-Ab positive animals cross the 75th centile more frequently than in controls.

Spectral changes associated with NMDAR-Ab, PTZ exposure and the interaction were each explained by several corresponding parameter changes. The biggest effects were associated with PTZ exposure, with a decrease in the superficial pyramidal cell population time constant (i.e. a faster return to baseline after perturbation), an increase in the spiny

stellate population time constant (i.e. a slower return to baseline after perturbation), and an increase in the excitatory connectivity from spiny stellate to superficial pyramidal cells. Notably those changes were further potentiated by NMDAR-Ab and the NMDAR-Ab x PTZ interaction (Figure 6.4 D).

6.3.3 Shifts in synaptic dynamics underlie emergence of low frequency power in mice

I further investigated the effect of changes in synaptic parameters on the main spectral data feature of interest (i.e. delta-band power). For this, I first performed a principal component analysis over the slow (between time-window) parameter fluctuations separately for time constants and connection strengths, retaining the first principal component of each (Figure 6.5 A,B). This analysis showed that most of the variance over time can be explained by fluctuations in a small subset of parameters; specifically, the time constants of superficial pyramidal and spiny stellate cells, and the excitatory coupling between them (as is also apparent in the analysis or second level model parameters shown in Figure 6.4).

I use these two components to project synaptic parameter estimates at each time window onto the two dimensions explaining most of the variance (i.e. one time constant component, and one connection strength component). To characterise different locations in this parameter space – in terms of the neuronal dynamics generated by the parameters – I used the mean delta band power of the predicted power spectral density. This functional characterisation of parameter space is shown (in log-scale) with a colour code, and as isoclines indicating mean delta-band power centiles across the parameter space considered (Figure 6.5 C). Whilst there is variation in delta-band power associated with both the time constant (x-axis) and the connection strength (y-axis) parameters, the time constants have the greatest effect on delta power: The difference between controls and NMDAR-Ab positive animals in the delta band power post-PTZ is largely conferred by shifting the time constant component, causing it to cross the 75th delta-band power centile much more frequently than in controls (Figure 6.5 D). This differential effect of PTZ can be seen by comparing the orange and purple scatter plot marks in Figure 6.5 C.

6.3.4 EEG paroxysms in patients are caused by fluctuations in synaptic dynamics

To identify which synaptic parameters cause paroxysmal EEG abnormalities commonly observed in NMDAR-Ab encephalitis, I used the above CMC model to perform a DCM analysis of 8 paediatric cases of NMDAR-Ab encephalitis, for whom EEG recordings were available and contained visually apparent EEG paroxysms. Briefly, routine visual EEG analysis was performed to identify paroxysmal abnormalities by two EEG-trained clinicians (RER, GC, see Table 6-2 for clinical details). For each patient, 2s time windows containing spontaneous activity, short isolated paroxysms, or rhythmic/ongoing epileptiform activity were extracted and used for further analysis (Figure 6.6 A).

Cortical source estimation for the paroxysmal EEG activity was performed and 'virtual electrode' responses extracted from the most active sources (Boly et al., 2012). For each patient, DCMs were independently fitted to power spectral density averages of each available condition (e.g. background, short paroxysms, ongoing rhythmic activity (Figure 6.6 B). Individually fitted DCMs (with near perfect model fits, Figure 6.6 C) were subsequently combined in (within-patient) between-condition hierarchical (PEB) models that explained the condition specific differences with changes in synaptic time constants (τ), between-population inhibitory connections (g_i), between-population excitatory connections (g_e), or within population modulatory connections (g_m). Across participants,

Table 6-2 – EEG features of NMDAR-Ab Encephalitis patients. Patients were selected from routine clinical service based on paroxysms identified on clinical EEG recordings

ID	Sex	Age (years)	EEG background	EEG paroxysms
N001	M	2	Normal	Isolated slow waves
N002	F	15	Normal	Intermittent rhythmic slow, regional left frontal
N003	F	9	Diffusely continuous slow	Intermittent rhythmic slow, generalised, maximum bifrontal
N004	F	1	Normal	Runs of spike and wave complexes, generalised; Isolated sharp waves
N005	F	3	Diffusely continuous slow	Intermittent slow, generalised, maximum bifrontal
N007	F	10	Diffusely continuous slow	Intermittent slow, generalised
N008	F	14	Diffusely continuous slow	Near continuous spike and wave complexes in sleep, generalised, max R frontal (ESES)
N009	F	11	Diffuse continuous slow	Intermittent slow, generalised, maximum bifrontal

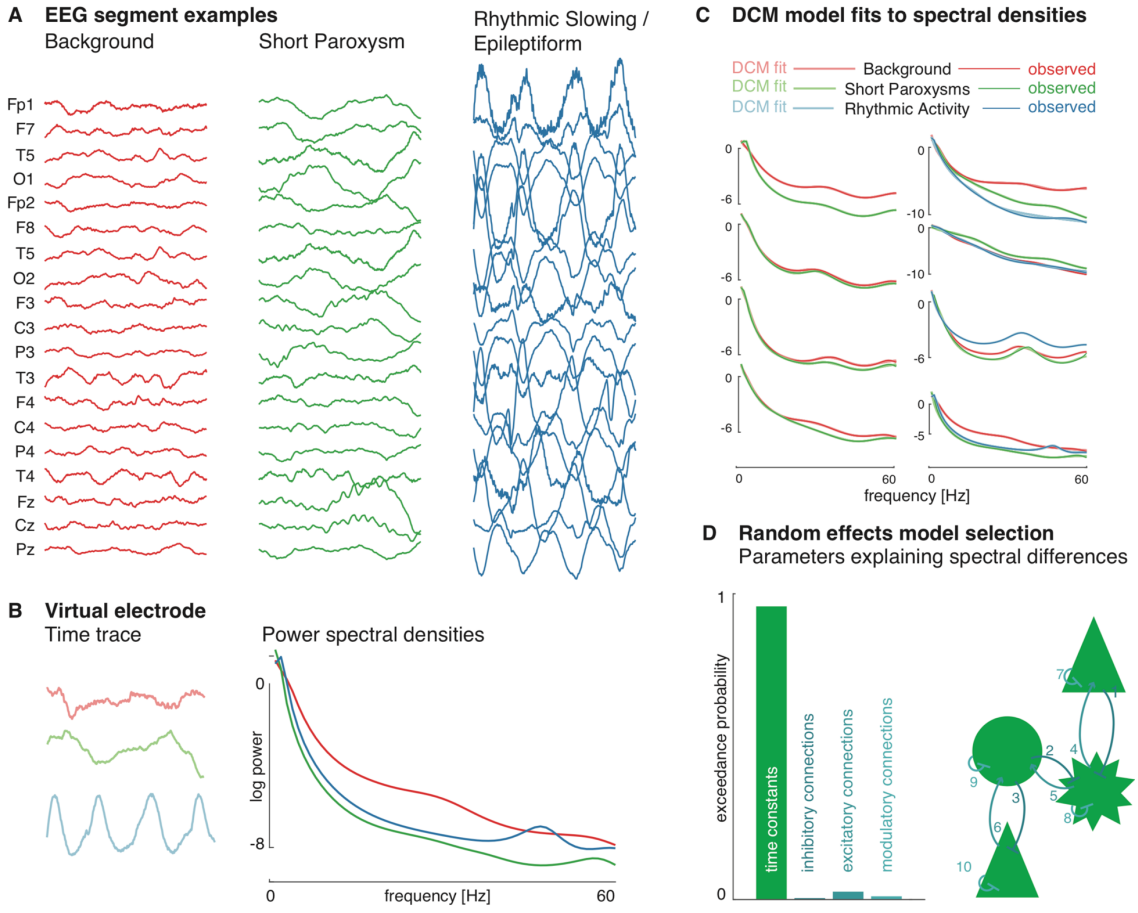

Figure 6.6 – EEG paroxysms in NMDAR-Ab encephalitis patients are best explained as time constant fluctuations. (A) For each individual patient, 2s time windows containing spontaneous activity, short EEG paroxysms and where available longer rhythmic EEG activity were extracted. (B) These were source localised and 'virtual electrode' time traces extracted at the estimated cortical source. Normalised power spectral density averages across all time windows were then fitted using separate DCMs for each condition. (C) The normalised spectral output of fitted DCMs show near perfect overlap with the observed spectral densities, illustrating that the fits provide good explanations for the observed (spectral) data features. (D) I then used Bayesian model reduction to test which subset of parameters best explains the differences between the different EEG states across the whole group: For each individual, between-condition effects were estimated in a number of reduced (parametric empirical Bayesian) models that different only in which parameters were free to explain the between-window spectral variations. Of these parametric empirical Bayesian summaries of individual participants, models explaining the spectral changes with fluctuations in time constants have an exceedance probability of > 95%.

models explaining spectral differences as arising from differences in time constants offer the best explanation of the virtual electrode data (with an exceedance probability of >95%, Figure 6.6 D).

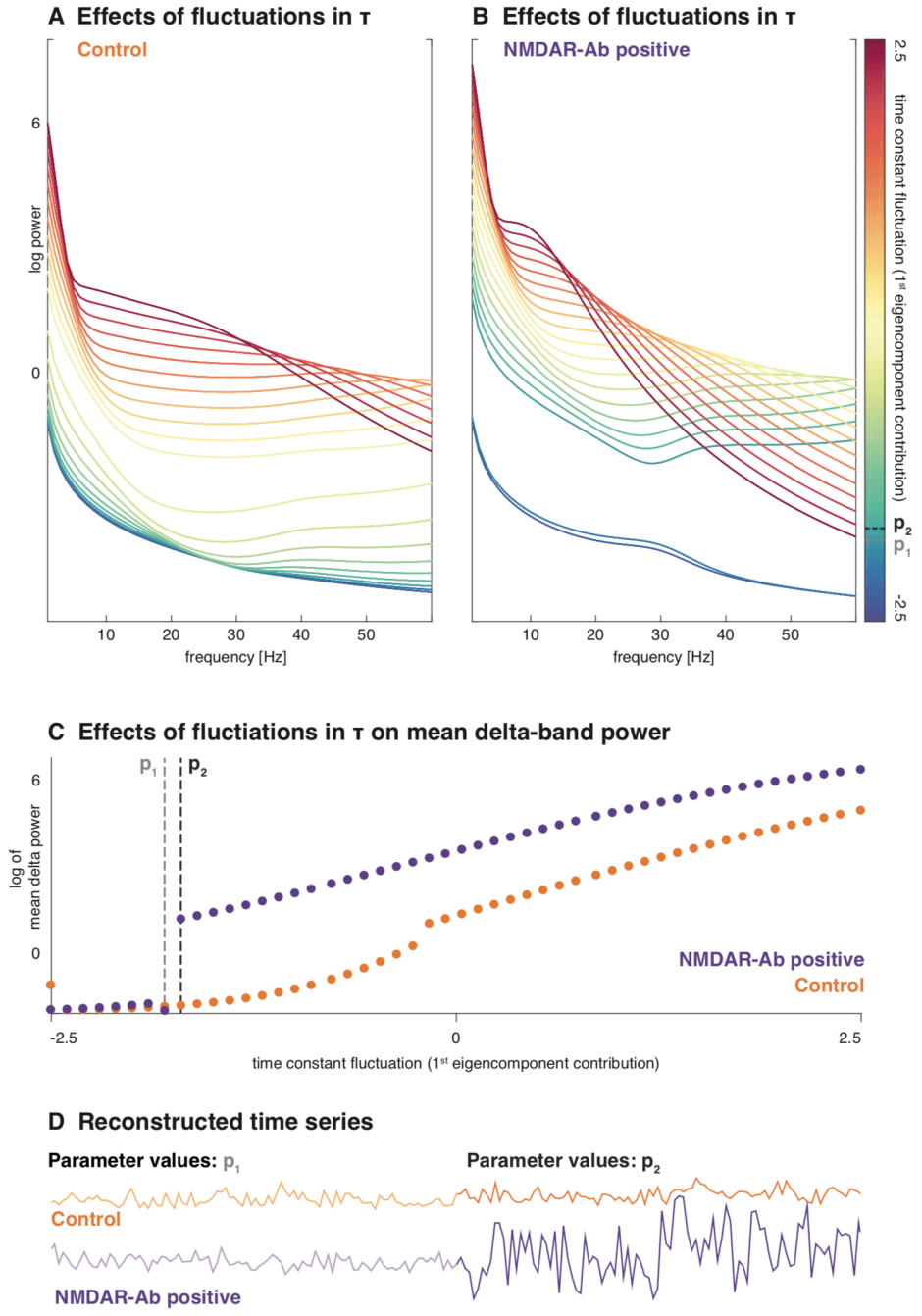

Figure 6.7 – NMDAR-Ab sensitise the microcircuit to intrinsic fluctuations in time constants. Here, I apply a summary component of the time constant fluctuations estimated from human patients to a cortical microcircuit model derived from the control mice (left), and the NMDAR-Ab positive mice (right). (A-B) The same fluctuations cause spectral outputs containing much higher relative delta power in the model estimated from NMDAR-Ab positive mice. (C) This figure shows log of mean delta power for a range of smoothly increasing time constant fluctuations. In the low parameter range (-2.5 to -1.5 of the time constant principal component contribution) there is a large jump in delta power, suggesting that there are two distinct dynamic states separated by small differences in parameter values. (D) Example reconstructions of time series for parameter values at two very close parameter values (p_1 and p_2) are shown for control and NMDAR-Ab positive models. The sudden increase in delta power is visible as paroxysmal change in the time series in the NMDAR-Ab positive context, whilst the control time series appears continuous. This sudden change in dynamics with a small change in parameter space is known as a phase transition.

6.3.5 NMDAR-Ab alter the response to intrinsic fluctuations in synaptic dynamics

The DCM of human data provides an estimate of the brain-state-specific changes in synaptic parameters: From the Bayesian model comparison of a set of reduced models, it emerged that the differences in EEG states in human patients are best explained through variations in neuronal population time constants. I extracted DCM parameter estimates of these time-constant changes for each patient, yielding a set of time constant parameters that explain the transition from background to paroxysmal EEG states for each participant individually. From this matrix of time constants (4 time constants in 8 participants with 2-3 EEG states), I extracted the first principal component, and applied them to the control, and the NMDAR-Ab positive mouse-derived CMC models. Conceptually I am thus enforcing the same degree of time constant fluctuations estimated from the patient models to the in-silico microcircuits derived from the mouse empirical experiments.

The differences between the parameter estimated from the control and NMDAR-Ab positive model result in qualitatively different spectral outputs; even when applying the same time constant changes. Overall, the NMDAR-Ab positive context results in higher delta-band power and less high frequency power (Figure 6.7 A-B). Crucially, delta power was higher in the NMDAR-Ab positive model across a wide range of time constant fluctuations (Figure 6.7 C). Furthermore, small changes in the synaptic parameters identified with the patient data cause large changes in delta power in – and only in – the NMDAR-Ab positive model. This is manifest as low frequency paroxysmal activity when the synaptic parameters change slightly in the NMDAR-Ab positive model, but not the control (Figure 6.7 D). Technically, this abrupt change in dynamics with a small change in parameters is known as a *phase transition*; suggesting that antibody-positive effects on synaptic coupling move the network towards a critical regime in which small fluctuations in synaptic time constants produce qualitatively different dynamics (i.e. paroxysmal EEG abnormalities).

6.4 Discussion

This study reveals common synaptic mechanisms underlying a range of electrophysiological disturbances associated with NMDAR-Ab in a mouse model, and in

paediatric patients: NMDAR-Ab cause a shift in cortical synaptic parameters that is associated with an increase in low frequency oscillations and which predisposes to the slow wave paroxysms seen in clinical EEG recordings.

6.4.1 NMDAR-Ab are associated with high-amplitude low-frequency discharges

NMDAR-Ab cause changes in the spectral composition of resting state LFP of the mouse strain tested. These differences are further revealed on additional exposure to PTZ, with a large PTZ-induced increase in mean delta power in the presence of NMDAR-Ab. This increase is largely due to intermittent rhythmic slowing without concurrent epileptic spikes. Previous analysis of seizure events shows that NMDAR-Ab also lower the seizure threshold (S. Wright et al., 2015b), but seizure events fall largely outside the frequency spectrum analysed here. These observations are in keeping with clinically reported EEG features: i.e. background slowing with or without additional slow wave paroxysms.

In mouse models of NMDAR-hypofunction, normal NMDAR function in parvalbumin (inhibitory) interneurons is required for gamma rhythm induction (Carlén et al., 2012). Furthermore, persistent NMDAR-hypofunction confers an increase of resting gamma power, with a concurrent reduction in stimulus-induced gamma oscillations (Gandal et al., 2012). In the mouse model presented here, I did not see such a change in gamma frequency power, which may reflect the modelled disease stage: Patients with NMDAR-Ab encephalitis progress through distinct stages of their disorders – initially presenting with neuropsychiatric symptoms before developing a more severe encephalopathic syndrome associated with slowing of the EEG (Irani et al., 2010). The findings of this study most closely relate to this second stage, and thus may relate to a pathophysiology distinct from 'neuropsychiatric' NMDAR hypofunction: Early on during the course of the disease, antibody effects may be limited to the inhibitory interneuronal system (Nakazawa et al., 2017). However, during the encephalopathic stages (including the emergence of paroxysmal EEG abnormalities and epileptic seizures), there may be more wide-ranging effects across cell-types that is partly recapitulated in the mouse model.

An increase in the power of slow frequency components in an EEG or LFP recording is thought to be associated with increased synchronisation of local cortical firing, itself regulated by interacting cortical and subcortical systems (e.g. thalamocortical loops

(Steriade et al., 1993), brain stem monoamine arousal systems (Krishnan et al., 2016), and intrinsic cortical effects such as astrocytic regulation of synaptic function (Fellin et al., 2012)). Firing synchrony can occur physiologically (e.g. during sleep), can be associated with non-specific cortical dysfunction (e.g. in the context of an encephalopathy), or be a component of epileptic discharges (apparent in slow-wave components in spike-wave discharges) (Beenhakker and Huguenard, 2009).

Synchrony by definition is an emergent feature of population dynamics, rather than a property of any single neuron, but an increase in cortical synchrony may arise from a whole range of different coupling changes at the synaptic level. Many of these can be captured in mesoscale models of neuronal ensembles (Lopes da Silva et al., 1974). The DCM approach uses this mesoscale perspective to identify changes that are underlying the emergence of hypersynchronous slow wave activity in the presence of NMDAR-Ab.

6.4.2 NMDAR-Ab cause laminar specific changes in cortical dynamics

DCM rests on neural mass modelling of coupled neuronal oscillators that are described using specific synaptic parameters (e.g. connection strengths, time constants, see Table 6-1) and that broadly resemble the laminar structure of mammalian cortex. The neural mass model of a single electromagnetic source contains two pairs of coupled neuronal oscillators that support slower (deep oscillator: deep pyramidal cells and inhibitory interneurons) and faster (superficial oscillator: superficial pyramidal cells and spiny stellate cells) activity (Bastos et al., 2015). These popuilations model the dynamics of an integrated cortical column. Individual parameters exert highly non-linear effects on the system's output. The parameterisation of these models is rooted in biophysical properties of individual neurons but describe average characteristics of populations of functionally related neurons; i.e. composite properties emerging from the features of individual cells.

At this mescosale, PTZ and NMDAR-Ab produce synergistic effects that result in excessive synchrony not seen in other experimental conditions. My results suggest that increases in low frequency power can be explained by a combination of: (1) an increase in superficial cortical excitatory coupling, largely associated with PTZ exposure, and (2) opposing changes in the dynamics of the superficial oscillator pair (spiny stellate and superficial pyramidal cells, Figure 6.5).

The changes in synaptic dynamics align time constants in a gradient along the CMC coupling chain, with the slowest time constants in the deep pyramidal cells, and fastest

time constants in the superficial pyramidal cells – and gradual steps between. This reduces the stepwise difference in time constants along the CMC chain compared to the standard CMC configuration. This parameterisation allows a dominant frequency to resonate across – and recruit – the whole column, thus producing the high amplitude slow frequency patterns observed. Thus interestingly, slow wave activity appears to be under control of the faster, superficial oscillator pair in the CMC model, with both NMDAR-Ab and PTZ having profound and relatively specific effects on their dynamics. This is in keeping with observations from invasive recordings of sloe wave activity in human patients with epilepsy, which implicate superficial cortical coupling in the regulation of slow wave sleep activity (Csercsa et al., 2010).

6.4.3 Different molecular changes show converging effects at the neuronal population level

The synaptic parameters of the CMC model employed in DCM are population summaries of a variety of cellular effects, encompassing emergent properties and multiple nonlinearities (Schmidt et al., 2014). Time constants at the population level are essentially descriptions of post-synaptic integration affected by multiple factors, such as background firing frequency, membrane conductance, intra- and extracellular ion composition, and the dynamics of receptor types present in the membrane to name but a few (Koch et al., 1996). Connection strengths at the population level summarise the effect one population has over another and may include effects mediated via subpopulations within (e.g. self-connections are modelled as direct connectivity but represent local intralaminar inhibitory interneuronal inhibition). Because a number of different effects may converge on the same population parameters – and individual molecular effects may only be expressed in certain conditions – the link between molecular change and population parameters is nontrivial.

The approach presented here deliberately collapses much of the diversity of cortical physiology into mathematical descriptions that have specifically been developed to capture the sort of abnormal responses observable in EEG. This offers the opportunity to integrate findings from diverse sets of recordings into a common mathematical framework describing ongoing cortical dynamics.

Exposure to NMDAR-Ab has been reported to cause a number of changes in the postsynaptic glutamate response, including a reduction in overall postsynaptic potentials,

a reduction in late postsynaptic currents, and a faster return to baseline after stimulation (Hughes et al., 2010; Moscato et al., 2014). In intact neuronal circuits, NMDAR exert differential control over excitatory and inhibitory populations, leaving the populations differentially affected by NMDAR-blockade (Moreau and Kullmann, 2013).

PTZ is believed to act as an antagonist to γ-Aminobutyric acid type A (GABA-A) receptors by directly blocking ionophores (Kalueff, 2007). GABA-A receptors are fast inhibitory receptors with a wide-spread, region and cell-type specific set of post-synaptic effects (Lee and Maguire, 2014). These include inhibitory post-synaptic potentials, but also inhibition of dendritic excitatory post synaptic potentials via extrasynaptic GABA-A receptors, which is particularly pronounced at the cortical pyramidal cells (Paulus and Rothwell, 2016). In some neuronal cell types and at certain developmental stages GABA-A can cause excitatory post synaptic potentials (Song et al., 2011), and GABA transmission can exert direct or indirect control over excitatory NMDAR-dependent synaptic transmission (Kapur et al., 1997).

With this range of different cellular effects, it is unlikely one can capture the breadth if NMDAR-Ab and PTZ related effects in a small subset of population model parameters. However, the effects on delta-band power specifically can be reproduced well with a. few principal components; comprising largely just two main effects: (1) decreasing the time constants of superficial pyramidal cells relative to excitatory spiny stellate cells, and (2) increasing the excitatory coupling between spiny stellate and superficial pyramidal cells.

There are a number pf possible and convergent changes at the molecular level associated with NMDAR-Ab and PTZ exposure that could explain these population level effects. The time constant changes in superficial pyramidal cells may result from being switched towards (faster) AMPA mediated excitatory inputs (due to the NMDAR-Ab mediated internalisation of NMDAR) and a change in membrane conductivity (due to PTZ-mediated blocking of extrasynaptic GABA-A receptors). The change in excitatory connection, on the other hand is consistent with a disinhibition of excitatory EPSPs under GABA-A blockade with PTZ (i.e. a reduction of so-called shunting inhibition) (Paulus and Rothwell, 2016). Furthermore, different inhibitory interneuron populations – characterised by different molecular markers, morphology and functional integration – show distinct, and at times opposing overall effects on cortical dynamics (Muñoz et al., 2017). Thus, features of neuronal dynamics that in my models appear as changes in

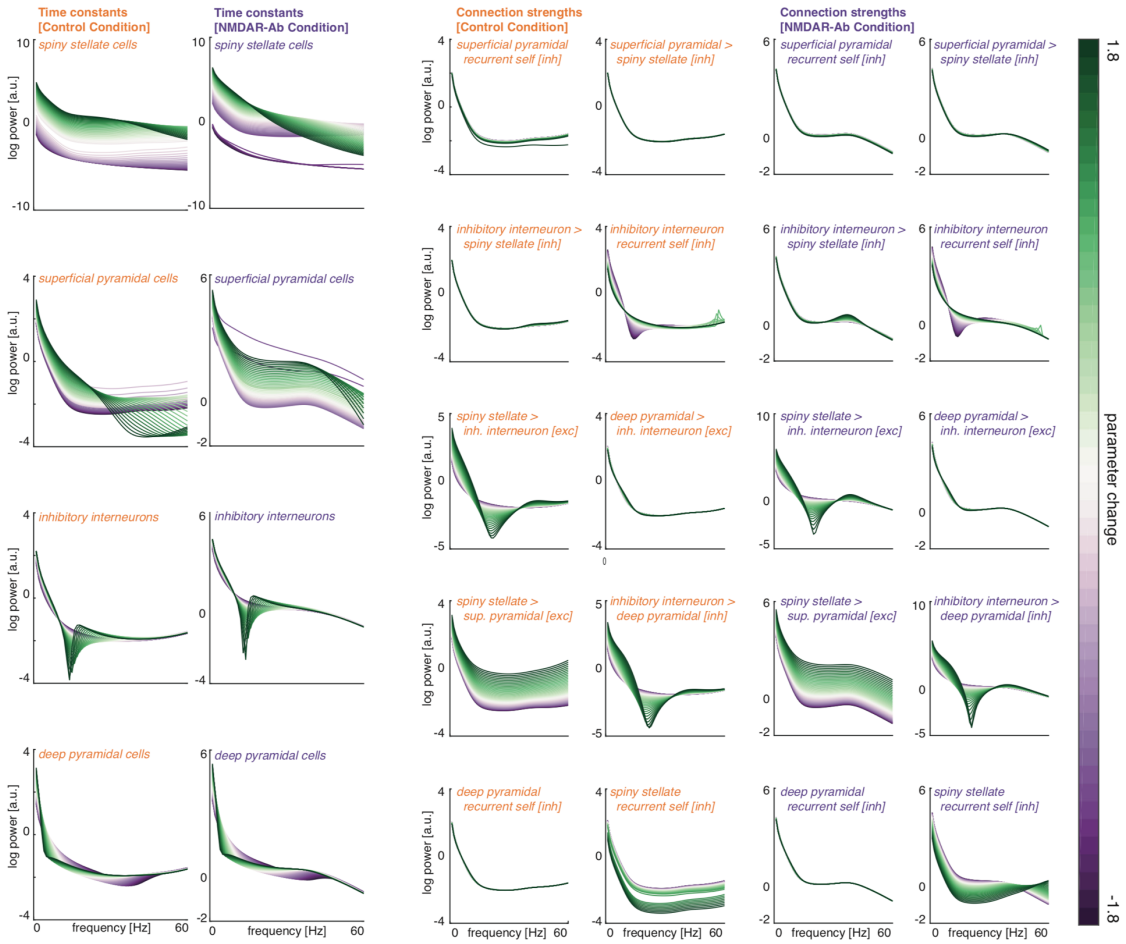

Figure 6.8 – Sensitivity analysis for canonical microcircuit models fitted to control and NMDAR-Ab positive mouse recordings. This figure shoes the effects of modulations of individual model parameters in the *in-silico* models fitted to LFP recorded from control mice, and NMDAR-Ab respectively. For each plot a single parameter was varied in small steps from values of -1.8 (purple) to 1.8 (green). The left-hand side two columns show time constant variations, the right-hand side fur columns show variations in individual connection strengths. These plots highlight a few key parameters that sensitively affect power spectra when varied in different conditions.
Notably spiny stellate time constants reproduce closely the phase transition also observed when implementing the empirical parameter variations observed in human patients. Note the spiny stellate to superficial pyramidal excitatory connection increases overall spectral output, as also indicated in the simulations in Figure 3 of the main report.

excitatory coupling at the population level, may result from subpopulation-specific changes in cortical (dis)inhibition.

Experimental methods to link detailed cell-type specific cortical physiology and population dynamics exist in experimental animals (Krook-Magnuson et al., 2013), but cannot be accessed directly in patient EEGs. By focussing on the mesoscale description here – whilst enforcing a simplified representation of cortical dynamics – I can describe the systemic effects of NMDAR antibodies in recordings from the mouse model as well as in patient EEGs. The increasingly detailed characterisation of mouse cortex circuitry

provides an important focus for progressively refining these sorts of models in future studies.

Each of these changes at the molecular level (approximated through the population model parameters) has nonlinear effect on neuronal responses. Thus, like in other complex systems, even small fluctuations in the parameters induced by only a relative shift in the balance of e.g. AMPAR and NDMAR mediated transmission can have profound effects on the activity of the dynamics of the whole circuit. These effects can be quantified using a sensitivity analysis, i.e. quantifying how changes in model parameters produce distinct spectral responses, as shown in Figure 6.8.

6.4.4 NMDAR-Ab sensitise the cortical column to spontaneous paroxysmal EEG abnormalities

In the patients with NDMAR-Ab encephalitis there is no experimental control over NMDAR-Ab exposure. Furthermore, the sample of patients is heterogeneous – representative of clinical practice (e.g. age, gender, timing of EEG, timing of initial diagnosis in relation to symptom onset, etc.). Yet these patients show a diverse range of paroxysmal, short-term changes in EEG dynamic patterns that are visually apparent, allowing me to probe spontaneous fluctuations of DCM parameters that may underlie discrete pathological brain states.

Patient-specific modelling as facilitated by DCM allows inference on patient-specific parameters in a generic model of the cortical column. Thus, applying DCM analysis to this diverse sample, one can access two types of results: (1) Qualitative: Identify the types of parameters whose changes underlie the dynamic abnormalities seen in EEG; (2) Quantitative: Establish the numerical range of parameter fluctuations that can be applied to other specified DCMs.

Consistently across patients, models with changes in time constants best explained the observed transitions between background activity and paroxysms. Furthermore, I summarised these parameter changes along a single (principal component) axis. I used this component to enforce similar fluctuations in the fully specified DCMs derived from the mouse model analysis; asking whether the baseline context (i.e. the parameterisation derived from NMDAR-Ab positive or control animals) alters the effect of parameter changes of the type and magnitude estimated from human patients.

Indeed, the dynamic responses of the two types of models are very different: In the context of NMDAR-Ab, overall greater delta-band power is observed, and there are regimes of parameter space that contain boundaries between very different dynamic states (Jirsa et al., 2014). This structural instability underwrites phase transitions of the sort seen in seizure activity or other EEG state transitions. In the control parametrisation, the same changes have a much less pronounced effect, and do not induce overt slow wave paroxysms. In short, it appears that paroxysmal EEG activity in patients may be best explained by *normal* fluctuations in synaptic time constants that occur in an *abnormal* regime of synaptic parameter space.

In the human patients I relied on EEG recordings that were obtained in the absence of external experimental control; effectively using the modelling to describe the kinds of neuronal coupling changes that cause spectral shifts in the EEG as observed during short term paroxysms. Furthermore, dynamic features observable in EEG are averages of larger scale network activity than e.g. the LFP recordings in mice. However, the insight the that spectral shift induced by changes in these parameters depends on NMDAR-Ab was only afforded through the experimentally constrained DCMs estimated from the animal model. The translation between species and modalities is afforded by explicit generative neuronal models that relate data features to underlying neuronal population activity: In the case of human EEGs, I first extract local cortical time series using a 'virtual electrode', i.e. a beamformer source reconstruction algorithm, before fitting mesoscopic neuronal population models using DCM; in the case of LFP recordings in mice, I can use DCM directly to explain the recorded LFPs (with the observation model consisting of a single scalar gain parameter). Crucially these generative models then allow for neurobiologically relevant features (i.e. the changes in connection strength and synaptic dynamics) to be translated at the same mesoscopic scales.

Overall these findings provide integrative evidence from human patients and a mouse model of NMDAR-Ab encephalitis suggesting that (a) NMDAR-Ab cause electrophysiological abnormalities via a small number of synaptic changes, which may lend themselves to targeted therapeutic interventions; e.g. by exploiting laminar and/or cell-type specific effects of transcranial current stimulation (Rahman et al., 2013). And (2) paroxysmal abnormalities can be explained by persistent baseline changes that render cortical microcircuitry particularly sensitive to (potentially normal) fluctuations in

synaptic coupling. Future research may reveal whether similar approaches have diagnostic value when performed on patient EEGs alone (Symmonds et al., 2018).

6.4.5 Limitations

The modelling approach presented here allows unique insights into possible mechanisms underlying empirically observed phenomena. Although DCM has been applied to a wide variety of neurophysiological studies – and its validity has been assessed repeatedly (Kiebel et al., 2009; Moran et al., 2011a) – there are certain limitations to the approach I have adopted for this study.

First, the modelling can only be applied to existing data – this places restrictions on study design (e.g. pre-NMDAR-Ab EEGs are not usually available from patients) and limit the approach to a subset of testable hypotheses. Second, like all inference, DCM is based on specific assumptions regarding the underlying neuronal architecture – all activity presented here is presumed to emerge from microcircuitry consistent with CMC models, and only given this assumption can I estimate the parameters and provide evidence for or against specific model parameterisations.

Most importantly, I have reduced a complex brain-wide pathology of interacting systems to changes in a cortical microcircuit. Thus, I are ignoring interactions between different cortical regions, as well as the influence of subcortical structures, such as thalamus and brain stem, which (especially in the context of encephalopathy and slow wave abnormalities) will exert a powerful influence over cortical states. Although these effects can be accommodated in the model as random effects, they are not modelled explicitly.

The approach here – by design – focusses not on single cell dynamics, but treats cortical patches as integrated units, which correspond to the mesoscale dynamics observable in EEG (Freeman, 2000b). My computational modelling of cortical microcircuits aims to link some of these observed dynamics with the themes that have emerged from detailed micro-anatomy and neurophysiology at the microscale and are implicated in NMDAR-related pathology. However, I am not attempting to make inference about single neurons. The models are describing the 'net' effect of NMDAR-Ab on integrated circuits of neuronal populations: Future studies should allow us to model how these effects emerge from single neuron interactions. Furthermore, I note that many of the 'canonical' models of cortical circuitry (including ours) have focussed on excitatory population coupling, and in the future may benefit from incorporating some of the more recent themes that have been

identified in the connectivity patterns of inhibitory interneuronal populations (Pfeffer et al., 2013). This study aimed to answer specific questions driven by observations in a particular pathology related to NMDAR-Ab. Whilst the models and results as presented here are appropriate for this focus, there are many observations related to abnormal NMDAR-function not currently captured in the model here. I hope that future research will integrate across different such experiments and observations and expect that generative models like the one presented here will help in this ongoing work.

7

7 Selective prefrontal disinhibition under NMDA receptor blockade §

7.1 Introduction

N-methyl-D-aspartate receptor (NMDAR) hypofunction is considered one of the primary causes of schizophrenia (Friston et al., 2016; Krystal, 1994), which itself is associated with a number of electrophysiological brain abnormalities (Näätänen and Kähkönen, 2009; Uhlhaas and Singer, 2010). NMDAR antagonism, e.g. with ketamine, can reproduce a set of symptoms and electrophysiological features of schizophrenia (Guo et al., 2009; Javitt et al., 1996; Nakazawa et al., 2017), including a reduction in auditory mismatch negativity (MMN) observed in patients (Ranlund et al., 2016; Umbricht et al., 2000; Umbricht and Krljes, 2005; Wynn et al., 2010). MMNs are difference waves of event-related potentials (ERPs) to an unexpected *deviant* stimulus and repeated *standard* stimuli (Cheour et al., 2000; Todd et al., 2014). One theory of the underlying perceptual inference is formalised in the predictive coding framework (Friston and Kiebel, 2009; Schröger et al., 2014): Based on Helmholtz's notion that the brain attempts to infer the causes of sensations (Dayan et al., 1995; Friston, 2005), predictive coding proposes that the brain generates predictions of

§ The work reported here has also been described in the following forthcoming publication:

Rosch, R.E., Auksztulewicz, R., Leung, P.D., Friston, K.J., Baldeweg, T. 2018. Selective prefrontal disinhibition in a roving auditory oddball paradigm under *N*-Methyl-D-Aspartate receptor blockade. *Biol Psychiat CNNI*, in press. doi: 10.1016/j.bpsc.2018.07.003

As part of this work, I proposed the computational analysis, independently performed the computational modelling, and wrote the manuscript. I was not directly involved in the acquisition of the recordings, which are reported here for completeness.

sensory input. When sensation deviates from these predictions, prediction error signals are generated, and passed along the sensory hierarchy. Evidence from different sensory domains and species suggests that this provides a good explanation of MMN-type responses (Wacongne et al., 2012; Ylinen et al., 2016). However, there is limited evidence on how the underlying mechanisms are affected by NMDAR transmission and its blockade.

Computational models offer a bridge between putative synaptic mechanisms, and electrophysiological and psychopathological features of disease phenotypes (Anticevic et al., 2012; Moran et al., 2011b). Dynamic causal modelling is one such approach: Here neural mass models of cortical microcircuitry are fitted to ERP data (Friston et al., 2003; Kiebel et al., 2009), an approach widely applied to auditory MMN paradigms (Garrido et al., 2009a; Phillips et al., 2015), including in patients with schizophrenia (Dima et al., 2012), patients with psychosis (Ranlund et al., 2016), and healthy volunteers exposed to ketamine (Schmidt et al., 2013).

Here I apply novel DCM techniques to data from a double-blind placebo-controlled study of the effects of ketamine on the auditory MMN. I employ a single hierarchical model to identify (1) within-session coupling changes explaining ERPs to deviants and standard stimuli (modelling MMN and repetition suppression effects respectively); and (2) group-wise between-session coupling differences induced by ketamine. Previous DCM studies have focussed on synaptic changes plausibly affected by sensory input directly. My approach here accommodates more fundamental effects of ketamine on neuronal circuits; e.g. on excitation/inhibition balance within cortical microcircuits, on intrinsic timescales of cortical areas, or on postsynaptic gain. I exploit the biophysically detailed microcircuit models implemented in DCM, linking neurobiological insights and theoretical accounts of sensory processing in the brain (Bastos et al., 2012). This, I use DCM to identify intrinsic (within-source), or extrinsic (between-source) synaptic connection changes induced by oddball stimuli, and how these changes were contextualised by altered neurobiology during the administration of ketamine.

7.2 Methods

7.2.1 Subjects

The study team recruited N=18 male volunteers (Table 7-1) through university advertisements. Subjects gave fully informed, written consent prior to participation, and were compensated. The study was approved by the University of Lübeck Research Ethics Committee. Participants completed a psychiatric questionnaire (SCL-90-R®) and routine clinical examination (including ECG, auscultation, and blood pressure measurements). Subjects with pre-existing conditions, a family history of psychotic illness or epilepsy, regular medication and subjects who were left handed, smoked, or were recreational drug users were excluded. Participants were invited for two sessions >3 weeks apart (placebo, and ketamine arms).

ID	Dose *(mg/kg/h)*	Age *(years)*	Gender
A	*0.250*	23	Male
C	*0.250*	21	Male
E	*0.250*	23	Male
G	*0.083*	22	Male
I	*0.083*	22	Male
J	*0.250*	22	Male
K	*0.083*	23	Male
M	*0.083*	26	Male
N	*0.083*	22	Male
O	*0.083*	24	Male
P	*0.083*	25	Male
R	*0.083*	22	Male
T	*0.083*	22	Male
U	*0.083*	22	Male
W	*0.083*	25	Male
X	*0.250*	21	Male
Y	*0.250*	25	Male
Z	*0.083*	23	Male

Table 7-1 - Study subject details

This was a randomised, placebo-controlled, double-blind cross-over experiment: Participants were randomly assigned to either ketamine- or placebo-first groups (9 in each group). Subjects and supervising researchers were blinded to session conditions (N.B., psychotomimetic effects of ketamine may reveal session conditions to participants). Ketamine, or the saline placebo were infused continuously over 2.5 hours, with ERP recording commencing at 1.5h post onset (Feld et al., 2013; Gais et al., 2008). An initially used higher ketamine dose was poorly tolerated by some participants, who suffered from

nausea, vomiting and some degree of disorientation. Because of this, the concentration of the infusion was reduced from *0.250* to *0.083 mg/kg/h* for subsequent data collection, as detailed in the subject specification table (Table 7-1).

7.2.2 Stimuli and ERP recording

ERPs were recorded using 20 electrodes (10-20 EASYCAP system, www.easycap.de; Compumedics Neuroscan© amplifier, sampling frequency 500Hz). Pure tones were presented in pseudorandom sequences: Sounds of the same frequency were repeated 2-36 times, before a frequency change (i.e., roving oddball paradigm). Sounds were presented at 80dB, with frequencies between 700-1200Hz (in 50Hz steps), and an inter-stimulus interval of 400ms, tones were 25ms in duration (Haenschel, 2005). Subjects were given an incidental reading task, and were instructed to ignore the sounds.

Data were analysed in average referential montage, bandpass-filtered (range *0.1-80Hz*) and divided into *-100ms* to *300ms* peristimulus epochs. In the roving paradigm, tones change from deviants (i.e. first in sequence) to standard stimuli through increasing repetitions. Average ERPs were calculated to capture the average waveforms of the 1st (deviant, D1; average 228 trials per participant), 2nd, 6th, and 36th (standards S2, S6, and S36; average of 76 (S36) to 209 (S2) trials per participant) presentation in a sequence. Baseline correction was performed based on the *-100* to *0ms* peristimulus time interval (D1), the *250* to *300ms* interval (S2), or both (S6, S36) in order to avoid large P3a components at the end of D1, and the beginning of S2 epochs.

7.2.3 Experimental design and statistical analysis

The experiment was designed to determine within-session effects of stimulus repetition and deviance, as well as between-session effects of ketamine in a crossover design. Within-sessions, I compared ERPs to standard tones after short (2 tones), and long (36 tones) sequences, as well as ERPs after 36 tones, and the deviant ERP (1st tone) using Bonferroni corrected t-tests for time-point by time-point differences. To evaluate between session group effects of ketamine vs placebo, I compared peak amplitude of the mean difference between the standard and deviant ERPs (i.e. mismatch negativity) with a t-test.

7.2.3.1 Dynamic causal modelling

Further detailed analysis using cortical source estimates of population output was performed using dynamic causal modelling (DCM). My analysis was based on low-density

EEG recordings (20 electrodes in the 10-20 electrodes system), resembling EEG recordings routinely used in the clinic. These data were sufficient for the purposes of this study, because the aim of the study was not to identify the functional architecture of the auditory mismatch response, which has been the focus of previous studies (Auksztulewicz and Friston, 2016; Garrido et al., 2009b). Rather, I wanted to infer the effects of ketamine on the neurobiology of an established MMN network. My models reflect this question, focussing on variations in model parameters as the explanation for the ERP differences. Prior knowledge about source locations was included in the DCM inversion as prior, enabling me to finesse the source reconstruction problem using low-density EEG data and thereby drill down specifically on the ketamine effects. I applied hierarchical (parametric empirical) Bayesian modelling to identify group effects across DCMs fitted to single subjects. This analysis was conducted using the free academic software SPM12 (http://www.fil.ion.ucl.ac.uk/spm/, Litvak et al. 2011), and custom code available online (doi.org/10.5281/zenodo.570595) – which is also included in the appendix of this thesis in section A.7.

Identifying prior parameter distributions from grand mean ERP inversions: In order to produce the best fits at the single-subject level, a DCM was fitted to grand mean ERPs as detailed below (Garrido et al., 2009a, 2009b). A standard electromagnetic forward model based on a boundary element method (BEM) standard head model in MNI spac implemented in SPM12 was used to calculate lead-fields and reconstruct source ERP waveforms at six cortical locations (Garrido et al., 2008; Phillips et al., 2015): bilateral primary auditory cortex (A1), bilateral superior temporal gyrus (STG), and bilateral inferior frontal gyrus (IFG) with MNI coordinates: ltA1 [-42, -22, 7], rtA1 [46, -14, 8], ltSTG [-61, -32, 8], rtSTG [59, -25, 8], ltIFG [-46, 20, 8], rtIFG [46, 20, 8].

Differences between ERPs were modelled as arising from extrinsic (between cortical regions), or intrinsic (within cortical regions) synaptic coupling changes. I modelled the effect of deviance and repetition as coupling changes (i.e. short-term plasticity) that are summarised as linear mixture of two temporal basis functions (Figure 7-1 A). This yields three types of coupling: (1) Subject specific connectivity conserved across repetitions (A parameters); (2) repetition-dependent changes in connectivity greatest for the deviant and subsequently decreasing (B parameters of the monophasic decay); and (3) repetition-

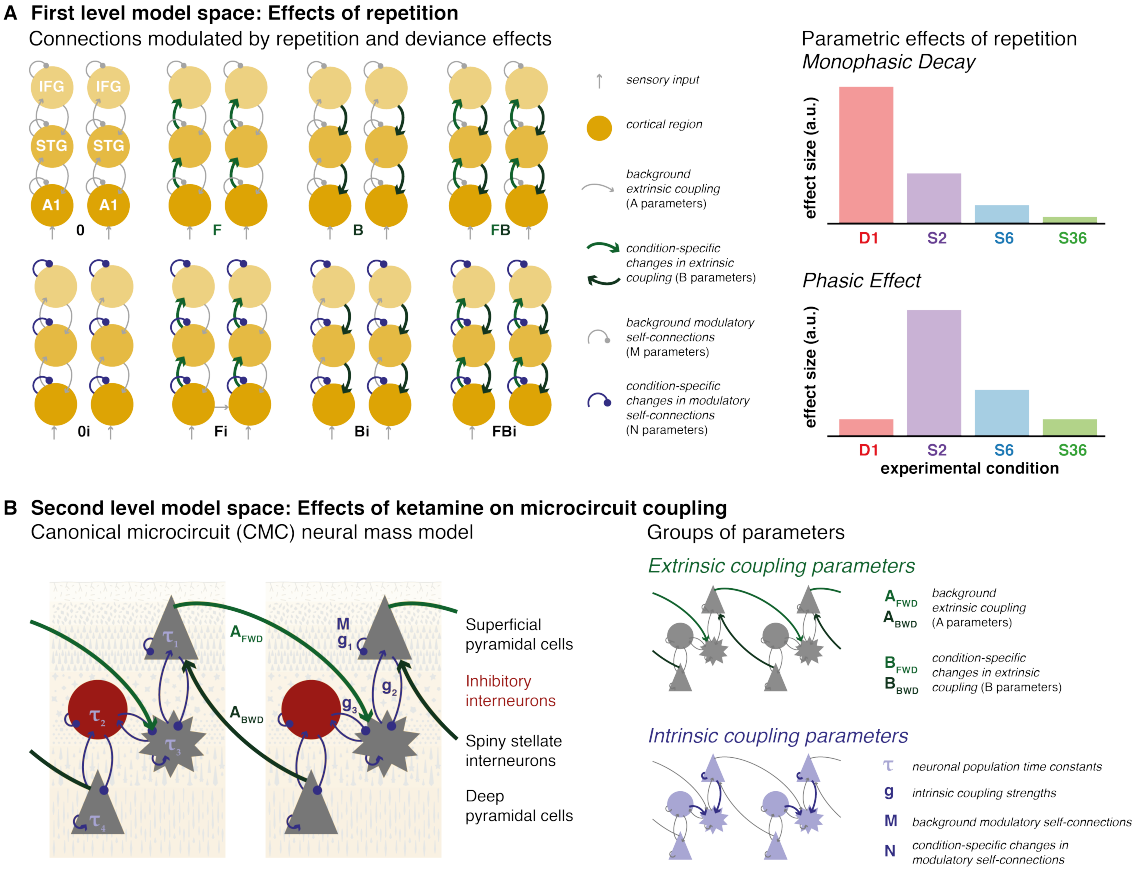

Figure 7-1 – Two-level hierarchical DCM model space. DCM represents cortical sensory processing as a network of (extrinsically) coupled cortical sources, each of which contains (intrinsically) coupled neuronal populations. Each population is modelled as a neural mass with characteristic synaptic time constants. The free parameters of this model include: extrinsic coupling parameters between cortical sources (average coupling: *A* parameters; condition-specific modulation *B* parameters); and intrinsic coupling parameters between neuronal populations within a source (population time constants: τ parameters; coupling strengths: *g* parameters; activity dependent modulation of recurrent self-connections: *M* parameters; and condition-specific modulation of activity dependent coupling: *N* parameters).
(A) Effects of repetition were modelled as condition-specific modulations of forward/backward extrinsic connections (*B* parameters) and intrinsic modulatory gain parameters (*N* parameters) in a coupled network of six cortical sources. The relative contribution of these parameters to each of the ERPs modelled here (i.e. D1, S2, S6, S36) is estimated using two temporal basis functions: a monophasic decay (where the contribution is maximal for the deviant stimulus D1), and a phasic change in connectivity (where the response is maximal at the standard stimulus S2), as shown in the right panels. (B) Ketamine effects were modelled at the second level, i.e. as group-level differences in DCM parameters between conditions that were conserved over subjects. The left panel illustrates the parameters in the canonical microcircuit representation of each source used in this DCM. My analysis addressed the following question: Which combination of parameter changes between placebo and ketamine conditions best explains the ketamine effect observed across the whole group? The model space is divided into models where ketamine affects combinations of extrinsic coupling parameters (right top panel), vs those where ketamine affects only combinations of intrinsic coupling parameters (right bottom panel).

A1 – primary auditory cortex; STG – superior temporal gyrus, IFG – inferior frontal gyrus; Extrinsic connectivity parameters: A_{FWD} – extrinsic forward coupling; A_{BWD} – extrinsic backward coupling; B_{FWD}, B_{BWD} – condition specific modulations of extrinsic connections; Intrinsic connectivity parameters: $g_{1\text{-}3}$ – intrinsic coupling; τ – time constants; M – modulatory self-connections; N – condition specific effects on modulatory connections

dependent changes in connectivity that peak with the first standard tone S2 (i.e. B parameters for the phasic temporal basis function).

The linear mixture of both types of temporal basis function – weighted by their respective B parameters – reproduces the estimated connectivity changes across the four conditions (i.e. repetitions) allowing for a range of different types of plasticity over time (Garrido et al., 2009b), The model inversion provides both a measure for the model evidence, and posterior densities of these model parameters, identifying their estimated values and a certainty measure around those estimates. Parameter estimates of this grand mean inversion were then used as priors for single-subject DCMs.

Individual model inversion and Bayesian model reduction to identify repetition effects:

Whole-scalp ERPs for each subject were extracted separately for placebo and the ketamine conditions, resulting in 36 separate sessions (18 subjects, 2 conditions) for DCM analysis. For each DCM, the full 6-region network was equipped with grand-mean derived priors and inverted, yielding 36 individually parameterised DCMs.

To test whether the effects of deviance (Garrido et al., 2009a) and the effect of repetition (Garrido et al., 2009b) replicate existing findings in the literature, I performed Bayesian model reduction. This identifies the best subset of DCM parameter changes that could explain the observed ERP responses: Based on inverted 'full' DCMs, I can estimate model-evidence for a number of reduced DCMs, in which some parameters do not allow condition-specific variations (Friston et al., 2015; Kiebel et al., 2009; Litvak et al., 2015). I then compared the models in which repetition modulated only a subset of network connections along three classes of models – (1) models in which forward connections change, vs models in which they do not; (2) models where backward connections change, vs those where they do not; and (3) models in which intrinsic modulatory gain parameters change, vs those where they do not (Garrido et al., 2009a; Phillips et al., 2015). This furnishes a combination of 2 * 2 * 2 = 8 models: 4 types of differences in between-source connectivity modulation; 2 types of differences in their within-source connectivity modulation (Figure 7-1 A). As each subject had a high model evidence for the same (winning) model (see Results section below), within-session effects across the group were summarised using Bayesian parameter averages.

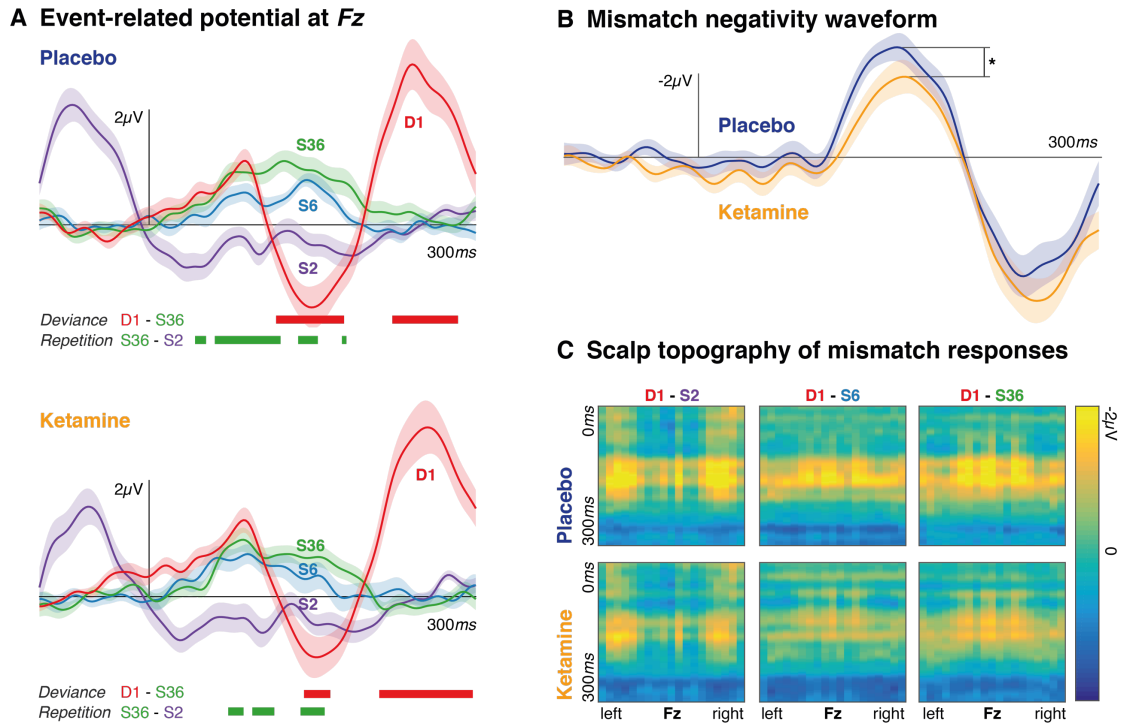

Figure 7-2 – Ketamine causes a reduction in the mismatch negativity. (A) ERPs are shown for repetitions of a sound within the roving oddball paradigm. The first exposure to a sound within a sequence, *D1*, provokes a typical deviance response at the *Fz* electrode. ERPs for three different repetitions, *S2*, *S6*, and *S36* show increasing positivity with a peak at approximately *120ms*. The bold red lines indicate time points for which the *S36* and *D1* are significantly different across the whole group (i.e. the effect of deviance, $p < 0.05$, Bonferroni-corrected for multiple comparisons); bold green lines indicate time points for which *S36* and *S2* are significantly different (i.e. the effect of repetition, $p < 0.05$, Bonferroni corrected for multiple comparisons; differences only evaluated for the *0 – 300ms* peristimulus interval). Ketamine reduces both the duration of the deviance and repetition effects. (B) Difference waveforms (i.e. mismatch negativity; plotted negative up) at *Fz* are shown for *D1 – S36*. The peak amplitude at around *150ms* is significantly larger for the placebo condition compared to ketamine. (C) The panels show the difference between *D1* and either *S2*, *S6*, or *S36* respectively. These are plotted across time (y-axis), and channels (x-axis, arranged from left to right). For each standard-deviant pair, there is a ketamine-related reduction in mismatch responses.

Parametric empirical Bayes and ketamine effects: To estimate systematic variations in model parameters caused by ketamine, I used a parametric empirical Bayesian (PEB) approach. In brief, PEB allows the Bayesian estimation of a general linear model explaining effects across DCMs at the level of model parameters. This second level model can be equipped with different regressors (across all sessions and subjects), with the inversion providing parameter estimates for these between-DCM effects (Friston et al., 2016).

Here I use PEB to (1) perform Bayesian model comparison across reduced models, and (2) quantify the parameter changes in the winning model where a subset of DCM parameters explains the ketamine effect. Regressors comprised (a) an effect of ketamine (0 for placebo,

1 for low dose ketamine, 2 for high dose ketamine; the two sessions from each individual subject were thus modelled as either 0-1, or 0-2, thus preserving differential effect sizes of ketamine across participants), (b) the group mean and (c) random subjects, or block effects. The parameters included time constants ($\tau_{1\text{-}4}$ parameterising the temporal dispersion of postsynaptic responses), intrinsic connectivity parameters ($g_{1\text{-}3}$ parameterising cortical microcircuit connection strengths), modulatory gain parameters

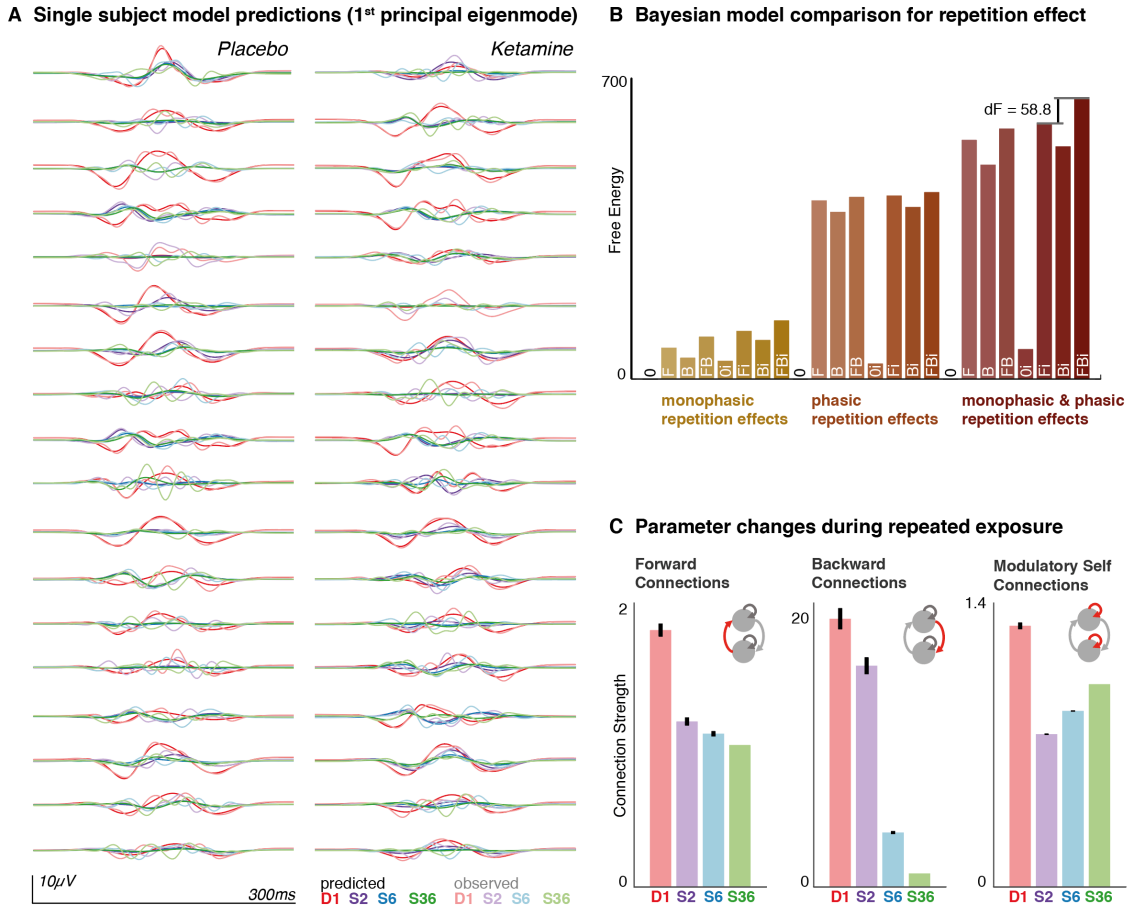

Figure 7-3 – Repetition effects. (A) ERPs to the 1st (Deviant, *D1*), 2nd, 6th, and 36th (Standards, *S2*, *S6*, *S36*) presentation of a sound within a sequence were modelled in subject-specific DCMs. The first principal eigenmode of the prediction in sensor space (bold colours), and the corresponding mode of the empirical scalp data (light colours) are shown for each individual. These suggest a good fit for the main components of the ERP waves. (B) Bayesian model comparison was performed to compared models in which the repetition effect was monophasic, phasic, or both, and included modulations of forward *F*, backward *B*, or intrinsic *I* connections and their combinations. The winning model across the group was the full model, where monophasic and phasic repetition effects impact on forward, backward and intrinsic connections. (C) Bayesian parameter averages for this full model across all subjects show changes in connection strength across repetitions for forward, backward and intrinsic modulatory connections. Error bars indicate 95% Bayesian confidence intervals.

(*M, N* parameterising modulations of superficial pyramidal cell gain), and extrinsic connectivity parameters (*A, B* parameterising connection strengths between cortical sources).

This model space addressed two classes of hypotheses: (a) ketamine affects extrinsic connections between sources (*A* and *B* parameters), and (b) ketamine modulates intrinsic properties within sources (*M, N, g,* and τ parameters). I allowed for both a non-specific (main) effect of ketamine on coupling (*M*, *A, g,* τ parameters) – and interaction effects specifically on plasticity (*N, B* parameters). I used Bayesian model reduction to compare the evidence for these (second-level) models, yielding approximate log-evidence for these second level models and estimates of the ketamine-induced parameter changes (with ayesian 95% confidence intervals). Finally, in order to further characterise these effects, I used parameter estimates in simulation mode (i.e. in a forward model based on the grand mean DCM across all participants) to visualise their impact on source space ERPs.

7.3 Results

7.3.1 Sensor space results

ERPs contain averaged responses to tones of different frequencies at fixed positions within a sequence. Grand mean ERPs at the frontocentral (*Fz*) electrode for D1, S2, S6, and S36 are shown for placebo and ketamine conditions (Figure 7-2 A). Deviance ERPs (to D1) constitute an early negative response (at MMN latency, approximately *150ms*) and later positivity (P3a, approx. *250ms*) that differs significantly from ERPs to standard tones (deviance effect). ERPs to S2, S6, S36 show the build-up of a positive 'memory trace' at around *120ms* with significant differences between S2 and S36 indicated in Figure 7-2 A (repetition effect).

Ketamine reduced the period during which there was a significant deviance effect (i.e. D1 – S36 ERPs under placebo: *112ms*, under ketamine: *90ms*); as well as the repetition effect (i.e. S36 – S2 ERPs under placebo: *120ms*, under ketamine: *98ms*). The MMN is attenuated by ketamine (paired t-test, $t(17) = 1.85;\ p = 0.04$) but not P3a ($t(17) = 1.10:\ p > 0.05$, Figure 7-2 B). The attenuation is also apparent across the whole scalp when plotting all channels.

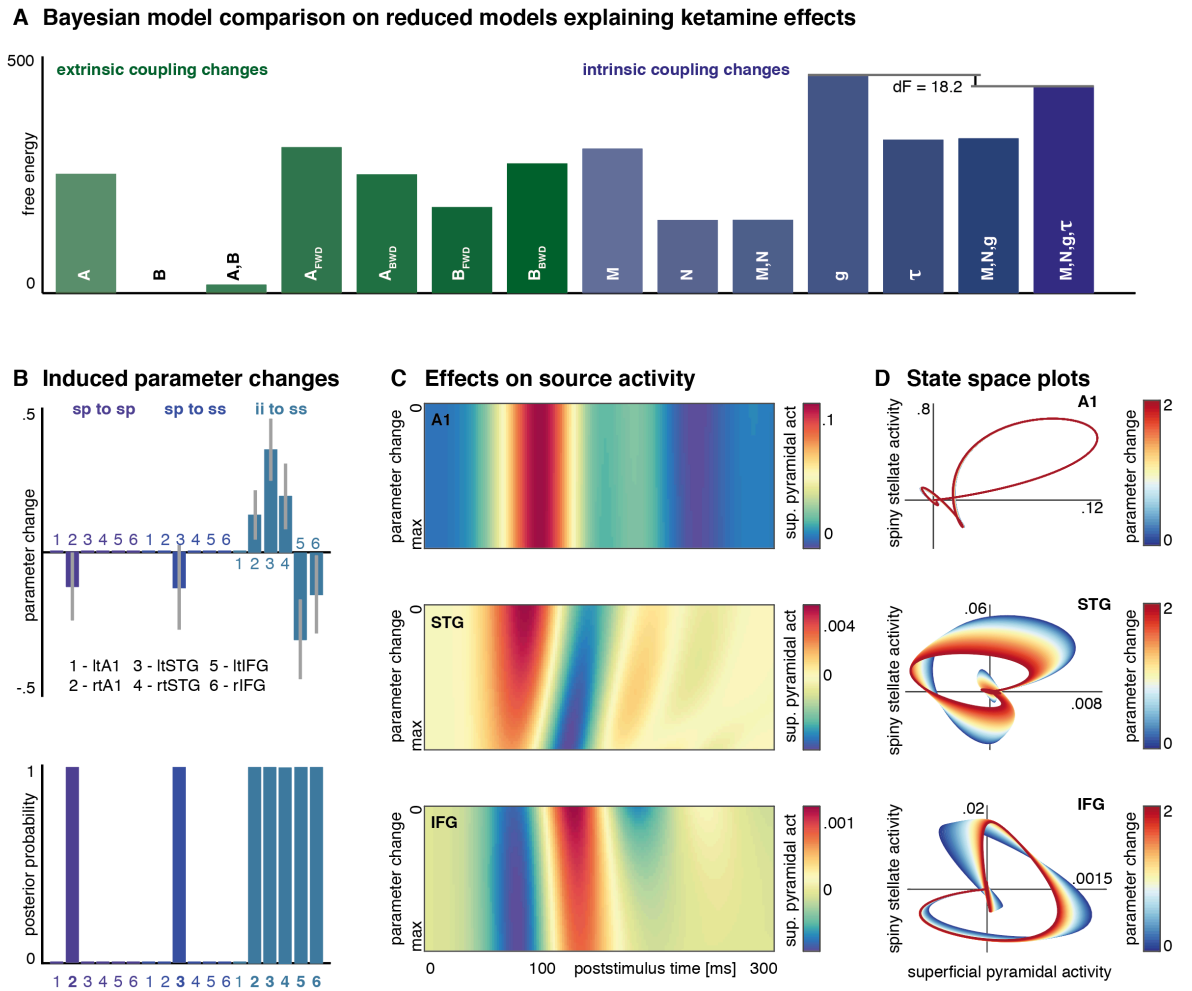

Figure 7-4 – Ketamine causes frontal lobe disinhibition. (A) Using PEB, 14 alternative second-level models were considered, explaining differences between ketamine and placebo with changes in combinations of parameters. Bayesian model reduction shows that the model with changes in intrinsic connection parameters (g) best explains the effects of ketamine on the ERPs. (B) Estimated parameter changes with Bayesian 95% confidence intervals (top), and posterior probability of the parameter being affected by ketamine (bottom) are shown. Significant changes were only observed in a subset of g parameters, with the largest effects estimated for inhibitory interneuron (*ii*) connections to spiny stellate (*ss*) cells. In the bilateral STG, there was an increase in *ii* inhibition on *ss*, while in the bilateral IFG there is a ketamine-induced disinhibition of *ss*. (C) Simulated effects of opposing changes in *ii* to *ss* inhibition at different hierarchical levels are shown in source space. Each graph shows superficial pyramidal cell (*sp*) activity in different regions for the *0 – 300ms* poststimulus interval with concurrent, but opposite modulation of parameter the *ii* to *ss* inhibition: In the STG the (log-scaled) connection strength is increased from 0 to 2, whilst in the IFG the strength is decreased from 0 to -2. This modulation causes an attenuation and increase in latency in the IFG response, with concurrent attenuation of early STG responses and a decrease in the latency of the response. (D) Neuronal state space plots show the relationship between *sp* and *ss* activity for different hierarchical levels and for increasing changes to the *ii* to *ss* inhibition. There is minimal effect on the A1. For STG, the parameter changes induce a reduction in *ss* response amplitude compared to *sp* and an overall shift towards more negative population output. In the IFG there is an inverse reduction of *sp* response amplitude compared to *ss*.

Intrinsic connectivity parameters: $g_{1\text{-}3}$ – intrinsic coupling; τ – time constants; M – modulatory self-connections; N – condition specific effects on modulatory connections

7.3.2 Effects of repetition on connectivity

Repetition effects were modelled as changes in connectivity of the cortical auditory network comprising three bilateral sources. This plasticity is captures in a linear mixture of two temporal basis functions (Figure 7-1 A): a monophasic decay and a phasic effect across repetitions. The combination of both effects on extrinsic and intrinsic coupling constitute the full model (model *FBi* in Figure 7-1 A; see Figure 7-3 A for subject specific model fits). A set of reduced models was compared using Bayesian model reduction.

These comprised each of the models in Figure 7-1 A, paired with either one, or both of the temporal basis functions, resulting in a total of 8 * 3 = 24 models. Bayesian model comparison provides decisive evidence for the full model (i.e. *FBi* with both monophasic and phasic effects) at the group level (Figure 7-1 B) and for each individual subject.

Bayesian parameter averages for forward connections, backward connections, and modulatory self-connections (shown here for A1) are shown in Figure 7-3 C, indicating distinct time courses of changes for different types of connections. Overall, extrinsic connectivity was reduced across repetitions: Biggest reductions were seen earlier in forward compared to backward connections. Modulatory gain parameters are reduced initially (D1 to S2) before increasing (S2 to S36). The combination of these parameters best explains the observed ERP changes with repetition.

7.3.3 Effects of ketamine on model parameters

I then combined DCMs for each subject and session in a single PEB model to identify between-session parameter changes induced by ketamine. Initially, I used Bayesian model reduction at this second level to compare reduced models that contained ketamine-related variation in only a subset of coupling parameters (Figure 7-4 A). This allowed me to identify the simplest models with greatest explanatory power: In my hypothesis space I allow for complex interactions between ketamine and the effects of repetition suppression on the network (through the selection of model parameters available to explain the ketamine effect). For example, the *N* parameters of the DCMs encode repetition-induced changes in cortical self-modulation. The second level (PEB) model space included models in which the ketamine effect could be explained through changes in these *N* parameters; e.g. ketamine could attenuate *changes* in self-modulation during repeated exposure to the same sound. However, the parameters encoding these effects were redundant and

eliminated after Bayesian model reduction. A better explanation for the ketamine effect on the MMN was instead a repetition-invariant change in cortical microcircuitry encoded in the *g* parameters.

An inspection of the winning second-level model revealed that of these *g* parameters, only a subset is affected by ketamine (Figure 7-4 B). The biggest effect size is seen in g_3, which represents the strength of inhibition supplied by inhibitory interneurons to excitatory spiny stellate cells. This parameter is modulated in opposite direction in the lower areas of the hierarchy (increased in right primary auditory cortex *A1*, left and right superior temporal gyrus *STG*; decreased in left and right inferior frontal gyrus *IFG*).

To simulate the (highly nonlinear) effects of these parameter changes on observed ERPs, I implemented a forward model based on the grand mean DCM inversion from the earlier stages of this analysis. This simulation gradually increased g_3 in bilateral *STG*, while decreasing the same parameter in bilateral *IFG*. The effects of these reciprocal changes in source space ERPs are shown in Figure 7-4 C. This analysis reveals an attenuation and small increase in latency in the *IFG* response that resembles the observed changes in the mismatch negativity response at the *Fz* electrode in Figure 7-2 B. The responses at *STG* level are overall reduced in amplitude with a decrease in response latency (also previously reported empirically, (Umbricht et al., 2000)) .

Further analysis of the relationship between excitatory interneurons (here modelled as spiny stellate cells) and the superficial pyramidal cells is shown in Figure 7-4 D. Plotted in terms of estimated neuronal responses, these graphs represent the evolution of population responses during the deviance ERPs in neuronal state space, starting from and returning to baseline. These plots show the relative impact of g_3 parameter changes on the different neuronal populations. In *IFG*, where interneuron inhibition on spiny stellate cells is reduced, this plot reveals a decrease in superficial pyramidal cell amplitude with relative preservation of spiny stellate cell activity. Conversely, in STG where g_3 is increased, the amplitude of spiny stellate cells is relatively decreased compared to superficial pyramidal cells.

7.4 Discussion

In this study, I identified region-specific changes in cortical microcircuits induced by ketamine during an auditory oddball paradigm. The approach presented, provides a

unifying hierarchical model explaining network-wide short-term sensory learning effects, mismatch effects and the effects of NMDAR-blockade with ketamine. I focussed on auditory ERPs – but mismatch responses are known to be attenuated by ketamine in other modalities (Schwertner et al., 2018). Furthermore, my results indicate that ketamine affects background (i.e. condition-invariant) cortical circuitry. These findings may thus represent generic aspects of how predictive coding is affected by ketamine, rather than domain-specific features of decoding the auditory environment.

7.4.1 Computational modelling links whole-brain observations with synaptic mechanisms

Mesoscale neuronal models can reproduce various normal (Bhattacharya et al., 2016; Bond et al., 2014), and abnormal (Jirsa et al., 2014; Wendling et al., 2016) brain responses, explaining complex sets of observations, such as ERP data (Moran et al., 2011b). I used this approach to compare a range of possible ketamine effects on auditory ERPs.

My results suggest that (1) acute NMDAR blockade effects can be explained by a small set of key parameters and (2) the parameters identified are consistent with a wealth of pervious related, but methodologically distinct studies. The non-trivial link between MMN changes and intrinsic inhibition within frontal microcircuits could not have been made without explicit computational modelling of EEG generators. With this approach I provide evidence for a localised and cell-type specific role of NMDAR hypofunction in psychotic pathophysiology in a placebo-controlled human experiment, with clear parallels in studies of schizophrenia and acute psychosis in patients (Geyer et al., 2001; Jentsch and Roth, 1999).

7.4.2 Deviance responses are caused by network-wide connectivity changes

Competing theories regarding the origin of the MMN can be summarised as (1) the *neural adaptatio*n hypothesis, according to which the MMN is explained by 'bottom-up' dishabituation (Jaaskelainen et al., 2004); and (2) the model adjustment hypothesis, according to which MMNs represent an error detection signal prompting predictive model updating (Näätänen and Winkler, 1999). Here I replicate findings from previous studies pertaining to the neurobiological implementation of these putative mechanisms. In this study, assume the same cortical sources previously identified and replicated in a number of auditory oddball EEG and MEG studies (Auksztulewicz and Friston, 2015; G.K. Cooray

et al., 2015; Garrido et al., 2009a; Phillips et al., 2015). This allowed me to focus on processing dynamics rather than network topology. The placebo results support previous DCM studies of the MMN showing that both neural adaptation and model adjustment are required to explain the phenomenon, as it requires changes in both intrinsic modulatory gain and extrinsic cortical coupling. This is in keeping with a predictive coding account of MMN generation. According to the predictive coding framework, sensory predictions are passed downstream along the sensory processing hierarchy. When they mismatch sensory evidence, a prediction error signal is evoked, which passes back up the cortical hierarchy (modulating extrinsic connectivity), whilst also causing adjustment of the intrinsic gain in primary sensory cortex (modulating intrinsic connectivity) (Friston, 2005b; Wacongne et al., 2012).

7.4.3 Sensory learning causes distinct patterns of change for different coupling parameters

In the roving oddball paradigm, deviant sounds are repeated until they become the new standard, no longer eliciting deviance responses. Previous DCM studies identified distinct temporal patterns in associated coupling changes: Using short auditory sequences, Garrido et al. (Garrido et al., 2009b) identified a clear difference in extrinsic connections, which were consistently reduced with each repetition; and intrinsic connections, which showed an initial phasic decrease before slowly increasing with repetition.

These findings are replicated independently here: extrinsic connectivity decreases with repetition, whilst intrinsic connectivity parameters show only a brief phasic decrease. There is also a temporal dissociation between forward and backward connections: while forward connection strengths quickly return to their baseline value, backward connection strengths remain higher for longer. This asymmetry in the time course of forward and backward plasticity may reflect more general differences in temporal dynamics at different points along the cortical hierarchy. Primate cortical areas are hierarchically ordered in their neuronal timescales (Chaudhuri et al., 2014; John D Murray et al., 2014). The resultant hierarchically segregated tracking of fast and slow changes at different level of the hierarchy may support efficient representation of complex sensory input (Kiebel et al., 2008a). My findings add further support for this hierarchical separation in time scales. After the deviant, short transient increases of forward connections reflect novel sensory

information (encoded in prediction errors) in lower cortical areas. More persistent changes in backward connections in contrast encode the preceding sensory context (i.e. the recent occurrence of the deviant), which persist for a number of repetitions.

7.4.4 NMDAR blockade has regionally specific effects on intrinsic connectivity

NMDARs are prevalent in the supragranular cortical layers, suggesting particular relevance of NMDAR transmission to backward connections in the cortical hierarchy, as they target superficial layers (Rosier et al., 1993). However, NMDAR are unevenly distributed across cortical interneuron subtypes, indicating that the overall effects of systematic NMDAR-blockade may be better represented in regionally-specific intrinsic coupling changes (excitatory, or inhibitory), corresponding to localised sub-population effects, rather than intrinsic coupling (Moreau and Kullmann, 2013).

In this study, changes in a limited set of regional intrinsic connections best explain the ketamine effects, with strongest effects in a single connection type: inhibitory interneurons to spiny stellate interneurons. This is one of the links between fast-oscillating superficial and slow-oscillating deep neuronal oscillators of cortical microcircuits (Bastos et al., 2015). This effect is region specific: Ketamine causes a decrease in inhibitory interneuron to spiny stellate inhibition in STG, but an increase in IFG, indicating a relative disinhibition of the IFG. My findings contain within them a replication of Schmidt et al. (Schmidt et al., 2013), who considered a subset of model parameters for the ketamine effect. They identified a single forward connection as the ketamine-induced change in connectivity during a roving oddball paradigm. However, in this more comprehensive model space the regionally distinctive disinhibition proves a more parsimonious explanation of ketamine effects. This is furthermore in keeping with previous DCM studies of ketamine in other model organisms also implicating prefrontal regions (Moran et al., 2015; Muthukumaraswamy et al., 2015), as well as an MMN study in people with psychosis and their relatives (Ranlund et al., 2016).

Functionally, the ketamine-related reduction in prefrontal inhibition results in a constitutive increase in prefrontal excitability, or gain. Dysfunctions on gain control have been put forward as explanations for aberrant sensory processing underlying hallucinations (Friston, 2005a), explaining hallucinations as a failure to encode sensory

uncertainty. Several clinical features of disorders characterised by psychotic symptoms, including attenuated mismatch negativity, can be explained through hierarchical failures in precision encoding, as discussed in detail in Adams et al (Adams et al., 2013).

Interestingly, cell-type specific knock-outs of NMDAR on inhibitory interneurons are already used in animal models of schizophrenia (Bygrave et al., 2016; Nakazawa et al., 2017). Invasive recordings in prefrontal cortex of such mouse models suggest that the overall effect of NMDAR-transmission is an inhibitory drive (Homayoun and Moghaddam, 2007). Detailed examination of the role of NMDAR-blockade on gamma oscillations (known to be abnormal in schizophrenia), also showed the effect to be mediated through inhibitory interneurons (Carlén et al., 2012). Although – by design – my study focussed on evoked and not oscillatory responses, it is worth noting the convergence on inhibitory dysfunction in these optogenetic mouse models, and in other EEG studies in human subjects (e.g. (Carlén et al., 2012; Homayoun and Moghaddam, 2007; Umbricht et al., 2000)). The regional specificity of the effects described here at the source level is furthermore mirrored by a literature on topographically specific impairments in schizophrenia (Baldeweg et al., 2002; Baldeweg and Hirsch, 2015). Prefrontal inhibitory interneuron dysfunction has also emerged as a potential mechanism underlying other features of schizophrenia (Cohen et al., 2015; Lewis et al., 2005), further supported by computational models of prefrontal cortex function (John D. Murray et al., 2014).

The focus of this study was to relate pharmacological perturbation of brain function with measurable ERP modulations. The results concerning the localisable effects of NMDAR-blockade have clear implications for NMDAR-focussed hypotheses of schizophrenia. Whilst previous studies have shown a link between MMN measures of abnormal physiology in schizophrenia and psychopathology (Umbricht et al., 2002), I have not specifically addressed psychopathology in the test subjects here. Previous studies have shown that MMN features (Thiebes et al., 2017) or MMN-derived DCM parameters (Schmidt et al., 2013) during ketamine exposure correlate with different aspects of psychopathology, which is clearly an important area of future research.

7.4.5 Limitations

This study uses complex dynamic causal models on low-density EEG, limiting robust source localisation without prior assumptions. Here, I am assuming cortical sources to be located at previously identified MNI coordinates (Auksztulewicz and Friston, 2015; G.K.

Cooray et al., 2015; Garrido et al., 2008; Phillips et al., 2015), focussing on exploring processing dynamics rather than MMN topology.

Bayesian model selection – as used in this study – can only provide relative evidence of models that are actually included in the model space. A more parsimonious explanation of the data may exist, but I cannot comment on alternative hypotheses that are not included explicitly. I chose the model space carefully, based on the MMN literature to (a) accommodate previous findings on repetition suppression and (b) test specific hypotheses about the effects of ketamine in this setting. In short, I cannot draw conclusions about whether other models may offer better explanations for the data, however, I can argue that the model space offers a broad repertoire that includes most neurobiologically plausible hypotheses currently entertained in the literature. Secondly, because of side effects for some of the participants, the dose of ketamine had to be adjusted for subsequent subject. This additional variation is explicitly accommodated in the model (as a parametrically modulated regressor in the parametric empirical Bayesian analysis), thus allowing integration of two distinct ketamine doses compared to placebo. Furthermore, drug level monitoring was not included in the study design, thus some inter-subject variability may be accounted for by differences in drug metabolism and excretion. However, the statistical modelling used in my analysis accommodates the ensuing random (between-subject) effects.

8

Conclusion

In this thesis, I have provided an illustration of the use of a range of computational models to draw neurobiological conclusions from model systems and datasets focussed on neurodevelopmental disorders. I have specifically focussed the research projects on examples where a single molecular (genetic, autoimmune, or pharmacological) mechanism has profound effects on neuronal dynamics. With this approach, I have obtained neurobiological insights that are specific to the neurodevelopmental condition that is being modelled in the particular experiment (discussed in more detail in Chapters 4-7), which I summarise briefly below.

8.1 Summary of main findings

- Chapter 4: Temperature-dependent gating abnormalities in an epilepsy-associated voltage-gated sodium channel variant confers a mixed loss-of-function, and a gain-of-function effect in an *in-silico* model of cortical neurons.
- Chapter 4**:** These gating abnormalities allows neurons carrying the mutant channel to continue firing at abnormally high input levels – a possible mechanism underlying the temperature-dependent seizure susceptibility this mutation confers in patients.
- Chapter 5: Dynamic causal modelling of synaptic coupling in PTZ-induced seizures in zebrafish larvae reveals that global synchronisation of brain-wide

activity can be explained largely by local, regional-specific changes in synaptic coupling.

- Chapter 5: The synaptic changes during seizures in zebrafish evolve cyclically over time, associated with specific spectral profiles at different time points in the seizure
- Chapter 6: In paediatric patients with NMDAR-Ab encephalitis, paroxysmal EEG abnormalities can be modelled with just a few key parameters describing the dynamics of intracortical synaptic coupling.
- Chapter 6: In a corresponding mouse model of NMDAR-Ab encephalitis, exposure to the antibodies sensitise the cortical circuitry to abnormal slow-wave paroxysms in response to additional chemoconvulsant exposure.
- Chapter 6: *In-silico* simulations reveals that small fluctuation of synaptic coupling cross a phase transition in the NMDAR-Ab model, but not the control.
- Chapter 7: NMDAR blockade with ketamine causes a reduction of MMN amplitude in healthy subjects in a placebo-controlled experiment
- Chapter 7: Network modelling of the ketamine effect reveals that it is best explained through selective prefrontal disinhibition

In addition to these main findings related to the specific neurobiological question posed within each of the empirical chapter of this thesis, these studies also provide some more general insights both in terms of the neurobiological basis of some of these neurodevelopmental disorders, and the use of computational models to link microscale pathomechanisms with macroscale phenotypic observations. It is these general principles that I will discuss in the following sections.

8.2 Multiscale pathophysiology in neurodevelopmental disorders

As indicated in Chapters 1 and 2 of this thesis, current genomic and molecular biology technologies have had a revolutionary impact on our understanding of the molecular basis of neurodevelopmental disorders. Yet from these technological advances, questions arise regarding the relationship between individual patient phenotypes and the underlying molecular disorder. In Chapters 4-7, I have used examples of empirical datasets that record phenotypic abnormalities associated with a well-defined molecular disruption. This

allowed me to explore what contribution models can make to our understanding of different phenotypic features associated with the particular molecular abnormality at hand. Across these worked examples, certain common themes about the neurobiology of some of these neurodevelopmental conditions emerge, which are discussed below.

8.2.1 Phenotypes are emergent features of complex neuronal systems

Biological systems – particularly neuronal systems – have long been recognised to be complex: Their components interact, often in non-linear ways and produce difficult to predict behaviours. Furthermore, "[c]omplex systems [...] display properties, often called "emergent properties", that are not demonstrated by their individual parts and cannot be predicted even with full understanding of the parts alone" (Aderem, 2005).

I have shown evidence of such emergent properties on a number of different scales – the changes in the neuronal firing behaviour of a simulated neuronal membrane equipped with the sodium channel dynamics of variant $Na_V1.1$ channels, coded for by a pathological *SCN1A* mutation (Chapter 4); the mostly local changes to neuronal population dynamics that give rise to global synchronous oscillatory bursts during PTZ-induced seizures in zebrafish larvae (Chapter 5); the unexpected sensitivity to small fluctuations in time constant parameters identified in the *in-silico* model of a cortical microcircuit exposed to NMDAR-Ab (Chapter 6).

Each of these was associated with features that is classically described as part of a patient phenotype: heat-induced seizures, abnormal slow wave paroxysms, abnormally synchronous activity on the EEG. Each of these would have been impossible to intuitively predict from just an analysis of the components of the system alone – either computational quantitative simulations, or model inversions allowed me to link the molecular abnormalities to the phenotypic observations. With all these features in mind, phenotypes appear as emergent features from disruptions at the molecular scale.

This has conceptual and practical implications in our approach to understanding the pathophysiology of complex neurodevelopmental disorders. First, we cannot understand the biology of a disease process with reductive approaches focussing at a single scale alone. Given the complexity of biological systems, and the number of factors we cannot experimentally control, we need to constrain our inference by integrating observations at several explanatory levels (Hood and Tian, 2012). In order to effectively do this, we need as high quality data about patient phenotypes as we have on patients' molecular biology

(e.g. genotypes) (Helbig and Lindhout, 2017). Where the specific phenotypic features can be paired with models of the underlying neurobiology this multilevel approach may not only improve our understanding of existing associations between diseases and specific molecular disruptions (Stephan et al., 2016), but also help us in establishing new such associations.

8.2.2 Single-effect disruptions at the cellular scale can have wide-spread and diverse effects on integrated neuronal systems

The aim of my work presented in this thesis was to utilise well established links between molecular disruption, and neurological/psychiatric disorders to illustrate the validity, and benefit of using specific computational modelling approaches. There is some evidence that such computational modelling approaches can identify underlying molecular pathologies from whole brain data with some specificity (Gilbert et al., 2016; Symmonds et al., 2018). Yet the picture that emerges from the studies I present in this thesis suggests a more complex picture: For example, NMDA-receptor disruption in models of NMDAR-Ab encephalitis produced broad changes in both the strength and the temporal dispersion of inhibitory as well as excitatory synaptic coupling, an effect further potentiated by the addition of the chemoconvulsant PTZ (Chapter 6); in contrast, in the ketamine model of acute psychosis, NMDA-receptor hypofunction was best described as a locally specific disinhibition in the prefrontal cortex (Chapter 7).

There are many differences in terms of the hypotheses tested, the experimental design, the model system, and the computational modelling approach between the different experiments in this thesis. However, one general observations across the different studies included in this thesis is the following: Even for interventions where the molecular effect is relatively well characterised at the molecular, or single-cell level (e.g. NMDAR antibodies), the models of integrated neuronal populations employed here often identify more than just a single effect type as underlying the phenotypic features under investigation.

In some ways this is unsurprising – NMDA receptor blockade for example blocks a single receptor-type but depending on (1) the relative distribution of NMDA/AMPA receptors, (2) the baseline NMDAR-mediated drive of inhibitory interneurons, and (3) the amount of synaptic and extra-synaptic NMDAR transmission, the net effect of NMDAR-blockade

on an integrated network can be very different. But the observation again highlights the context-dependence of even 'simple' disruptions in molecular processes – speaking to the phenotypic diversity that seem to be associated with overlapping risk factors across patient cohorts with different neurodevelopmental disorders.

Evidence of such context-dependence is already being identified through genetic methods (e.g. *CACNA1G* as modulator of epilepsy risk in a mouse model of *SCN1A*-associated Dravet syndrome). Hypotheses about what type of context changes a specific molecular process might be most sensitive to can be generated *in-silico* by exploring the stability of the dynamical systems that are being modelled (cf. Chapter 4, and Chapter 5 of this thesis).

8.3 Modelling dynamic neuronal pathologies

In the different projects that constitute the empirical component of this thesis, I rely on a range of different modelling approaches – ranging from models of neuronal membrane, to cortical microcircuit, and whole-brain network models. Whilst the specific conclusions arising from these approaches are discussed in Chapters 4-7, I will discuss some insights that span multiple of the experiments below.

8.3.1 Quantitative models link smooth parameter changes to apparently distinct states

The kind of models used in this thesis (Hodgkin-Huxley type conductance models of neuronal membranes, Chapter 4; convolution-based neural mass models, Chapters 5-7) are based on ordinary differential equations that describe the flow of interacting systems in time. All of them contain a nonlinear mapping between input and the neuronal states – with the convolution-based models being more weakly nonlinear than the conductance based models. This combination – a coupled dynamical system with a nonlinearity is sufficient to generate a whole range of dynamic behaviours, many of which are illustrated in the thesis: the difference between fixed point and oscillatory states in Chapter 4, the critical transition identified in the NMDAR-Ab *in-silico* simulations in Chapter 6, and even the complex changes a local disinhibition produced in the models of an auditory processing network in Chapter 7.

The simple nonlinear mapping between neuronal model parameters and neuronal dynamic states has wide ranging implications: Depending on the precise parameterisation

of the model, small fluctuations in parameters may have a drastic effect on the neuronal states, whereas under different parameter combinations, even large changes in model parameters may have very limited effects on neuronal oscillatory outputs that are being modelled (most comprehensively discussed in Chapter 6 of this thesis). This feature of dynamical systems bears a deep relationship to how we understand brain dynamics to date. For example, even quite drastic changes in EEG dynamics – such as the appearance of a posterior dominant rhythm, or the change between qualitatively very distinct sleep stages – can appear very suddenly without drastic changes to synaptic parameters. From the dynamical systems approach illustrated throughout this thesis, we can conclude that the same qualitative neurobiology (i.e. the same model architecture, with the same types of parameters at play) can support very distinct appearing states through gradual changes such as neuromodulation (i.e. small changes in the parameters of the model system).

Whilst the nonlinearities in these neuronal models (particularly in the case of the conductance models) make model inversion challenging, the insight that dynamical systems can produce distinctive states from (neurobiologically plausible) smooth transitions in parameters makes them an appropriate model for these neurobiological questions. This insight in itself is not new (Breakspear, 2005; Phillips and Robinson, 2007), the meaningful results provided by linking these modelling approaches to quantitative data of human pathophysiology makes this a promising avenue of further research.

8.3.2 Modelling neuronal dynamics across multiple temporal scales

In the model-based inference presented here, I was interested in how pathological processes (such as a genetic mutation, or antibodies against particular neuronal surface targets) entrain the dynamical system and relate to observable, quantitative features in the associated phenotypes (such as particular EEG patterns). The principal assumption in this modelling approach is that disruptions in the molecular neurobiology cause persistent changes in the parameters of the model (e.g. the excitatory coupling between different neuronal populations), which in turn makes certain neuronal states (e.g. specific oscillatory patterns) more or less likely to occur. This is illustrated e.g. by Chapter 7 of this thesis, where the experimental factors (standard vs. deviant sound; placebo vs. ketamine condition) are represented as discrete modulations of the network model parameters.

In contrast, for some other experimental designs (e.g. the PTZ exposure as an experimental factor in Chapters 5 and 6), the system parameters are not organised into discrete

conditions, but rather change slowly over time – giving rise to transient excursions into abnormal dynamic regimes, such as seizure activity. Elsewhere such processes – fast changing neuronal states that are constrained by a slowly changing synaptic parameters – is modelled through an adiabatic separation of time scales of multiple neuronal states, i.e. the slowly changing process is so slow that within short time windows they can be assumed to be stationary (Jirsa et al., 2014).

Such models with separate dynamics in their neuronal states can provide in-depth insights into the dynamic regimes that the model can operate under through simulations (Jirsa et al., 2017; Petkoski et al., 2016), but they are challenging to invert based on empirical data, because long recordings (and many data points) would have to be inverted in a single model inversion, tracking multiple types of neuronal states – quickly making such model inversions computationally intractable (although some processes, such as Kalman filters can alleviate some of the computational constraints (Schiff and Sauer, 2008)).

An alternative approach developed by my collaborators and me is the complete separation of fast and slow states into (1) neuronal states (included in a steady state dynamical model), constrained by (2) parameters that fluctuate slowly over successive epochs or time-windows. This approach has been particularly useful when modelling seizure activity (Papadopoulou et al., 2017), or where the experimental design includes time varying interventions (such a PTZ injection with known pharmacokinetics). This has been made possible by recent developments in the computationally efficient Bayesian inversion of hierarchically structured dynamic causal models, originally designed for group studies (Friston et al., 2015).

This approach is useful not only in the application shown in the applications reviewed in this thesis (Chapter 5, Chapter 6), but also more broadly for research in neurodevelopmental disorders. For the purposes of this thesis, I have not specifically investigated the developmental aspects of neurodevelopmental disorder – clearly, studies over longitudinal datasets will be invaluable for deriving an account of how synaptic coupling underlying, e.g. particular EEG phenomena, changes in development and diverges between disease groups. The computational approach that allowed me to track slow synaptic variations across the duration of a single experiment can be used on those datasets to identify age-specific and longitudinal effects. With the current establishment of large, developmental, public multimodal EEG and phenotyping datasets for patients with

neurodevelopmental disorders and healthy controls (Di Martino et al., 2017; Langer et al., 2017), methods that can comprehensively capture dynamic changes across computational models of neuronal dynamics will be essential for future research into the neurobiological basis of neurodevelopmental disorders.

8.4 Future directions

The empirical work presented in the chapters of this thesis covered a broad range of computational models (Hodgkin-Huxley models of the neuronal membrane, neural mass models of single microcircuits, and network models of whole brain function); a diversity of data of neuronal function (local field potentials, light-sheet calcium imaging, EEG); and a broad range of models pertinent to different neurodevelopmental conditions (early infantile epilepsies, NMDA receptor antibody encephalitis, acute psychosis and schizophrenia). There is therefore a huge number of possible directions into which this work could continue in the future, a selection of which I will outline here.

8.4.1 Translational neuroscience through computational models

Animal models and other model systems are essential to improving our understanding of neurodevelopmental disorders, and in fact were incorporated in Chapter 4, 5, and 6 of this thesis. Yet many observations from the animal models do not translate easily into human studies, or even clinical practice. This may relate to neurobiological differences between the model systems that do not allow for easy interpretation of shared phenotypic features – e.g. a synaptic change that could cause epileptic seizures in human patients may have no easily detectable ictal phenotype in an animal model.

Computational models can act as a bridge between clinical observations and experimentally controlled data that other disease models can yield. With the work illustrated in this thesis, I have but scratched the surface of the potential of quantitatively exploring the effects of human disease-causing mutations. For early infantile epilepsies alone, we now routinely sequence >100 genes per patient attending the clinic (Oates et al., 2018; Trump et al., 2016) – each of which with likely more than one reported pathogenic mutation.

Characterising a broader range of such genetic mutations in conjunction with associated animal models may offer a better mapping between human and animal model phenotypes

– as computational models may show that data features that appear quite different in calcium imaging in zebrafish, and in EEG recordings in human patients may in fact be caused by similar synaptic mechanism revealed by computational models such those considered in this thesis. Identifying such shared mechanisms between human patients and animal models is a necessary first step when testing possible future new therapies and the focus of ongoing future research.

8.4.2 Quantitative models of mechanistic phenotypes in patients

The chapters concerning the analysis of human EEG data (Chapters 5, 6) showcase the amount of additional information contained in non-invasive, quantitative recordings of human brain function. Classically analysis of clinical EEG has focussed on visual feature detection and qualitative reporting of abnormalities (e.g. the presence or absence of epileptiform activity), there is scope to utilise routine clinical EEG recordings in more model-based investigations.

Bayesian model inference strategies (such as dynamic causal modelling) allow the quantitative link of EEG phenotypes and biophysically plausible models of neuronal (dys)function. Especially where there are particular informed hypotheses that may explain particular epileptic phenotypes (e.g. an interneuron-specific disruption in patients with *SCN1A* (Favero et al., 2018)), we can provide evidence for the explanatory potential of such hypotheses directly from human EEG data. Taken together with other lines of evidence – this approach may help us distinguish epiphenomena from actual pathophysiology, and target interventions appropriately to markers of pathophysiological mechanisms.

8.4.3 Building predictive models for therapeutic interventions

Ultimately one of the aims of translational neuroscience, and the neuroscience of human disorders is to inform novel strategies for the treatment of human conditions. Yet whilst there are a multitude of possible interventions that show promise from pre-clinical animal and disease model trials (Griffin et al., 2017), translation to wide-spread human use remains challenging – in part because it is challenging *a priori* to identify from all promising strategies those that are most likely to work and prioritise them for clinical studies.

Using computational models that (1) explain phenotypic features across different disease models through identifying a shared pathomechanisms and (2) can generate predictions

of how the system responds after intervention may offer a promising novel approach to this problem. There is some evidence, for example, that computational models of epileptogenic networks can help predict the outcome following epilepsy surgery (Sinha et al., 2017; Taylor et al., 2018). Such models have the promise to allow us to use inexpensive *in-silico* simulations to prioritise those most promising (more expensive and time-consuming) *in-vivo* experiments, when developing novel therapies.

Bibliography

Aburn, M.J., Holmes, C.A., Roberts, J.A., Boonstra, T.W., Breakspear, M., (2012). Critical Fluctuations in Cortical Models Near Instability. *Front. Physiol.* **3**, 331.

Adachi, N., Alarcon, G., Binnie, C.D., Elwes, R.D.C., Polkey, C.E., et al., (1998). Predictive value of interictal epileptiform discharges during non-REM sleep on scalp EEG recordings for the lateralization of epileptogenesis. *Epilepsia* **39**, 628–632.

Adams, R.A., Stephan, K.E., Brown, H.R., Frith, C.D., Friston, K.J., (2013). The Computational Anatomy of Psychosis. *Front. Psychiatry* **4**, 1–26.

Aderem, A., (2005). Systems biology: Its practice and challenges. *Cell* **121**, 511–513.

Adler, S., Lorio, S., Jacques, T.S., Benova, B., Gunny, R., et al., (2017). Towards in vivo focal cortical dysplasia phenotyping using quantitative MRI. *NeuroImage Clin.* **15**, 95–105.

Afrikanova, T., Serruys, A.S.K., Buenafe, O.E.M., Clinckers, R., Smolders, I., et al., (2013). Validation of the Zebrafish Pentylenetetrazol Seizure Model: Locomotor versus Electrographic Responses to Antiepileptic Drugs. *PLoS One* **8**, 1–9.

Ahrens, M.B., Orger, M.B., Robson, D.N., Li, J.M., Keller, P.J., (2013). Whole-brain functional imaging at cellular resolution using light-sheet microscopy. *Nat. Methods* **10**, 413–420.

Akbarian, S., Sucher, N.J., Bradley, D., Tafazzoli, A., Trinh, D., et al., (1996). Selective alterations in gene expression for NMDA receptor subunits in prefrontal cortex of schizophrenics. *J. Neurosci.* **16**, 19–30.

Anticevic, A., Gancsos, M., Murray, J.D., Repovs, G., Driesen, N.R., et al., (2012). NMDA receptor function in large-scale anticorrelated neural systems with implications for cognition and schizophrenia. *Proc. Natl. Acad. Sci.* **109**, 16720–16725.

Asato, M.R., Terwilliger, R., Woo, J., Luna, B., (2010). White matter development in adolescence: A DTI study. *Cereb. Cortex* **20**, 2122–2131.

Auksztulewicz, R., Friston, K., (2016). Repetition suppression and its contextual determinants in predictive coding. *Cortex* **80**, 125–140.

Auksztulewicz, R., Friston, K., (2015). Attentional Enhancement of Auditory Mismatch Responses: a DCM/MEG Study. *Cereb. Cortex* **25**, 4273–4283.

Babajani-Feremi, A., Soltanian-Zadeh, H., (2010). Multi-area neural mass modeling of EEG and MEG signals. *Neuroimage* **52**, 793–811.

Baldeweg, T., Hirsch, S.R., (2015). Mismatch negativity indexes illness-specific impairments of cortical plasticity in schizophrenia: A comparison with bipolar disorder and Alzheimer's disease. *Int. J. Psychophysiol.* **95**, 145–155.

Baldeweg, T., Klugman, A., Gruzelier, J.H., Hirsch, S.R., (2002). Impairment in frontal but not temporal components of mismatch negativity in schizophrenia. *Int. J. Psychophysiol.* **43**, 111–122.

Baraban, S.C., Dinday, M.T., Hortopan, G.A., (2013). Drug screening in Scn1a zebrafish mutant identifies clemizole as a potential Dravet syndrome treatment. *Nat. Commun.*

4, 2410.

Baraban, S.C., Taylor, M.R., Castro, P.A., Baier, H., (2005). Pentylenetetrazole induced changes in zebrafish behavior, neural activity and c-fos expression. *Neuroscience* **131**, 759–768.

Bastos, A.M., Litvak, V., Moran, R., Bosman, C.A., Fries, P., et al., (2015). A DCM study of spectral asymmetries in feedforward and feedback connections between visual areas V1 and V4 in the monkey. *Neuroimage* **108**, 460–475.

Bastos, A.M., Usrey, W.M., Adams, R.A., Mangun, G.R., Fries, P., et al., (2012). Canonical Microcircuits for Predictive Coding. *Neuron* **76**, 695–711.

Baude, A., Nusser, Z., Roberts, J.D.B., Mulvihill, E., Jeffrey Mcllhinney, R.A., et al., (1993). The metabotropic glutamate receptor (mGluRlα) is concentrated at perisynaptic membrane of neuronal subpopulations as detected by immunogold reaction. *Neuron* **11**, 771–787.

Beenhakker, M.P., Huguenard, J.R., (2009). Neurons that fire together also conspire together: is normal sleep circuitry hijacked to generate epilepsy? *Neuron* **62**, 612–632.

Ben-Ari, Y., Khalilov, I., Kahle, K.T., Cherubini, E., (2012). The GABA excitatory/inhibitory shift in brain maturation and neurological disorders. *Neurosci.* **18**, 467–86.

Ben-Shalom, R., Keeshen, C.M., Berrios, K.N., An, J.Y., Sanders, S.J., et al., (2017). Opposing Effects on NaV1.2 Function Underlie Differences Between SCN2A Variants Observed in Individuals With Autism Spectrum Disorder or Infantile Seizures. *Biol. Psychiatry* **82**, 224–232.

Berg, A.T., Berkovic, S.F., Brodie, M.J., Buchhalter, J., Cross, J.H., et al., (2010). Revised terminology and concepts for organization of seizures and epilepsies: Report of the ILAE Commission on Classification and Terminology, 2005-2009. *Epilepsia* **51**, 676–685.

Berg, A.T., Rychlik, K., (2015). The course of childhood-onset epilepsy over the first two decades: A prospective, longitudinal study. *Epilepsia* **56**, 40–48.

Berkovic, S.F., Howell, R.A., Hay, D.A., Hopper, J.L., (1998). Epilepsies in twins: Genetics of the major epilepsy syndromes. *Ann. Neurol.* **43**, 435–445.

Betzel, R.F., Erickson, M.A., Abell, M., O'Donnell, B.F., Hetrick, W.P., et al., (2012). Synchronization dynamics and evidence for a repertoire of network states in resting EEG. *Front. Comput. Neurosci.* **6**, 1–13.

Bhatt, M.B., Bowen, S., Rossiter, H.E., Dupont-Hadwen, J., Moran, R.J., et al., (2016). Computational modelling of movement-related beta-oscillatory dynamics in human motor cortex. *Neuroimage* **133**, 224–232.

Bhattacharya, B. Sen, Bond, T.P., O'Hare, L., Turner, D., Durrant, S.J., (2016). Causal Role of Thalamic Interneurons in Brain State Transitions: A Study Using a Neural Mass Model Implementing Synaptic Kinetics. *Front. Comput. Neurosci.* **10**, 1–18.

Blakemore, S.J., Choudhury, S., (2006). Development of the adolescent brain: Implications for executive function and social cognition. *J. Child Psychol. Psychiatry Allied Discip.* **47**, 296–312.

Blenkinsop, A., Valentin, A., Richardson, M.P., Terry, J.R., (2012). The dynamic evolution of focal-onset epilepsies - combining theoretical and clinical observations. *Eur. J. Neurosci.* **36**, 2188–2200.

Boly, M., Moran, R., Murphy, M., Boveroux, P., Bruno, M. -a., et al., (2012). Connectivity Changes Underlying Spectral EEG Changes during Propofol-Induced Loss of Consciousness. *J. Neurosci.* **32**, 7082–7090.

Bond, T., Durrant, S., O'Hare, L., Turner, D., Sen-Bhattacharya, B., (2014). Studying the effects of thalamic interneurons in a thalamocortical neural mass model. *BMC Neurosci.* **15**, P219.

Bourgeois, J.P., Jastreboff, P.J., Rakic, P., (1989). Synaptogenesis in visual cortex of normal and preterm monkeys: evidence for intrinsic regulation of synaptic overproduction. *Proc. Natl. Acad. Sci.* **86**, 4297–4301.

Bourgeois, J.P., Rakic, P., (1993). Changes of synaptic density in the primary visual cortex of the macaque monkey from fetal to adult stage. *J. Neurosci.* **13**, 2801–2820.

Boys, A., Farrell, M., Taylor, C., Marsden, J., Goodman, R., et al., (2003). Psychiatric morbidity and substance use in young people aged 13 – 15 years : results from the Child and Adolescent Survey of Mental Health. *Br. J. Psychiatry* **182**, 509–517.

Bragin, A., Penttonen, M., Buzsáki, G., (1997). Termination of epileptic afterdischarge in the hippocampus. *J. Neurosci.* **17**, 2567–2579.

Breakspear, M., (2005). A Unifying Explanation of Primary Generalized Seizures Through Nonlinear Brain Modeling and Bifurcation Analysis. *Cereb. Cortex* **16**, 1296–1313.

Breakspear, M., Roberts, G., Green, M.J., Nguyen, V.T., Frankland, A., et al., (2015). Network dysfunction of emotional and cognitive processes in those at genetic risk of bipolar disorder. *Brain* **138**, 3427–3439.

Brodersen, K.H., Schofield, T.M., Leff, A.P., Ong, C.S., Lomakina, E.I., et al., (2011). Generative Embedding for Model-Based Classification of fMRI Data. *PLoS Comput. Biol.* **7**, e1002079.

Brown, H.R., Friston, K.J., (2013). The functional anatomy of attention: a DCM study. *Front. Hum. Neurosci.* **7**, 784.

Bruck, I., Antoniuk, S.A., Spessatto, A., Bem, R.S. de, Hausberger, R., et al., (2001). Epilepsy in children with cerebral palsy. *Arq. Neuropsiquiatr.* **59**, 35–39.

Buchmann, A., Ringli, M., Kurth, S., Schaerer, M., Geiger, A., et al., (2011). EEG sleep slow-wave activity as a mirror of cortical maturation. *Cereb. Cortex* **21**, 607–615.

Bullmore, E., Sporns, O., (2009). Complex brain networks: graph theoretical analysis of structural and functional systems. *Nat. Rev. Neurosci.* **10**, 186–198.

Burns, S.P., Santaniello, S., Yaffe, R.B., Jouny, C.C., Crone, N.E., et al., (2014). Network dynamics of the brain and influence of the epileptic seizure onset zone. *Proc. Natl. Acad. Sci.* **111**, E5321–E5330.

Buzsáki, G., Anastassiou, C. a, Koch, C., (2012). The origin of extracellular fields and currents — EEG, ECoG, LFP and spikes. *Nat. Rev. Neurosci.* **13**, 407–420.

Bygrave, A.M., Masiulis, S., Nicholson, E., Berkemann, M., Barkus, C., et al., (2016).

Knockout of NMDA-receptors from parvalbumin interneurons sensitizes to schizophrenia-related deficits induced by MK-801. *Transl. Psychiatry* **6**, e778–e778.

Canolty, R.T., Knight, R.T., (2010). The functional role of cross-frequency coupling. *Trends Cogn. Sci.* **14**, 506–515.

Capes, D.L., Goldschen-Ohm, M.P., Arcisio-Miranda, M., Bezanilla, F., Chanda, B., (2013). Domain IV voltage-sensor movement is both sufficient and rate limiting for fast inactivation in sodium channels. *J. Gen. Physiol.* **142**, 101–112.

Carandini, M., (2012). From circuits to behavior: a bridge too far? *Nat. Neurosci.* **15**, 507–509.

Cardno, A., Marshall, E.J.E., Coid, B., Macdonald, A.M., Ribchester, T.R., et al., (1999). Heritability Estimates for Psychotic Disorders. *Arch. Gen. Psychiatry* **56**, 162.

Carlén, M., Meletis, K., Siegle, J.H., Cardin, J.A., Futai, K., et al., (2012). A critical role for NMDA receptors in parvalbumin interneurons for gamma rhythm induction and behavior. *Mol. Psychiatry* **17**, 537–548.

Catterall, W. a., Raman, I.M., Robinson, H.P.C., Sejnowski, T.J., Paulsen, O., (2012). The Hodgkin-Huxley Heritage: From Channels to Circuits. *J. Neurosci.* **32**, 14064–14073.

Catterall, W. a, Kalume, F., Oakley, J.C., (2010). Na V 1.1 channels and epilepsy. *J. Physiol.* **588**, 1849–1859.

Ceulemans, B., Boel, M., Claes, L., Dom, L., Willekens, H., et al., (2004). Severe Myoclonic Epilepsy in Infancy: Toward an Optimal Treatment. *J. Child Neurol.* **19**, 516–521.

Cha, A., Ruben, P.C., George, A.L., Fujimoto, E., Bezanilla, F., (1999). Voltage sensors in domains III and IV, but not I and II, are immobilized by Na+ channel fast inactivation. *Neuron* **22**, 73–87.

Chan, A.W., Mohajerani, M.H., LeDue, J.M., Wang, Y.T., Murphy, T.H., (2015). Mesoscale infraslow spontaneous membrane potential fluctuations recapitulate high-frequency activity cortical motifs. *Nat. Commun.* **6**, 7738.

Chanda, B., (2004). Coupling Interactions between Voltage Sensors of the Sodium Channel as Revealed by Site-specific Measurements. *J. Gen. Physiol.* **123**, 217–230.

Chanda, B., (2002). Tracking Voltage-dependent Conformational Changes in Skeletal Muscle Sodium Channel during Activation. *J. Gen. Physiol.* **120**, 629–645.

Chaudhuri, R., Bernacchia, A., Wang, X.-J., (2014). A diversity of localized timescales in network activity. *Elife* **3**, e01239.

Chen, T.-W., Wardill, T.J., Sun, Y., Pulver, S.R., Renninger, S.L., et al., (2013). Ultrasensitive fluorescent proteins for imaging neuronal activity. *Nature* **499**, 295–300.

Chen, W., Liu, J., Zhang, L., Xu, H., Guo, X., et al., (2015). Generation of the SCN1A epilepsy mutation in hiPS cells using the TALEN technique. *Sci. Rep.* **4**, 5404.

Chen, X., Mu, Y., Hu, Y., Kuan, A.T., Randlett, O., et al., (2018). Brain-wide organization of neuronal activity in larval zebrafish. *bioRxiv* **289413**, 1–38.

Cheour, M., H.T. Leppänen, P., Kraus, N., (2000). Mismatch negativity (MMN) as a tool for investigating auditory discrimination and sensory memory in infants and

children. *Clin. Neurophysiol.* **111**, 4–16.

Chiron, C., Dulac, O., (2011). The pharmacologic treatment of Dravet syndrome. *Epilepsia* **52**, 72–75.

Chowdhury, F.A., Woldman, W., FitzGerald, T.H.B., Elwes, R.D.C., Nashef, L., et al., (2014). Revealing a brain network endophenotype in families with idiopathic generalised epilepsy. *PLoS One* **9**, e110136.

Chugani, H.T., Asano, E., Sood, S., (2010). Infantile spasms: Who are the ideal surgical candidates? *Epilepsia* **51**, 94–96.

Claes, L., Del-Favero, J., Ceulemans, B., Lagae, L., Van Broeckhoven, C., et al., (2001). De novo mutations in the sodium-channel gene SCN1A cause severe myoclonic epilepsy of infancy. *Am. J. Hum. Genet.* **68**, 1327–1332.

Cohen, S.M., Tsien, R.W., Goff, D.C., Halassa, M.M., (2015). The impact of NMDA receptor hypofunction on GABAergic neurons in the pathophysiology of schizophrenia. *Schizophr. Res.* **167**, 98–107.

Commission on Classification and Terminology of the International League Against Epilepsy, (1989). Proposal for Revised Classification of Epilepsies and Epileptic Syndromes. *Epilepsia* **30**, 389–399.

Cooray, G.K., Garrido, M.I., Brismar, T., Hyllienmark, L., (2015). The maturation of mismatch negativity networks in normal adolescence. *Clin. Neurophysiol.* **127**, 520–529.

Cooray, G.K., Sengupta, B., Douglas, P., Englund, M., Wickstrom, R., et al., (2015). Characterising seizures in anti-NMDA-receptor encephalitis with dynamic causal modelling. *Neuroimage* **118**, 508–19.

Cooray, G.K., Sengupta, B., Douglas, P.K., Friston, K., (2016). Dynamic causal modelling of electrographic seizure activity using Bayesian belief updating. *Neuroimage* **125**, 1142–1154.

Courchesne, E., (1990). Chronology of postnatal human brain development: Event-related potential, positron emission tomography, myelinogenesis, and synaptogenesis studies., in: Rohrbaugh, J.W., Parasuraman, R., Johnson, R. (Eds.), Event-Related Brain Potentials: Basic Issues and Applications. Oxford University Press, New York, NY, pp. 210–41.

Crisp, S.J., Kullmann, D.M., Vincent, A., (2016). Autoimmune synaptopathies. *Nat. Rev. Neurosci.* **17**, 103–117.

Csercsa, R., Dombovári, B., Fabó, D., Wittner, L., Erss, L., et al., (2010). Laminar analysis of slow wave activity in humans. *Brain* **133**, 2814–2829.

D'Agostino, A., Castelnovo, A., Cavallotti, S., Casetta, C., Marcatili, M., et al., (2018). Sleep endophenotypes of schizophrenia: slow waves and sleep spindles in unaffected first-degree relatives. *npj Schizophr.* **4**, 2.

Dalmau, J., Gleichman, A.J., Hughes, E.G., Rossi, J.E., Peng, X., et al., (2008). Anti-NMDA-receptor encephalitis: case series and analysis of the effects of antibodies. *Lancet Neurol.* **7**, 1091–1098.

Dalmau, J., Tüzün, E., Wu, H.Y., Masjuan, J., Rossi, J.E., et al., (2007). Paraneoplastic anti-

N-methyl-D-aspartate receptor encephalitis associated with ovarian teratoma. *Ann. Neurol.* **61**, 25–36.

David, O., Friston, K.J., (2003). A neural mass model for MEG/EEG: *Neuroimage* **20**, 1743–1755.

Dayan, P., Hinton, G.E., Neal, R.M., Zemel, R.S., (1995). The Helmholtz Machine. *Neural Comput.* **7**, 889–904.

Deciphering Developmental Disorders Study, (2017). Prevalence and architecture of de novo mutations in developmental disorders. *Nature* **542**, 433–438.

DeLisi, L.E., (2008). The concept of progressive brain change in schizophrenia: Implications for understanding schizophrenia. *Schizophr. Bull.* **34**, 312–321.

Demontis, D., Nyegaard, M., Buttenschøn, H.N., Hedemand, A., Pedersen, C.B., et al., (2011). Association of GRIN1 and GRIN2A-D With schizophrenia and genetic interaction with maternal herpes simplex virus-2 infection affecting disease risk. *Am. J. Med. Genet. Part B Neuropsychiatr. Genet.* **156**, 913–922.

Deoni, S.C.L., Dean, D.C., O'Muircheartaigh, J., Dirks, H., Jerskey, B. a, (2012). Investigating white matter development in infancy and early childhood using myelin water faction and relaxation time mapping. *Neuroimage* **63**, 1038–53.

Depaulis, A., David, O., Charpier, S., (2015). The genetic absence epilepsy rat from Strasbourg as a model to decipher the neuronal and network mechanisms of generalized idiopathic epilepsies. *J. Neurosci. Methods* 1–16.

Dhamija, R., Patterson, M.C., Wirrell, E.C., (2012). Epilepsy in children-when should we think neurometabolic disease? *J. Child Neurol.* **27**, 663–671.

Dhindsa, R.S., Goldstein, D.B., (2015). Genetic Discoveries Drive Molecular Analyses and Targeted Therapeutic Options in the Epilepsies. *Curr. Neurol. Neurosci. Rep.* **15**, 70.

Di Lollo, V., (2012). The feature-binding problem is an ill-posed problem. *Trends Cogn. Sci.* **16**, 317–321.

Di Martino, A., O'Connor, D., Chen, B., Alaerts, K., Anderson, J.S., et al., (2017). Enhancing studies of the connectome in autism using the autism brain imaging data exchange II. *Sci. Data* **4**, 1–15.

Dima, D., Frangou, S., Burge, L., Braeutigam, S., James, A.C., (2012). Abnormal intrinsic and extrinsic connectivity within the magnetic mismatch negativity brain network in schizophrenia: A preliminary study. *Schizophr. Res.* **135**, 23–27.

Dinday, M.T., Baraban, S.C., (2015). Large-Scale Phenotype-Based Antiepileptic Drug Screening in a Zebrafish Model of Dravet Syndrome. *eNeuro* **2**, 1–19.

Do, C.B., Batzoglou, S., (2008). What is the expectation maximization algorithm? *Nat. Biotechnol.* **26**, 897–899.

Donnelly, P., Barroso, I., Blackwell, J.M., Bramon, E., Brown, M.A., et al., (2012). Genome-Wide Association Study Implicates HLA-C*01:02 as a Risk Factor at the Major Histocompatibility Complex Locus in Schizophrenia. *Biol. Psychiatry* **72**, 620–628.

Du, J., Vegh, V., Reutens, D.C., (2012). The Laminar Cortex Model: A New Continuum Cortex Model Incorporating Laminar Architecture. *PLoS Comput. Biol.* **8**, e1002733.

Du, W., Bautista, J.F., Yang, H., Diez-Sampedro, A., You, S.-A., et al., (2005). Calcium-sensitive potassium channelopathy in human epilepsy and paroxysmal movement disorder. *Nat. Genet.* **37**, 733–738.

Dunn, T.W., Mu, Y., Narayan, S., Randlett, O., Naumann, E. a., et al., (2016). Brain-wide mapping of neural activity controlling zebrafish exploratory locomotion. *Elife* **5**, 1–29.

Dutta, S., Sengupta, P., (2016). Men and mice: Relating their ages. *Life Sci.* **152**, 244–248.

Eadie, M.J., Bladin, P.F., (2001). A Disease Once Sacred. A History of the Medical Understanding of Epilepsy, 1st ed. John Libbey & Co Ltd, New Barnet.

Eisermann, M., Kaminska, A., Moutard, M.-L., Soufflet, C., Plouin, P., (2013). Normal EEG in childhood: From neonates to adolescents. *Neurophysiol. Clin. Neurophysiol.* **43**, 35–65.

Epi4K Consortium, Epilepsy Phenome/Genome Project, (2013). De novo mutations in epileptic encephalopathies. *Nature* **501**, 217–221.

Erskine, H.E., Moffitt, T.E., Copeland, W.E., Costello, E.J., Ferrari, A.J., et al., (2015). A heavy burden on young minds: the global burden of mental and substance abuse disorders in children and youth. *Psychol. Med.* **45**, 1551–1563.

Escayg, A., MacDonald, B.T., Meisler, M.H., Baulac, S., Huberfeld, G., et al., (2000). Mutations of SCN1A, encoding a neuronal sodium channel, in two families with GEFS+2. *Nat. Genet.* **24**, 343–345.

Farber, N.B., Kim, S.H., Dikranian, K., Jiang, X.P., Heinkel, C., (2002). Receptor mechanisms and circuitry underlying NMDA antagonist neurotoxicity. *Mol. Psychiatry* **7**, 32–43.

Favero, M., Sotuyo, N.P., Lopez, E., Kearney, J.A., Goldberg, E.M., (2018). A transient developmental window of fast-spiking interneuron dysfunction in a mouse model of Dravet syndrome. *J. Neurosci.* **38**, 0193-18.

Feinberg, I., Campbell, I.G., (2010). Sleep EEG changes during adolescence: An index of a fundamental brain reorganization. *Brain Cogn.* **72**, 56–65.

Feld, G.B., Lange, T., Gais, S., Born, J., (2013). Sleep-Dependent Declarative Memory Consolidation—Unaffected after Blocking NMDA or AMPA Receptors but Enhanced by NMDA Coagonist D-Cycloserine. *Neuropsychopharmacology* **38**, 2688–2697.

Fellin, T., Ellenbogen, J.M., De Pittà, M., Ben-Jacob, E., Halassa, M.M., (2012). Astrocyte regulation of sleep circuits: experimental and modeling perspectives. *Front. Comput. Neurosci.* **6**, 1–10.

Fenton, W.S., (1991). Natural History of Schizophrenia Subtypes. *Arch. Gen. Psychiatry* **48**, 978.

Fish, B., Kendler, K.S., (2005). Abnormal Infant Neurodevelopment Predicts Schizophrenia Spectrum Disorders. *J. Child Adolesc. Psychopharmacol.* **15**, 348–361.

Fisher, H.L., Caspi, A., Poulton, R., Meier, M.H., Houts, R., et al., (2013). Specificity of childhood psychotic symptoms for predicting schizophrenia by 38 years of age: A birth cohort study. *Psychol. Med.* **43**, 2077–2086.

Fisher, R.S., Acevedo, C., Arzimanoglou, A., Bogacz, A., Cross, J.H., et al., (2014). ILAE Official Report: A practical clinical definition of epilepsy. *Epilepsia* **55**, 475–482.

Fisher, R.S., Boas, W. van E., Blume, W., Elger, C., Genton, P., et al., (2005). Epileptic Seizures and Epilepsy: Definitions Proposed by the International League Against Epilepsy (ILAE) and the International Bureau for Epilepsy (IBE). *Epilepsia* **46**, 470–472.

Florance, N.R., Davis, R.L., Lam, C., Szperka, C., Zhou, L., et al., (2009). Anti-N-methyl-D-aspartate receptor (NMDAR) encephalitis in children and adolescents. *Ann. Neurol.* **66**, 11–18.

Fransson, P., Skiold, B., Horsch, S., Nordell, A., Blennow, M., et al., (2007). Resting-state networks in the infant brain. *Proc. Natl. Acad. Sci.* **104**, 15531–15536.

Freedman, R., Coon, H., Myles-Worsley, M., Orr-Urtreger, A., Olincy, A., et al., (1997). Linkage of a neurophysiological deficit in schizophrenia to a chromosome 15 locus. *Proc. Natl. Acad. Sci.* **94**, 587–592.

Freeman, W.J., (2000a). Mesoscopic brain dynamics. *Scholarpedia* **7**, 1–11.

Freeman, W.J., (2000b). Neurodynamics: An Exploration in Mesoscopic Brain Dynamics. Springer, London, UK.

Freestone, D.R., Karoly, P.J., Nesic, D., Aram, P., Cook, M.J., et al., (2014). Estimation of effective connectivity via data-driven neural modeling. *Front. Neurosci.* **8**, 383.

Friston, K.J., (2014). On the modelling of seizure dynamics. *Brain* **137**, 2110–2113.

Friston, K.J., (2012). Predictive coding, precision and synchrony. *Cogn. Neurosci.* **3**, 238–239.

Friston, K.J., (2005a). Hallucinations and perceptual inference. *Behav. Brain Sci.* **28**, 764–766.

Friston, K.J., (2005b). A theory of cortical responses. *Philos. Trans. R. Soc. B Biol. Sci.* **360**, 815–836.

Friston, K.J., (1998). The disconnection hypothesis. *Schizophr. Res.* **30**, 115–125.

Friston, K.J., Brown, H.R., Siemerkus, J., Stephan, K.E., (2016a). The dysconnection hypothesis (2016). *Schizophr. Res.* **176**, 83–94.

Friston, K.J., Harrison, L., Daunizeau, J., Kiebel, S., Phillips, C., et al., (2008). Multiple sparse priors for the M/EEG inverse problem. *Neuroimage* **39**, 1104–1120.

Friston, K.J., Harrison, L., Penny, W., (2003). Dynamic causal modelling. *Neuroimage* **19**, 1273–1302.

Friston, K.J., Kiebel, S., (2009). Predictive coding under the free-energy principle. *Philos. Trans. R. Soc. B Biol. Sci.* **364**, 1211–1221.

Friston, K.J., Litvak, V., Oswal, A., Razi, A., Stephan, K.E., et al., (2016b). Bayesian model reduction and empirical Bayes for group (DCM) studies. *Neuroimage* **128**, 413–431.

Friston, K.J., Mattout, J., Trujillo-Barreto, N., Ashburner, J., Penny, W., (2007). Variational free energy and the Laplace approximation. *Neuroimage* **34**, 220–234.

Friston, K.J., Parr, T., Zeidman, P., (2018). Bayesian model reduction. *arXiv* **1805**, 1–20.

Friston, K.J., Zeidman, P., Litvak, V., (2015). Empirical Bayes for DCM: A Group Inversion Scheme. *Front. Syst. Neurosci.* **9**, 1–10.

Fromer, M., Pocklington, A.J., Kavanagh, D.H., Williams, H.J., Dwyer, S., et al., (2014). De novo mutations in schizophrenia implicate synaptic networks. *Nature* **506**, 179–184.

Fuhrmann, D., Knoll, L.J., Blakemore, S.J., (2015). Adolescence as a Sensitive Period of Brain Development. *Trends Cogn. Sci.* **19**, 558–566.

Gais, S., Rasch, B., Wagner, U., Born, J., (2008). Visual-Procedural Memory Consolidation during Sleep Blocked by Glutamatergic Receptor Antagonists. *J. Neurosci.* **28**, 5513–5518.

Gandal, M.J., Sisti, J., Klook, K., Ortinski, P.I., Leitman, V., et al., (2012). GABA B - mediated rescue of altered excitatory-inhibitory balance, gamma synchrony and behavioral deficits following constitutive NMDAR-hypofunction. *Transl. Psychiatry* **2**, e142-9.

Garrido, M.I., Friston, K.J., Kiebel, S.J., Stephan, K.E., Baldeweg, T., et al., (2008). The functional anatomy of the MMN: A DCM study of the roving paradigm. *Neuroimage* **42**, 936–944.

Garrido, M.I., Kilner, J.M., Kiebel, S.J., Friston, K.J., (2009a). Dynamic Causal Modeling of the Response to Frequency Deviants. *J. Neurophysiol.* **101**, 2620–2631.

Garrido, M.I., Kilner, J.M., Kiebel, S.J., Stephan, K.E., Baldeweg, T., et al., (2009b). Repetition suppression and plasticity in the human brain. *Neuroimage* **48**, 269–279.

Geyer, M.A., Krebs-Thomson, K., Braff, D.L., Swerdlow, N.R., (2001). Pharmacological studies of prepulse inhibition models of sensorimotor gating deficits in schizophrenia: a decade in review. *Psychopharmacology (Berl).* **156**, 117–154.

Gibson, G., (2012). Rare and common variants: twenty arguments. *Nat. Rev. Genet.* **13**, 135–145.

Gilbert, C.D., Wiesel, T.N., (1983). Functional organization of the visual cortex. *Prog. Brain Res.* **58**, 209–218.

Gilbert, J.R., Symmonds, M., Hanna, M.G., Dolan, R.J., Friston, K.J., et al., (2016). Profiling neuronal ion channelopathies with non-invasive brain imaging and dynamic causal models: Case studies of single gene mutations. *Neuroimage* **124**, 43–53.

Gitiaux, C., Simonnet, H., Eisermann, M., Leunen, D., Dulac, O., et al., (2013). Early electro-clinical features may contribute to diagnosis of the anti-NMDA receptor encephalitis in children. *Clin. Neurophysiol.* **124**, 2354–2361.

Glantz, L.A., Lewis, D.A., (2000). Decreased dendritic spine density on prefrontal cortical pyramidal neurons in schizophrenia. *Arch. Gen. Psychiatry* **57**, 65–73.

Gogtay, N., Giedd, J.N., Lusk, L., Hayashi, K.M., Greenstein, D., et al., (2004). Dynamic mapping of human cortical development during childhood through early adulthood. *Proc. Natl. Acad. Sci.* **101**, 8174–8179.

Gollas, F., Tetzlaff, R., (2005). Modeling brain electrical activity in epilepsy by reaction-diffusion cellular neural networks, in: Carmona, R.A., Linan-Cembrano, G. (Eds.), Bioengineered and Bioinspired Systems II. p. 219.

Gonzalez-Burgos, G., Kroener, S., Zaitsev, A. V., Povysheva, N. V., Krimer, L.S., et al., (2008). Functional maturation of excitatory synapses in layer 3 pyramidal neurons during postnatal development of the primate prefrontal cortex. *Cereb. Cortex* **18**, 626–637.

Goodfellow, M., Schindler, K., Baier, G., (2012). Self-organised transients in a neural mass model of epileptogenic tissue dynamics. *Neuroimage* **59**, 2644–2660.

Graus, F., Titulaer, M.J., Balu, R., Benseler, S., Bien, C.G., et al., (2016). A clinical approach to diagnosis of autoimmune encephalitis. *Lancet Neurol.* **15**, 391–404.

Grayton, H.M., Fernandes, C., Rujescu, D., Collier, D.A., (2012). Copy number variations in neurodevelopmental disorders. *Prog. Neurobiol.* **99**, 81–91.

Greenwood, T.A., Light, G.A., Swerdlow, N.R., Radant, A.D., Braff, D.L., (2012). Association analysis of 94 candidate genes and schizophrenia-related endophenotypes. *PLoS One* **7**, e29630.

Griffin, A., Hamling, K.R., Knupp, K., Hong, S., Lee, L.P., et al., (2017). Clemizole and modulators of serotonin signalling suppress seizures in Dravet syndrome. *Brain* aww342.

Guo, X., Hamilton, P.J., Reish, N.J., Sweatt, J.D., Miller, C.A., et al., (2009). Reduced Expression of the NMDA Receptor-Interacting Protein SynGAP Causes Behavioral Abnormalities that Model Symptoms of Schizophrenia. *Neuropsychopharmacology* **34**, 1659–1672.

Gurney, K., (2006). Single neuron models 5 Part I : Theory of gate dynamics : voltage clamp formulation [https://www.sheffield.ac.uk/polopoly_fs/1.13306!/file/single-neuron-models.pdf] *accessed*: 04/13/2016.

Haenschel, C., (2005). Event-Related Brain Potential Correlates of Human Auditory Sensory Memory-Trace Formation. *J. Neurosci.* **25**, 10494–10501.

Häfner, H., Maurer, K., Löffler, W., Riecher-Rössler, A., (1993). The influence of age and sex on the onset and early course of schizophrenia. *Br. J. Psychiatry* **162**, 80–6.

Hagmann, P., Sporns, O., Madan, N., Cammoun, L., Pienaar, R., et al., (2010). White matter maturation reshapes structural connectivity in the late developing human brain. *Proc. Natl. Acad. Sci.* **107**, 19067–19072.

Hall, M.-H., Chen, C.-Y., Cohen, B.M., Spencer, K.M., Levy, D.L., et al., (2015). Genomewide association analyses of electrophysiological endophenotypes for schizophrenia and psychotic bipolar disorders: A preliminary report. *Am. J. Med. Genet. Part B Neuropsychiatr. Genet.* **168**, 151–161.

Hansen, S.T., Hansen, L.K., (2015). EEG source reconstruction performance as a function of skull conductance contrast, in: 2015 IEEE International Conference on Acoustics, Speech and Signal Processing (ICASSP). IEEE, pp. 827–831.

Harris, K.D., Shepherd, G.M.G., (2015). The neocortical circuit: themes and variations. *Nat. Neurosci.* **18**, 170–181.

Harris, P.A., Taylor, R., Thielke, R., Payne, J., Gonzalez, N., et al., (2009). Research electronic data capture (REDCap)--a metadata-driven methodology and workflow process for providing translational research informatics support. *J. Biomed. Inform.*

42, 377–81.

Hattori, H., Yamano, T., Hayashi, K., Osawa, M., Kondo, K., et al., (2008). Effectiveness of lidocaine infusion for status epilepticus in childhood: a retrospective multi-institutional study in Japan. *Brain Dev.* **30**, 504–12.

Hegelstad, W.T.V., Larsen, T.K., Auestad, B., Evensen, J., Haahr, U., et al., (2012). Long-term follow-up of the TIPS early detection in psychosis study: Effects on 10-year outcome. *Am. J. Psychiatry* **169**, 374–380.

Heitmann, S., Gong, P., Breakspear, M., (2012). A computational role for bistability and traveling waves in motor cortex. *Front. Comput. Neurosci.* **6**, 67.

Helbig, I., (2015). Genetic Causes of Generalized Epilepsies. *Semin. Neurol.* **35**, 288–292.

Helbig, I., Hartmann, C., Mefford, H.C., (2013). The unexpected role of copy number variations in juvenile myoclonic epilepsy. *Epilepsy Behav.* **28 Suppl 1**, S66-8.

Helbig, I., Lindhout, Di., (2017). Advancing the phenome alongside the genome in epilepsy studies. *Neurology* **89**, 14–15.

Helbig, I., Scheffer, I.E., Mulley, J.C., Berkovic, S.F., (2008). Navigating the channels and beyond: unravelling the genetics of the epilepsies. *Lancet Neurol.* **7**, 231–245.

Hildebrand, M.S., Dahl, H.-H.M., Damiano, J.A., Smith, R.J.H., Scheffer, I.E., et al., (2013). Recent advances in the molecular genetics of epilepsy. *J. Med. Genet.* **50**, 271–279.

Hill, R.A., Li, A.M., Grutzendler, J., (2018). Lifelong cortical myelin plasticity and age-related degeneration in the live mammalian brain. *Nat. Neurosci.* **21**, 683–695.

Hodgkin, A.L., Huxley, A.F., (1952). A quantitative description of membrane current and its application to conduction and excitation in nerve. *J. Physiol.* **117**, 500–44.

Homayoun, H., Moghaddam, B., (2007). NMDA Receptor Hypofunction Produces Opposite Effects on Prefrontal Cortex Interneurons and Pyramidal Neurons. *J. Neurosci.* **27**, 11496–11500.

Hong, S., Lee, P., Baraban, S.C., Lee, L.P., (2016). A Novel Long-term, Multi-Channel and Non-invasive Electrophysiology Platform for Zebrafish. *Sci. Rep.* **6**, 28248.

Hood, L., Tian, Q., (2012). Systems Approaches to Biology and Disease Enable Translational Systems Medicine. *Genomics, Proteomics Bioinforma.* **10**, 181–185.

Hu, W.F., Chahrour, M.H., Walsh, C.A., (2014). The Diverse Genetic Landscape of Neurodevelopmental Disorders. *Annu. Rev. Genomics Hum. Genet.* **15**, 195–213.

Huang, R.Q., Bell-Horner, C.L., Dibas, M.I., Covey, D.F., Drewe, J. a, et al., (2001). Pentylenetetrazole-induced inhibition of recombinant gamma-aminobutyric acid type A (GABA(A)) receptors: mechanism and site of action. *J. Pharmacol. Exp. Ther.* **298**, 986–995.

Hughes, E.G., Peng, X., Gleichman, A.J., Lai, M., Zhou, L., et al., (2010). Cellular and Synaptic Mechanisms of Anti-NMDA Receptor Encephalitis. *J. Neurosci.* **30**, 5866–5875.

Hulvershorn, L.A., Cullen, K.R., M. Francis, M., Westlund, M.K., (2014). Developmental Resting State Functional Connectivity for Clinicians. *Curr. Behav. Neurosci. Reports* **1**, 161–169.

Huttenlocher, P.R., Dabholkar, A.S., (1997). Regional differences in synaptogenesis in human cerebral cortex. *J. Comp. Neurol.* **387**, 167–178.

Huttenlocher, P.R., de Courten, C., (1987). The development of synapses in striate cortex of man. *Hum. Neurobiol.* **6**, 1–9.

Ignjatovic, P., (2009). Clinical aspects of epilepsy in children and adolescents with cerebral palsy. *Epilepsia* **50**, 244.

International League Against Epilepsy Consortium on Complex Epilepsies, (2014). Genetic determinants of common epilepsies: a meta-analysis of genome-wide association studies. *Lancet Neurol.* **13**, 893–903.

Irani, S.R., Bera, K., Waters, P., Zuliani, L., Maxwell, S., et al., (2010). N-methyl-D-aspartate antibody encephalitis: temporal progression of clinical and paraclinical observations in a predominantly non-paraneoplastic disorder of both sexes. *Brain* **133**, 1655–1667.

Izhikevich, E.M., (2007). Dynamical Systems in Neuroscience Computational Neuroscience, Dynamical Systems. MIT Press, Cambridge, MA.

Jaaskelainen, I.P., Ahveninen, J., Bonmassar, G., Dale, A.M., Ilmoniemi, R.J., et al., (2004). Human posterior auditory cortex gates novel sounds to consciousness. *Proc. Natl. Acad. Sci.* **101**, 6809–6814.

Jansen, B.H., Rit, V.G., (1995). Electroencephalogram and visual evoked potential generation in a mathematical model of coupled cortical columns. *Biol. Cybern.* **73**, 357–66.

Javitt, D.C., Steinschneider, M., Schroeder, C.E., Arezzo, J.C., (1996). Role of cortical N-methyl-D-aspartate receptors in auditory sensory memory and mismatch negativity generation: implications for schizophrenia. *Proc. Natl. Acad. Sci.* **93**, 11962–11967.

Jentsch, J., Roth, R., (1999). The Neuropsychopharmacology of Phencyclidine From NMDA Receptor Hypofunction to the Dopamine Hypothesis of Schizophrenia. *Neuropsychopharmacology* **20**, 201–225.

Jiang, X., Nardelli, J., (2016). Cellular and molecular introduction to brain development. *Neurobiol. Dis.* **92**, 3–17.

Jiang, X., Shen, S., Cadwell, C.R., Berens, P., Sinz, F., et al., (2015). Principles of connectivity among morphologically defined cell types in adult neocortex. *Science'* **350**, aac9462.

Jirsa, V.K., Proix, T., Perdikis, D., Woodman, M.M., Wang, H., et al., (2017). The Virtual Epileptic Patient: Individualized whole-brain models of epilepsy spread. *Neuroimage* **145**, 377–388.

Jirsa, V.K., Stacey, W.C., Quilichini, P.P., Ivanov, A.I., Bernard, C., (2014). On the nature of seizure dynamics. *Brain* **137**, 2210–2230.

Jones, P., (1997). The early origins of schizophrenia. *Br. Med. Bull.* **53**, 135–155.

Julier, S.J., Uhlmann, J.K., (2004). Unscented Filtering and Nonlinear Estimation. *Proc. IEEE* **92**, 401–422.

Jung, R., Berger, W., (1979). Hans Bergers Entdeckung des Elektrenkephalogramms und

seine ersten Befunde 1924-1931. *Arch. fuer Psychiatr. und Nervenkrankheiten* **227**, 279–300.

Kabat, J., Król, P., (2012). Focal cortical dysplasia - review. *Pol. J. Radiol.* **77**, 35–43.

Kahlig, K.M., Misra, S.N., George, a. L., (2006). Impaired Inactivation Gate Stabilization Predicts Increased Persistent Current for an Epilepsy-Associated SCN1A Mutation. *J. Neurosci.* **26**, 10958–10966.

Kaiser, M., (2017). Mechanisms of Connectome Development. *Trends Cogn. Sci.* **21**, 703–717.

Kalueff, A.V., (2007). Mapping convulsants' binding to the GABA-A receptor chloride ionophore: A proposed model for channel binding sites. *Neurochem. Int.* **50**, 61–68.

Kameneva, T., Ying, T., Guo, B., Freestone, D.R., (2017). Neural mass models as a tool to investigate neural dynamics during seizures. *J. Comput. Neurosci.*

Kapur, a, Lytton, W.W., Ketchum, K.L., Haberly, L.B., (1997). Regulation of the NMDA component of EPSPs by different components of postsynaptic GABAergic inhibition: computer simulation analysis in piriform cortex. *J. Neurophysiol.* **78**, 2546–2559.

Kass, H.R., Winesett, S.P., Bessone, S.K., Turner, Z., Kossoff, E.H., (2016). Use of dietary therapies amongst patients with GLUT1 deficiency syndrome. *Seizure* **35**, 83–87.

Kawato, M., Hayakawa, H., Inui, T., (1993). A forward-inverse optics model of reciprocal connections between visual cortical areas. *Network* **4**, 4150422.

Keller, P.J., Ahrens, M.B., Freeman, J., (2014). Light-sheet imaging for systems neuroscience. *Nat. Methods* **12**, 27–29.

Khan, S., Al Baradie, R., (2012). Epileptic Encephalopathies: An Overview. *Epilepsy Res. Treat.* **2012**, 1–8.

Kibat, C., Krishnan, S., Ramaswamy, M., Baker, B.J., Jesuthasan, S., (2016). Imaging voltage in zebrafish as a route to characterizing a vertebrate functional connectome: promises and pitfalls of genetically encoded indicators. *J. Neurogenet.* **30**, 80–88.

Kiebel, S.J., Daunizeau, J., Friston, K.J., (2008a). A Hierarchy of Time-Scales and the Brain. *PLoS Comput. Biol.* **4**, e1000209.

Kiebel, S.J., Garrido, M.I., Moran, R., Chen, C.-C., Friston, K.J., (2009). Dynamic causal modeling for EEG and MEG. *Hum. Brain Mapp.* **30**, 1866–1876.

Kiebel, S.J., Garrido, M.I., Moran, R.J., Friston, K.J., (2008b). Dynamic causal modelling for EEG and MEG. *Cogn. Neurodyn.* **2**, 121–136.

Kitamura, K., Judkewitz, B., Kano, M., Denk, W., Hausser, M., (2008). Targeted patch-clamp recordings and single-cell electroporation of unlabeled neurons in vivo. *Nat Methods* **5**, 61–67.

Ko, H., Cossell, L., Baragli, C., Antolik, J., Clopath, C., et al., (2013). The emergence of functional microcircuits in visual cortex. *Nature* **496**, 96–100.

Koch, C., Rapp, M., Segev, I., (1996). A brief history of time (constants). *Cerebr Cortex* **6**, 93–101.

Kontis, K.J., Rounaghi, A., Goldin, A.L., (1997). Sodium Channel Activation Gating Is

Affected by Substitutions of Voltage Sensor Positive Charges in All Four Domains. *J. Gen. Physiol.* **110**, 391–401.

Kopell, N.J., Gritton, H.J., Whittington, M.A., Kramer, M.A., (2014). Perspective Beyond the Connectome : The Dynome. *Neuron* **83**, 1319–1328.

Kornreich, B.G., (2007). The patch clamp technique: Principles and technical considerations. *J. Vet. Cardiol.* **9**, 25–37.

Krishnan, G.P., Chauvette, S., Shamie, I., Soltani, S., Timofeev, I., et al., (2016). Cellular and neurochemical basis of sleep stages in the thalamocortical network. *Elife* **5**, 1–29.

Krook-Magnuson, E., Armstrong, C., Oijala, M., Soltesz, I., (2013). On-demand optogenetic control of spontaneous seizures in temporal lobe epilepsy. *Nat. Commun.* **4**, 1376.

Krystal, J.H., (1994). Subanesthetic Effects of the Noncompetitive NMDA Antagonist, Ketamine, in Humans. *Arch. Gen. Psychiatry* **51**, 199.

Kuhlmann, L., Grayden, D.B., Wendling, F., Schiff, S.J., (2015). Role of Multiple-Scale Modeling of Epilepsy in Seizure Forecasting. *J. Clin. Neurophysiol.* **32**, 220–226.

Kullmann, D.M., Erdemli, G., Asztély, F., (1996). LTP of AMPA and NMDA receptor-mediated signals: Evidence for presynaptic expression and extrasynaptic glutamate spill-over. *Neuron* **17**, 461–474.

Kurokawa, T., Goya, N., Fukuyama, Y., Suzukim, M., Seki, T., et al., (1980). West Syndrome and Lennox-Gastaut Syndrome: A Survey of Natural History. *Pediatrics1* **65**, 81–88.

Kushnerenko, E., Winkler, I., Horváth, J., Näätänen, R., Pavlov, I., et al., (2007). Processing acoustic change and novelty in newborn infants. *Eur. J. Neurosci.* **26**, 265–74.

Lado, F.A., Rubboli, G., Capovilla, P., Avanzini, G., Moshé, S.L., (2013). Pathophysiology of epileptic encephalopathies. *Epilepsia* **54**, 6–13.

Landwehrmeyer, G.B., Standaert, D.G., Testa, C.M., Penney, J.B., Young, A.B., (1995). NMDA Receptor and Interneurons Subunit mRNA Expression by Projection Neurons and Interneurons in Rat Striatum. *J. Neurosci.* **15**, 5297–5307.

Langer, N., Ho, E.J., Alexander, L.M., Xu, H.Y., Jozanovic, R.K., et al., (2017). A resource for assessing information processing in the developing brain using EEG and eye tracking. *Sci. data* **4**, 170040.

Lantz, G., Grouiller, F., Spinelli, L., (2011). Localisation of Focal Epileptic Activity in Children Using High Density EEG Source Imaging. *Epileptologie* **28**, 84–90.

Laursen, T.M., Nordentoft, M., Mortensen, P.B., (2014). Excess Early Mortality in Schizophrenia. *Ssrn*.

Lawson, R.P., Friston, K.J., Rees, G., (2015). A more precise look at context in autism. *Proc. Natl. Acad. Sci.* 201514212.

Lee, V., Maguire, J., (2014). The impact of tonic GABAA receptor-mediated inhibition on neuronal excitability varies across brain region and cell type. *Front. Neural Circuits* **8**, 3.

Lemke, J.R., Hendrickx, R., Geider, K., Laube, B., Schwake, M., et al., (2014). GRIN2B

mutations in West syndrome and intellectual disability with focal epilepsy. *Ann. Neurol.* **75**, 147–154.

Lesca, G., Rudolf, G., Bruneau, N., Lozovaya, N., Labalme, A., et al., (2013). GRIN2A mutations in acquired epileptic aphasia and related childhood focal epilepsies and encephalopathies with speech and language dysfunction. *Nat. Genet.* **45**, 1061–1066.

Leventer, R.J., Guerrini, R., Dobyns, W.B., (2008). Malformations of cortical development and epilepsy. *Dialogues Clin. Neurosci.* **10**, 47–62.

Lewis, D. a, Hashimoto, T., Volk, D.W., (2005). Cortical inhibitory neurons and schizophrenia. *Nat. Rev. Neurosci.* **6**, 312–324.

Lewis, D.A., Lieberman, J.A., (2000). Catching Up on Schizophrenia. *Neuron* **28**, 325–334.

Lie, O. V., van Mierlo, P., (2017). Seizure-Onset Mapping Based on Time-Variant Multivariate Functional Connectivity Analysis of High-Dimensional Intracranial EEG: A Kalman Filter Approach. *Brain Topogr.* **30**, 46–59.

Liou, J.Y., Ma, H., Wenzel, M., Zhao, M., Baird-Daniel, E., et al., (2018). Role of inhibitory control in modulating focal seizure spread. *Brain* **141**, 2083–2097.

Litvak, V., Garrido, M.I., Zeidman, P., Friston, K., (2015). Empirical Bayes for Group (DCM) Studies: A Reproducibility Study. *Front. Hum. Neurosci.* **9**, 1–12.

Litvak, V., Mattout, J., Kiebel, S., Phillips, C., Henson, R., et al., (2011). EEG and MEG Data Analysis in SPM8. *Comput. Intell. Neurosci.* **2011**, 1–32.

Liu, X.-B., (2004). Switching of NMDA Receptor 2A and 2B Subunits at Thalamic and Cortical Synapses during Early Postnatal Development. *J. Neurosci.* **24**, 8885–8895.

Liu, Y., Lopez-Santiago, L.F., Yuan, Y., Jones, J.M., Zhang, H., et al., (2013). Dravet syndrome patient-derived neurons suggest a novel epilepsy mechanism. *Ann. Neurol.* **74**, 128–139.

Lopes da Silva, F., (1991). Neural mechanisms underlying brain waves: from neural membranes to networks. *Electroencephalogr. Clin. Neurophysiol.* **79**, 81–93.

Lopes da Silva, F.H., (2010). MEG: An Introduction to Methods. Oxford University Press.

Lopes da Silva, F.H., Hoeks, A., Smits, H., Zetterberg, L.H., (1974). Model of brain rhythmic activity. The alpha-rhythm of the thalamus. *Kybernetik* **15**, 27–37.

Lovett-Barron, M., Andalman, A.S., Allen, W.E., Vesuna, S., Kauvar, I., et al., (2017). Ancestral Circuits for the Coordinated Modulation of Brain State. *Cell* 1–13.

Luo, J., Norris, R.H., Gordon, S.L., Nithianantharajah, J., (2018). Neurodevelopmental synaptopathies: Insights from behaviour in rodent models of synapse gene mutations. *Prog. Neuro-Psychopharmacology Biol. Psychiatry* **84**, 424–439.

Lytton, W.W., (2008). Computer modelling of epilepsy. *Nat. Rev. Neurosci.* **9**, 626–637.

Magri, C., Sacchetti, E., Traversa, M., Valsecchi, P., Gardella, R., et al., (2010). New copy number variations in schizophrenia. *PLoS One* **5**, e13422.

Malenka, R.C., Nicoll, R.A., (1993). NMDA-receptor-dependent synaptic plasticity: multiple forms and mechanisms. *Trends Neurosci.* **16**, 521–527.

Malhotra, D., Sebat, J., (2012). CNVs: harbingers of a rare variant revolution in psychiatric

genetics. *Cell* **148**, 1223–1241.

Mann, K., Gallen, C.L., Clandinin, T.R., (2017). Whole-Brain Calcium Imaging Reveals an Intrinsic Functional Network in Drosophila. *Curr. Biol.* **27**, 2389–2396.e4.

Marreiros, A.C., Daunizeau, J., Kiebel, S.J., Friston, K.J., (2008). Population dynamics: Variance and the sigmoid activation function. *Neuroimage* **42**, 147–157.

Martin, H.C., Kim, G.E., Pagnamenta, A.T., Murakami, Y., Carvill, G.L., et al., (2014). Clinical whole-genome sequencing in severe early-onset epilepsy reveals new genes and improves molecular diagnosis. *Hum. Mol. Genet.* **23**, 3200–3211.

May, P., Girard, S., Harrer, M., Bobbili, D.R., Schubert, J., et al., (2018). Rare coding variants in genes encoding GABAAreceptors in genetic generalised epilepsies: an exome-based case-control study. *Lancet Neurol.* **17**, 699–708.

McGlashan, T.H., Hoffman, R.E., (2000). Schizophrenia as a disorder of developmental reduced synaptic connectivity. *Arch Gen Psychiatry* **57**, 637–48.

McLean, M., Macdonald, R., (1986). Sodium valproate, but not ethosuximide, produces use- and voltage- dependent limitation of high frequency repetitive firing of action potentials of mouse central neurons in cell culture. *J. Pharmacol. Exp. Ther.* **237**, 1001–1011.

McTague, A., Howell, K.B., Cross, J.H., Kurian, M.A., Scheffer, I.E., (2016). The genetic landscape of the epileptic encephalopathies of infancy and childhood. *Lancet Neurol.* **15**, 304–316.

McTague, A., Nair, U., Malhotra, S., Meyer, E., Trump, N., et al., (2018). Clinical and molecular characterization of KCNT1 -related severe early-onset epilepsy. *Neurology* **90**, e55–e66.

Meijer, H.G.E., Eissa, T.L., Kiewiet, B., Neuman, J.F., Schevon, C. a, et al., (2015). Modeling Focal Epileptic Activity in the Wilson–Cowan Model with Depolarization Block. *J. Math. Neurosci.* **5**, 7.

Meyer, M., Dhamne, S.C., LaCoursiere, C.M., Tambunan, D., Poduri, A., et al., (2016). Microarray noninvasive neuronal seizure recordings from intact larval zebrafish. *PLoS One* **11**, 1–17.

Meyer, M.P., (2006). Evidence from In Vivo Imaging That Synaptogenesis Guides the Growth and Branching of Axonal Arbors by Two Distinct Mechanisms. *J. Neurosci.* **26**, 3604–3614.

Miller, I.O., Sotero de Menezes, M.A., (2014). SCN1A-Related Seizure Disorders [https://www.ncbi.nlm.nih.gov/books/NBK1318/] *accessed*: 02/09/2016. *GeneReviews*.

Møller, R.S., Dahl, H.A., Helbig, I., (2015). The contribution of next generation sequencing to epilepsy genetics. *Expert Rev. Mol. Diagn.* **7159**, 1–8.

Monyer, H., Sprengel, R., Schoepfer, R., Herb, A., Higuchi, M., et al., (1992). Heteromeric NMDA Receptors: Molecular and Functional Distinction of Subtypes. *Science'* **256**, 1217–1221.

Moran, R., Pinotsis, D.A., Friston, K., (2013). Neural masses and fields in dynamic causal modeling. *Front. Comput. Neurosci.* **7**, 57.

Moran, R.J., Jones, M.W., Blockeel, A.J., Adams, R. a, Stephan, K.E., et al., (2015). Losing Control Under Ketamine: Suppressed Cortico-Hippocampal Drive Following Acute Ketamine in Rats. *Neuropsychopharmacology* **40**, 268–277.

Moran, R.J., Stephan, K.E., Dolan, R.J., Friston, K.J., (2011a). Consistent spectral predictors for dynamic causal models of steady-state responses. *Neuroimage* **55**, 1694–1708.

Moran, R.J., Symmonds, M., Stephan, K.E., Friston, K.J., Dolan, R.J., (2011b). An In Vivo Assay of Synaptic Function Mediating Human Cognition. *Curr. Biol.* **21**, 1320–1325.

Moreau, A.W., Kullmann, D.M., (2013). NMDA receptor-dependent function and plasticity in inhibitory circuits. *Neuropharmacology* **74**, 23–31.

Moreno-De-Luca, A., Myers, S.M., Challman, T.D., Moreno-De-Luca, D., Evans, D.W., et al., (2013). Developmental brain dysfunction: Revival and expansion of old concepts based on new genetic evidence. *Lancet Neurol.* **12**, 406–414.

Moscato, E.H., Peng, X., Jain, A., Parsons, T.D., Dalmau, J., et al., (2014). Acute mechanisms underlying antibody effects in anti-N-methyl-D-aspartate receptor encephalitis. *Ann. Neurol.* **76**, 108–119.

Mullen, S.A., Carvill, G.L., Bellows, S., Bayly, M.A., Trucks, H., et al., (2013). Copy number variants are frequent in genetic generalized epilepsy with intellectual disability. *Neurology* **81**, 1507–1514.

Mulley, J.C., Mefford, H.C., (2011). Epilepsy and the new cytogenetics. *Epilepsia* **52**, 423–432.

Muñoz, W., Tremblay, R., Levenstein, D., Rudy, B., (2017). Layer-specific modulation of neocortical dendritic inhibition during active wakefulness. *Science'* **355**, 954–959.

Murray, J.D., Anticevic, A., Gancsos, M., Ichinose, M., Corlett, P.R., et al., (2014). Linking Microcircuit Dysfunction to Cognitive Impairment: Effects of Disinhibition Associated with Schizophrenia in a Cortical Working Memory Model. *Cereb. Cortex* **24**, 859–872.

Murray, J.D., Bernacchia, A., Freedman, D.J., Romo, R., Wallis, J.D., et al., (2014). A hierarchy of intrinsic timescales across primate cortex. *Nat. Neurosci.* **17**, 1661–1663.

Muthukumaraswamy, S.D., Shaw, A.D., Jackson, L.E., Hall, J., Moran, R., et al., (2015). Evidence that Subanesthetic Doses of Ketamine Cause Sustained Disruptions of NMDA and AMPA-Mediated Frontoparietal Connectivity in Humans. *J. Neurosci.* **35**, 11694–11706.

Näätänen, R., Kähkönen, S., (2009). Central auditory dysfunction in schizophrenia as revealed by the mismatch negativity (MMN) and its magnetic equivalent MMNm: a review. *Int. J. Neuropsychopharmacol.* **12**, 125.

Näätänen, R., Winkler, I., (1999). The concept of auditory stimulus representation in cognitive neuroscience. *Psychol. Bull.* **125**, 826–859.

Nakazawa, K., Jeevakumar, V., Nakao, K., (2017). Spatial and temporal boundaries of NMDA receptor hypofunction leading to schizophrenia. *npj Schizophr.* **3**, 7.

Nam, R.H., Kim, W., Lee, C.J., (2004). NMDA receptor-dependent long-term potentiation in the telencephalon of the zebrafish. *Neurosci. Lett.* **370**, 248–251.

Neal, E.G., Maciver, S., Vale, F.L., (2018). Multimodal, noninvasive seizure network mapping software: A novel tool for preoperative epilepsy evaluation. *Epilepsy Behav.* **81**, 25–32.

Neher, E., Sakmann, B., (1976). Single-channel currents recorded from membrane of denervated frog muscle fibres. *Nature* **260**, 799–802.

Nehlig, A., (1998). Mapping of neuronal networks underlying generalized seizures induced by increasing doses of pentylenetetrazol in the immature and adult rat: A c-Fos immunohistochemical study. *Eur. J. Neurosci.* **10**, 2094–2106.

Netoff, T.I., Clewley, R., Arno, S., Keck, T., White, J. a, (2004). Epilepsy in Small-World Networks. *J. Neurosci.* **24**, 8075–8083.

Nevado-Holgado, A.J., Marten, F., Richardson, M.P., Terry, J.R., (2012). Characterising the dynamics of EEG waveforms as the path through parameter space of a neural mass model: Application to epilepsy seizure evolution. *Neuroimage* **59**, 2374–2392.

Newton, C.R., Garcia, H.H., (2012). Epilepsy in poor regions of the world. *Lancet* **380**, 1193–1201.

Niell, C.M., Meyer, M.P., Smith, S.J., (2004). In vivo imaging of synapse formation on a growing dendritic arbor. *Nat. Neurosci.* **7**, 254–260.

Niell, C.M., Smith, S.J., (2005). Functional imaging reveals rapid development of visual response properties in the zebrafish tectum. *Neuron* **45**, 941–951.

Noda, M., Shimizu, S., Tanabe, T., Takai, T., Kayano, T., et al., (1984). Primary structure of Electrophorus electricus sodium channel deduced from cDNA sequence. *Nature* **312**, 121–127.

Nosadini, M., Boniver, C., Zuliani, L., de Palma, L., Cainelli, E., et al., (2015). Longitudinal Electroencephalographic (EEG) Findings in Pediatric Anti-N-Methyl-D-Aspartate (Anti-NMDA) Receptor Encephalitis: The Padua Experience. *J. Child Neurol.* **30**, 238–245.

Oakley, J.C., Kalume, F., Catterall, W. a., (2011). Insights into pathophysiology and therapy from a mouse model of Dravet syndrome. *Epilepsia* **52**, 59–61.

Oates, S., Tang, S., Rosch, R., Lear, R., Hughes, E.F., et al., (2018). Incorporating epilepsy genetics into clinical practice: a 360°evaluation. *npj Genomic Med.* **3**, 13.

Ogawa, R., Nakashima, I., Takahashi, T., Kaneko, K., Akaishi, T., et al., (2017). MOG antibody–positive, benign, unilateral, cerebral cortical encephalitis with epilepsy. *Neurol. - Neuroimmunol. Neuroinflammation* **4**, e322.

Ogiwara, I., Miyamoto, H., Morita, N., Atapour, N., Mazaki, E., et al., (2007). Nav1.1 Localizes to Axons of Parvalbumin-Positive Inhibitory Interneurons. *Sci. Technol.* **27**, 5903–5914.

Olafsson, E., Ludvigsson, P., Hesdorffer, D., Kjartansson, O., Hauser, W.A., et al., (2005). Incidence of unprovoked seizures and epilepsy in Iceland and assessment of the epilepsy syndrome classification: a prospective study. *Lancet Neurol.* **4**, 627–634.

Omidvarnia, A., Pedersen, M., Rosch, R.E., Friston, K.J., Jackson, G.D., (2017). Hierarchical disruption in the Bayesian brain: Focal epilepsy and brain networks. *NeuroImage Clin.* **15**, 682–688.

Owens, E.M., Bachman, P., Glahn, D.C., Bearden, C.E., (2016). Electrophysiological Endophenotypes for Schizophrenia. *Harv. Rev. Psychiatry* **24**, 129–147.

Paciorkowski, A.R., Thio, L.L., Dobyns, W.B., (2011). Genetic and biologic classification of infantile spasms. *Pediatr. Neurol.* **45**, 355–367.

Pal, D., Helbig, I., (2015). Commentary: Pathogenic EFHC1 mutations are tolerated in healthy individuals dependent on reported ancestry. *Epilepsia* **56**, 195–196.

Pankevich, D.E., Davis, M., Altevogt, B.M., (2011). Glutamate-Related Biomarkers in Drug Development for Disorders of the Nervous System Workshop Summary, Institute of Medicine (US) Forum on Neuroscience and Nervous System Disorders. National Academies Press, Washington, DC.

Papadopoulou, M., Cooray, G., Rosch, R., Moran, R., Marinazzo, D., et al., (2017). Dynamic causal modelling of seizure activity in a rat model. *Neuroimage* **146**, 518–532.

Papadopoulou, M., Leite, M., van Mierlo, P., Vonck, K., Lemieux, L., et al., (2015). Tracking slow modulations in synaptic gain using dynamic causal modelling: Validation in epilepsy. *Neuroimage* **107**, 117–126.

Parker, L., Padilla, M., Du, Y., Dong, K., Tanouye, M. a., (2011). Drosophila as a model for epilepsy: bss is a gain-of-function mutation in the para sodium channel gene that leads to seizures. *Genetics* **187**, 523–534.

Patton, G.C., Coffey, C., Sawyer, S.M., Viner, R.M., Haller, D.M., et al., (2009). Global patterns of mortality in young people: a systematic analysis of population health data. *Lancet* **374**, 881–892.

Paulus, W., Rothwell, J.C., (2016). Membrane resistance and shunting inhibition: where biophysics meets state-dependent human neurophysiology. *J. Physiol.* **594**, 2719–28.

Paus, T., Keshavan, M., Giedd, J.N., (2008). Why do many psychiatric disorders emerge during adolescence? *Nat. Rev. Neurosci.* **9**, 947–957.

Pavone, P., Striano, P., Falsaperla, R., Pavone, L., Ruggieri, M., (2013). Infantile spasms syndrome, West syndrome and related phenotypes: What we know in 2013. *Brain Dev.* **36**, 739–751.

Pelc, K., Boyd, S.G., Cheron, G., Dan, B., (2008). Epilepsy in Angelman syndrome. *Seizure* **17**, 211–217.

Perucca, P., Dubeau, F., Gotman, J., (2014). Intracranial electroencephalographic seizure-onset patterns: Effect of underlying pathology. *Brain* **137**, 183–196.

Peters, C., Rosch, R.E., Hughes, E., Ruben, P.C., (2016). Temperature-dependent changes in neuronal dynamics in a patient with an SCN1A mutation and hyperthermia induced seizures. *Sci. Rep.* **6**, 31879.

Petkoski, S., Spiegler, A., Proix, T., Aram, P., Temprado, J.-J., et al., (2016). Heterogeneity of time delays determines synchronization of coupled oscillators. *Phys. Rev. E* **94**, 012209.

Pettersson-Yeo, W., Allen, P., Benetti, S., McGuire, P., Mechelli, A., (2011). Dysconnectivity in schizophrenia: Where are we now? *Neurosci. Biobehav. Rev.* **35**, 1110–1124.

Pfeffer, C.K., Xue, M., He, M., Huang, Z.J., Scanziani, M., (2013). Inhibition of inhibition in visual cortex: The logic of connections between molecularly distinct interneurons. *Nat. Neurosci.* **16**, 1068–1076.

Phillips, A.J.K., Robinson, P.A., (2007). A quantitative model of sleep-wake dynamics based on the physiology of the brainstem ascending arousal system. *J. Biol. Rhythms* **22**, 167–179.

Phillips, H.N., Blenkmann, A., Hughes, L.E., Bekinschtein, T. a., Rowe, J.B., (2015). Hierarchical Organization of Frontotemporal Networks for the Prediction of Stimuli across Multiple Dimensions. *J. Neurosci.* **35**, 9255–9264.

Pinotsis, D.A., Brunet, N., Bastos, A., Bosman, C.A., Litvak, V., et al., (2014). Contrast gain control and horizontal interactions in V1: A DCM study. *Neuroimage* **92**, 143–155.

Pinto, D.J., (2005). Initiation, Propagation, and Termination of Epileptiform Activity in Rodent Neocortex In Vitro Involve Distinct Mechanisms. *J. Neurosci.* **25**, 8131–8140.

Porcelli, S., Van Der Wee, N., van der Werff, S., Aghajani, M., Glennon, J.C., et al., (2018). Social brain, social dysfunction and social withdrawal. *Neurosci. Biobehav. Rev.* **in press**.

Portugues, R., Engert, F., (2009). The neural basis of visual behaviors in the larval zebrafish. *Curr. Opin. Neurobiol.* **19**, 644–647.

Pospischil, M., Toledo-Rodriguez, M., Monier, C., Piwkowska, Z., Bal, T., et al., (2008). Minimal Hodgkin-Huxley type models for different classes of cortical and thalamic neurons. *Biol. Cybern.* **99**, 427–441.

Power, J.D., Barnes, K.A., Snyder, A.Z., Schlaggar, B.L., Petersen, S.E., (2012). Spurious but systematic correlations in functional connectivity MRI networks arise from subject motion. *Neuroimage* **59**, 2142–2154.

Proix, T., Bartolomei, F., Chauvel, P., Bernard, C., Jirsa, V.K., (2014). Permittivity Coupling across Brain Regions Determines Seizure Recruitment in Partial Epilepsy. *J. Neurosci.* **34**, 15009–15021.

Proix, T., Jirsa, V.K., Bartolomei, F., Guye, M., Truccolo, W., (2018). Predicting the spatiotemporal diversity of seizure propagation and termination in human focal epilepsy. *Nat. Commun.* **9**, 1088.

Purcell, S.M., Wray, N.R., Stone, J.L., Visscher, P.M., O'Donovan, M.C., et al., (2009). Common polygenic variation contributes to risk of schizophrenia and bipolar disorder. *Nature* **460**, 748–752.

Quintáns, B., Ordóñez-Ugalde, A., Cacheiro, P., Carracedo, A., Sobrido, M.J., (2014). Medical genomics: The intricate path from genetic variant identification to clinical interpretation. *Appl. Transl. Genomics* **3**, 60–67.

Rabinovich, M.I., Varona, P., Selverston, A.I., Abarbanel, H.D.I., (2006). Dynamical principles in neuroscience. *Rev. Mod. Phys.* **78**, 1213–1265.

Rahman, A., Reato, D., Arlotti, M., Gasca, F., Datta, A., et al., (2013). Cellular effects of acute direct current stimulation: somatic and synaptic terminal effects. *J. Physiol.* **591**, 2563–2578.

Rahmati, V., Kirmse, K., Markovi?, D., Holthoff, K., Kiebel, S.J., (2016). Inferring Neuronal

Dynamics from Calcium Imaging Data Using Biophysical Models and Bayesian Inference. *PLOS Comput. Biol.* **12**, e1004736.

Rakhade, S.N., Jensen, F.E., (2009). Epileptogenesis in the immature brain: Emerging mechanisms. *Nat. Rev. Neurol.* **5**, 380–391.

Randlett, O., Wee, C.L., Naumann, E. a, Nnaemeka, O., Schoppik, D., et al., (2015). Whole-brain activity mapping onto a zebrafish brain atlas. *Nat. Methods* **12**, 1039–1046.

Ranlund, S., Adams, R.A., Díez, Á., Constante, M., Dutt, A., et al., (2016). Impaired prefrontal synaptic gain in people with psychosis and their relatives during the mismatch negativity. *Hum. Brain Mapp.* **37**, 351–365.

Richardson, M.P., (2011). New observations may inform seizure models: very fast and very slow oscillations. *Prog. Biophys. Mol. Biol.* **105**, 5–13.

Roopun, A.K., Cunningham, M.O., Racca, C., Alter, K., Traub, R.D., et al., (2008). Region-specific changes in gamma and beta2 rhythms in NMDA receptor dysfunction models of schizophrenia. *Schizophr. Bull.* **34**, 962–973.

Rosch, R., Baldeweg, T., Moeller, F., Baier, G., (2018). Network dynamics in the healthy and epileptic developing brain. *Netw. Neurosci.* **2**, 41–59.

Rosch, R.E., Cooray, G., Friston, K.J., (2017). Dynamic Causal Modelling of Dynamic Dysfunction in NMDA-Receptor Antibody Encephalitis. Springer, Cham, pp. 121–148.

Rosier, A.M., Arckens, L., Orban, G.A., Vandesande, F., (1993). Laminar distribution of NMDA receptors in cat and monkey visual cortex visualized by [3H]-MK-801 binding. *J. Comp. Neurol.* **335**, 369–380.

Rowitch, D.H., Kriegstein, A.R., (2010). Developmental genetics of vertebrate glial-cell specification. *Nature* **468**, 214–222.

Rubinov, M., Sporns, O., Thivierge, J.P., Breakspear, M., (2011). Neurobiologically realistic determinants of Self-Organized criticality in networks of spiking neurons. *PLoS Comput. Biol.* **7**.

Sadleir, L.G., Mountier, E.I., Gill, D., Davis, S., Joshi, C., et al., (2017). Not all *SCN1A*epileptic encephalopathies are Dravet syndrome. *Neurology* **89**, 1035–1042.

Saggio, M.L., Ritter, P., Jirsa, V.K., (2016). Analytical Operations Relate Structural and Functional Connectivity in the Brain. *PLoS One* **11**, e0157292.

Sanchez, J.T., Ghelani, S., Otto-Meyer, S., (2015). From development to disease: Diverse functions of NMDA-type glutamate receptors in the lower auditory pathway. *Neuroscience* **285**, 248–259.

Scheffer, I.E., (2011). Does genotype determine phenotype?: Sodium channel mutations in Dravet syndrome and GEFS+. *Neurology* **76**, 588–589.

Scheffer, I.E., Berkovic, S., Capovilla, G., Connolly, M.B., French, J., et al., (2017). ILAE classification of the epilepsies: Position paper of the ILAE Commission for Classification and Terminology. *Epilepsia* **58**, 512–521.

Schiff, S.J., Sauer, T., (2008). Kalman filter control of a model of spatiotemporal cortical dynamics. *J. Neural Eng.* **5**, 1–8.

Schindler, K. a., Bialonski, S., Horstmann, M.T., Elger, C.E., Lehnertz, K., (2008). Evolving functional network properties and synchronizability during human epileptic seizures. *Chaos* **18**.

Schizophrenia Working Group of the Psychiatric Genomics Consortium, (2014). Biological insights from 108 schizophrenia-associated genetic loci. *Nature* **511**, 421–427.

Schmidt, A., Diaconescu, A.O., Kometer, M., Friston, K.J., Stephan, K.E., et al., (2013). Modeling Ketamine Effects on Synaptic Plasticity During the Mismatch Negativity. *Cereb. Cortex* **23**, 2394–2406.

Schmidt, H., Petkov, G., Richardson, M.P., Terry, J.R., (2014). Dynamics on Networks: The Role of Local Dynamics and Global Networks on the Emergence of Hypersynchronous Neural Activity. *PLoS Comput. Biol.* **10**, e1003947.

Schmitt, S.E., Pargeon, K., Frechette, E.S., Hirsch, L.J., Dalmau, J., et al., (2012). Extreme delta brush: A unique EEG pattern in adults with anti-NMDA receptor encephalitis. *Neurology* **79**, 1094–1100.

Schröder, J., Niethammer, R., Geider, F.-J., Reitz, C., Binkert, M., et al., (1991). Neurological soft signs in schizophrenia. *Schizophr. Res.* **6**, 25–30.

Schröder, W., Hinterkeuser, S., Seifert, G., Schramm, J., Jabs, R., et al., (2000). Functional and molecular properties of human astrocytes in acute hippocampal slices obtained from patients with temporal lobe epilepsy. *Epilepsia* **41 Suppl 6**, S181-4.

Schröger, E., Bendixen, A., Denham, S.L., Mill, R.W., Bőhm, T.M., et al., (2014). Predictive Regularity Representations in Violation Detection and Auditory Stream Segregation: From Conceptual to Computational Models. *Brain Topogr.* **27**, 565–577.

Schubert, D., Kotter, R., Zilles, K., Luhmann, H.J., Staiger, J.F., (2003). Cell Type-Specific Circuits of Cortical Layer IV Spiny Neurons. *J. Neurosci.* **23**, 2961–2970.

Schulz, R., Lüders, H.O., Hoppe, M., Tuxhorn, I., May, T., et al., (2000). Interictal EEG and ictal scalp EEG propagation are highly predictive of surgical outcome in mesial temporal lobe epilepsy. *Epilepsia* **41**, 564–570.

Schwertner, A., Zortea, M., Torres, F. V, Caumo, W., (2018). Effects of Subanesthetic Ketamine Administration on Visual and Auditory Event-Related Potentials (ERP) in Humans: A Systematic Review. *Front. Behav. Neurosci.* **12**.

Seo, S., Leitch, B., (2014). Altered thalamic GABAA-receptor subunit expression in the stargazer mouse model of absence epilepsy. *Epilepsia* **55**, 224–232.

Sham, P.C., MacLean, C.J., Kendler, K.S., (1994). A typological model of schizophrenia based on age at onset, sex and familial morbidity. *Acta Psychiatr. Scand.* **89**, 135–141.

Shifman, S., Bronstein, M., Sternfeld, M., Pisanté-Shalom, A., Lev-Lehman, E., et al., (2002). A Highly Significant Association between a COMT Haplotype and Schizophrenia. *Am. J. Hum. Genet.* **71**, 1296–1302.

Shipp, S., (2016). Neural elements for predictive coding. *Front. Psychol.* **7**, 1–21.

Shirvany, Y., Edelvik, F., Jakobsson, S., Hedstrom, A., Mahmood, Q., et al., (2012). Non-invasive EEG source localization using particle swarm optimization: A clinical experiment, in: 2012 Annual International Conference of the IEEE Engineering in

Medicine and Biology Society. IEEE, pp. 6232–6235.

Shu, Y., Hasenstaub, A., McCormick, D. a., (2003). Turning on and off recurrent balanced cortical activity. *Nature* **423**, 288–293.

Shultz, S., Klin, A., Jones, W., (2018). Neonatal Transitions in Social Behavior and Their Implications for Autism. *Trends Cogn. Sci.* **22**, 452–469.

Silbereis, J.C., Pochareddy, S., Zhu, Y., Li, M., Sestan, N., (2016). The Cellular and Molecular Landscapes of the Developing Human Central Nervous System. *Neuron* **89**, 268.

Sinha, N., Dauwels, J., Kaiser, M., Cash, S.S., Brandon Westover, M., et al., (2017). Predicting neurosurgical outcomes in focal epilepsy patients using computational modelling. *Brain* **140**, 319–332.

Sitnikova, E., Dikanev, T., Smirnov, D., Bezruchko, B., van Luijtelaar, G., (2008). Granger causality: Cortico-thalamic interdependencies during absence seizures in WAG/Rij rats. *J. Neurosci. Methods* **170**, 245–254.

Smith, E.H., Liou, J., Davis, T.S., Merricks, E.M., Kellis, S.S., et al., (2016). The ictal wavefront is the spatiotemporal source of discharges during spontaneous human seizures. *Nat. Commun.* **7**, 11098.

Smith, S.J.M., (2005). EEG in the diagnosis, classification, and management of patients with epilepsy. *J. Neurol. Neurosurg. Psychiatry* **76**, ii2-ii7.

Song, I., Savtchenko, L., Semyanov, A., (2011). Tonic excitation or inhibition is set by GABA(A) conductance in hippocampal interneurons. *Nat. Commun.* **2**, 376.

Spampanato, J., Aradi, I., Soltesz, I., Goldin, a L., (2004). Increased neuronal firing in computer simulations of sodium channel mutations that cause generalized epilepsy with febrile seizures plus. *J Neurophysiol* **91**, 2040–2050.

Speckmann, E.-J., Elger, C.E., (2005). Introduction to the Neurophysiological Basis of the EEG and DC Potentials, in: Niedermeyer, E., Lopes da Silva, F.H. (Eds.), Electroencephalography: Basic Principles, Clinical Applications, and Related Fields. Lippincott Williams & Wilkins, p. 1309.

Spencer, S., Huh, L., (2008). Outcomes of epilepsy surgery in adults and children. *Lancet Neurol.* **7**, 525–537.

Spillane, J., Kullmann, D.M., Hanna, M.G., (2016). Genetic neurological channelopathies: molecular genetics and clinical phenotypes. *J. Neurol. Neurosurg. Psychiatry* **87**.

Stephan, K.E., Binder, E.B., Breakspear, M., Dayan, P., Johnstone, E.C., et al., (2016). Charting the landscape of priority problems in psychiatry, part 2: Pathogenesis and aetiology. *The Lancet Psychiatry* **3**, 84–90.

Stephan, K.E., Penny, W.D., Moran, R.J., den Ouden, H.E.M., Daunizeau, J., et al., (2010). Ten simple rules for dynamic causal modeling. *Neuroimage* **49**, 3099–3109.

Steriade, M., McCormick, D., Sejnowski, T., (1993). Thalamocortical oscillations in the sleeping and aroused brain. *Science'* **262**, 679–685.

Strauss, G.P., Cohen, A.S., (2017). A Transdiagnostic Review of Negative Symptom Phenomenology and Etiology. *Schizophr. Bull.* **43**, 712–729.

Strohman, R., (2002). Maneuvering in the complex path from genotype to phenotype. *Science* **296**, 701–703.

Sullivan, P.F., Kendler, K.S., Neale, M.C., (2003). Schizophrenia as a Complex Trait. *Arch. Gen. Psychiatry* **60**, 1187.

Sun, L., Gilligan, J., Staber, C., Schutte, R.J., Nguyen, V., et al., (2012). A Knock-In Model of Human Epilepsy in Drosophila Reveals a Novel Cellular Mechanism Associated with Heat-Induced Seizure. *J. Neurosci.* **32**, 14145–14155.

Symmonds, M., Moran, C.H., Leite, M.I., Buckley, C., Irani, S.R., et al., (2018). Ion channels in EEG: isolating channel dysfunction in NMDA receptor antibody encephalitis. *Brain* **141**, 1691–1702.

Takeda, K., Sumiyoshi, T., Matsumoto, M., Murayama, K., Ikezawa, S., et al., (2018). Neural correlates for intrinsic motivational deficits of schizophrenia; implications for therapeutics of cognitive impairment. *Front. Psychiatry* **9**.

Tandon, R., Gaebel, W., Barch, D.M., Bustillo, J., Gur, R.E., et al., (2013). Definition and description of schizophrenia in the DSM-5. *Schizophr. Res.* **150**, 3–10.

Taylor, P.N., Sinha, N., Wang, Y., Vos, S.B., de Tisi, J., et al., (2018). The impact of epilepsy surgery on the structural connectome and its relation to outcome. *NeuroImage Clin.* **18**, 202–214.

Thiebes, S., Leicht, G., Curic, S., Steinmann, S., Polomac, N., et al., (2017). Glutamatergic deficit and schizophrenia-like negative symptoms: new evidence from ketamine-induced mismatch negativity alterations in healthy male humans. *J. Psychiatry Neurosci.* **42**, 273–283.

Thiele, A., (2012). NMDA receptors figure it out. *Proc. Natl. Acad. Sci.* **109**, 10749–10750.

Thomas, E.M., Greene, B.R., Lightbody, G., Marnane, W.P., Boylan, G.B., (2008). Seizure detection in neonates: Improved classification through supervised adaptation, in: 2008 30th Annual International Conference of the IEEE Engineering in Medicine and Biology Society. IEEE, pp. 903–906.

Thomas, R.H., Berkovic, S.F., (2014). The hidden genetics of epilepsy—a clinically important new paradigm. *Nat. Rev. Neurol.* **10**, 283–292.

Thomson, A.M., (2003). Interlaminar Connections in the Neocortex. *Cereb. Cortex* **13**, 5–14.

Thornton, R., Vulliemoz, S., Rodionov, R., Carmichael, D.W., Chaudhary, U.J., et al., (2011). Epileptic networks in focal cortical dysplasia revealed using electroencephalography-functional magnetic resonance imaging. *Ann. Neurol.* **70**, 822–837.

Tierney, T.M., Weiss-Croft, L.J., Centeno, M., Shamshiri, E. a., Perani, S., et al., (2016). FIACH: A biophysical model for automatic retrospective noise control in fMRI. *Neuroimage* **124**, 1009–1020.

Todd, J., Heathcote, A., Whitson, L.R., Mullens, D., Provost, A., et al., (2014). Mismatch negativity (MMN) to pitch change is susceptible to order-dependent bias. *Front. Neurosci.* **8**, 1–9.

Tong, S., Thakor, N.V., (2009). Quantitative EEG Analysis. Methods and Clinical

Applications. Artech House, Boston.

Tononi, G., Cirelli, C., (2006). Sleep function and synaptic homeostasis. *Sleep Med. Rev.* **10**, 49–62.

Trump, N., McTague, A., Brittain, H., Papandreou, A., Meyer, E., et al., (2016). Improving diagnosis and broadening the phenotypes in early-onset seizure and severe developmental delay disorders through gene panel analysis. *J. Med. Genet.* **53**, 310–317.

Turrini, L., Fornetto, C., Marchetto, G., M?llenbroich, M.C., Tiso, N., et al., (2017). Optical mapping of neuronal activity during seizures in zebrafish. *Sci. Rep.* **7**, 3025.

Uhlhaas, P.J., Roux, F., Singer, W., Haenschel, C., Sireteanu, R., et al., (2009). The development of neural synchrony reflects late maturation and restructuring of functional networks in humans. *Proc. Natl. Acad. Sci.* **106**, 9866–9871.

Uhlhaas, P.J., Singer, W., (2010). Abnormal neural oscillations and synchrony in schizophrenia. *Nat. Rev. Neurosci.* **11**, 100–113.

Ullah, G., Schiff, S.J., (2010). Assimilating seizure dynamics. *PLoS Comput. Biol.* **6**, e1000776.

Umbricht, D., Koller, R., Vollenweider, F.X., Schmid, L., (2002). Mismatch negativity predicts psychotic experiences induced by NMDA receptor antagonist in healthy volunteers. *Biol. Psychiatry* **51**, 400–406.

Umbricht, D., Krljes, S., (2005). Mismatch negativity in schizophrenia: a meta-analysis. *Schizophr. Res.* **76**, 1–23.

Umbricht, D., Schmid, L., Koller, R., Vollenweider, F.X., Hell, D., et al., (2000). Ketamine-Induced Deficits in Auditory and Visual Context-Dependent Processing in Healthy Volunteers. *Arch. Gen. Psychiatry* **57**, 1139.

Uppal, N., Foxe, J.J., Butler, J.S., Acluche, F., Molholm, S., (2016). The neural dynamics of somatosensory processing and adaptation across childhood: a high-density electrical mapping study. *J. Neurophysiol.* **115**, 1605–1619.

van Dellen, E., Douw, L., Hillebrand, A., Ris-Hilgersom, I.H.M., Schoonheim, M.M., et al., (2012). MEG Network Differences between Low- and High-Grade Glioma Related to Epilepsy and Cognition. *PLoS One* **7**, e50122.

Van Essen, D.C., Glasser, M.F., (2016). The human connectome project: Progress and prospects. *Cerebrum Dana Forum Brain Sci.* **2016**, cer-10-16.

Vértes, P.E., Rittman, T., Whitaker, K.J., Romero-Garcia, R., Váša, F., et al., (2016). Gene transcription profiles associated with inter-modular hubs and connection distance in human functional magnetic resonance imaging networks. *Philos. Trans. R. Soc. B Biol. Sci.* **371**, 20150362.

Volkers, L., Kahlig, K.M., Das, J.H.G.G., van Kempen, M.J.A.A., Lindhout, D., et al., (2013). Febrile temperatures unmask biophysical defects in Nav1.1 epilepsy mutations supportive of seizure initiation. *J. Gen. Physiol.* **142**, 641–653.

von Spiczak, S., Muhle, H., Helbig, I., de Kovel, C.G.F., Hampe, J., et al., (2010). Association study of TRPC4 as a candidate gene for generalized epilepsy with photosensitivity. *Neuromolecular Med.* **12**, 292–299.

Vonberg, F.W., Bigdeli, T.B., (2015). Genetic Correlation Between Schizophrenia and Epilepsy. *JAMA Neurol.* **02115**, 1–2.

Wacongne, C., Changeux, J.-P., Dehaene, S., (2012). A Neuronal Model of Predictive Coding Accounting for the Mismatch Negativity. *J. Neurosci.* **32**, 3665–3678.

Walsh, T., McClellan, J.M., McCarthy, S.E., Addington, A.M., Pierce, S.B., et al., (2008). Rare Structural Variants Disrupt Multiple Genes in Neurodevelopmental Pathways in Schizophrenia. *Science'* **320**, 539–543.

Wandinger, K.P., Saschenbrecker, S., Stoecker, W., Dalmau, J., (2011). Anti-NMDA-receptor encephalitis: A severe, multistage, treatable disorder presenting with psychosis. *J. Neuroimmunol.* **231**, 86–91.

Wang, Y., Goodfellow, M., Taylor, P.N., Baier, G., (2014). Dynamic Mechanisms of Neocortical Focal Seizure Onset. *PLoS Comput. Biol.* **10**, e1003787.

Wang, Y., Goodfellow, M., Taylor, P.N., Baier, G., (2012). Phase space approach for modeling of epileptic dynamics. *Phys. Rev. E* **85**, 061918.

Weinberger, D.R., (1993). A connectionist approach to the prefrontal cortex. *J. Neuropsychiatry Clin. Neurosci.* **5**, 241–53.

Weiss-Croft, L.J., Baldeweg, T., (2015). Maturation of language networks in children: A systematic review of 22years of functional MRI. *Neuroimage* **123**, 269–281.

Wendling, F., Bartolomei, F., Bellanger, J.J., Chauvel, P., (2002). Epileptic fast activity can be explained by a model of impaired GABAergic dendritic inhibition. *Eur. J. Neurosci.* **15**, 1499–1508.

Wendling, F., Benquet, P., Bartolomei, F., Jirsa, V., (2016). Computational models of epileptiform activity. *J. Neurosci. Methods* **260**, 233–251.

Wenzel, A., Fritschy, J.M., Mohler, H., Benke, D., (1997). NMDA Receptor Heterogeneity During Postnatal Development of the Rat Brain: Differential Expression of the NR2A, NR2B, and NR2C Subunit Proteins. *J. Neurochem.* **68**, 469–478.

Werner, G., (2007). Metastability, criticality and phase transitions in brain and its models. *Biosystems* **90**, 496–508.

West, J.W., Patton, D.E., Scheuer, T., Wang, Y., Goldin, A.L., et al., (1992). A cluster of hydrophobic amino acid residues required for fast Na (+)-channel inactivation. *Proc. Natl. Acad. Sci.* **89**, 10910–10914.

Whitaker, K.J., Vértes, P.E., Romero-Garcia, R., Váša, F., Moutoussis, M., et al., (2016). Adolescence is associated with transcriptionally patterned consolidation of the hubs of the human brain connectome. *Proc. Natl. Acad. Sci.* 2–7.

Whitford, T.J., Rennie, C.J., Grieve, S.M., Clark, C.R., Gordon, E., et al., (2007). Brain maturation in adolescence: concurrent changes in neuroanatomy and neurophysiology. *Hum. Brain Mapp.* **28**, 228–37.

Willms, A.R., Baro, D.J., Harris-Warrick, R.M., Guckenheimer, J., (1999). An improved parameter estimation method for Hodgkin-Huxley models. *J. Comput. Neurosci.* **6**, 145–168.

Wilson, H.R., Cowan, J.D., (1972). Excitatory and inhibitory interactions in localized

populations of model neurons. *Biophys. J.* **12**, 1–24.

Winter, M.J., Redfern, W.S., Hayfield, A.J., Owen, S.F., Valentin, J.-P., et al., (2008). Validation of a larval zebrafish locomotor assay for assessing the seizure liability of early-stage development drugs. *J. Pharmacol. Toxicol. Methods* **57**, 176–187.

Winter, M.J., Windell, D., Metz, J., Matthews, P., Pinion, J., et al., (2017). 4-Dimensional Functional Profiling in the Convulsant-Treated Larval Zebrafish Brain. *Sci. Rep.* **7**, 6581.

Wittchen, H.W., Nelson, C.B., Lachner, G., (1998). Prevalence of mental disorders and psychosocial impairments in adolescents and young adults. *Psychol. Med.* **28**, 109–126.

Wolf, S., Supatto, W., Debrégeas, G., Mahou, P., Kruglik, S.G., et al., (2015). Whole-brain functional imaging with two-photon light-sheet microscopy. *Nat. Methods* **12**, 379–380.

Wolff, M., Cassé-Perrot, C., Dravet, C., (2006). Severe Myoclonic Epilepsy of Infants (Dravet Syndrome): Natural History and Neuropsychological Findings. *Epilepsia* **47**, 45–48.

World Health Organization, (2005). Atlas: Epilepsy care in the world 2005 [http://apps.who.int/iris/handle/10665/43298] *accessed*: 12/12/2016.

Wright, C.F., Fitzgerald, T.W., Jones, W.D., Clayton, S., McRae, J.F., et al., (2015). Genetic diagnosis of developmental disorders in the DDD study: a scalable analysis of genome-wide research data. *Lancet* **385**, 1305–1314.

Wright, S., Hacohen, Y., Jacobson, L., Agrawal, S., Gupta, R., et al., (2015a). N-methyl-D-aspartate receptor antibody-mediated neurological disease: results of a UK-based surveillance study in children. *Arch. Dis. Child.* **100**, 521–526.

Wright, S., Hashemi, K., Stasiak, L., Bartram, J., Lang, B., et al., (2015b). Epileptogenic effects of NMDAR antibodies in a passive transfer mouse model. *Brain* **138**, 1–9.

Wynn, J.K., Sugar, C., Horan, W.P., Kern, R., Green, M.F., (2010). Mismatch Negativity, Social Cognition, and Functioning in Schizophrenia Patients. *Biol. Psychiatry* **67**, 940–947.

Yang, Y., Higashimori, H., Morel, L., (2013). Developmental maturation of astrocytes and pathogenesis of neurodevelopmental disorders. *J. Neurodev. Disord.* **5**, 22.

Ylinen, S., Huuskonen, M., Mikkola, K., Saure, E., Sinkkonen, T., et al., (2016). Predictive coding of phonological rules in auditory cortex: A mismatch negativity study. *Brain Lang.* **162**, 72–80.

Yu, F.H., Mantegazza, M., Westenbroek, R.E., Robbins, C. a, Kalume, F., et al., (2006). Reduced sodium current in GABAergic interneurons in a mouse model of severe myoclonic epilepsy in infancy. *Nat. Neurosci.* **9**, 1142–1149.

Zschocke, S., Hansen, H.-C., (2012). Klinische Elektroenzepalographie, 3rd ed. Springer-Verlag, Berlin, Heidelberg.

Zuberi, S.M., Brunklaus, A., Birch, R., Reavey, E., Duncan, J., et al., (2011). Genotype-phenotype associations in SCN1A-related epilepsies. *Neurology* **76**, 594–600.

Appendix

A.1 HRA Approval Letter for patient consent waiver

NHS
Health Research Authority

Dr Richard Rosch
Honorary Clinical Fellow
Great Ormond Street Hospital for Children
Department of Clinical Neurophysiology
Great Ormond Street
London
WC1N 3JH

Email: hra.approval@nhs.net

22 June 2017

Dear Dr Rosch

Letter of HRA Approval

Study title:	**Modelling Molecular Seizures**
IRAS project ID:	**229772**
Sponsor	**Great Ormond Street Hospital for Children NHS Foundation Trust**

I am pleased to confirm that **HRA Approval** has been given for the above referenced study, on the basis described in the application form, protocol, supporting documentation and any clarifications noted in this letter.

Participation of NHS Organisations in England

The sponsor should now provide a copy of this letter to all participating NHS organisations in England.

Appendix B provides important information for sponsors and participating NHS organisations in England for arranging and confirming capacity and capability. **Please read *Appendix B* carefully**, in particular the following sections:

- *Participating NHS organisations in England* – this clarifies the types of participating organisations in the study and whether or not all organisations will be undertaking the same activities
- *Confirmation of capacity and capability* - this confirms whether or not each type of participating NHS organisation in England is expected to give formal confirmation of capacity and capability. Where formal confirmation is not expected, the section also provides details on the time limit given to participating organisations to opt out of the study, or request additional time, before their participation is assumed.
- *Allocation of responsibilities and rights are agreed and documented (4.1 of HRA assessment criteria)* - this provides detail on the form of agreement to be used in the study to confirm capacity and capability, where applicable.

Further information on funding, HR processes, and compliance with HRA criteria and standards is also provided.

It is critical that you involve both the research management function (e.g. R&D office) supporting each organisation and the local research team (where there is one) in setting up your study. Contact details and further information about working with the research management function for each organisation can be accessed from www.hra.nhs.uk/hra-approval.

Appendices

The HRA Approval letter contains the following appendices:

- A – List of documents reviewed during HRA assessment
- B – Summary of HRA assessment

After HRA Approval

The attached document *"After HRA Approval – guidance for sponsors and investigators"* gives detailed guidance on reporting expectations for studies with HRA Approval, including:

- Working with organisations hosting the research
- Registration of Research
- Notifying amendments
- Notifying the end of the study

The HRA website also provides guidance on these topics and is updated in the light of changes in reporting expectations or procedures.

Scope

HRA Approval provides an approval for research involving patients or staff in NHS organisations in England.

If your study involves NHS organisations in other countries in the UK, please contact the relevant national coordinating functions for support and advice. Further information can be found at http://www.hra.nhs.uk/resources/applying-for-reviews/nhs-hsc-rd-review/.

If there are participating non-NHS organisations, local agreement should be obtained in accordance with the procedures of the local participating non-NHS organisation.

User Feedback

The Health Research Authority is continually striving to provide a high quality service to all applicants and sponsors. You are invited to give your view of the service you have received and the application procedure. If you wish to make your views known please use the feedback form available on the HRA website: http://www.hra.nhs.uk/about-the-hra/governance/quality-assurance/.

HRA Training

We are pleased to welcome researchers and research management staff at our training days – see details at http://www.hra.nhs.uk/hra-training/

Your IRAS project ID is **229772**. Please quote this on all correspondence.

IRAS project ID	229772

Yours sincerely,

Natalie Wilson
Assessor

Email: hra.approval@nhs.net

Copy to: *Ms Emma Pendleton, UCL Great Ormond Street Institute of Child Health, Sponsor contact*
Dr Thomas Lewis, UCL Great Ormond Street Institute of Child Health, Lead NHS R&D contact

Appendix A - List of Documents

The final document set assessed and approved by HRA Approval is listed below.

Document	*Version*	*Date*
IRAS Application Form [IRAS_Form_26052017]		26 May 2017
IRAS Application Form XML file [IRAS_Form_26052017]		26 May 2017
IRAS Checklist XML [Checklist_26052017]		26 May 2017
Letter from funder [award letter]		07 June 2017
Other [Statement of Activities]	1	19 June 2017
Other [Schedule of Events]	1	19 June 2017
Research protocol or project proposal [Research Protocol]	1.0	24 May 2017
Summary CV for Chief Investigator (CI) [Chief Investigator CV]		22 May 2017

Appendix B - Summary of HRA Assessment

This appendix provides assurance to you, the sponsor and the NHS in England that the study, as reviewed for HRA Approval, is compliant with relevant standards. It also provides information and clarification, where appropriate, to participating NHS organisations in England to assist in assessing and arranging capacity and capability.

For information on how the sponsor should be working with participating NHS organisations in England, please refer to the, *participating NHS organisations, capacity and capability* and *Allocation of responsibilities and rights are agreed and documented (4.1 of HRA assessment criteria)* sections in this appendix.

The following person is the sponsor contact for the purpose of addressing participating organisation questions relating to the study:

Name: Richard Rosch

Email: r.rosch@ucl.ac.uk

HRA assessment criteria

Section	HRA Assessment Criteria	Compliant with Standards	Comments
1.1	IRAS application completed correctly	Yes	No comments
2.1	Participant information/consent documents and consent process	Yes	No comments
3.1	Protocol assessment	Yes	No comments
4.1	Allocation of responsibilities and rights are agreed and documented	Yes	This is a non-commercial, multicentre study taking place in the NHS. A Statement of Activities has been submitted. This will act as the agreement between Sponsor and participating NHS organisations. No other agreements are expected.
4.2	Insurance/indemnity arrangements assessed	Yes	Where applicable, independent contractors (e.g. General Practitioners) should ensure that the professional indemnity provided by their medical

Section	HRA Assessment Criteria	Compliant with Standards	Comments
			defence organisation covers the activities expected of them for this research study
4.3	Financial arrangements assessed	Yes	Sponsor is not providing funding to participating NHS organisations.
5.1	Compliance with the Data Protection Act and data security issues assessed	Yes	No comments
5.2	CTIMPS – Arrangements for compliance with the Clinical Trials Regulations assessed	Not Applicable	
5.3	Compliance with any applicable laws or regulations	Yes	No comments
6.1	NHS Research Ethics Committee favourable opinion received for applicable studies	Not Applicable	
6.2	CTIMPS – Clinical Trials Authorisation (CTA) letter received	Not Applicable	
6.3	Devices – MHRA notice of no objection received	Not Applicable	
6.4	Other regulatory approvals and authorisations received	Not Applicable	

Participating NHS Organisations in England

This provides detail on the types of participating NHS organisations in the study and a statement as to whether the activities at all organisations are the same or different.
This is a non-commercial, multicentre study. There is only one site-type involved in the research. Activities and procedures as described in the protocol will take place at participating NHS organisations. The Chief Investigator or sponsor should share relevant study documents with participating NHS organisations in England in order to put arrangements in place to deliver the study. The documents should be sent to both the local study team, where applicable, and the office providing the research management function at the participating organisation. For NIHR CRN Portfolio studies, the Local

LCRN contact should also be copied into this correspondence. For further guidance on working with participating NHS organisations please see the HRA website.
If chief investigators, sponsors or principal investigators are asked to complete site level forms for participating NHS organisations in England which are not provided in IRAS or on the HRA website, the chief investigator, sponsor or principal investigator should notify the HRA immediately at hra.approval@nhs.net. The HRA will work with these organisations to achieve a consistent approach to information provision.

Confirmation of Capacity and Capability

This describes whether formal confirmation of capacity and capability is expected from participating NHS organisations in England.

Participating NHS organisations in England **will be expected to formally confirm their capacity and capability to host this research**.

- Following issue of this letter, participating NHS organisations in England may now confirm to the sponsor their capacity and capability to host this research, when ready to do so. How capacity and capacity will be confirmed is detailed in the *Allocation of responsibilities and rights are agreed and documented (4.1 of HRA assessment criteria)* section of this appendix.
- The Assessing, Arranging, and Confirming document on the HRA website provides further information for the sponsor and NHS organisations on assessing, arranging and confirming capacity and capability.

Principal Investigator Suitability

This confirms whether the sponsor position on whether a PI, LC or neither should be in place is correct for each type of participating NHS organisation in England and the minimum expectations for education, training and experience that PIs should meet (where applicable).

Neither a Principal Investigator (PI) nor Local Collaborator (LC) is expected at participating NHS organisations.

Sponsor recommends that research staff undertake Good Clinical Practice Training.

GCP training is not a generic training expectation, in line with the HRA statement on training expectations.

HR Good Practice Resource Pack Expectations

This confirms the HR Good Practice Resource Pack expectations for the study and the pre-engagement checks that should and should not be undertaken

Due to the nature of the research, no Honorary Research Contracts, Letters of Access or pre-engagement checks would be expected.

Other Information to Aid Study Set-up

This details any other information that may be helpful to sponsors and participating NHS organisations in England to aid study set-up.
The applicant has indicated that they do not intend to apply for inclusion on the NIHR CRN Portfolio.

A.2 Integrated research application system (IRAS) - Protocol

MODELLING MOLECULAR SEIZURES

STUDY INVESTIGATOR(S)

Principal Investigator: Dr Richard Rosch

Clinical Research Fellow

Email: r.rosch@ucl.ac.uk

1. UCL Great Ormond Street Institute of Child Health, WC1N 3EH, London, UK

1. INTRODUCTION

Genetic and other molecular diagnostics have revolutionised our understanding of many neurological conditions in childhood, including many different paediatric epilepsy syndromes. Based on these findings, many conditions can now be understood as disturbances in synaptic function caused by specific molecular alterations in channel and other synaptic proteins. However, how problems with individual molecular at the neuronal membrane translate to abnormal brain function is still poorly understood. This study aims to improve this understanding by using *in silico*, computational modelling of brain dynamics to link patients' phenotypes with underlying neuronal abnormalities.

2. BACKGROUND

Computational modelling already has an established role in furthering our understand of mechanisms underlying different types of epilepsy (Lytton, 2008). In the context of epilepsies with a known molecular cause, computational models offer two conceptually complementary approaches: Models can be used in a *bottom up* approach, predicting the dynamic dysfunction caused by molecular abnormalities the whole neuron, or microcircuit (Peters et al., 2016); Alternatively, in a *top-down* approach, modelling of EEG recordings at the level of integrated

neuronal assemblies can help identify specific changes in microcircuitry associated with known molecular abnormalities (Gilbert et al., 2016).

The results from these complementary approaches can then be used in two different ways: (1) They can outline a mechanism linking molecular abnormalities with whole-brain phenotypes in a single mechanistic understanding of the condition (Kopell et al., 2014), (2) They may support more neurobiologically relevant classification of patients into different categories (Brodersen et al., 2011), (3) They may in the future be used to predict treatment outcomes for individual patients (Sinha et al., 2017).

Recent advances in computational modelling (Friston et al., 2015), and molecular diagnostics (Møller et al., 2015) have set the context in which this proposed study now can take place: There are now established cohorts of patients with shared molecular causes for their neurological condition (e.g. genetic mutations, neuronal antibodies); and computational modelling of the molecular and microcircuit basis of neuronal dynamics allows us to identify shared abnormalities between patients.

3. AIM(S) OF STUDY

The aim of this study is to identify possible mechanisms that underlie disorders in neuronal function in paediatric patients with known molecular abnormalities. In order to address this overall aim, the study will address the following objectives

4. OBJECTIVES

1) **Collate anonymised, basic clinical information** on cohorts of patients with disturbance of neuronal function and shared molecular abnormality (e.g. identified gene mutation, identified antibody to neuronal surface molecule).
2) **Bottom-up Modelling:** Predicting dynamic consequences of genetic mutations at the neuronal membrane and neuronal microcircuits (e.g. from miss-sense mutations identified in single genes)
3) **Top-down Modelling:** Identifying network disturbances underlying specific EEG features observed in patients with known molecular talk (e.g. dynamic EEG abnormalities in patients with antibodies to NMDA-receptor abnormalities)

5. HYPOTHESIS

5b. Primary Hypothesis

H1) Similar molecular disturbances cause similar disturbances in neuronal function, as estimated from computational models of neuronal populations

5b. Secondary Hypotheses

H2) Computational models of molecular disturbance at the 'microscale' can predict the abnormalities identified from computational models of the EEG 'macroscale'

H3) Model parameters may be used to distinguish different patient groups in a machine learning classification appraoch

6. STUDY DESIGN

This study is a retrospective, observational cohort study, applying quantitative analysis to clinical data, such as single gene sequencing results and clinical EEG recordings.

7. STUDY SETTING/LOCATION

The study will be conducted from 01/06/2017 – 01/06/2020, and data collation will include historical records of patients identified prior to the study date. The study will be conducted at approximately 4 investigative sites across England, and Ireland. Collation will stop when approximately 50 subjects across all cohorts have been identified.

Study sites will include: Great Ormond Street Hospital NHS Foundation Trust, London, UK; Evelina London Children's Hospital, Guy's and St. Thomas' NHS Foundation Trust, London, UK; King's College Hospital NHS Foundation Trust, London, UK; Children's University Hospital, Dublin, Ireland.

8. STUDY POPULATION

The study will collate several distinct cohorts with identified molecular abnormalities according to the inclusion and exclusion criteria below. Broadly selection will be based on identified molecular causes for the patients' neurological conditions (i.e. genetic testing results, identification of neuronal surface antibodies, etc).

9. ELIGIBILITY CRITERIA

9a. Inclusion criteria

1) Paediatric patients: Age of clinical symptom onset 0 – 16 years
2) Abnormal EEG recordings on record and accessible at one of the study sites
3) Laboratory confirmed clinical diagnosis of one of
    a. *SCN1A* – mutation associated epilepsy
    b. *NMDA*-receptor antibody associated encephalitis
    c. *GRIN2A* – mutation associated epilepsy
    d. Tuberous sclerosis
    e. Other genetic, or autoimmune epileptic or encephalopathic conditions of childhood with confirmed molecular cause

9b. Exclusion criteria

1) Laboratory results of molecular diagnostics not available

10. STUDY OUTCOMES

10a. Primary Outcome

The primary outcome measure will be statistical evidence for shared parameter abnormalities between patients with the same molecular abnormalities, estimated from the computational models and using a Bayesian analysis framework (where a Bayes factor > 3 will be considered strong evidence)

10b. Secondary Outcome(s)

The modelling will also provide more quantitative outcome measures regarding the types of dynamic abnormalities seen in patient cohorts (corresponding to seizure susceptibility, or instability of certain dynamic states)

11. STUDY PROCEDURES

The study procedures are limited to review of existing medical records and will not require access to any biological specimens or patient identifiers by the research team.

11a. Recruitment of participants

Cases will be ascertained and summarised by treating clinicians. All analyses will be completed on anonymised case summaries only. Cases will be identified from routine clinical service by the clinicians responsible for clinical care (including but not limited to paediatric epileptologists, paediatricians, clinical neurophysiologists, clinical geneticist) in accordance with the inclusion and exclusion criteria outlined above. Cases can be included from clinical cohorts, historical records in existing research databases, and clinical databases held in the respective departments.

11b. Study procedure

Basic demographic information and case histories will be summarised from the clinical notes (including electronic patient records, clinic letters, etc). EEG recordings will be copied in electronically from the recording EEG department. Genetic and antibody diagnostics will be derived from the clinical notes, or directly from the performing laboratory and summarised.

11c. Measurement tools used

Clinical case will be included in anonymised and summarised form. The variables included in the case summaries will include the following domains

Basic Demographics	**EEG**	**Molecular Diagnostics**	**Clinical History**
Age at symptom onset	Background EEG (description)	Diagnostic summary	Diagnostic Label
Gender	Interictal abnormalities (description)	Identified abnormality (e.g. gene mutation, antibody titre)	Current and past medication and other treatments
Ethnicity	Ictal abnormalities (description)	Time between symptom onset and diagnostic test	Past medical history (including related conditions)
	Electroclinical diagnostic label		Family history of related conditions

11d. Safety considerations/Patient safety

All data will be stored in compliance with UCL and national regulations. Specifically all effort will be made to maintain anonymity of the patients:

1) No patient identifiers will be accessed by the research team
2) No patient identifiers will be stored with the anonymised clinical record
3) All electronic data will be stored in anonymised form on encrypted hard drive, or fully secured and compliant electronic databases hosted by UCL (Harris et al., 2009)

Clinical records (i.e. source documents) will only be accessed by the clinicians directly involved with the patients' care. Clinical summaries, and test results will be anonymised associated with unique study IDs that are used to link clinical data and EEG records; those anonymised summaries are transferred to the research team.

Anonymous records will be kept as paper case forms in a securely locked cupboard on UCL premises, and/or will be stored electronically on a fully data-protection regulation compliant database, hosted on UCL servers (Harris et al., 2009). EEG data will be anonymised and then transferred on an encrypted hard drive from the study site to a UCL based desktop computer, where they will be stored in encrypted files on a desktop computer. Backups of the encrypted files will occur regularly (every day) on the institutional server, but only the research team will have access to the decryption key, and thus only the research team will have access to the anonymised EEG data for quantitative analysis.

Anonymised data will be stored for 15 years post-publication date of any publications arising from this research on UCL premises and UCL electronic database systems before they will be destroyed.

11e. Data monitoring

The principal investigators will regularly review the progress of the study, and alert the Sponsor, and clinical study sites of any problems with data collection, data safety or irregularities.

11f. Data protection arrangements

All data collection and storage will be fully compliant with local and national regulation. Data will be collected on paper pro-forma, or directly recorded into an electronic database hosted by UCL servers (with write-only access granted to local study partners). Paper forms will be transferred through recorded mail to the UCL address of the chief investigator, and transferred onto the electronic database there. Paper forms will then be shredded and disposed of in confidential waste bins.

The database will be located on encrypted servers hosted within the UCL Institute of Neurology, which will be backed up regularly. Data will be stored for 15 years, after which it will be destroyed.

12. STATISTICAL CONSIDERATIONS AND DATA ANALYSIS

12a. Sample size and statistical power

12b. Statistical methods

Data will be analysing by developing data-informed individualised models of (1) whole-brain dysfunction based on EEG recordings, and (2) molecular dysfunction based on molecular diagnostic results.

EEG Modelling

EEG recordings will be analysed in the following stages:

1) Routine preprocessing, including bandpass filtering (0.1 – 70Hz)
2) Visual inspection to identify paroxysmal abnormalities and pertinent EEG features (e.g. intermittent rhythmic slowing, epileptiform discharges, etc).
3) Calculating cross spectral density summaries of EEG signals across different types of EEG features for windowed segments of EEG
4) *Within individuals:* Applying dynamic causal modelling approach to explain transitions between different EEG features as fluctuations in synaptic connectivity parameters (Kiebel et al., 2008b)
5) *Between individuals:* Applying a parametric empirical Bayesian approach to identify shared parameter alterations between patients with the same molecular conditions (Friston et al., 2016b)

This approach will provide a summary of shared changes in computational model microcircuitry that underlies a range of EEG abnormalities between patients. Analysis of statistical significance will be based on Bayesian model comparison with a Bayes factor of >3 considered strong evidence (Stephan et al., 2010). We will aim to include approximately 10 patients for group analyses in each cohort (5 cohorts)

Modelling of Receptor Function

In those patients where mutations affect an ion channel (e.g. *SCN1A*), computational models will be used to predict functional outcomes of the channel alteration at the level of the neuron, or a neuronal ensemble. This analysis will be performed in the following states:

1) Use of the PolyPhen-2 (http://genetics.bwh.harvard.edu/pph2/) online mutation effect prediction tools to predict likely pathogenicity and impact of individual mutations on channel function
2) Where available, retrieve existing molecular characterisation parameters of specific mutation (Peters et al., 2016)

3) Integrate abnormalities in model of neuronal membrane (e.g. Hodgkin Huxley model), or neuronal ensembles (e.g. conduction-based neural mass models) to predict mutation effects
4) Compare predictions with findings reported in EEG recordings and where possible with computational modelling analysis above.

This approach will provide qualitative insights into different ranges of dynamic behaviour associated with specific receptor abnormalities (Jirsa et al., 2014) and may be used to classify disease related mutations according to the degree of functional abnormalities induced. These will be used to infer common, or convergent mechanisms of dysfunction arising from different patient mutations in the same gene. We will aim to include approximately 20 patients in total for this part of the analysis.

13. ETHICAL CONSIDERATIONS

This study will be conducted in full conformance with the principles of the "Declaration of Helsinki", Good Clinical Practice and within the laws and regulations of the countries in which the research is conducted.

No study is completely risk free, but in this retrospective data review study, the risk is limited only to a breach in confidentiality, which as this study involves genetic results may involve risks to people other than the patient him- or herself (i.e. related family members).

The study of breaching confidentiality will be minimised as stated above by

1) Case ascertainment by treating clinicians,
2) Minimal data collection
3) Only anonymised data kept in research database / files

In principle, some of the genetic sequencing information may identify the patients (as they constitute a rare diagnosis), however the risk for breach of confidentiality based on the genetic sequencing information is considered minimal: Cases will be congregated in cohorts of at least 10 or more patients with similar mutations (e.g. missense mutations in *SCN1A* gene). The more detailed information regarding specific sequence alterations are usually not known to patients or people not directly involved with the patients clinical care related to the condition: Thus revealing this specific mutation information will only infer a minimal risk of confidentiality breach (i.e. reveal patient identity to the clinical team already involved in their care).
Furthermore, we will not access any genomic data (e.g. SNP array, whole exome sequencing, whole genome sequencing) that may reveal patient identities and other clinical information not in the remit of this current study.

No clinical analysis of the data will be performed, and therefore the incidental discovery of actionable clinical information is extremely unlikely. However, should unexpected clinical information be identified, we will report this back to the clinical teams for further action.

Whilst there are no direct benefits to the patients included in this study, there may be future benefits arising from this work improving future diagnostic, prognostic and treatment approaches to cohorts of patients with similar conditions.

Overall, we conclude that this study infers only a minimal risk to the patients, with the potential for indirect future benefits to the patient cohorts in question. We feel that the benefit here outweighs the risks for individual patients.

Consent

This study is investigating rare neurological conditions of childhood and as such will require inclusion of historical patient records on patients that may not currently be actively followed-up by the contributing clinical departments. The study would therefore not feasibly be possible if informed consent was required for each participating. Thus we request a waiver of consent and assent (for paediatric patients) as justified below

Waiver of Consent

This study requires a waiver of consent requirements because:

1) The study will pose no more than minimal risk to the subjects
2) Waiver right will not adversely affect the rights and welfare of the subjects
3) The research could not practicably be carried out without the consent waiver

Waiver of Assent

This study requires a waiver of assent requirements for paediatric patients because:

1) The study will pose no more than minimal risk to the subjects
2) Waiver right will not adversely affect the rights and welfare of the subjects
3) The research could not practicably be carried out without the assent waiver
4)

14. OUTCOMES AND SIGNIFICANCE

It may be of value to reiterate the potential benefits of answering the research question and conducting the project. This section restates the justification for the study in terms of the anticipated

results. It may be important to specify the implications of the potential results and how the results of this study may inform future research or policy makers.

A.3 Local trust approval for use of patient data

A.3.1 Evelina London Children's Hospital, Guy's and St Thomas' NHS Foundation Trust

From: **Shearman Kirstie** Kirstie.Shearman@gstt.nhs.uk
Subject: Confirmation of capacity and capability at GSTT: IRAS ID - 229772 Modelling Molecular Seizures
Date: 22 August 2017 at 14:21
To: research.governance@gosh.nhs.uk, Thomas.Lewis@gosh.nhs.uk
Cc: r.rosch@ucl.ac.uk, Lim Ming Ming.Lim@gstt.nhs.uk

SK

Dear Sponsor Representative,

RE: IRAS 229772. Confirmation of Capacity and Capability at Guy's and St Thomas' NHS Foundation Trust.
Full Study Title: Modelling Molecular Seizures

This email confirms that **Guy's and St Thomas' NHS FT** has the capacity and capability to deliver the above referenced study. Please find attached our agreed Statement of Activities as confirmation.

If you wish to discuss further, please do not hesitate to contact me.

Kind regards
Kirstie

Kirstie Shearman
Research & Development Facilitator
NIHR GSTFT/KCL Biomedical Research Centre
T: +44 (0)20 7188 7188 | Ext: 51071 | F: 0207 188 8330 |
E: kirstie.shearman@gstt.nhs.uk | W: www.guysandstthomas.nhs.uk/

Upcoming annual leave: 25th – 30th August (inclusive)

Guy's and St Thomas' and King's College London working together with our partners to deliver better health through research www.guysandstthomasbrc.nihr.ac.uk

A.3.2 Great Ormond Street Hospital NHS Foundation Trust

Thomas Lewis

Notification of No Objection 17NP05

Molecular Epilepsies 26 June 2017 at 12:59

Details

TL

To: Rosch, Richard (r.rosch@ucl.ac.uk) <r.rosch@ucl.ac.uk>, Cc: Rachel Thornton

Dear Richard,

Project Title	Modelling molecular seizures
IRAS Number:	229772
REC Reference	N/A
R&D Reference	17NP05
Date of REC Favourable Opinion	N/A
Protocol version	V1.0 24th May 2017
HRA Approval Notification Date	22nd June 2017
Statement of Activities/Issues	**This approval is for data collection from the Neurophysiology Department only.** **As data analysis will be taking place at ICH then an ICH risk assessment approval may be required. Please liaise with kate.thornton@ucl.ac.uk for further guidance.**

This research project has been reviewed locally at Great Ormond Street Hospital NHS Foundation Trust for capacity and capability. After review we can confirm a **Notification of No Objection** to this research being conducted at GOSH .

Please contact us using the contact details below if you require any further information.

We wish you all the best with your research.

Kind regards

Dr Thomas Lewis

UCL INSTITUTE OF CHILD HEALTH
Great Ormond Street Hospital for Children NHS Foundation Trust
Joint Research and Development Office Division of Research and Innovation

Dr Thomas Lewis | Research Governance Manager
Division of Research & Innovation | Joint R&D Office for GOSH/ICH | UCL Institute of Child Health | 30 Guilford Street | London, WC1N 1EH
www.gosh.nhs.uk/research-and-innovation
+44 (0) 207 905 2249 | **thomas.lewis@gosh.nhs.uk**

A.4 Modelling dynamic abnormalities caused by an *SCN1A* mutation – custom code

The Matlab scripts shown here implement a Hodgkin-Huxley type neuronal model with parameterisation derived directly from experimental voltage clamp results. They correspond to chapter 4 of this thesis.

Below is a short summary of the code (included in the README file for the online repository), followed with excerpts of the custom code written for the analysis. The code can be downloaded and run in full from an online repository accessible here: https://github.com/roschkoenig/SCN1A_HodgkinHuxley

A.4.1 README description of code function

A.4.1.1 Fitting Boltzmann Equations and Plotting Steady-State Parameters

`steady_state_curves`

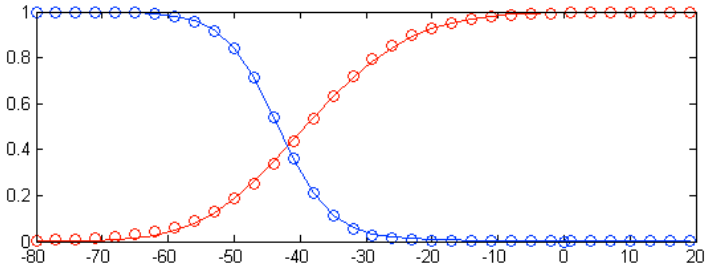

In the first instance, Boltzmann equations were fitted to an existing formulation of the Hodgkin Huxley Model that describes the dynamics at the membrane of a mammalian cortical neuron. The first component of the script `steady_state_curves` fits the Boltzmann equations. This formulation is taken as the baseline for all further modelling - i.e. the wildtype at 37°C is modelled as this baseline parameter composition.

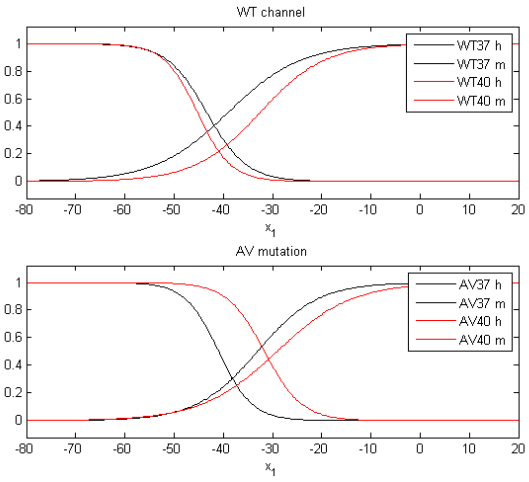

Remaining empirical values are represented as absolute (voltage parameters), or relative (slope parameters) deviations from the baseline in the model. The steady states that this produces for the sodium channel gating parameters are plotted in the second half of the `steady_state_curves` script.

A.4.1.2 Virtual Voltage Clamp to Assess for Fast Inactivation

`cort_fastinactivation.m`

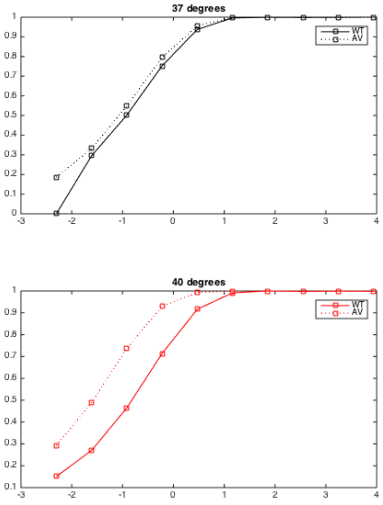

This function evaluates model dynamics by performing a 'virtual voltage clamp' experiments for the four parameterisations of the model (i.e. baseline, wild type sodium channels at 40ºC, SCN1A mutation at 37 and 40ºC). This consists of voltage clamp (i.e.

specific voltages being enforced on the model), delivering paired voltage pulses with increasing inter-pulse intervals. Changes in sodium conductance are estimated in a reduced Hodgkin Huxley Model implemented in `cort_hh_fastinactivation.m`. Current peaks resulting from these paired stimuli are estimated and plotted for each of the individual parameterisations of the model in the figure.

A.4.1.3 Running Models Under Different Conditions

`cort_variable_hh_eval`

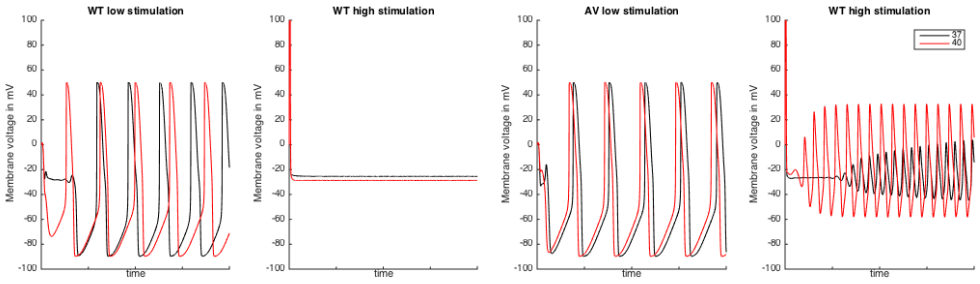

This script calls cort_variable_hh.m and uses Matlab ODE solver to integrate the model and plot the time course. The parameters are derived from a baseline model of cortical dynamics with experimental values implemented in terms of their deviations from those baseline parameters.

A.4.1.4 Evaluation of Model Bifurcations

`cort_bifurcation.m`

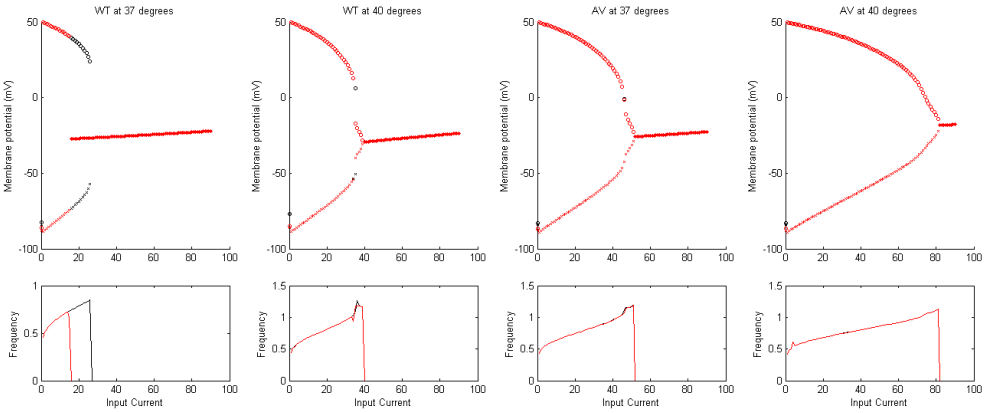

This routine calls `cort_variable_hh.m` and to run simulations of the cortical Hodgkin Huxley model across the four different parameterisations (i.e. baseline, wild type sodium

channels at 40°C, SCN1A mutation at 37 and 40°C). The model is estimated to steady state, and final state values from one simulation are used as initial values for the next simulation. This simulation is performed repeatedly across increasing, and then decreasing values of the input current Parameter I_{stim}. The steady state values of each model run are then plotted as bifurcation plots, separately for the four parameterisations of the model.

A.4.2 Custom Routines

A.4.2.1 steady_state_curves

```
% Simulate data from cortical parameterisation of HH
%=========================================================================
===
% This routine will simulate datapoints for the cortical parameterisation
% of the HH model according to Traub (1991) and fit the parameters of the
% steady state / voltage clamp formulation to these data in order to find
% the baseline for the further modelling steps
%
% This script is the basis for Figure 5a and c in the publication below:
%
% Peters C, Rosch RE, Hughes E, Ruben P (2016) Temperature-dependent
% changes in neuronal dynamics in a patient with an SCN1A mutation and
% hyperthermia induced seizures

%
% Setting up the HH equations
%-------------------------------------------------------------------------
---
clear all
syms a_m b_m a_h b_h V m_inf(V) h_inf(V) t_m(V) t_h(V)
V_t = -65;

a_m = -0.32 * ( V - V_t - 13 ) / (exp(-(V - V_t - 13) / 4) - 1);
a_h = 0.128 * exp( -( V - V_t - 17 )/18 );
b_m = 0.28 * ( V - V_t - 40 ) / ( exp( (V - V_t - 40)/5 )-1 );
b_h = 4 / ( 1 + exp( -(V-V_t-40)/5 ) );

m_inf(V) = a_m / (a_m + b_m);
h_inf(V) = a_h / (a_h + b_h);

t_m(V) = 1/(a_m + b_m);
t_h(V) = 1/(a_h + b_h);

% Calculating simulated datapoints
%-------------------------------------------------------------------------
---
i = 0;
for V = -80:3:20
    i = i+1;
    hh_cort(1,i) = V;
    hh_cort(2,i) = m_inf(V);
    hh_cort(3,i) = t_m(V);
    hh_cort(4,i) = h_inf(V);
    hh_cort(5,i) = t_h(V);
end
```

```
% Fitting steady state formulation to simulated datapoints
%-------------------------------------------------------------------------
---
clear V

V = hh_cort(1,:);
m = hh_cort(2,:);
h = hh_cort(4,:);

F_m   = @(x_m,xdata_m) 1 ./ (1 + exp(-(xdata_m-x_m(1))./x_m(2)));
F_h   = @(x_h,xdata_h) 1 ./ (1 + exp((xdata_h-x_h(1))./x_h(2)));
x0  = [-12,3];
[x_m, resnorm, ~, exitflag, output] = lsqcurvefit(F_m,x0,V,m);
[x_h, resnorm, ~, exitflag, output] = lsqcurvefit(F_h,x0,V,h);

% Plotting the estimated and simulated steady state curves
%-------------------------------------------------------------------------
---
for V = -80:3:20
    i = i+1;
    estimated(1,i) = V;
    estimated(2,i) = F_m(x_m,V);
    estimated(4,i) = F_h(x_h,V);
end

figure(1)
subplot(3,1,1)
    plot(estimated(1,:),estimated(2,:),'ro'); hold on
    plot(hh_cort(1,:), hh_cort(2,:), 'r');
    plot(estimated(1,:),estimated(4,:),'bo'); hold on
    plot(hh_cort(1,:), hh_cort(4,:), 'b');


% Plotting steady state curves for different experimental values
%=========================================================================
===
% This routine will take the experimentally derived voltage clamp values
% and plot the respective steady state curves for the different gating
% parameters of the Hodgkin Huxley Model


% Choosing parmeterisation
%-------------------------------------------------------------------------
---
n_exp = {'WT37','WT40','AV37','AV40'};
exp_parameters = 1:4; % 1 = WT37 (norm), 2 = WT40, 3 = AV37, 3 = AV40;


for e = exp_parameters
% Set according to literature
%-------------------------------------------------------------------------
---
params(1) = 0.010;      % C         HH
params(2) = 0.0000205;  % g_L       Posposchil 2008, Fig 2
params(3) = 5;          % g_K       Traub 1991
params(4) = 56;         % g_Na      Posposchil 2008, Fig 2
params(5) = -90;        % E_K       Traub 1991
params(6) = -70.3;      % E_L       Posposchil 2008, Fig 2
params(7) = 50;         % E_Na      Traub 1991
params(8) = .2;         % I_stim    HH
params(11) = -55;       % V_t       arbitrary (guided by Posposchil)
```

```
% Set according to experimental values (with WT37 as baseline)
%-------------------------------------------------------------------------
---
switch e
    case 1  % standard HH formulation (WT37)
        temperature = 37 + 273;
        dV2_m   = 0;
        dV2_h   = 0;
        t_off   = 0;
        m_z     =  3.6089;
        h_z     = -6.6210;

    case 2  % Experimental parameters for WT40
        temperature = 40 + 273;
        dV2_m   =  6.49;
        dV2_h   = -1.9;
        t_off   = 1.9;
        m_z     =  2.43*3.6089/2.14;
        h_z     = -3.79*6.6210/3.14;

    case 3  % Experimental parameters for AV37
        temperature = 37 + 273;
        dV2_m   =  5.94;
        dV2_h   =  2.4;
        t_off   = -2.4;
        m_z     =  2.58*3.6089/2.14;
        h_z     = -3.73*6.6210/3.14;

    case 4  % Experimental parameters for AV40
        temperature = 40 + 273;
        dV2_m   = 9.93;
        dV2_h   = 11.7;
        t_off   = -11.7;
        m_z     = 2.1*3.6089/2.14;
        h_z     = -3.38*6.6210/3.14;
end

s_m         = (0.0863 * temperature)/m_z;
s_h         = -(0.0863 * temperature)/h_z;

params(9) = x_m(1) + dV2_m; % V_2m, baseline estimated above
params(10) = s_m;           % s_m

params(12) = x_h(1) + dV2_h; % V_2h, baseline estimated above
params(13) = -s_h;          % s_h
params(14) = t_off;

%-------------------------------------------------------------------------
---

syms x1
m_inf = (1 / (1 + exp(-(x1-params(9))/s_m)));
h_inf = 1 / (1 + exp(-(x1-params(12))/-s_h));

figure(1);
if rem(e,2) == 0, col = 'r'; else col = 'k'; end
if e <= 2
    subplot(3,1,2)
    h = ezplot(h_inf, [-80 20]); hold on
```

```
    g = ezplot(m_inf, [-80 20]); hold on
    set(h, 'Color', col);
    set(g, 'Color', col);
    legend({'WT37 h','WT37 m','WT40 h','WT40 m'});
    title('WT channel');
else
    subplot(3,1,3)
    h = ezplot(h_inf, [-80 20]); hold on
    g = ezplot(m_inf, [-80 20]); hold on
    set(h, 'Color', col);
    set(g, 'Color', col);
    legend({'AV37 h','AV37 m','AV40 h','AV40 m'});
    title('AV mutation');
end

dis = figure(1);
set(dis, 'Position', [100 100 400 700]);
end

%=========================================================================
===
%=========================================================================
===
```

A.4.2.2 cort_fastinactivation

```
%% Conducting a virtual experiment estimating fast inactivation
%=========================================================================
===
% The appropriateness of the model is evaluated by conducting virtual
% voltage clamp experiments in order to evaluate whether the model
predicts
% real empirical measures.
% The routine below performs an two-pulse voltage clamp experiment aimed
to
% evaluate the dynamics of fast inactivation. A reduced set of HH equations
% only including sodium channel function is probed with a specific set of
% paired input pulses with increasing inter-pulse intervals. Short
% intervals leave little time for inactivation to recover, and therefore
% diminish model output.
% The model performs the experiment across a range of inter-pulse
intervals
% and plots the maximally achieved pulse amplitude of the second pulse
for
% a wild type sodium channel (baseline), as well as a specific SCN1A
% mutation causing epilepsy.
%
% The routine produces a figure that was the basis for Figure 5b and d in
% the publication below:
%
% Peters C, Rosch RE, Hughes E, Ruben P (2016) Temperature-dependent
% changes in neuronal dynamics in a patient with an SCN1A mutation and
% hyperthermia induced seizures (under review)

% Housekeeping
%=========================================================================
===
clear all
clf
count = 1;
```

```
% Manual parameters
%=========================================================================
===
% Define manually the name of the experiments and which experimental
% parameters are going to be modelled in this evaluation

% Choose experiments to be modelled
%-------------------------------------------------------------------------
---
n_exp           = {'WT37','WT40','AV37','AV40'};
exp_parameters  = [1 2 3 4];        % 1 = WT37 (norm), 2 = WT40, 3 = AV37,
3 = AV40;
plot_phase      = 0;
I_stim          = 0;                % I_stim    HH value = 0.200 nA

% Set parameters (currently done according to literature
%-------------------------------------------------------------------------
---
params(1) = 0.010;      % C         HH
params(2) = 0.0000205;  % g_L       Pospischil 2008, Fig 2
params(3) = 5;          % g_K       Traub 1991
params(4) = 56;         % g_Na      Pospischil 2008, Fig 2
params(5) = -90;        % E_K       Traub 1991
params(6) = -70.3;      % E_L       Pospischil 2008, Fig 2
params(7) = 50;         % E_Na      Traub 1991
params(11) = -60;       % V_t       arbitrary (guided by Posposchil)
params(8) = I_stim;

for e = 1:4; %exp_parameters

% Parameters defined according to experimental values (with WT37 as
baseline)
%=========================================================================
===
switch e
    case 1  % standard HH formulation (WT37)
    %---------------------------------------------------------------------
---
        temperature = 37 + 273;
        dV2_m   = 0;        % normalised to 0
        dV2_h   = 0;        % normalised to 0
        t_off   = 0;        % normalised to 0
        m_z     =  3.6089;  % normalised to cortical neuron values
        h_z     = -6.6210;  % normalised to cortical neuron values

    case 2  % Experimental parameters for WT40
    %---------------------------------------------------------------------
---
        temperature = 40 + 273;
        dV2_m   =  6.49;    % absolute difference to WT37
        dV2_h   = -1.9;     % absolute difference to WT37
        t_off   = 1.9;      % absolute difference to WT37
        m_z     =  2.43*3.6089/2.14;    % relative difference to WT37
        h_z     = -3.79*6.6210/3.14;    % relative difference to WT37

    case 3  % Experimental parameters for AV37
    %---------------------------------------------------------------------
---
        temperature = 37 + 273;
        dV2_m   =  5.94;    % absolute difference to WT37
```

```
        dV2_h    =  2.4;      % absolute difference to WT37
        t_off    = -2.4;      % absolute difference to WT37
        m_z      =  2.58*3.6089/2.14;     % relative difference to WT37
        h_z      = -3.73*6.6210/3.14;     % relative difference to WT37

    case 4  % Experimental parameters for AV40
    %-------------------------------------------------------------------
---
        temperature = 40 + 273;
        dV2_m    = 9.93;      % absolute difference to WT37
        dV2_h    = 11.7;      % absolute difference to WT37
        t_off    = -11.7;     % absolute difference to WT37
        m_z      = 2.1*3.6089/2.14;       % relative difference to WT37
        h_z      = -3.38*6.6210/3.14;     % relative difference to WT37
end

% Calculate model parameters from values given above
%-------------------------------------------------------------------
---
s_m         = (0.0863 * temperature)/m_z;   % slope derived from m_z
s_h         = -(0.0863 * temperature)/h_z;  % slope derived from h_z

params(9)   = -39.0 + dV2_m;    % difference from standard cortical neuron
params(10)  = s_m;
params(12)  = -43.2 + dV2_h;    % difference from standard cortical neuron
params(13)  = s_h;

params(14) = t_off;


g_Na        = params(4);
E_Na        = params(7);
x_ini       = [0 0 0 0];

% Run Model
%===================================================================
===
rec_t(1) = 0.1;      % recovery time in miliseconds
for r = 1:10
p1          = [100 200];
p2          = [0 10] + [p1(2) + rec_t(r)];
t_range     = [0 p2(2)+100];

options     = odeset('InitialStep',0.005,'MaxStep',t_range(2)/1000);
[t,x]           =  ode45(@(t,x)cort_hh_fastinactivation(t,x,params,  p1,
p2),t_range,x_ini,options);

% Estimate currents for each time point
%-------------------------------------------------------------------
---
% Estimate actual currents from model output (sodium channel conductance)
% and the set voltages as per voltage clamp experimental design

for s = 1:length(t)

    if t(s) < p1(1), vol(s) = -130;                         % Initial cond
    elseif t(s) > p1(1) && t(s) < p1(2), vol(s) = 0;        % Pulse 1
    elseif t(s) > p2(1) && t(s) < p2(2), vol(s) = 0;        % Pulse 2
    else vol(s) = -90;                                      % Recovery Time
    end
```

```
    x(s,3) = (-g_Na * x(s,1)^3 * x(s,2) * (vol(s) - E_Na));
end

% Estimate current peak after second pulse
%-------------------------------------------------------------------------
---
count = 1;
for i = 1:length(t)
    if t(i) > p2(1) && t(i) < (p2(1) + 10)
        ind(count) = i;
        count = count+1;
    end
end

[val loc]    = findpeaks(x(ind,3));
IR(e,r,1)    = rec_t(r);
IR(e,r,2)    = max(val);

rec_t(r+1)   = rec_t(r) * 2;
end
clear rec_t p1 p2 ind
end

subplot(2,1,1)
plot(log(IR(1,:,1)), IR(1,:,2)/max(IR(1,:,2)), 'ks-'); hold on
plot(log(IR(3,:,1)), IR(3,:,2)/max(IR(3,:,2)), 'ks:')
title('37 degrees');
legend({'WT', 'AV'});

subplot(2,1,2)
plot(log(IR(2,:,1)), IR(2,:,2)/max(IR(2,:,2)), 'rs-'); hold on
plot(log(IR(4,:,1)), IR(4,:,2)/max(IR(4,:,2)), 'rs:')
title('40 degrees');
legend({'WT', 'AV'});

%=========================================================================
===
%=========================================================================
===
```

A.4.2.3 cort_variable_hh.m

```
%% Calculate and Plot Bifurcations for cortical HH model
%=========================================================================
===
% This routine will simulate a Hodgkin-Huxley model adapted to capture
% dynamics of cortical neurons for different parameterisations: the
%  wildtype sodium channels at 37, and 40 degrees; an SCN1A mutation
causing
% epilepsy at 37, and 40 degrees; and all of these at two different input
% current strengths.
%
% The routine produces a figure that was the basis for Figure 6A in the
% publication below:
%
% Peters C, Rosch RE, Hughes E, Ruben P (2016) Temperature-dependent
% changes in neuronal dynamics in a patient with an SCN1A mutation and
% hyperthermia induced seizures (under review)
```

```
% Housekeeping
%-------------------------------------------------------------------------
---
clear all
clf
count = 1;

% Manual parameters
%=========================================================================
===
% Define manually the name of the experiments and which experimental
% parameters are going to be modelled in this evaluation

% Choose experiments to be modelled
%-------------------------------------------------------------------------
---
n_exp           = {'WT37','WT40','AV37','AV40'};
exp_parameters  = [1 2 3 4];  % 1 = WT37 (norm), 2 = WT40, 3 = AV37, 3 =
AV40;
plot_phase      = 0;
I_stim          = [0.2 45];         % I_stim    HH value = 0.200 nA
direction       = [1 -1];           % 1 = forward, -1 = backward
forward         = 0:2:90;           % defines range of I_stim parameter

% Set parameters (currently done according to literature
%-------------------------------------------------------------------------
---
params(1) = 0.010;      % C         HH
params(2) = 0.0000205;  % g_L       Pospischil 2008, Fig 2
params(3) = 5;          % g_K       Traub 1991
params(4) = 56;         % g_Na      Pospischil 2008, Fig 2
params(5) = -90;        % E_K       Traub 1991
params(6) = -70.3;      % E_L       Pospischil 2008, Fig 2
params(7) = 50;         % E_Na      Traub 1991
params(11) = -60;       % V_t       arbitrary (guided by Posposchil)

for e = 1:4; %exp_parameters

% Parameters defined according to experimental values (with WT37 as
baseline)
%=========================================================================
===
switch e
    case 1  % standard HH formulation (WT37)
    %---------------------------------------------------------------------
---
        temperature = 37 + 273;
        dV2_m   = 0;        % normalised to 0
        dV2_h   = 0;        % normalised to 0
        t_off   = 0;        % normalised to 0
        m_z     =  3.6089;  % normalised to cortical neuron values
        h_z     = -6.6210;  % normalised to cortical neuron values

    case 2  % Experimental parameters for WT40
    %---------------------------------------------------------------------
---
        temperature = 40 + 273;
        dV2_m   =  6.49;    % absolute difference to WT37
        dV2_h   = -1.9;     % absolute difference to WT37
        t_off   = 1.9;      % absolute difference to WT37
```

```
        m_z     =  2.43*3.6089/2.14;    % relative difference to WT37
        h_z     = -3.79*6.6210/3.14;    % relative difference to WT37

    case 3  % Experimental parameters for AV37
    %-------------------------------------------------------------------
---
        temperature = 37 + 273;
        dV2_m   =  5.94;    % absolute difference to WT37
        dV2_h   =  2.4;     % absolute difference to WT37
        t_off   = -2.4;     % absolute difference to WT37
        m_z     =  2.58*3.6089/2.14;    % relative difference to WT37
        h_z     = -3.73*6.6210/3.14;    % relative difference to WT37

    case 4  % Experimental parameters for AV40
    %-------------------------------------------------------------------
---
        temperature = 40 + 273;
        dV2_m   = 9.93;     % absolute difference to WT37
        dV2_h   = 11.7;     % absolute difference to WT37
        t_off   = -11.7;    % absolute difference to WT37
        m_z     = 2.1*3.6089/2.14;      % relative difference to WT37
        h_z     = -3.38*6.6210/3.14;    % relative difference to WT37
end

% Calculate model parameters from values given above
%-------------------------------------------------------------------
---
s_m         = (0.0863 * temperature)/m_z;   % slope derived from m_z
s_h         = -(0.0863 * temperature)/h_z;  % slope derived from h_z

params(9)   = -39.0 + dV2_m;    % difference from standard cortical neuron
params(10)  = s_m;
params(12)  = -43.2 + dV2_h;    % difference from standard cortical neuron
params(13)  = s_h;

params(14) = t_off;


for i = 1:2;
% Run Model
%===================================================================
===
params(8)   = I_stim(i);
options     = odeset('InitialStep',0.005,'MaxStep',0.05);
t_range     = [0 50];
x_ini       = [0 0 0 0];
[t,x]                                                               =
ode45(@(t,x)cort_variable_hh(t,x,params),t_range,x_ini,options);

% Plot time courses
% -----------------------------------------------------------------
----
Figure1     = figure(1);
xplot = linspace(1,length(t),5000);
xplot = floor(xplot);

if e <= 2,  sp_no = 0;
else        sp_no = 2;
end

if rem(e,2) == 0,   col = 'r';
```

```
else                col = 'k';
end

subplot(1,4,sp_no+i);
    plot(t(xplot),x(xplot,1), col); hold on
    title(n_exp{e});
    axis([0,20,-100,100]);
    set(gca, 'XTickLabel', [], 'Box', 'off');
    xlabel('time');
    if count > 1
        set(gca, 'YTickLabel', []);
    else
        ylabel('Membrane voltage in mV');
    end

set(Figure1, 'Position', [100 100 1000 350]);
subplot(1,4,1), title('WT low stimulation');
subplot(1,4,2), title('WT high stimulation');
subplot(1,4,3), title('AV low stimulation');
subplot(1,4,4), title('WT high stimulation'); legend({'37', '40'});
end

end
```

A.4.2.4 cort_bifurcation

```
%% Calculate and Plot Bifurcations for cortical HH model
%=========================================================================
===
% This routine will recursively simulate steady state responses of a HH
% model adapted to resemble cortical neuronal function, for wild type
% sodium channels, and parameters derived from an epilepsy causing SCN1A
% mutation. Simulations will be performed at a range of input currents
% (defined as 'forward' variable below), with steady state values of one
% parameter step acting as initial conditions for the next parameter step.
% This is performed in two directions (forward and backward) in order to
% plot a bifurcation diagram of action potential generation.
%
% The routine produces a figure that was the basis for Figure 6 in the
% publication below:
%
% Peters C, Rosch RE, Hughes E, Ruben P (2016) Temperature-dependent
% changes in neuronal dynamics in a patient with an SCN1A mutation and
% hyperthermia induced seizures (under review)


% Manual definitions
%-------------------------------------------------------------------------
---
direction       = [1 -1];           % 1 = forward, -1 = backward
forward         = 0:1:90;           % defines range of I_stim parameter
n_exp           = {'WT37','WT40','AV37','AV40'};
exp_parameters  = [1 2 3 4];       % 1 = WT37 (norm), 2 = WT40, 3 = AV37,
3 = AV40;
count_e         = 1;

for e = exp_parameters
```

```
% Parameters defined according to experimental values (with WT37 as
baseline)
%=========================================================================
===
switch e
    case 1  % standard HH formulation (WT37)
    %---------------------------------------------------------------------
---
        temperature = 37 + 273;
        dV2_m   = 0;        % normalised to 0
        dV2_h   = 0;        % normalised to 0
        t_off   = 0;        % normalised to 0
        m_z     =  3.6089;  % normalised to cortical neuron values
        h_z     = -6.6210;  % normalised to cortical neuron values

    case 2  % Experimental parameters for WT40
    %---------------------------------------------------------------------
---
        temperature = 40 + 273;
        dV2_m   =  6.49;    % absolute difference to WT37
        dV2_h   = -1.9;     % absolute difference to WT37
        t_off   = 1.9;      % absolute difference to WT37
        m_z     =  2.43*3.6089/2.14;    % relative difference to WT37
        h_z     = -3.79*6.6210/3.14;    % relative difference to WT37

    case 3  % Experimental parameters for AV37
    %---------------------------------------------------------------------
---
        temperature = 37 + 273;
        dV2_m   =  5.94;    % absolute difference to WT37
        dV2_h   =  2.4;     % absolute difference to WT37
        t_off   = -2.4;     % absolute difference to WT37
        m_z     =  2.58*3.6089/2.14;    % relative difference to WT37
        h_z     = -3.73*6.6210/3.14;    % relative difference to WT37

    case 4  % Experimental parameters for AV40
    %---------------------------------------------------------------------
---
        temperature = 40 + 273;
        dV2_m   = 9.93;     % absolute difference to WT37
        dV2_h   = 11.7;     % absolute difference to WT37
        t_off   = -11.7;    % absolute difference to WT37
        m_z     = 2.1*3.6089/2.14;      % relative difference to WT37
        h_z     = -3.38*6.6210/3.14;    % relative difference to WT37
end

% Calculate model parameters from values given above
%-------------------------------------------------------------------------
---
s_m         = (0.0863 * temperature)/m_z;   % slope derived from m_z
s_h         = -(0.0863 * temperature)/h_z;  % slope derived from h_z

params(9)   = -39.0 + dV2_m;    % difference from standard cortical neuron
params(10)  = s_m;
params(12)  = -43.2 + dV2_h;    % difference from standard cortical neuron
params(13)  = s_h;

params(14) = t_off;

for d = direction
```

```
% Use variables
%-------------------------------------------------------------------------
---
i   = 0;                % counts number of model runs
cyc = length(exp_parameters);

if d == 1
    steps = forward;
    disp('Forward');
else
    steps = flip(forward);
    disp('Back');
end

% Run model to steady state from random initial
%-------------------------------------------------------------------------
---
options     = odeset('InitialStep',0.0025,'MaxStep',0.05);
t_range     = [0 100];
x_ini       = [0 0 0 0];
[t,x]                                                                   =
ode45(@(t,x)cort_variable_hh(t,x,params),t_range,x_ini,options);

% Run model iteratively across parameterspace
%-------------------------------------------------------------------------
---
for para = steps;

    disp(length(steps)-i)
    params(8) = para;
    i = i+1;

    bif(1,i)    = para;
    options     = odeset('InitialStep',0.0025,'MaxStep',0.05);
    t_range     = [0 100];
    x_ini       = x(end,:);
    [t,x]                                                               =
ode45(@(t,x)cort_variable_hh(t,x,params),t_range,x_ini,options);

    bif(2,i) = max(x(floor(3/5*end):end,1));
    bif(3,i) = min(x(floor(3/5*end):end,1));

    if bif(2,i)-bif(3,i)>0.5
        [pks,locs] = findpeaks(x(floor(4/5*end):end));
        bif(4,i) = 1/mean(diff(t(locs)));
    else
        bif(4,i) = 0;
    end
end

% Draw figures: Top panel - bifurcation diagram, bottom panel - frequency
%=========================================================================
===
figure(2);
set(gcf, 'Position', [100 200 1200 300]);
hold on
subplot(3,cyc,[count_e cyc+count_e])

% Bifurcation diagram
%-------------------------------------------------------------------------
---
```

```
for i = 1:length(bif(1,:));
    if bif(2,i)-bif(3,i)<0.5
        if d == 1
            scatter(bif(1,i), bif(2,i),'k.'); hold on
        else
            scatter(bif(1,i), bif(2,i),'r.'); hold on
        end
    else
        if d == 1
            scatter(bif(1,i), bif(2,i), 10, 'ko'); hold on
            scatter(bif(1,i), bif(3,i), 10, 'kx');
        else
            scatter(bif(1,i), bif(2,i), 10, 'ro'); hold on
            scatter(bif(1,i), bif(3,i), 10, 'rx');
        end
    end
end

ylabel('Membrane potential (mV)');
switch e
    case 1, title('WT at 37 degrees');
    case 2, title('WT at 40 degrees');
    case 3, title('AV at 37 degrees');
    case 4, title('AV at 40 degrees');
end

% Frequency
%-------------------------------------------------------------------------
---
subplot(3,cyc,2*cyc+count_e)
if d == 1
    plot(bif(1,:),bif(4,:), 'k');
    xlabel('Input Current');
    ylabel('Frequency');
else
    plot(bif(1,:),bif(4,:), 'r');
    xlabel('Input Current');
    ylabel('Frequency');
end

end     % from for loop over directions
count_e = count_e+1;
clear x t x_ini bif
end     % from loop over experimental conditions
```

A.4.2.5 cort_variable_hh

```
function dxdt = cort_variable_hh(t,x,params)
dxdt=zeros(4,1);

% Constant values
%-------------------------------------------------------------------------
---
C       = params(1);
g_L     = params(2);
g_K     = params(3);
g_Na    = params(4);
E_K     = params(5);
E_L     = params(6);
```

```
E_Na    = params(7);

I_stim  = params(8);

V_2m    = params(9);
s_m     = params(10);
V_t     = params(11);

V_2h    = params(12);
s_h     = params(13);
t_off     = params(14);

% Parameter equations
%=========================================================================
===
% Opening probabilities
%-------------------------------------------------------------------------
---
aV_n = -0.032 * ( x(1) - V_t - 15 ) / ( exp( -(x(1)-V_t-15)/5)-1 );
aV_m = -0.32 * ( x(1) - V_t - 13 ) / (exp(-(x(1) - V_t - 13) / 4) - 1);
aV_h = 0.128 * exp( -( x(1) - V_t - 17 + t_off )/18 );

% Closing probabilities
%-------------------------------------------------------------------------
---
bV_n = 0.5 * exp( -(x(1) - V_t - 10)/40);
bV_m = 0.28 * ( x(1) - V_t - 40 ) / ( exp( (x(1) - V_t - 40)/5 )-1 );
bV_h = 4 / ( 1 + exp( -(x(1)-V_t-40+t_off)/5 ) );

% Steady state values
%-------------------------------------------------------------------------
---
m_inf = 1 / (1 + exp(-(x(1)-V_2m)/s_m));
h_inf = 1 / (1 + exp(-(x(1)-V_2h)/-s_h));
t_h   = 1/(aV_h + bV_h);
t_m   = 1/(aV_m + bV_m);

% Differential equations
%-------------------------------------------------------------------------
% dxdt(1) = V
% dxdt(2) = n potassium channel activation gate
% dxdt(3) = m sodium channel activation gate
% dxdt(4) = h sodium channel inactivation gate

dxdt(1) = ( -g_Na * x(3)^3 * x(4) * (x(1) - E_Na)  ...
            -g_K * x(2)^4 * (x(1) - E_K)  ...
            -g_L * (x(1) - E_L) + I_stim ) / C;

dxdt(2) = aV_n * (1-x(2)) - bV_n * x(2);    % n
dxdt(3) = (m_inf - x(3)) / t_m;             % m
dxdt(4) = (h_inf - x(4)) / t_h;             % h

end
```

A.5 Analysing light-sheet imaging data of acute epileptic seizures in zebrafish

The Matlab scripts below show were custom written and used to perform the analysis of light-sheet recordings of epileptic seizures discussed in chapter 7 of this thesis. Below there is a short summary of the package content and script segments for the key analysis scripts. The code can be downloaded in full from an online repository accessible here: https://github.com/roschkoenig/Zebrafish_Seizures

A.5.1 README description of code function

The analysis is done by way of a number of custom routines, that in conjunction can be used to reproduce the findings from chapter 7. Below is a summary of what each of the routines does. Broadly, the code is trying to accomplish the following 5 objectives:

1. Identify induced network-wide changes in neuronal activity in 'sensor space' – i.e. directly from the measured signals
2. Use simulations to test whether DCM can resurrect neuronal parameters from calcium imaging signals
3. Use DCM and Bayesian model comparison to identify a parsimonious baseline network architecture
4. Use a time-windowed, hierarchical DCM to identify slow changes in neuronal parameters induced by the induced seizures
5. Simulate the effects of the indentified parameter changes to identify their effects on the network

The different steps will be discussed in more detail below.

A.5.1.1 Visualise sensor space changes in neuronal dynamics using a sliding window

`zf_seizureexplore`

This code performs a sliding window analysis of the regionally averaged light sheet microscopy data. The code will look for the original data files (stored in 'Data' in the repository, and called something like this single_plane_ROI_MEAN_TRACES.mat). The code will then take 60s time windows in 10s steps to estimate time changing fourier spectra of the calcium signal and plot these (if specified). This function is also used to generate the

SPM files (called MEEG objects) that will be required for the later analysis and are stored in the 'Matlab Files' folder.

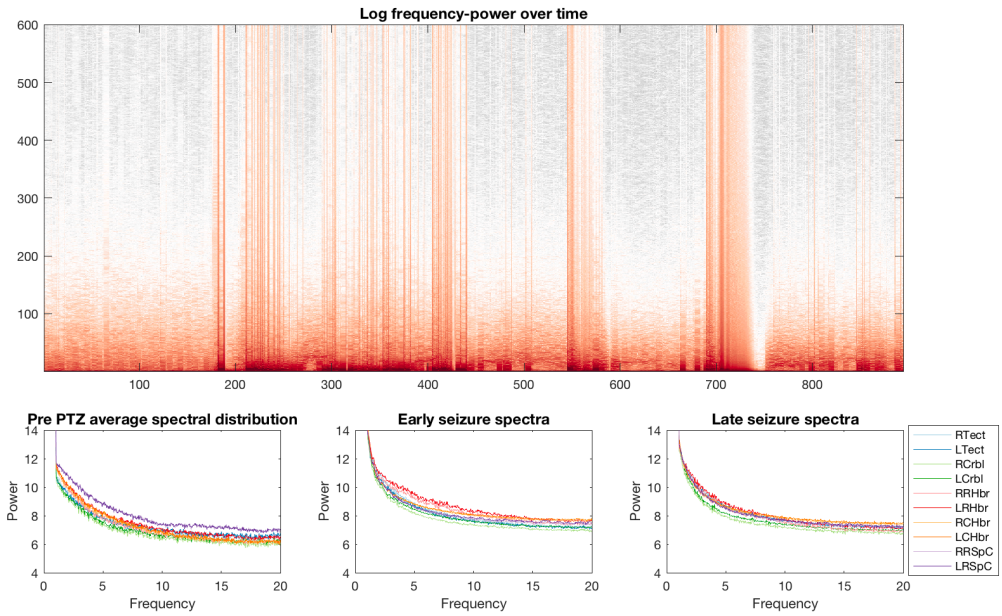

The windowed spectral estimates are also used to estimate a power dynamics correlation matrix (see discussion of the methods in (Rosch et al., 2018)) - for which the average across all fish is plotted as output. This matrix shows the correlation of each time window's

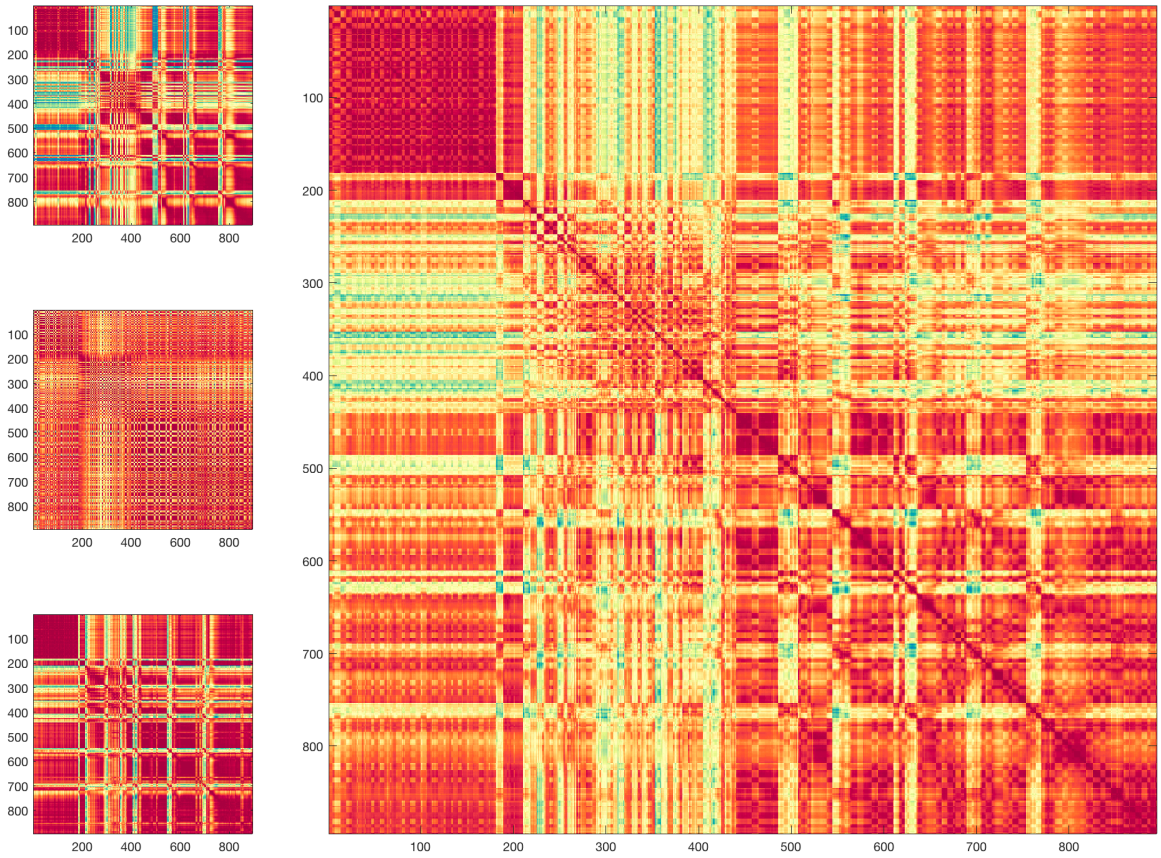

channel-resolved frequency-power spectra with each other time window. The leading diagonal of the matrix is therefore always = 1 (i.e. fully correlated), and time periods where the overall output remains relatively static appear as blocks on the dynamics matrix. The function's output is shown above.

A.5.1.2 Simulate dynamic causal modelling based on calcium traces

`zf_calciumsim`

This code illustrates how parameter changes that correspond to underlying synaptic changes can be retrieved from both neurophysiological recordings, and calcium imaging data. For this, we are first simulating some LFP data, and illustrating a convolution with a kernel that resembles the temporal dynamics of a GCaMP6f probe (also used in the experimental paradigm). The results are shown below and will be given as putput from this code – they show the LFP, the calcium kernel, and calcium imaging time series both in the temporal domain (left) and the frequency domain (right).

Temporal Domain

Top to bottom: Calcium kernel; example LFP; convolved calcium time series

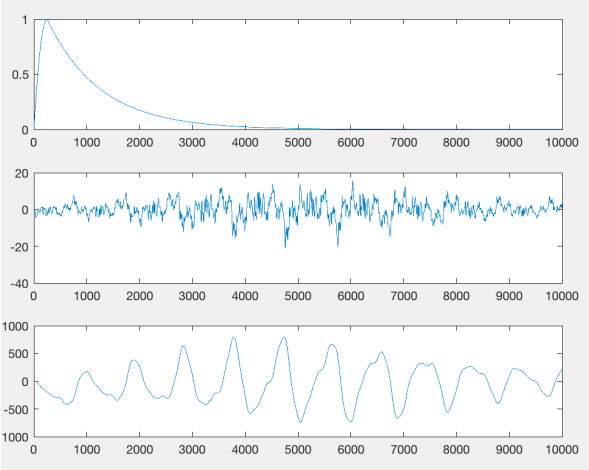

Frequency Domain

Top to bottom: LFP spectral density; Calcium kernel spectral density; resultant calcium time series spectral density

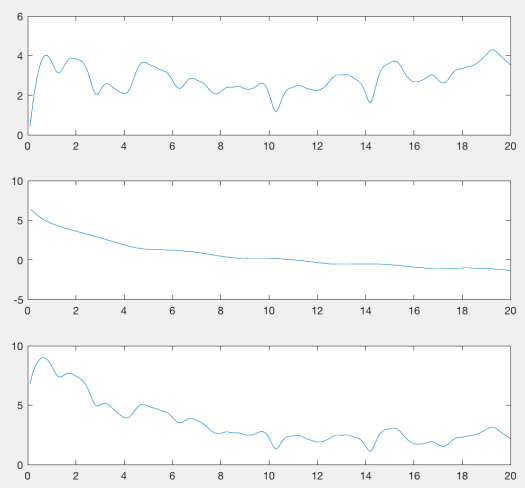

The code witll then generate a number of time series with a known set of neuronal parameters, where one of the parameters is varied across the different repeated simulations. These are then used as the basis to estimate the underlying neuronal parameter changes. For each of the (calcium-) time series, we will invert a single-node DCM for cross-spectral densities. Using a Parametric empirical Bayesian approach, we will

then identify the single parameter disturbance that best explains the differences between these individual time traces.

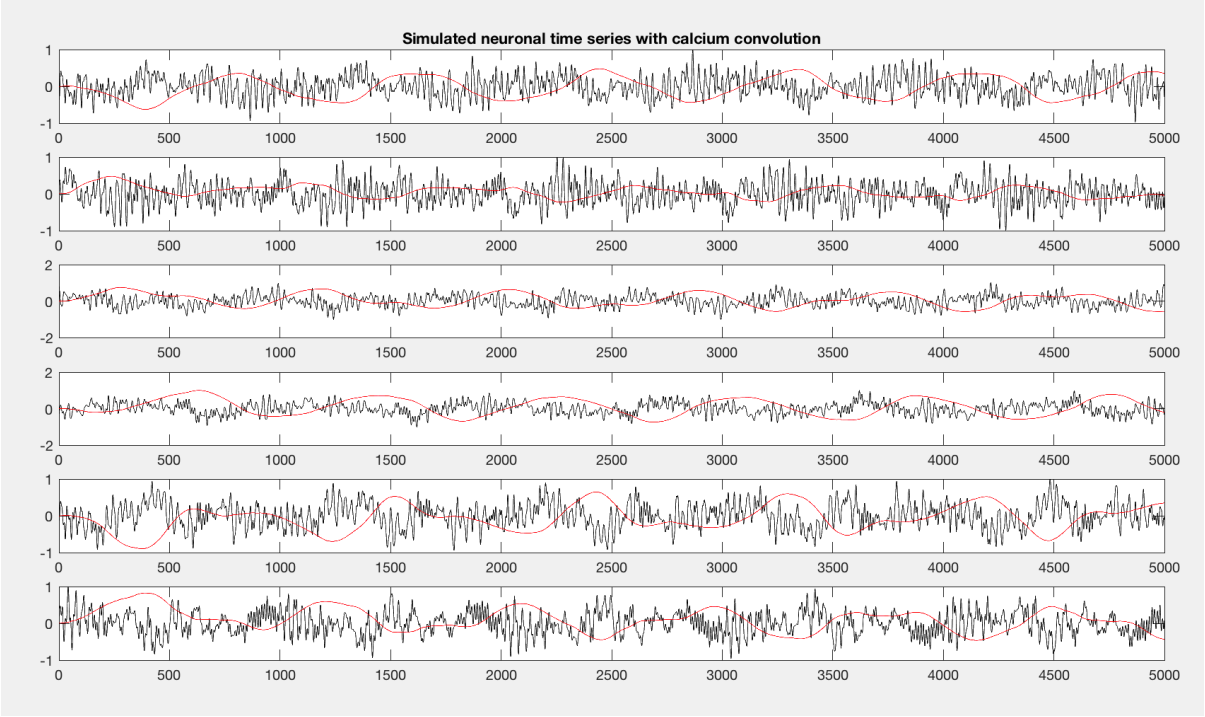

This will yield both a free energy approximation of the model evidence for a any individual parameter to explain the observed effect (top panel of the figure below); and posterior estimates of the parameter change that best explains the transitions between the different time series. In this case the correct parameter was identified from the PEB analysis (i.e. the one that was manipulated to simulate the origin al LFP traces; bottom panel of the figure below).

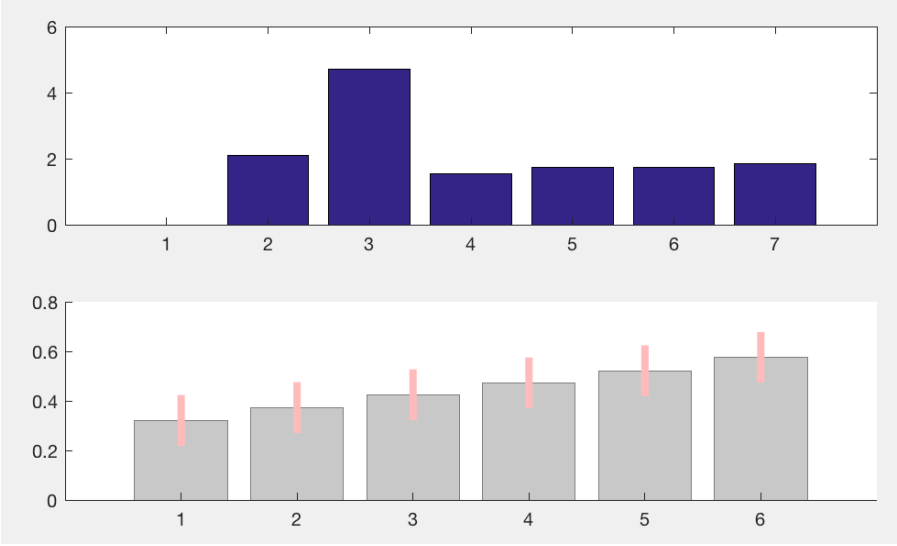

A.5.1.3 Set up and invert baseline DCM

`zf_dcm` *(time intensive step)*

In the next step, we are using DCM to infer the model architecture that best explains the cross-spectral density summaries of baseline network activity. For the DCM we are loading baseline data for each animal and set up model architecture and inversion parameters:

```
DCM.options.analysis = 'CSD';       % cross-spectral density
DCM.options.model    = 'LFP';       % three-population model
DCM.options.spatial  = 'LFP';       % virtual electrode input
```

This section defines the basic features of the model inversion – here we are analysing ongoing neuronal oscillatory activity using cross-spectral densities (CSD). We are assuming a basic structure that is currently described as the 'LFP' model – a three population summary of microcircuitry, consisting of a single main (excitatory) output population and one inhibitory and one excitatory interneuronal population respectively. This is all analysed, treating the signal as direct neuronal recordings (i.e. as local field potentials – LFP – as the spatial model).

A.5.1.4 Use Bayesian model reduction to make inference on model architecture at baseline

`zf_bmr`

Based on the full model inversion for the baseline model performed at the preceding step, this function now fills the remainder of the parameter estimates and approximates the model evidence across the model space using Bayesian model reduction, or BMR. This routine will set up a new DCM structure for each of the investigated models, then load the already inverted full DCM from the step above. Using the free energy approximation for the model evidence, this will then allow Bayesioan model comparison, which the code will present as family-wise comparison as shown below.

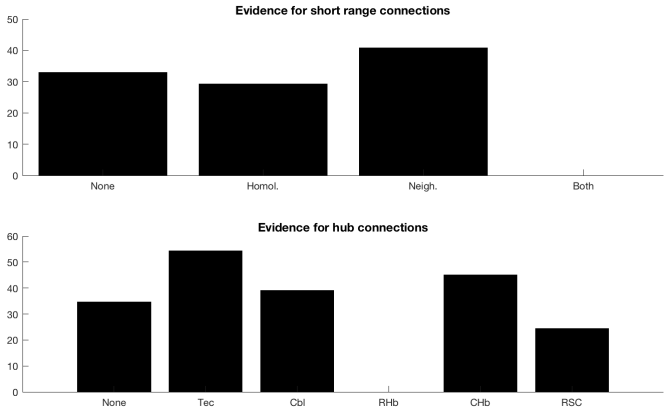

A.5.1.5 Set up (sliding window) files for DCM analysis

(This is a very time intensive step, and will need setting up within your local infrastructure with `zf_slide`*; and* `zf_slide_for_cluster`*)*

Based on the winning model architecture selected from the baseline model inversion performed in the previous two steps, we now invert DCMs for each individual time step separately – the idea here is that over a short time period (i.e. 60s), a network of neural mass models is fitted to an assumed stationary oscillatory signal. By doing this with overlapping windows separated by only short time steps, we will be able to track the slow parameter changes that underlie the transition between different neuronal states – such as here, the baseline and the induced seizure state.

The version included in the code here will specify the model for each time window and invert them in a single loop (over many days). The `zf_slide_for_cluster` version will specify the DCM structure needed for inversion, but not actually invert the DCMs. This will need to be done on a computing cluster with Matlab installed, where a custom inversion function (`zf_spm_dcm_fit`) should be called.

A.5.1.6 Using parametric empirical Bayes to make inference across time windows

`zf_peb`

As we are interested in the changes of DCM parameters over time (i.e. between-DCM parameter changes), we can use parametric empirical Bayes (PEB) to specifically estimate between DCM effects that correspond to particular trajectories. For PEB we will specify a model space at the second (between-DCM) level that describes possible trajectories, and in the inversion we will identify the most parsimonious combination of effects of this second-level general linear model on DCM parameters to explain the data.

Specifically in this instance the code will first load the DCMs that were inverted at the previous step. It will then define the types of between-DCM effects that we are looking forms in terms of a second level design matrix in the variable 'X'. For the purposes of this analysis, individual fish are treated as repeat measurements. We can visualise the design matrix by typing in `imgagesc(X)` and should get the following output, where each row is a DCM / time window and each column is an experimental effect or regressor.

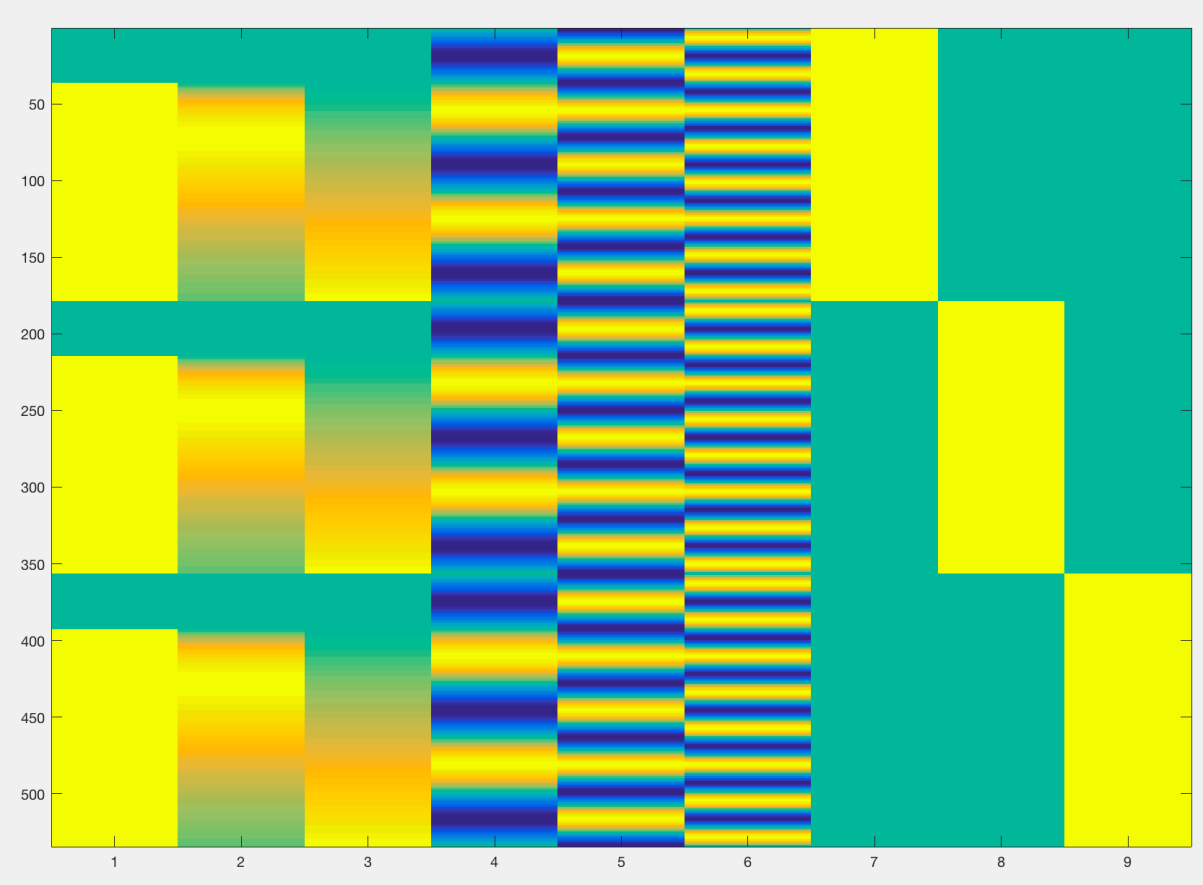

Similarly to the Bayesian model reduction performed above to identify a simpler baseline architecture, we can then use a similar approach to define a set of models to compare at the second level – i.e. which of the model parameters affected by the changes observed during seizure activity offer the most parsimonious explanation of across-time-window effects. We can then perform Bayesian model comparison between these reduced models, and plot the second level parameter estimates.

Extrinisc parameters

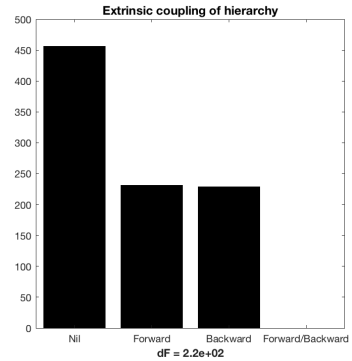

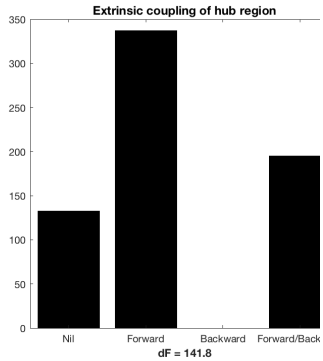

Intrinsic Parameters

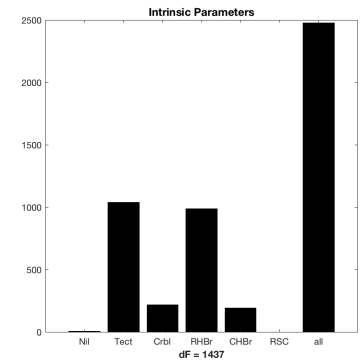

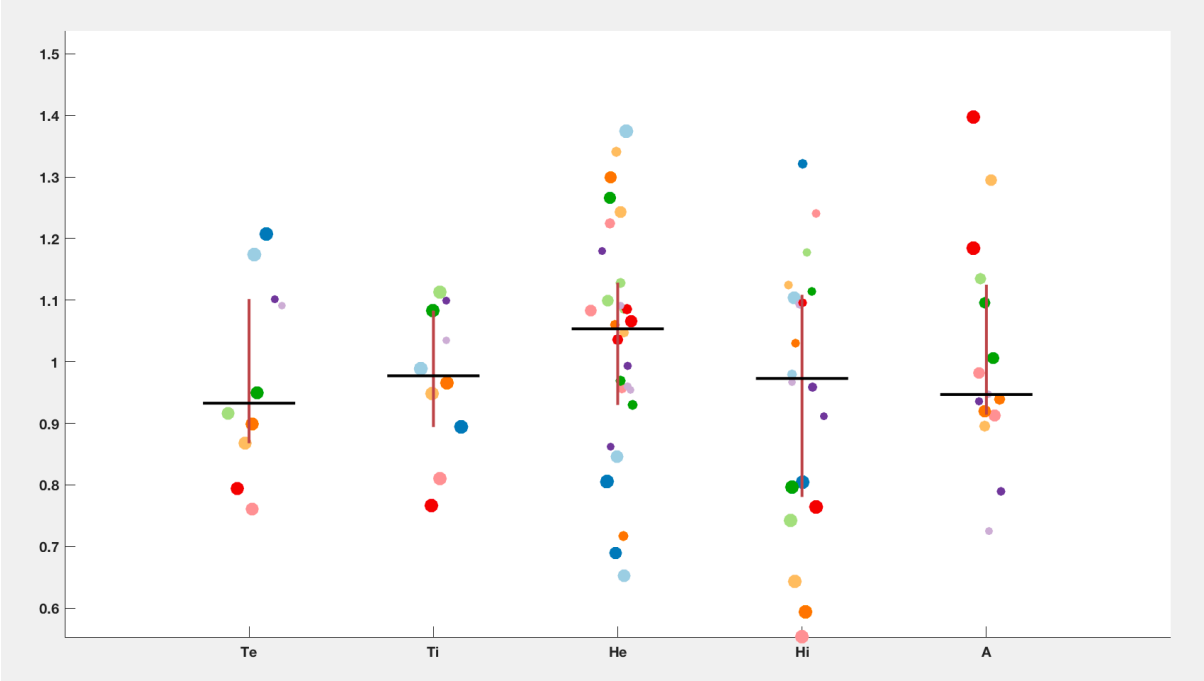

A.5.1.7 Simulate neuronal responses across parameter space

`zf_simulate`

Once we have identified a simple representation of consistent parameter changes across fish and time windows, we want to explore what effect those specific parameters have on the neuronal output. Because the DCM / PEB approach yields fully generative models that will produce predictions of neuronal oscillatory activity (in the shape of cross-spectral densities), we can simulate the effects of specific parameter changes.

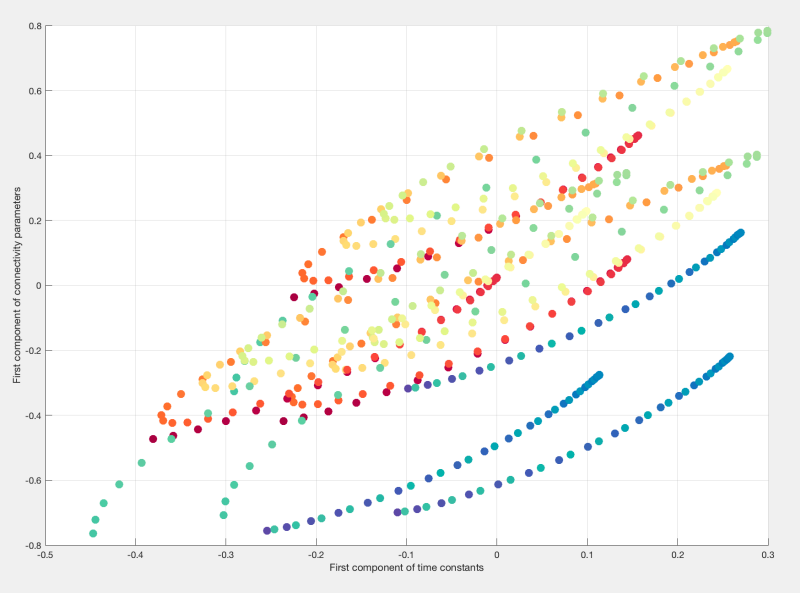

This is illustrated in the paper using a single brain region as an example. For this we first use a low-dimensional representation of the data (through a principal component analysis of the windowed parameter estimates) and project each time window onto this low dimensional representation. Having mapped out the space of the maximum variance, we can then simulate output spectra at each point, plotting the landscape of low-frequency power, but also high frequency powere components not originally included in the data (as this is a simulation).

A.5.1.8 Edits of SPM12 functions called by the routines above

- `zf_spm_dcm_csd_data` – adapted to allow for smaller frequency bins (standard limit: 1Hz)
- `zf_spm_dcm_csd` – adapted to call `zf_spm_dcm_csd_data`
- `zf_spm_dcm_fit` – adapted to call `zf_spm_dcm_csd_csd`
- `zf_spm_dcm_csd` – adapted to use log-scales of cross-spectral densities
- `zf_spm_rand_power_law` – use additional scheme to generate random power law dynamics

A.5.2 Custom Routines

A.5.2.1 zf_seizureexplore

```
% This code performs a sliding window analysis on the seizure data in
order
% to visualise power distribution dynamics across the recording duration
%-----------------------------------------------------------------------
---

clear all

sliding  = 1;
plotting = 1;
saveplot = 0;

extrctBL = 0;
make_spm = 0;

% Housekeeping
%=======================================================================
===
fs          = filesep;
D           = zf_housekeeping;
Fbase       = D.Fbase;
```

```
Forig       = D.Forig;
Fanalysis   = D.Fanalysis;
lbl         = D.lbl;
subs        = D.subs;
scount = 0;


for sub = subs
scount = scount + 1

Fsub        = [Fanalysis fs 'Data Files' fs sub{:}];


switch sub{:}
    case 'S1', load([Forig fs 'single_plane_ROI_MEAN_TRACES']);
    case 'S2', load([Forig fs 'single_plane_s2_ROI_MEAN_TRACES']);
    case 'S3', load([Forig fs 'single_plane_s3_ROI_MEAN_TRACES']);
end

Z = ROI_MEAN_TRACES.data;

clear fullc fullt
Fs      = 20;
win     = 60 * Fs;
stp     = 10 * Fs;
l       = length(Z);
fstps   = win;
i       = 0;

if sliding
for s = 1:stp:l-win
    i               = i+1
    w               = Z(s:s+win, :);
    tfullt          = fft(w, fstps);
    fullt(i,:,:)   = abs(tfullt(1:floor(end/2),:));
    ft(i, :)        = mean(squeeze(fullt(i,:,:)), 1);

    fullc       = corr(w);
    halfc       = tril(fullc, -1);
    v           = halfc(find(halfc));
    co(i, :)    = v;
end

ccor{scount} = corr(co');
cpow{scount} = corr(abs(ft)');
end

% Plot spectral changes before and during seizure
%=========================================================================
===
% if plotting,
alft(scount,:,:) = mean(log(fullt),3);

figure(scount)

cs = flip(cbrewer('div', 'RdGy', 100));
colormap(cs);
frq_axis = linspace(1, Fs, fstps / 2);
set(gcf, 'Color', 'w');
```

```
subplot(3,3,1:6)
    imagesc(mean(log(fullt),3)', [0 14]); hold on
    title('Log frequency-power over time', 'fontsize', 12, 'fontweight',
'bold');
    set(gca, 'YDir', 'normal');
    seg = floor(size(fullt,1)/6);

cp = cbrewer('qual', 'Paired', 10);

subplot(3,3,7)
    for i = 1:10
        plot(frq_axis, log(squeeze(mean(fullt(50:150,:,i),1))), 'Color',
cp(i,:)); hold on
    end
    title('Pre PTZ average spectral distribution', 'fontsize', 12,
'fontweight', 'bold');
    ylim([4 14]);
    ylabel('Power');
    xlabel('Frequency');

subplot(3,3,8)
    for i = 1:10
        plot(frq_axis, log(squeeze(mean(fullt(300:400,:,i),1))),
'Color', cp(i,:)); hold on
    end
    title('Early seizure spectra', 'fontsize', 12, 'fontweight',
'bold');
    ylim([4 14]);
    ylabel('Power');
    xlabel('Frequency');

subplot(3,3,9)
    for i = 1:10
        plot(frq_axis, log(squeeze(mean(fullt(500:600,:,i),1))),
'Color', cp(i,:)); hold on
    end
    title('Late seizure spectra', 'fontsize', 12, 'fontweight', 'bold');
    ylim([4 14]);
    ylabel('Power');
    xlabel('Frequency');
    legend(lbl);

end

figure(4)
imagesc(squeeze(mean(alft,1))', [4 14]);
set(gca, 'Ydir', 'normal');
colormap(cs);

%% Generate SPM Files
%=========================================================================
===
if make_spm
tim_ax  = linspace(0, ((1 / Fs)-1)/60, l);
i       = 0;
ftdata  = [];

% Sliding window to separate out time windows
%-------------------------------------------------------------------------
---
for s = 1:stp:l-win
```

```
    i   = i+1;
    dw  = Z(s:s+win, :)';
    tw  = tim_ax(1:win);
    conds{i} = num2str(tim_ax(s));

    ftdata.trial{i}     = dw;
    ftdata.time{i}      = tw;
end

lbl = {'RTect'; 'LTect'; 'RCrbl'; 'LCrbl'; 'RRHbr'; 'LRHbr'; 'RCHbr';
'LCHbr'; 'RRSpC'; 'LRSpC'};
ftdata.label = lbl;
ftdata.label = ftdata.label(:);

winstr  = num2str(floor(win/Fs));
stpstr  = num2str(floor(stp/Fs));

D = spm_eeg_ft2spm(ftdata, [Fsub fs 'Z_' winstr 'by' stpstr]);
D = type(D, 'single');
for c = 1:length(conds)
    D = conditions(D, c, conds{c});
end;

S = [];
S.task = 'defaulteegsens';
S.D = D;
D = spm_eeg_prep(S);

save(D);
end


%% Generate SPM Files
%=========================================================================
===
if extrctBL

l       = 4800;
tim_ax  = linspace(0, ((l / Fs)-1)/60, l);
ftdata  = [];


% Extract time window
%-------------------------------------------------------------------------
---
dw = Z(1:l,:)';
tw = tim_ax;

conds{1} = 'Baseline';

ftdata.trial{1}     = dw;
ftdata.time{1}      = tw;

lbl = {'RTect'; 'LTect'; 'RCrbl'; 'LCrbl'; 'RRHbr'; 'LRHbr'; 'RCHbr';
'LCHbr'; 'RRSpC'; 'LRSpC'};
ftdata.label = lbl;
ftdata.label = ftdata.label(:);

D = spm_eeg_ft2spm(ftdata, [Fsub fs 'Baseline_data']);
D = type(D, 'single');
```

```
for c = 1:length(conds)
    D = conditions(D, c, conds{c});
end;

S = [];
S.task = 'defaulteegsens';
S.D = D;
D = spm_eeg_prep(S);

save(D);
end


end
%%
cols = flip(cbrewer('div', 'Spectral', 100));
colormap(cols)

subplot(3,4,1), imagesc(cpow{1}); axis square
subplot(3,4,5), imagesc(cpow{2}); axis square
subplot(3,4,9), imagesc(cpow{3}); axis square

mcpow = zeros(size(cpow{1},1), size(cpow{1},2));
for cc = 1:length(cpow), mcpow = mcpow + cpow{cc}; end
mcpow = mcpow ./ length(cpow);

subplot(3,4,[2:4, 6:8, 10:12]);
imagesc(mcpow)
axis square

%% Plot Power dynamics and do statistics
%-----------------------------------------------------------------------
---
r1 = 1:240;    r2 = 241:400;   r3 = 401:800;

d{1} = [cpow{1}(1,r1), cpow{2}(1,r1), cpow{3}(1,r1)];
d{2} = [cpow{1}(1,r2), cpow{2}(1,r2), cpow{3}(1,r2)];
d{3} = [cpow{1}(1,r3), cpow{2}(1,r3), cpow{3}(1,r3)];

for dd = 1:length(d)
    c{dd} = ones(1,length(d{dd}));
end

zf_dotplot(d, {'Baseline', 'Seizure', 'Prolonged Seizure'}, 1, c, 0.1);
set(gcf, 'Color', 'w');
title('Power distribution correlations', 'fontsize', 12, 'fontweight',
'bold');
ylabel('Correlation with first time window');
```

A.5.2.2 zf_calciumsim

```
%% Housekeeping
%=======================================================================
===
D           = zf_housekeeping(1);
fs          = filesep;

Fbase       = D.Fbase;
```

```
Fscripts    = D.Fscripts;
Fanalysis   = D.Fanalysis;
Fdata       = [Fanalysis fs 'Data Files' fs 'Synth'];
Fdcm        = [Fanalysis fs 'DCM' fs 'Synth'];

spm('defaults', 'EEG');
addpath(Fscripts);
params = [];

if ~isempty(params)
    k = params.k;
    H = params.H;
    latency = params.latency;
else
    k = 1/1000;   % Inverse time constant
    H = 1;        % Maximum height
    latency = 250;
end


%% Set up convolution kernel
%==========================================================================
===
clear cal ca

for ms = 1:10000
    ca(ms) = H * exp(-k*ms);
end

[val ind]   = max(ca);
uprise      = flip( (latency-1)^2 - [0:latency-1].^2 );
uprise      = uprise / max(uprise) * val;
cal = [uprise, ca];
ca  = cal(1:length(ca));

% Illustrate convolution kernel using spiking
% --------------------------------------------------------------------------
----
figure(1), clf

subplot(3,1,1), plot(ca);
rng('default')

Hz          = 1:50;
dt          = .001;
N           = 10000;

nsd         = [1./Hz]';
lfp         = real(zf_spm_rand_power_law(nsd,Hz,dt,N));

fc          = degtorad(360);
csrange     = linspace(0,fc,length(lfp));
mdt         = -cos(csrange) + 1;
intmt       = lfp .* mdt' + lfp;

subplot(3,1,2), plot(intmt);
con = conv(intmt, ca);
subplot(3,1,3), plot(con(1:N));
```

```
%% Model specification
%=========================================================================
===
range   = linspace(-1, 1, 6);
par     = 'H(1)';

sP = range;
rng('default')

% number of regions in simulated seizure activity and model
specification
%-------------------------------------------------------------------------
---
Nc  = 1;                                        % number of channels
Ns  = 1;                                        % number of sources
options.spatial  = 'LFP';
options.model    = 'LFP';
options.analysis = 'CSD';
M.dipfit.model   = options.model;
M.dipfit.type    = options.spatial;
M.dipfit.Nc      = Nc;
M.dipfit.Ns      = Ns;
M.Hz             = 0.5:0.5:60;

% get associated priors
%-------------------------------------------------------------------------
---
A      = {0 0 0};
B      = {};
C      = 1;
pE     = spm_dcm_neural_priors(A,B,C,options.model);
pE     = spm_L_priors(M.dipfit,pE);
pE     = spm_ssr_priors(pE);
[x,f]  = spm_dcm_x_neural(pE,options.model);


% suppress channel noise (assuming many trials would be averaged)
%-------------------------------------------------------------------------
---
pE.a   = [ 0; 0];                  % log amplitude and f^(-a) exponent
pE.b   = [-2; 0];                  % log amplitude and f^(-a) exponent
pE.c   = [-2; 0];                  % log amplitude and f^(-a) exponent

% number of hidden states and endogenous inputs
%-------------------------------------------------------------------------
---
nx     = length(spm_vec(x));
nu     = size(pE.C,2);

% create LFP model
%=========================================================================
===
M.f    = f;
M.g    = 'spm_gx_erp';
M.x    = x;
M.n    = nx;
M.pE   = pE;
M.m    = nu;
M.l    = Nc;
M.u    = sparse(Ns,1);
```

```
P      = pE;

U.dt  = 1/500;
N     = 10/U.dt;
M.p   = 8;
M.dt  = U.dt;


clear nsd noise timsr convr
for t = 1:length(sP)

% Generate time series from predicted spectral densities
%-----------------------------------------------------------------------
---
switch par
    case 'T(1)', P.T(1) = sP(t);
    case 'T(2)', P.T(2) = sP(t);
    case 'H(1)', P.H(1) = sP(t);
    case 'H(2)', P.H(2) = sP(t);
    case 'H(3)', P.H(3) = sP(t);
    case 'H(4)', P.H(4) = sP(t);
    case 'H(5)', P.H(5) = sP(t);
end

nsd         = [1./M.Hz]';
noise(t,:)  = real(zf_spm_rand_power_law(nsd,M.Hz,U.dt,N));
noise(t,:)  = noise(t,:) / max(noise(t,:)) / 100;

psd         = spm_csd_mtf(P,M,U);
timsr(t,:)  = real(zf_spm_rand_power_law(psd{1},M.Hz,U.dt,N));
timsr(t,:)  = timsr(t,:)/ max(timsr(t,:)) + noise(t,:);

tonvr       = conv(timsr(t,:), ca);
convr(t,:)  = tonvr(1:length(timsr(t,:)));

mar    = spm_mar(timsr(t,:)', M.p);
mar    = spm_mar_spectra(mar,M.Hz,1/U.dt);
csd    = mar.P;
clear mar

mar = spm_mar(convr(t,:)', M.p);
mar = spm_mar_spectra(mar, M.Hz, 1/U.dt);
ssd = mar.P;

end

timsr = timsr/max(max(timsr));
convr = convr/max(max(convr));

figure(2); clf;
for i = 1:size(timsr,1)
subplot(length(sP), 1, i),
    plot(timsr(i,:), 'k'); hold on
    plot(convr(i,:), 'r');

subplot(length(sP), 1, 1),
    title('Simulated neuronal time series with calcium convolution');
end

% Make MEEG object with the time series
```

```
%=========================================================================
===
Fs = 1/U.dt;
ns = size(timsr,2);
nt = size(timsr,1);

ftdata.fsample  = Fs;
ftdata.label    = {'SynC'};
timaxis         = linspace(0, ns*U.dt, ns);

for s = 1:nt
    ftdata.trial{s} = timsr(s,:);
    ftdata.time{s}  = timaxis;
    conds{s}        = ['LFP_' num2str(s)];

    ftdata.trial{nt + s}    = convr(s,:);
    ftdata.time{nt + s}     = timaxis;
    conds{nt+s}             = ['CAI_' num2str(s)];
end

cfg.resamplefs = 20;
cfg.detrend    = 'yes';
cfg.demean     = 'yes';
cfg.feedback   = 'textbar';

ftdata = ft_resampledata(cfg, ftdata);

D = spm_eeg_ft2spm(ftdata, [Fdata fs 'syn.mat']);
D = type(D, 'single');
for c = 1:length(conds)
    D = conditions(D, c, conds{c});
end

S       = [];
S.task  = 'defaulteegsens';
S.D     = D;
D       = spm_eeg_prep(S);
save(D);

Fs20Time = ftdata.time{1}*1000;

% Set up DCM structure and invert
%=========================================================================
===
DCM = [];                               % create DCM struct
DCM.options.analysis = 'CSD';           % cross-spectral density
DCM.options.model    = 'LFP';           %
DCM.options.spatial  = 'LFP';            % virtual electrode input
DCM.options.Tdcm     = [Fs20Time(1) Fs20Time(end)];    % 1-30k ms
DCM.options.Fdcm     = [0.5 10];
DCM.options.D        = 1;               % frequency bin, 1 = no downsampling

DCM.options.Nmodes   = 8;               % cosine reduction components used
DCM.options.han      = 0;               % no hanning


DCM.Sname           = {'SynC'};
DCM.Hz              = DCM.options.Fdcm(1):0.5:DCM.options.Fdcm(2);
DCM.xY.Dfile        = [Fdata fs 'syn.mat'];
```

```
DCM.A{1}         = 0;
DCM.A{2}         = 0;
DCM.A{3}         = 1;
DCM.B            = {};
DCM.C            = sparse(length(DCM.A{1}),0);

% Define spatial inversion model (simple LFP)
%-----------------------------------------------------------------------
---
DCM.M.dipfit.Nm    = DCM.options.Nmodes;
DCM.M.dipfit.model = DCM.options.model;
DCM.M.dipfit.type  = DCM.options.spatial;
DCM.M.dipfit.Nc    = 1;
DCM.M.dipfit.Ns    = 1;

% Get priors
%-----------------------------------------------------------------------
---
[pE,pC]  = spm_dcm_neural_priors(DCM.A,DCM.B,DCM.C,DCM.options.model);
[pE,pC]  = spm_L_priors(DCM.M.dipfit,pE,pC);
[pE,pC]  = spm_ssr_priors(pE,pC);
DCM.pE   = pE;
DCM.pC   = pC;

% Run CAI
%-----------------------------------------------------------------------
---
for c = nt+1:length(conds)
    DCM.name = [Fdcm fs 'SynC_' conds{c}];
    DCM.options.trials  = [c];
    SYN{c} = zf_spm_dcm_fit(DCM);
end

for i = 1:(length(SYN)/2)
    CAI{i} = SYN{i+(length(SYN)/2)}{1};
end

% PEB to identify group mean
%=======================================================================
===
clear M;

% Set second level model parameters
%-----------------------------------------------------------------------
---
M.hE  = 0;
M.hC  = 1/16;
M.bE  = spm_vec(CAI{2}.M.pE);
M.bC  = diag(spm_vec(CAI{2}.M.pC));

M.X(:,1) = ones(1,length(CAI));
M.Q      = 'all';

% Run PEB
%-----------------------------------------------------------------------
---
CEB      = spm_dcm_peb(CAI', M, 'all');


% Rerun first level with new group means
```

```
%=========================================================================
===
% Equip first level DCM with new group mean priors
%-------------------------------------------------------------------------
---
[pE,pC]  = spm_dcm_neural_priors(DCM.A,DCM.B,DCM.C,DCM.options.model);
[pE,pC]  = spm_L_priors(DCM.M.dipfit,pE,pC);
[pE,pC]  = spm_ssr_priors(pE,pC);

vE               = spm_vec(pE);
vE(CEB.Pind)     = vE(CEB.Pind) + CEB.Ep(:,1);
pE               = spm_unvec(vE, pE);
DCM.M.pE   = pE;
DCM.M.pC   = pC;

clear CEB M CAI

% Run DCMs
%-------------------------------------------------------------------------
---
for c = nt+1:length(conds)
    DCM.name = [Fdcm fs 'SynC_' conds{c}];
    DCM.options.trials  = [c];
    SYN{c} = zf_spm_dcm_fit(DCM);
end

for i = 1:(length(SYN)/2)
    CAI{i} = SYN{i+(length(SYN)/2)}{1};
end


%% Run PEB for difference between conditions
%=========================================================================
===
clear M

%  Define model space in terms of parameters allowed to vary
%-------------------------------------------------------------------------
---
field = {'T(1)', 'T(2)', 'H(1)', 'H(2)', 'H(3)', 'H(4)', 'H(5)'};
M.X(:,1) = ones(1,length(CAI));
M.X(:,2) = [1:length(CAI)] - length(CAI)/2;

M.Q     = 'all';

for i = 1:length(field)
    [CEB{i} RCM{i}]  = spm_dcm_peb(CAI',M, field{i});
    CF(i,1) = CEB{i}.F;
end

[score winner] = max(CF);

BMC.CF  = CF;
BMC.CEB = CEB{winner};
BMC.CAI = CAI;

for r = 1:length(RCM{winner})
    Ep(r) = RCM{winner}{r}.Ep.H(1);
    Cps   = diag(RCM{winner}{r}.Cp);
    Cps   = spm_unvec(Cps, RCM{winner}{r}.Ep);
```

```
    Cp(r) = Cps.H(1);
end

figure
subplot(2,1,1), bar(BMC.CF - min(BMC.CF))
subplot(2,1,2), spm_plot_ci(Ep', Cp')


%% Plot convolution in frequency domain
%==========================================================================
===

lfp = timsr(1,:);

ftl = abs(fft(lfp)); fl = ceil(length(ftl)/2);
ftl = ftl(1:fl);
ftl = smoothts(ftl, 'g', 50, 6);

fraxis = linspace(1/10, 250, fl);

dscal = cal(1:2:end);
tftc = abs(fft(dscal)); fl = ceil(length(tftc)/2);
tftc = tftc(1:fl);
ftc  = zeros(1,length(ftl));
ftc(1:length(tftc)) = tftc;
ftc     = ftc(1:length(ftl));

subplot(3,1,1), plot(fraxis, log(ftl));  xlim([0 20]);
subplot(3,1,2), plot(fraxis, log(ftc));  xlim([0 20]);
subplot(3,1,3), plot(fraxis, log(ftl .* ftc));    xlim([0 20]);
```

A.5.2.3 zf_dcm

```
for sub = {'S1', 'S2', 'S3'};
%% Housekeeping
%--------------------------------------------------------------------------
---
clear DCM
fs          = filesep;
Fbase       = '/Users/roschkoenig/Dropbox/Research/Friston Lab/1608
Zebrafish';
Fscripts    = [Fbase fs 'Scripts'];
Fanalysis   = [Fbase fs 'Matlab Files'];
Fdata       = [Fanalysis fs 'Data Files'];
Forig       = [Fbase fs 'Data'];
Fdcm        = [Fanalysis fs 'DCM' fs sub{:}];
datafile    = [Fdata fs sub{:} fs 'Baseline_data'];
spm('defaults', 'EEG');
addpath(Fscripts);

load([Forig fs 'single_plane_ROI_MEAN_TRACES']);
Z = ROI_MEAN_TRACES.data;
l = length(Z);

Fs          = 20;
fstps       = 200;
frq_ax      = linspace(1, Fs, fstps / 2);
tim_ax      = linspace(0, ((l / Fs)-1)/60, l);
win         = 60*Fs;
```

```
stp         = 10*Fs;
windows     = 1:stp:l-win;
lbl = {'RTect'; 'LTect'; 'RCrbl'; 'LCrbl'; 'RRHbr'; 'LRHbr'; 'RCHbr';
'LCHbr'; 'RRSpC'; 'LRSpC'};

%% Set up DCM structure and invert baselne
%=========================================================================
===
Amod = zf_modelspace;

DCM = [];                              % create DCM struct
DCM.options.analysis = 'CSD';          % cross-spectral density
DCM.options.model    = 'LFP';          % structure cannonical microcircuit
(for now)
DCM.options.spatial  = 'LFP';           % virtual electrode input
DCM.options.Tdcm     = [tim_ax(1) tim_ax(end)];    % 1-30k ms

DCM.options.Fdcm    = [frq_ax(1) frq_ax(end)];      % frequency range
DCM.options.Rft     = 5;               % delay
DCM.options.onset   = 64;              % time delays between sources
DCM.options.dur     = 16;              % time dur
DCM.options.D       = 0.2;             % frequncy bin, 1 = no downsampling

DCM.options.Nmodes  = 8;               % cosine reduction components used
DCM.options.han     = 0;               % no hanning

DCM.options.lock    = 0;               % lock the trial-specific effects
DCM.options.multiC  = 0;               % multichannel effects
DCM.options.location = 0;              % optmise location
DCM.options.symmetry = 0;              % symmeterical dipoles

DCM.Sname           = lbl;
DCM.M.Hz            = frq_ax;
DCM.xY.Dfile        = datafile;

for a = 1:3
    DCM.A{a}    = Amod{end}.A{a};
end
DCM.B           = {};
DCM.C           = sparse(length(DCM.A{1}),0);

DCM.M.dipfit.Nm    = DCM.options.Nmodes;
DCM.M.dipfit.model = DCM.options.model;
DCM.M.dipfit.type  = DCM.options.spatial;
DCM.M.dipfit.Nc    = 10;
DCM.M.dipfit.Ns    = 10;

[pE,pC]  = spm_dcm_neural_priors(DCM.A,DCM.B,DCM.C,DCM.options.model);
[pE,pC]  = spm_L_priors(DCM.M.dipfit,pE,pC);
[pE,pC]  = spm_ssr_priors(pE,pC);
DCM.pE   = pE;
DCM.pC   = pC;

DCM.name = [Fdcm fs 'Full_BLN'];
DCM.options.trials  = [1];
BLN = spm_dcm_fit(DCM);
end
```

A.5.2.4 zf_bmr

```
%% Housekeeping
%=========================================================================
===
fs          = filesep;
D           = zf_housekeeping;

Fbase       = D.Fbase;
Fscripts    = D.Fscripts;
Fanalysis   = D.Fanalysis;
Forig       = D.Forig;
sub         = D.subs;

% Set up Bayesian Model Reduction across models of interest
%=========================================================================
===
% Set up BMR structure
%-------------------------------------------------------------------------
---
clear P
Amod = zf_modelspace;

% Collate all models in single matrix of models
%-------------------------------------------------------------------------
---
for s = 1:length(sub)
clear DCM
Fdcm    = [Fanalysis fs 'DCM' fs sub{s}];
load([Fdcm fs 'Full_BLN.mat']);
FCM     = DCM;
DCM     = rmfield(DCM, 'Ep');
DCM     = rmfield(DCM, 'Cp');

for m = 1:(length(Amod)-1)
    for a = 1:3
        DCM.pE.A{a} = Amod{m}.A{a};
        DCM.pC.A{a} = DCM.pE.A{a} .* FCM.pC.A{a};
        DCM.M.pE    = DCM.pE;
        DCM.M.pC    = DCM.pC;
    end
    DCM.name    = Amod{m}.name;
    P{s,m}      = DCM;
end

% Add full model to model matrix
%-------------------------------------------------------------------------
---
P{s,length(Amod)} = FCM;

end

% Run Bayesian model reduction
%=========================================================================
===
[BLCM BLMC BLMA] = spm_dcm_bmr(P);

% Extract free energies
%-------------------------------------------------------------------------
---
clear F Fs
for b = 1:length(BLMC)
    F(b,:) = BLMC(b).F;
```

```
end

% Extract model names
%-------------------------------------------------------------------------
---
for m = 1:length(Amod)
    mlab{m} = Amod{m}.name;
end

%% Family wise comparison - draw figures
%=========================================================================
===
% Define families
%-------------------------------------------------------------------------
---
Flr = F(1:6) + F(7:12) + F(13:18) + F(19:24);
Fsr = F(1:6:24) + F(2:6:24) + F(3:6:24) + F(4:6:24) + F(5:6:24) +
F(6:6:24);

figure(2)
set(gcf, 'color', 'w');
colormap gray

% Plot Hub connection BMC
%-------------------------------------------------------------------------
---
subplot(2,1,2),
    % Plot
    bar(Flr - min(Flr));

    % Titles and legends
    title('Evidence for hub connections', 'FontSize', 12, 'FontWeight',
'bold');
    set(gca, 'XTick', 1:6);
    set(gca, 'XTickLabel', {'None', 'Tec', 'Cbl', 'RHb', 'CHb', 'RSC'});

    % Settings
%     axis square
    box off

% Plot Hub connection BMC
%-------------------------------------------------------------------------
---
subplot(2,1,1),

    % Plot
    bar(Fsr - min(Fsr));

    % Titles and Legends
    title('Evidence for short range connections', 'FontSize', 12,
'FontWeight', 'bold');
    set(gca, 'XTick', 1:4);
    set(gca, 'XTickLabel', {'None', 'Homol.', 'Neigh.', 'Both'})

    % Settings
    box off
```

A.5.2.6 zf_slide

```
%% Manual Definitions
%=========================================================================
===
wins = 60;
stps = 10;

% Housekeeping
%-------------------------------------------------------------------------
---
clear DCM
fs          = filesep;
if strcmp('PCWIN64', computer);
    Fbase = 'C:\Users\rrosch\Dropbox\Research\Friston Lab\1608
Zebrafish';
else
    Fbase = '/Users/roschkoenig/Dropbox/Research/Friston Lab/1608
Zebrafish';
end

Fscripts    = [Fbase fs 'Scripts'];
Fanalysis   = [Fbase fs 'Matlab Files'];
Fdata       = [Fanalysis fs 'Data Files'];
Forig       = [Fbase fs 'Data'];
Fdcm        = [Fanalysis fs 'DCM'];
datafile    = [Fdata fs 'Z_180by90.mat'];
spm('defaults', 'EEG');
addpath(Fscripts);

load([Forig fs 'single_plane_ROI_MEAN_TRACES']);
Z = ROI_MEAN_TRACES.data;
l = length(Z);
clear Z;

load([Fdata fs 'Z_' num2str(wins) 'by' num2str(stps) '.mat']);
Ntrials     = length(D.trials);
clear D;

Fs          = 20;
fstps       = 200;
frq_ax      = linspace(1, Fs, fstps / 2);
tim_ax      = linspace(0, ((l / Fs)-1)/60, l);
win         = wins*Fs;
stp         = stps*Fs;
windows     = 1:stp:l-win;
lbl = {'RTect'; 'LTect'; 'RCrbl'; 'LCrbl'; 'RRHbr'; 'LRHbr'; 'RCHbr';
'LCHbr'; 'RRSpC'; 'LRSpC'};

%% Set up DCM structure
%=========================================================================
===
Amod = zf_modelspace;

DCM = [];                           % create DCM struct
DCM.options.analysis = 'CSD';       % cross-spectral density
DCM.options.model    = 'LFP';       % structure cannonical microcircuit
(for now)
DCM.options.spatial  = 'LFP';        % virtual electrode input
DCM.options.Tdcm     = [tim_ax(1) tim_ax(end)];   % 1-30k ms
DCM.option.DATA      = [];
```

```
DCM.options.Fdcm    = [frq_ax(1) frq_ax(end)];      % frequency range
DCM.options.Rft     = 5;            % delay
DCM.options.onset   = 64;           % time delays between sources
DCM.options.dur     = 16;           % time dur
DCM.options.D       = 0.2;          % frequncy bin, 1 = no downsampling

DCM.options.Nmodes  = 8;            % cosine reduction components used
DCM.options.han     = 0;            % no hanning

DCM.options.lock    = 0;            % lock the trial-specific effects
DCM.options.multiC  = 0;            % multichannel effects
DCM.options.location = 0;           % optmise location
DCM.options.symmetry = 0;           % symmeterical dipoles

DCM.Sname           = lbl;
DCM.M.Hz            = frq_ax;
DCM.xY.Dfile        = datafile;
DCM.xY.Hz           = frq_ax;

for a = 1:3
    DCM.A{a}    = Amod{4}.A{a};     % Tectum Hub Model
end
DCM.B           = {};
DCM.C           = sparse(length(DCM.A{1}),0);

DCM.M.dipfit.Nm    = DCM.options.Nmodes;
DCM.M.dipfit.model = DCM.options.model;
DCM.M.dipfit.type  = DCM.options.spatial;
DCM.M.dipfit.Nc    = 10;
DCM.M.dipfit.Ns    = 10;

[pE,pC]  = spm_dcm_neural_priors(DCM.A,DCM.B,DCM.C,DCM.options.model);
[pE,pC]  = spm_L_priors(DCM.M.dipfit,pE,pC);
[pE,pC]  = spm_ssr_priors(pE,pC);
DCM.pE   = pE;
DCM.pC   = pC;

for s = 1 :Ntrials
    if s < 10, ns = ['00' num2str(s)];
    elseif s < 100, ns = ['0' num2str(s)];
    else ns = num2str(s);
    end
    DCM.options.trials  = [s];
    DCM = spm_dcm_fit(DCM);
end
```

A.5.2.7 zf_peb

```
%% Housekeeping
%=========================================================================
===
% Generic Housekeeping
%-------------------------------------------------------------------------
---
clear all
fs          = filesep;
D           = zf_housekeeping;
Fbase       = D.Fbase;
Fscripts    = D.Fscripts;
```

```
Forig       = D.Forig;
Fanalysis   = D.Fanalysis;

sub         = D.subs;
Fs          = D.Fs;
win         = D.win;
stp         = D.stp;
lbl         = D.lbl;
frq_ax      = D.frq_ax;
endtime     = D.endtime;

i   = 0;
clear DCM

for s = 1:length(sub)

% Subject specific housekeeping
%-------------------------------------------------------------------------
---
Fdata       = [Fanalysis fs sub{s} 'Data Files'];
Fdcm        = [Fanalysis fs 'DCM' fs sub{s}];
Finv        = [Fanalysis fs 'Cluster Files' fs sub{s} fs 'Inverted
DCMs'];
datafile    = [Fdata fs 'Z_60by10.mat'];


% Load DCMs
%=========================================================================
===
files = cellstr(spm_select('FPList', Finv, 'DCM_*'));
for f = 5:5:892
    i = i + 1;
    TCM = load(files{f});
    DCM{i} = TCM.DCM{1};
    clear TCM;
end
end

DCM = DCM';

%% Set up PEB model
%=========================================================================
===
% Make second level model space
%=========================================================================
===
ldcm    = length(DCM)/3;
tim_ax  = linspace(0, endtime, ldcm);
ti      = find(tim_ax > 30);

% PTZ time curves
%-------------------------------------------------------------------------
---
clear ptz

k = 1/30;           % Inverse time constant
H = 1 * 1/0.37;     % Maximum height
i = 0;
ptz_t   = [];

for w = (tim_ax(tim_ax > 30))-30
```

```
    i = i+1;
    ptz(ti(i)) = H*k*w * exp(-k*w);
end

% Tonic effect
%-------------------------------------------------------------------------
---
tnc = zeros(1,ldcm);
tnc(ti) = ones(1,length(ti));

% Prolonged seizure effect
%-------------------------------------------------------------------------
---
plg = zeros(1,ldcm);
plg(ti) = linspace(0,1,length(ti));

% Direct cosine transforms
%-------------------------------------------------------------------------
---
dct = spm_dctmtx(1,4,linspace(0, 5, ldcm));
dct = dct(:,2:end)' ./ max(max(dct));

% Static effects
%-------------------------------------------------------------------------
---
stc = ones(1,ldcm);

% Empty filler
%-------------------------------------------------------------------------
---
emp = zeros(1,ldcm);

% Run PEB
%=========================================================================
===
clear X Xnames M PEB RCM BMA
X       = [ tnc, tnc, tnc; ...
            ptz, ptz, ptz; ...
            plg, plg, plg; ...
            dct, dct, dct;
            stc, emp, emp; ...
            emp, stc, emp; ...
            emp, emp, stc]';
Xnames  = {'Tonic', 'Monophasic', 'Prolonged', 'DCT1', 'DCT2', 'DCT2',
'S1', 'S2', 'S3'};
M.X         = X;
M.Xnames    = Xnames;

imagesc(X);
[PEB RCM] = spm_dcm_peb(DCM, M, {'A', 'H', 'T'});

%% Create reduced model space at second level
%=========================================================================
===
clear T H

% Intrinsic effects
%=========================================================================
===
for t = 1:7, T{t} = zeros(10,2); H{t} = zeros(10,5); end
for f = 1:5
```

```
    idx     = [1:2]+(f-1)*2;
    T{f+1}(idx,:)   = DCM{1}.pC.T(idx,:);
    H{f+1}(idx,:)   = DCM{1}.pC.H(idx,:);
end
T{7}      = DCM{1}.pC.T;        H{7}    = DCM{1}.pC.H;

% Extrinsic effects
%=========================================================================
===
Amod = zf_modelspace;
clear Hom Nei Hub hub nei extr

% Homologue lateral connectivity
%-------------------------------------------------------------------------
---
Hom{1} = Amod{1}.A;                                 % none

% Neighbouring forward/backward connectivity
%-------------------------------------------------------------------------
---
empt    = zeros(length(Amod{1}.A{1}));
neimat  = zeros(length(Amod{1}.A{1}));

for m = 3:length(neimat)
    neimat(m, m-2) = 1;
    neimat(m-2, m) = 1;
end

Nei{1} = Amod{1}.A;                                 % none
Nei{2} = Amod{1}.A;                                 % forward
    Nei{2}{1} = empt + triu(neimat);
Nei{3} = Amod{1}.A;                                 % backward
    Nei{3}{2} = empt + tril(neimat);
Nei{4} = Amod{1}.A;                                 % forward and backward
    Nei{4}{1} = Nei{2}{1};
    Nei{4}{2} = Nei{3}{2};

% Optic Tectum hub forward/backward connectivity
%-------------------------------------------------------------------------
---
Hub{1} = Amod{1}.A;                                 % none
Hub{2} = Amod{1}.A;                                 % forward
    Hub{2}{1} = Amod{2}.A{1};
Hub{3} = Amod{1}.A;                                 % backward
    Hub{3}{2} = Amod{2}.A{2};
Hub{4} = Amod{1}.A;                                 % forward and backward
    Hub{4}{1} = Hub{2}{1};
    Hub{4}{2} = Hub{3}{2};

% Assemble into 4 * 4 = 32 model space
%-------------------------------------------------------------------------
---
count = 0;
h     = 1;
for n = 1:length(Nei)
for b = 1:length(Hub)
    count = count+1;
    ext{count}.A{1} = Nei{n}{1} + Hub{b}{1};
    ext{count}.A{2} = Nei{n}{2} + Hub{b}{2};
    ext{count}.A{3} = Hom{h}{3};
```

```
    hub(count) = b;
    nei(count) = n;
end
end

% PEB BMC for Extrinsic Connections
%=========================================================================
===
% Assemble model matrix
%-------------------------------------------------------------------------
---
clear MOD

for tw = 1:length(DCM)
    count = 0;

    for i = length(T)
    for e = 1:length(ext)
        count = count+1;
        MOD{tw,count} = DCM{tw};

        MOD{tw,count}.M.pC.A     = ext{e}.A;
        MOD{tw,count}.M.pC.T     = T{i};
        MOD{tw,count}.M.pC.H     = H{i};
    end
    end
end

% Run PEB for Extrinsic Connections
%-------------------------------------------------------------------------
---
PMA     = spm_dcm_peb_bmc(PEB, MOD(1,:));

% Family Wise Comparison - Extrinsic Connections
%=========================================================================
===
figure
F = sum(PMA.F,2);
for ni = 1:length(Nei)
    n(ni) = sum(F(find(nei == ni)));
end
sn  = sort(n);
dFn = sn(end) - sn(end-1);

for hi = 1:length(Hub)
    h(hi) = sum(F(find(hub == hi)));
end
sh  = sort(h);
dFh = sh(end) - sh(end-1);

% Plot family-wise comparison for free energies
%-------------------------------------------------------------------------
---
set(gcf, 'Color', 'w');

subplot(1,2,1)
bar(n - min(n))

    % Labels and Fonts
    title('Extrinsic coupling of hierarchy', 'FontSize', 12,
'FontWeight', 'bold');
```

```
    set(gca, 'XTick', [1 2 3 4], 'XTickLabel', {'Nil', 'Forward',
'Backward', 'Forward/Backward'});
    xlabel(['dF = ' num2str(dFn,2)], 'FontWeight', 'bold');

    % Plotting Parameters
    axis square
    colormap gray

subplot(1,2,2)
bar(h - min(h))

    % Labels and Fonts
    title('Extrinsic coupling of hub region', 'FontSize', 12,
'FontWeight', 'bold');
    set(gca, 'XTick', [1 2 3 4], 'XTickLabel', {'Nil', 'Forward',
'Backward', 'Forward/Backward'});
    xlabel(['dF = ' num2str(dFh, 4)], 'FontWeight', 'bold');

    % Plotting Parameters
    axis square
    colormap gray


%% PEB BMC for Intrinsic connections
%=========================================================================
===
% Assemble model matrix
%-------------------------------------------------------------------------
---
clear MOD t F

for tw = 1:length(DCM)
    count = 0;
    for i = 1:length(T)
    for e = length(ext)
        count = count+1;

        MOD{tw,count} = DCM{tw};

        MOD{tw,count}.M.pC.A     = ext{e}.A;
        MOD{tw,count}.M.pC.T     = T{i};
        MOD{tw,count}.M.pC.H     = H{i};

        int(count) = i;
    end
    end
end

% Run PEB for Intrinsic Connections
%-------------------------------------------------------------------------
---
[PMA]   = spm_dcm_peb_bmc(PEB, MOD(1,:));

% Family Wise Comparison - Intrinsic Connections
%=========================================================================
===
clear t ti
F   = sum(PMA.F,2);
st  = sort(F);
dFn = st(end) - st(end-1);
```

```
% Plot family-wise comparison for free energies
%-------------------------------------------------------------------------
---
figure
bar(F - min(F))
set(gcf, 'Color', 'w');

% Labels and Fonts
title('Intrinsic Parameters', 'FontSize', 12, 'FontWeight', 'bold');
set(gca, 'XTick', [1 2 3 4 5 6 7], 'XTickLabel', {'Nil', 'Tect', 'Crbl',
'RHBr', 'CHBr', 'RSC', 'all'});
xlabel(['dF = ' num2str(dFn,4)], 'FontWeight', 'bold');

% Plotting Parameters
axis square
colormap gray

%% Generate winning model average within model families
%=========================================================================
===
clear M
Xnames      = {'Tonic', 'Monophasic', 'Prolonged', 'DCT1', 'DCT2',
'DCT2', 'S1', 'S2', 'S3'};
M.X         = X;
M.Xnames    = Xnames;

Fhub        = { 'A{1}(1,3)', 'A{1}(1,4)', 'A{1}(1,5)', 'A{1}(1,6)',
'A{1}(1,7)', 'A{1}(1,8)', 'A{1}(1,9)', 'A{1}(1,10)', ...
                'A{1}(2,4)', 'A{1}(2,5)', 'A{1}(2,6)', 'A{1}(2,7)',
'A{1}(2,8)', 'A{1}(2,9)', 'A{1}(2,10)'};

[PEB, RCM]  = spm_dcm_peb(DCM, M, {'H', 'T', Fhub{:}});
[PMA]       = spm_dcm_peb_bmc(PEB);

%% Extract and plot Parameters
%=========================================================================
===
clear PEB PMA RCM

% Load outputs of PEB analysis
%-------------------------------------------------------------------------
---
Fpeb        = [Fanalysis fs 'PEB'];
load([Fpeb fs 'PEB']);
load([Fpeb fs 'PMA']);

Rlist  = cellstr(spm_select('FPList', Fpeb, '^R'));
for r = 1:length(Rlist)
    load(Rlist{r});
    RCM{r}  = rcm;
    clear rcm
end

%% Define time window to plot
%-------------------------------------------------------------------------
---
clear xEp xCp Te Ti He Hi Aa Ep Cp c d
X         = PEB.M.X;
[val loc] = max(diff(PEB.M.X(:,2)));      % Maximum acute effect
```

```
G         = PEB;
for i = 1:2
    Np      = length(G.Pnames);
    Ep(:,i) = G.Ep( [1:Np] + (i-1)*Np ) * X(loc,i);
    Cps     = diag(G.Cp);
    Cp(:,i) = Cps( [1:Np] + (i-1)*Np );
end

xCp     = sum(Cp,2);
xEp     = sum(Ep,2);  xEp = exp(xEp);

Te      = zeros(1,Np);  Ti  = zeros(1,Np);
He      = zeros(1,Np);  Hi  = zeros(1,Np);
Aa      = zeros(1,Np);

for p = 1:Np
    if ~isempty(regexp(PEB.Pnames{p}, 'T.*,1)')), Te(p) = 1;    end
    if ~isempty(regexp(PEB.Pnames{p}, 'T.*,2)')), Ti(p) = 1;    end
    if ~isempty(regexp(PEB.Pnames{p}, 'H.*,[1 2 3])')), He(p) = 1;  end
    if ~isempty(regexp(PEB.Pnames{p}, 'H.*,[4,5])')), Hi(p) = 1;    end
    if ~isempty(regexp(PEB.Pnames{p}, 'A.*')), Aa(p) = 1;    end
end

Te = find(Te);  Ti = find(Ti);
He = find(He);  Hi = find(Hi);
Aa = find(Aa);

clear cols colblock
colblock = cbrewer('qual', 'Paired', 10);

d{1} = xEp(Te)';     lab{1} = 'Te';  c{1} = xCp(Te)'; cols{1} =
[colblock];
d{2} = xEp(Ti)';     lab{2} = 'Ti';  c{2} = xCp(Ti)'; cols{2} =
[colblock];
d{3} = xEp(He)';     lab{3} = 'He';  c{3} = xCp(He)'; cols{3} =
[colblock; colblock; colblock];
d{4} = xEp(Hi)';     lab{4} = 'Hi';  c{4} = xCp(Hi)'; cols{4} =
[colblock; colblock];
d{5} = xEp(Aa)';     lab{5} = 'A';   c{5} = xCp(Aa)'; cols{5} = [];

for a = 1:length(Aa)
    dgt         = str2double(PEB.Pnames{Aa(a)}(end-1));
    if dgt == 0, dgt = 10; end
    cols{5}     = [cols{5}; colblock(dgt,:)];
end

figure
zf_dotplot(d, lab, 1, c, cols);
```

A.5.2.8 zf_simulate

```
% Generic Housekeeping
%-------------------------------------------------------------------------
---
clear all
fs          = filesep;
D           = zf_housekeeping;
Fbase       = D.Fbase;
Fscripts    = D.Fscripts;
Forig       = D.Forig;
```

```
Fanalysis   = D.Fanalysis;
Fpeb        = [Fanalysis fs 'PEB'];

sub         = D.subs;
Fs          = D.Fs;
win         = D.win;
stp         = D.stp;
lbl         = D.lbl;
frq_ax      = D.frq_ax;
endtime     = D.endtime;

% Load outputs of PEB analysis
%-------------------------------------------------------------------------
---
Rlist  = cellstr(spm_select('FPList', Fpeb, '^R'));
for r = 1:length(Rlist)
    load(Rlist{r});
    RCM{r}  = rcm;
    clear rcm
end

load([Fpeb fs 'PEB']);
load([Fpeb fs 'PMA']);

%% Principal component analysis
%-------------------------------------------------------------------------
---
Np  = length(PEB.Pnames);
Nw  = length(PEB.Snames);
Ep  = [PEB.Ep(:,1:9) * PEB.M.X(:,1:9)'];

T = [];         H = [];
for p = 1:Np
    if ~isempty(regexp(PEB.Pnames{p}, ['T(.*[2],[1 2])'])),         T(p)
= 1;    end
    if ~isempty(regexp(PEB.Pnames{p}, ['H(.*[2],[1 2 3 4 5])'])),   H(p)
= 1;    end
end
T = find(T);    H = find(H);
colblock = flip(cbrewer('div', 'Spectral', Nw/3));
cols     = [colblock; colblock; colblock];

[Tcf Tsc Tlat Tt2 Texp]     = pca(Ep(:,T), 'Algorithm', 'eig');
[Hcf Hsc Hlat Ht2 Hexp]     = pca(Ep(:,H), 'Algorithm', 'eig');

clear CA

CA.Tcf      = Tcf;          CA.Hcf      = Hcf;
CA.Tsc      = Tsc;          CA.Hsc      = Hsc;

scatter(Tsc(:,1), Hsc(:,1), 80, cols, 'filled')
xlabel('T component');
ylabel('H component');

figure
scatter3(Tsc(:,1), Hsc(:,1), Hsc(:,2), 80, cols, 'filled');
xlabel('First component of time constants');
ylabel('First component of connectivity parameters');
zlabel('Second component of connectivity parameters');

%% Model single node output
```

```
%=========================================================================
===
frq_ax      = D.frq_ax;
BCM.A{1}    = 0;
BCM.A{2}    = 0;
BCM.A{3}    = 1;
BCM.B       = {};
BCM.C       = sparse(length(BCM.A{1}),0);

BCM.options.model    = 'LFP';

BCM.M.dipfit.Nm    = 8;
BCM.M.dipfit.model = BCM.options.model;
BCM.M.dipfit.type  = 'LFP';
BCM.M.dipfit.Nc    = 1;
BCM.M.dipfit.Ns    = 1;

frqsim      = .5:.5:50;
BCM.M.Hz    = frqsim;
BCM.M.f     = 'spm_fx_lfp';
BCM.M.g     = 'spm_gx_erp';
BCM.M.l     = BCM.M.dipfit.Nm;
BCM.M.x     = zeros(1,13);
BCM.M.u     = 0;
BCM.xU.X    = zeros(1,0);

[pE,pC]  = spm_dcm_neural_priors(BCM.A,BCM.B,BCM.C,BCM.options.model);
[pE,pC]  = spm_L_priors(BCM.M.dipfit,pE,pC);
[pE,pC]  = spm_ssr_priors(pE,pC);

% Setup baseline
%-------------------------------------------------------------------------
----
Ep  = PEB.Ep(:,7);
Np  = length(PEB.Pnames);

% clear T H
% for p = 1:Np
%     if ~isempty(regexp(PEB.Pnames{p}, ['T.*[2],[1 2])'])),
T(p) = 1;    end
%     if ~isempty(regexp(PEB.Pnames{p}, ['H.*[2],[1 2 3 4 5])'])),  H(p)
= 1;    end
% end
% T   = find(T);
% H   = find(H);

Sp  = pE;
Sp.T    = Ep(T)';
Sp.H    = Ep(H)';

%
% mnSc  = -50;
% mxSc  = 30;

steps = 100;
grad1  = linspace(-.5,.5,steps);
grad2  = linspace(-1,1,steps);
dim1  = grad1 .* CA.Tcf(:,1);
dim2  = grad2 .* CA.Hcf(:,1);

clear CSD POW
```

```
for d1 = 1:size(dim1,2)-1
for d2 = 1:size(dim2,2)
    pS      = Sp;
    ti      = [1 2];
    hi      = [1 2 3 4 5];
    pS.T    = pS.T + dim1(ti,d1);
    pS.H    = pS.H + dim2(hi,d2);

    csd         = spm_csd_mtf(pS, BCM.M, BCM.xU);
    CSD(d1,d2,:)= abs(csd{1}(:,1,1));
    POW(d1,d2)  = mean(CSD(d1,d2,1:8));
end
end

%%
for d1 = 1:size(dim1,2)-1
for d2 = 1:size(dim2,2)
    POW(d1,d2)  = mean(CSD(d1,d2,find(frqsim >= 25)));
end
end
subplot(2,1,1)
contour(grad1(1:end-1), grad2, log(POW)', [-3 -2 -1 0 1]);
title('Log gamma power in parameter space');
colormap gray, axis square
colorbar;
set(gca, 'YDir', 'normal');

for d1 = 1:size(dim1,2)-1
for d2 = 1:size(dim2,2)
    POW(d1,d2)  = mean(CSD(d1,d2,find(frqsim <= 4)));
end
end

subplot(2,1,2)
imagesc(grad1(1:end-1), grad2, log(POW)'); hold on
title('Log delta power in parameter space')
colormap gray, axis square
colorbar
set(gca, 'YDir', 'normal');

scatter(Tsc(:,1), Hsc(:,1), 80, cols, 'filled')
xlabel('T component');
ylabel('H component');



%% Plot individual fish predictions of parameter changes over time
%-----------------------------------------------------------------------
---
for d1 = 1:length(Tsc(:,1))
    Ti(d1) = nearest(grad1, Tsc(d1,1));   % T dimension
end

for d2 = 1:length(Hsc(:,1))
    Hi(d2) = nearest(grad2, Hsc(d2,1));   % T dimension
end

ss = 1:floor(length(Ti) / 3);     % indices for single subject
for s = 1:3
subplot(1,3,s)
    Tplot = Ti(ss + (s-1)*ss(end));
```

```
    Hplot = Hi(ss + (s-1)*ss(end));
    for t = 1:length(Tplot)
        csd     = squeeze(log(CSD(Tplot(t), Hplot(t), :)));
        plot(csd, 'color', cols(t,:)); hold on
    end
    ylim([-5 1]);
end
```

A.6 DCM analysis of NMDAR-Ab effects in patients and a mouse model of NMDAR-Ab encephalitis

A.6.1 README description of code function

The matlab scripts shown here implement the analysis discussed in detail in chapter 5 of this thesis – using invasive electrophysiological recordings in a mouse model of NMDAR-Ab encephalitis, as well as EEG recordings in human patients, the analysis applies DCM to extract neural mass model descriptions of the NMDAR-Ab induced abnormalities.

The full code and data for this project have been made publicly available in an open science repository that can be found online here: https://www.doi.org/10.17605/OSF.IO/YXKWD

A.6.2 Custom functions

A.6.2.1 mab_dcm

```
%% mab_dcm
%=========================================================================
===
% This routine implements and runs DCMs on the windowed spectral single
% channel data

D           = mab_housekeeping;
Fbase       = D.Fbase;
Fscripts    = D.Fscripts;
Fanalysis   = D.Fanalysis;
Fdcm        = D.Fdcm;
mind        = D.mind;
fs          = filesep;
clear D

%% Model specification
%=========================================================================
===
rng('default')
clear DCM SLIDE

DCM.xY.Dfile    = [Fanalysis fs 'LFP_MEEG'];
LFP             = spm_eeg_load(DCM.xY.Dfile);
Fs              = fsample(LFP);
smpls           = size(LFP,2);
timax           = linspace(0, smpls/Fs, smpls);
LFP_conds       = condlist(LFP);

for c = 1:length(LFP_conds)
disp(['Currently at ' num2str(c) ' of ' num2str(length(LFP_conds)) '
windows']);

% Set up DCM details
%-------------------------------------------------------------------------
---
DCM.options.analysis    = 'CSD';    % cross-spectral density
```

```
DCM.options.model       = 'CMC';    % structure cannonical microcircuit
(for now)
DCM.options.spatial     = 'LFP';    % virtual electrode input
DCM.options.Tdcm        = [timax(1) timax(end)] * 1000;     % time in ms

DCM.options.Fdcm    = [1 60];       % frequency range
DCM.options.D       = 1;            % frequency bin, 1 = no downsampling
DCM.options.Nmodes  = 8;            % cosine reduction components used
DCM.options.han     = 0;            % no hanning
DCM.options.trials  = c;            % index of ERPs within file

DCM.Sname           = chanlabels(LFP);
DCM.M.Hz            =
DCM.options.Fdcm(1):DCM.options.D:DCM.options.Fdcm(2);
DCM.xY.Hz           = DCM.M.Hz;

% Create DCM Struct and specify DCM.options
%-----------------------------------------------------------------------
---
DCM.A       = {1 1 1};
DCM.B       = {};
DCM.C       = sparse(length(DCM.A{1}),0);

% Reorganise model parameters in specific structure
%=======================================================================
===
DCM.M.dipfit.Nm     = DCM.options.Nmodes;
DCM.M.dipfit.model  = DCM.options.model;
DCM.M.dipfit.type   = DCM.options.spatial;

DCM.M.dipfit.Nc     = size(LFP,1);
DCM.M.dipfit.Ns     = length(DCM.A{1});
DCM.name            = [Fdcm fs 'DCM_' LFP_conds{DCM.options.trials}
'.mat'];

SLIDE{c}            = mab_spm_dcm_csd(DCM);
SLIDE{c}.xY.R       = diag(SLIDE{c}.xY.R);
save([Fanalysis fs 'DCM_All'], 'SLIDE');
end
```

A.6.2.2 mab_peb

```
%% mab_peb
%=======================================================================
===
% This routine loads the inverted individual time window DCMs and
performs
% parametric empirical Bayesian analyiss

clear all

% Housekeeping
%=======================================================================
===
D           = mab_housekeeping;
fs          = filesep;
Fbase       = D.Fbase;
Fscripts    = D.Fscripts;
Fdcm        = D.Fdcm;
Fanalysis   = D.Fanalysis;
```

```
mind        = D.mind;
Tplot       = D.Tplot;      Tlabel      = D.Tlabel;
Gplot       = D.Gplot;      Glabel      = D.Glabel;

load([Fanalysis fs 'DCM_All.mat']);
LFP = spm_eeg_load([Fanalysis fs 'LFP_MEEG']);
clear D

% PEB Analysis
%=========================================================================
===
% Make second level model space
%-------------------------------------------------------------------------
---
clear M ptz atb itx
k = 1/10;           % Inverse time constant
H = 1 * 1/0.37;     % Maximum height
i       = 0;
ptz_t   = [];

% PTZ time curves
%-------------------------------------------------------------------------
---
seg     = 1:fix(length(SLIDE)/4);
tim_ax  = linspace(0, 60, length(seg));

for w = tim_ax
    i = i+1;
    ptz_t(i) = H*k*w * exp(-k*w);
end

ptz(seg) = zeros(1,length(seg));
ptz(seg + seg(end)) = ptz_t;
ptz     = [ptz, ptz];

% Antibody definitions
%-------------------------------------------------------------------------
---
atb     = zeros(1, 2*seg(end));
atb_2   = ones(1, 2*seg(end));
atb     = [atb, atb_2];

% Interaction modelling
%-------------------------------------------------------------------------
---
for i = 1:length(atb),
    if ptz(i) == 0,
        itx(i) = 0;
    else
        if atb(i) > 0
            itx(i) = ptz(i);
        else
            itx(i) = -ptz(i);
        end
    end
end

clist   = condlist(LFP);
for c = 1:length(clist)
    uscores = find(clist{c} == '_');
```

```
    for u = uscores, clist{c}(u) = ' '; end
end

subplot(3,1,1), plot(atb); title('Main effect of Antibody');
subplot(3,1,2), plot(ptz); title('Main effect of PTZ');
subplot(3,1,3), plot(itx); title('Interaction');
set(gca, 'XTick', 1:seg(end):length(SLIDE))
set(gca, 'XTickLabel', clist(1:seg(end):length(SLIDE)));

% Run PEB
%-----------------------------------------------------------------------
---
FCM         = SLIDE';
X           = [atb; ptz; itx; ones(1,length(atb)); ]';
Xnames      = {'Antibody', 'PTZ', 'Interaction', 'Static'};

M.X         = X;
M.Xnames    = Xnames;
M.Q         = 'all';

% The model space below yields the full model as winning
%=======================================================================
===
% Time constant parameters mab_spm_fx_cmc
%-----------------------------------------------------------------------
---
% G(:,1)  ss -> ss (-ve self)  4    MOD
% G(:,2)  sp -> ss (-ve rec )  4    INH
% G(:,3)  ii -> ss (-ve rec )  4    INH
% G(:,4)  ii -> ii (-ve self)  4    MOD
% G(:,5)  ss -> ii (+ve rec )  4    EXC
% G(:,6)  dp -> ii (+ve rec )  2    EXC
% G(:,7)  sp -> sp (-ve self)  4    MOD
% G(:,8)  ss -> sp (+ve rec )  4    EXC
% G(:,9)  ii -> dp (-ve rec )  2    INH
% G(:,10) dp -> dp (-ve self)  1    MOD
%
% The order in the DCM structure is as follows
% j     = [7 2 3 4 5 6 8 9 10 1];
% i.e.     M I I M E E E I M  M
% new   =  1 2 3 4 5 6 7 8 9 10

fields{1}   = {'T(1)', 'T(2)', 'T(3)', 'T(4)'};     % time constants
fields{2}   = {'G(2)', 'G(3)', 'G(8)'};             % inh connections
fields{3}   = {'G(5)', 'G(6)', 'G(7)'};             % exc connections
fields{4}   = {'G(1)', 'G(4)', 'G(9)', 'G(10)'};    % mod connections
fields{5}   = {fields{1}{:}, fields{2}{:}};         % time and inh
fields{6}   = {fields{1}{:}, fields{3}{:}};         % time and exc
fields{7}   = {fields{1}{:}, fields{4}{:}};         % time and mod
fields{8}   = {fields{1}{:}, fields{2}{:}, fields{4}{:}};   % time, inh,
and mod
fields{9}   = {fields{1}{:}, fields{2}{:}, fields{3}{:}};   % time, inh,
and exc
fields{10}   = {fields{2}{:}, fields{3}{:}};         % inh and exc
fields{11}   = {fields{2}{:}, fields{4}{:}};         % inh and mod
fields{12}  = {fields{3}{:}, fields{4}{:}};         % exc and mod
fields{13}  = {fields{2}{:}, fields{3}{:}, fields{4}{:}}; % all coupling
fields{14}  = {fields{1}{:}, fields{2}{:}, fields{3}{:}, fields{4}{:}};
% all

labels  = { 't', 'g_i', 'g_e', 'g_m', ...
```

```
            't, g_i', 't, g_e', 't, g_m', 't, g_i, g_m', 't, g_i, g_e',
...
            'g_i, g_e', 'g_i, g_m', 'g_e, g_m', 'g_{all}', 'all'};
%
% % Run PEB across reduced second level model space
%
%=========================================================================
===
% for f = 1:length(fields)
%     [PEB, RCM]  = spm_dcm_peb(FCM, M, fields{f});
%     P(f).PEB = PEB;
%     P(f).F   = PEB.F;
%     F(f) = PEB.F;
% end
% save([Fdcm fs 'PEB.mat'], 'P');
%
% % Calculate the Free energy difference between winning and second
model
% %-------------------------------------------------------------------------
-----
% [Fstd Fstg] = sort(F, 'descend');
% dF          = Fstd(1) - Fstd(2);
%
% % Plot Bayesian model comparison over second level model space
% %-------------------------------------------------------------------------
-----
% subplot(2,1,1), bar(F - min(F));          title(['Free Energy, dF = '
num2str(dF)]);
% subplot(2,1,2), bar(spm_softmax(F'));     title('Posterior
Probability');

% Bayesian model reduction over winning PEB (full model)
%-------------------------------------------------------------------------
---

[PEB RCM]   = spm_dcm_peb(FCM, M, fields{end});
BMA         = spm_dcm_peb_bmc(PEB);
FEB.BMA     = BMA;
FEB.RCM     = RCM;
FEB.PEB     = PEB;

save([Fdcm fs 'Full Empirical Bayes.mat'], 'FEB');

%% Plot DCM outputs
%=========================================================================
===
load([Fdcm fs 'Full Empirical Bayes']);
RCM     = FEB.RCM;

% Extract predicted and observed spectra
%-------------------------------------------------------------------------
---
for r = 1:length(RCM)
    pre(:,r) = log(abs(RCM{r}.Hc{1}));
    obs(:,r) = log(abs(RCM{r}.xY.y{1}));
end

% Define plotting ranges
%-------------------------------------------------------------------------
---
cbar    = [-2.8 1];
yrange  = [2 15];
```

```
fqaxis  = RCM{1}.M.Hz;
tmaxis  = linspace(-45, 45, length(RCM)/2);

first   = 1:length(RCM)/2;
second  = first + length(RCM)/2;

subplot(2,2,1)
    imagesc(tmaxis, fqaxis, obs(:,first), cbar);
    ylim(yrange);
    set(gca, 'ydir', 'normal');
    title('Control, observed');

subplot(2,2,2)
    imagesc(tmaxis, fqaxis, obs(:,second), cbar);
    ylim(yrange);
    set(gca, 'ydir', 'normal');
    title('Patient, observed');

subplot(2,2,3)
    imagesc(tmaxis, fqaxis, pre(:, first), cbar);
    ylim(yrange);
    set(gca, 'ydir', 'normal');
    title('Control, predicted');

subplot(2,2,4)
    imagesc(tmaxis, fqaxis, pre(:, second), cbar);
    ylim(yrange);
    set(gca, 'ydir', 'normal');
    title('Patient, predicted');

cmap = flip(cbrewer('div', 'Spectral', 100));
colormap(cmap);

%% Plot individual Parameter Values
%-------------------------------------------------------------------------
---
Np      = length(FEB.BMA.Pnames);
ploti   = [Tplot, Gplot+length(Tplot)];

Ep = reshape(FEB.BMA.Ep, [Np,4]);
Cp = reshape(diag(FEB.BMA.Cp), [Np,4]);

for e = 1:3
    subplot(3,1,e)
    spm_plot_ci(Ep(ploti,e), Cp(ploti,e));
    ylim([-1 2]);
end
set(gca, 'XTick', 1:Np, 'XTickLabel', {Tlabel{:}, Glabel{:}});
```

A.6.2.3 mab_parameterspace

```
% mab_parameterspace
clear all

% Housekeeping
%=========================================================================
===
D           = mab_housekeeping;
```

```
fs          = filesep;
Fbase       = D.Fbase;
Fscripts    = D.Fscripts;
Fdcm        = D.Fdcm;
Fanalysis   = D.Fanalysis;

mind        = D.mind;
Tplot       = D.Tplot;      Tlabel      = D.Tlabel;
Gplot       = D.Gplot;      Glabel      = D.Glabel;

load([Fanalysis fs 'DCM_All.mat']);
LFP = spm_eeg_load([Fanalysis fs 'LFP_MEEG']);
clear D

load([Fdcm fs 'Full Empirical Bayes.mat'])

%% Illustrate parameter space using first principal eigenmodes
%=========================================================================
===
% Extract parameters from reduced first level models
%-------------------------------------------------------------------------
---
for r = 1:length(FEB.RCM)
    T(r,:) = FEB.RCM{r}.Ep.T;
    G(r,:) = FEB.RCM{r}.Ep.G;
end

% Do principal component decomposition
%-------------------------------------------------------------------------
---
T = full(T);
G = full(G);

[Tcf Tsc] = pca(T, 'Algorithm', 'eig');
[Gcf Gsc] = pca(G, 'Algorithm', 'eig');

% Map first principal components separately for T and G parameters
%-------------------------------------------------------------------------
---
seps = linspace(0, length(FEB.RCM), 5);
cols = cbrewer('qual', 'Paired', 10);
cols = cols([7 8 9 10],:);

for s = 2:length(seps)
    plid    = seps(s-1) + 1:seps(s);

    subplot(2,5,[2 3 7 8]);
    % Plot
        scatter(Tsc(plid,1), Gsc(plid,1), [], cols(s-1,:), 'filled');
hold on
    % Labels
        xlabel('Time constant component');
        ylabel('Connection strength component');
    % Settings
        xlim([-3 3]); ylim([-5 5]);
        axis square
end
legend({'Control, pre PTZ', 'Control, post PTZ', 'Antibody, pre PTZ',
'Antibody, post PTZ'});

subplot(2,5,1),
```

```
% Plot
    bar(Tcf(Tplot,1));
% Labels
    title('Time constants: First component')
% Settings
    xlim([0 length(Tlabel)+1]);
    set(gca, 'XTick', 1:length(Tlabel), 'XTickLabel', Tlabel);

subplot(2,5,6),
% Plot
    bar(Gcf(Gplot,1));
% Labels
    title('Connection strengths: First component');
% Settings
    xlim([0 length(Glabel)+1]);
    set(gca, 'XTick', 1:length(Glabel), 'XTickLabel', Glabel);

subplot(2,5,[5 5 9 10]);
for s = 2:length(seps)
    plid    = seps(s-1) + 1:seps(s);
    scatter3(T(plid,1), T(plid,2), G(plid,7), [], cols(s-1,:),
'filled'); hold on
    xlabel('T(1)');
    ylabel('T(2)');
    zlabel('G(7)');
end

set(gcf, 'Position', [300 300 1200 500]);

%% Forward modelling
%--------------------------------------------------------------------------
---
range1 = [-4 3];
range2 = [-5 5];
stps   = 200;
steps1 = linspace(range1(1), range1(2), stps);
steps2 = linspace(range2(1), range2(2), stps);
Ts     = Tcf(:,1) * steps1;
Gs     = Gcf(:,2) * steps2;

OCM    = FEB.RCM{1};
Nc     = length(FEB.BMA.Xnames);
Np     = length(FEB.BMA.Pnames);

BasePs.T    = OCM.M.pE.T + FEB.BMA.Ep([1:4] + (Np * (Nc - 1)))';
BasePs.G    = OCM.M.pE.G + FEB.BMA.Ep([5:Np] + (Np * (Nc - 1)))';

clear delta_all Hc_all

for d1 = 1:length(steps1)-1
d1
for d2 = 1:length(steps2)
    Ps          = OCM.Ep;
    Ps.T        = BasePs.T + Ts(:,d1)';
    Ps.G        = BasePs.G + Gs(:,d2)';
    Hctemp      = spm_csd_mtf(Ps, OCM.M, OCM.xU);
    Hc_all{d1,d2}   = Hctemp{1};
    delta_all(d2,d1)    = mean(abs(Hc_all{d1,d2}(1:4)));
end
end
```

```
%%

figure
imagesc(steps1, steps2, log(delta_all));
set(gca, 'Ydir', 'normal');
axis square; colorbar
colormap gray
xlim([-3 3]); ylim([-5 5]);

%% Calculate and plot heatmaps
%-------------------------------------------------------------------------
---
clear dens plid

seps = linspace(0, length(FEB.RCM), 5);
for s = 2:length(seps)
    plid{s-1} = seps(s-1) + 1:seps(s);
end

for p = 1:length(plid)
for s1 = 2:length(steps1)-1
for s2 = 2:length(steps2)

    % find parameters in t-range
    tT  = Tsc(plid{p});
    hTi = find(tT >= steps1(s1-1) );
    lTi = find(tT < steps1(s1));
    Ti  = intersect(hTi, lTi);

    % find parametrs in g-range
    tG  = Gsc(plid{p});
    hGi = find(tG >= steps2(s2-1));
    lGi = find(tG < steps2(s2));
    Gi  = intersect(hGi, lGi);

    % find overlap and save occurance number
    both = intersect(Ti, Gi);
    dens{p}(s2,s1) = length(both);

end
end
end

%% Plotting routine
heatcols = flip(cbrewer('div', 'Spectral', 100));

for d = 1:length(dens)

    sm          = fspecial('gaussian', 20, 20);
    sdens{d}     = filter2(sm, dens{d});
    for sm = 1:3
        sdens{d}     = filter2(sm, sdens{d});
    end

    subplot(1,4,d),
        limz = [min(min([sdens{:}])) max(max([sdens{:}])) ];
        imagesc(steps1, steps2, sdens{d}, limz); hold on
        axis square
        set(gca, 'Ydir', 'normal');
        colormap(heatcols)
```

```
        xlim([-3 3]); ylim([-5 5]);

end

figure
subplot(1,3,1)
    contour(steps1(1:end-1), steps2, delta_all, 4);
    xlim([-3 3]); ylim([-5 5]);
    set(gca, 'Ydir', 'normal');

    title('Delta power contours');
    colormap gray; axis square

subplot(1,3,2)
    contour(steps1(1:end-1), steps2, log(delta_all), 4);
    xlim([-3 3]); ylim([-5 5]);
    set(gca, 'Ydir', 'normal');

    title('Delta power contours: Log transformed');
    colormap gray; axis square

subplot(1,3,3)
    delts       = reshape(delta_all,
[size(delta_all,1)*size(delta_all,2), 1]);
    dlimvalues  = [50 75 95 99];

    for l = 1:length(dlimvalues)
        deltlims(l)   = prctile(delts,dlimvalues(l));
    end

    contour(steps1(1:end-1), steps2, delta_all, deltlims)
    xlim([-3 3]); ylim([-5 5]);
    set(gca, 'Ydir', 'normal');
    colormap gray; axis square

    title('Delta power contours: Centiles');




%% Integrating Testing for additional variance based on human data
%=========================================================================
===
% Find human data file and organise everything in structures
%-------------------------------------------------------------------------
---
Base    = fileparts(Fbase);
load([Base fs 'Patients' fs 'Matlab Files' fs 'Patient_PCA.mat']);

% Mouse PCA
%-------------------------------------------------------------------------
---
M.BasePs    = BasePs;
M.Tsc       = Tsc;      M.Tcf   = Tcf;
M.Gsc       = Gsc;      M.Gcf   = Gcf;

% Human PCA
%-------------------------------------------------------------------------
---
H.Tsc       = Pt.dTsc;  H.Tcf   = Pt.dTcf;
```

```
% Collate (M) condition specific indices
%-------------------------------------------------------------------------
---
seps = linspace(0, length(FEB.RCM), 5);
clear plid

for s = 2:length(seps)
    plid{s-1}    = seps(s-1) + 1:seps(s);
end

pid{1} = [plid{1} plid{2}];
pid{2} = [plid{3} plid{4}];

conds = [1 2];  % Control vs Antibody
clear Hc mDelta

for c = 1:length(conds)

condid  = conds(c);
M.Tmd   = median(M.Tsc(pid{condid}));
M.Gmd   = median(M.Gsc(pid{condid}));

% Set up 'median' antibody condition for mice
%-------------------------------------------------------------------------
---
BPs     = M.BasePs;
BPs.T   = BPs.T + M.Tmd * M.Tcf(:,1)';
BPs.G   = BPs.G + M.Gmd * M.Gcf(:,1)';

stps    = 200;
steps   = linspace(-2.5, 2.5, stps);
cols    = flip(cbrewer('div', 'Spectral', stps));

for s = 1:length(steps)
    Ps          = OCM.Ep;
    Ps.T        = BPs.T + steps(s) * H.Tcf(:,1)';
    Ps.G        = BPs.G;
    Hctemp      = spm_csd_mtf(Ps, OCM.M, OCM.xU);
    Hc{c}(s,:)     = abs(Hctemp{1});

    figure(1)
        subplot(2,1,c)
        if ~mod(s,10)
        plot(log(abs(Hctemp{1})), 'color', cols(s,:)); hold on
        xlim([1 60]);
        ylim([-6 8]);
        end

    mDelta{c}(s) = mean(Hc{c}(s,1:4));
end
end

mx = max(max(log([Hc{1} Hc{2}])));
mn = min(min(log([Hc{1} Hc{2}])));
sccols = cbrewer('qual', 'Paired', 10);
sccols = sccols([8 10],:);

for h = 1:length(Hc)
    figure(2)
```

```
    subplot(2,2,h)
        imagesc(OCM.M.Hz, steps, log(Hc{h}), [mn mx]);
        set(gca, 'Ydir', 'normal')

    subplot(2,2,[3 4])
        scplot = fix(linspace(1,length(steps), 50));
        scatter(steps(scplot), log(mDelta{h}(scplot)), [], sccols(h,:),
'filled'); hold on
end
```

A.6.2.4 nae_sources

```
% nae sources
%=========================================================================
===
% This function will source localise the abnormal activity (paroxysmal
and
% rhythmic) using an IID approach and extract a virtual-electrode
response
% at the cortical source of maximal power

clear all
D       = nae_housekeeping;
fs      = filesep;
Fdata   = D.Fdata;
files   = cellstr(spm_select('List', Fdata, '^N.*\.mat$'));

%% Prepare files
%=========================================================================
===
for f = 1:length(files)

% Set default 10/20 EEG sensors
%-------------------------------------------------------------------------
---
MEEG        = spm_eeg_load([Fdata fs files{f}]);
S.task      = 'defaulteegsens';
S.D         = MEEG;
MEEG        = spm_eeg_prep(S);
S           = [];
save(MEEG)

% Compute leadfields for inverse solutions
%-------------------------------------------------------------------------
---
conds = condlist(MEEG);
clear job
job{1}.spm.meeg.source.invert.D = {[Fdata fs files{f}]};
job{1}.spm.meeg.source.invert.val = 1;
job{1}.spm.meeg.source.invert.whatconditions.condlabel = conds(2:end);
job{1}.spm.meeg.source.invert.isstandard.custom.invtype = 'IID';
job{1}.spm.meeg.source.invert.isstandard.custom.woi = [-Inf Inf];
job{1}.spm.meeg.source.invert.isstandard.custom.foi = [0 256];
job{1}.spm.meeg.source.invert.isstandard.custom.hanning = 1;
job{1}.spm.meeg.source.invert.isstandard.custom.priors.priorsmask =
{''};
job{1}.spm.meeg.source.invert.isstandard.custom.priors.space = 1;
job{1}.spm.meeg.source.invert.isstandard.custom.restrict.locs = zeros(0,
3);
```

```
job{1}.spm.meeg.source.invert.isstandard.custom.restrict.radius = 32;
job{1}.spm.meeg.source.invert.isstandard.custom.restrict.mask = {''};
job{1}.spm.meeg.source.invert.modality = {'EEG'};
spm_jobman('run', job)
end

%% Extract maximum intensity MNI voxel locations from source inversion
%=========================================================================
===
for f = 1:length(files)
    load(files{f})

    clear mMAP xMAP
    for d = 1:length(D.other.inv{1}.inverse.J)
        mMAP{d} = mean(D.other.inv{1}.inverse.J{d},2);
        xMAP(d) = max(mMAP{d});
    end
    [v i] = max(xMAP);
    [v l] = max(mMAP{i});

    L(f).xyz = fix(D.other.inv{1}.forward.mesh.vert(l,:) * 1000);
    L(f).name = files{f}(1:end-4);
end
save([Fdata fs 'MIP_Locations.mat'], 'L');

%% Extract source waveforms
%=========================================================================
===
clear L
load([Fdata fs 'MIP_Locations.mat']);

for l = 1:length(L)
    MEEG            = spm_eeg_load([Fdata fs L(l).name '.mat']);
    xyz             = L(l).xyz;
    scalefactor     = sqrt(xyz(1)^2 + xyz(2)^2 + xyz(3)^2);

    S.D             = [Fdata fs L(l).name '.mat'];
    S.dipoles.pnt   = L(l).xyz;
    S.dipoles.ori   = L(l).xyz / scalefactor;
    S.dipoles.label = {'LFP'};

    sD              = spm_eeg_dipole_waveforms(S);
    save(sD);
end
```

A.6.2.5 nae_dcm

```
% Housekeeping
%=========================================================================
===
clear all
D           = nae_housekeeping;
fs          = filesep;
Fdata       = D.Fdata;
Fdcm        = D.Fdcm;
files       = cellstr(spm_select('List', Fdata, '^N.*\.mat$'));

%%
for f = 1:length(files)
```

```
% Set up DCM structure and invert baseline
%=========================================================================
===
DCM = [];

sub = files{f}(1:end-4);
% Fix directory of canonical forward matrix
%-------------------------------------------------------------------------
---
DCM.xY.Dfile        = [Fdata fs 'M' files{f}];

% Load MEEG object and extract sampling rate and info
%-------------------------------------------------------------------------
---
LFP                 = spm_eeg_load(DCM.xY.Dfile);
Fs                  = fsample(LFP);
smpls               = size(LFP,2);
timax               = linspace(0, smpls/Fs, smpls);
clist               = condlist(LFP);

for c = 1:length(clist)
% Set up DCM details
%-------------------------------------------------------------------------
---
DCM.options.analysis    = 'CSD';    % cross-spectral density
DCM.options.model       = 'CMC';    % structure cannonical microcircuit
(for now)
DCM.options.spatial     = 'LFP';    % virtual electrode input
DCM.options.Tdcm        = [timax(1) timax(end)] * 1000;     % time in ms

DCM.options.Fdcm    = [1 60];       % frequency range
DCM.options.D       = 1;            % frequency bin, 1 = no downsampling
DCM.options.Nmodes  = 8;            % number of eigenmodes
DCM.options.han     = 0;            % no hanning
DCM.options.trials  = c;            % index of ERPs within file

DCM.Sname           = chanlabels(LFP);
DCM.M.Hz            =
DCM.options.Fdcm(1):DCM.options.D:DCM.options.Fdcm(2);
DCM.xY.Hz           = DCM.M.Hz;

% Create DCM Struct and specify DCM.options
%-------------------------------------------------------------------------
---
DCM.A       = {1 1 1};
DCM.B       = {};
DCM.C       = sparse(length(DCM.A{1}),0);

% Reorganise model parameters in specific structure
%=========================================================================
===
DCM.M.dipfit.Nm     = DCM.options.Nmodes;
DCM.M.dipfit.model  = DCM.options.model;
DCM.M.dipfit.type   = DCM.options.spatial;
DCM.M.dipfit.Nc     = size(LFP,1);
DCM.M.dipfit.Ns     = length(DCM.A{1});

% Load empirical priors
%-------------------------------------------------------------------------
---
```

```
[pE,pC]             = nae_spm_cmc_priors(DCM.A,DCM.B,DCM.C);
load([Fdcm fs 'Priors' fs 'Priors.mat']);
pE                  = Priors.pE;
pC                  = Priors.pC;

DCM.M.pE    = pE;
DCM.M.pC    = pC;

DCM.name            = [Fdcm fs 'DCM_' sub '_' clist{c} '.mat'];
DCM                 = nae_spm_dcm_csd(DCM);
end
end

%% Review DCM fits
%=========================================================================
===
subfiles = cellstr(spm_select('List', Fdata, '^N.*\.mat$'));

for s = 1:length(subfiles)

sub         = subfiles{s}(1:end-4);
dcmfiles    = cellstr(spm_select('FPList', Fdcm, ['^DCM_' sub
'.*.mat$']));
conds       = [];
cols        = flip(cbrewer('qual','Paired', 6));

for d = 1:length(dcmfiles)
    conds{d} = dcmfiles{d}(end-4);
    load(dcmfiles{d});
    subplot(4,2,s)
    plot(log(abs(DCM.Hc{1})), 'color', cols(2*d,:)); hold on
    plot(log(abs(DCM.xY.y{1})), 'color', cols(2*d-1,:)); hold on
end
end
legend({'B pred', 'B obs', 'P pred', 'P obs', 'R pred', 'R obs'});
hold off

%% Plot N004 example traces
%-------------------------------------------------------------------------
---
subfiles = cellstr(spm_select('List', Fdata, '^N.*\.mat$'));
s = 4;

sub         = subfiles{s}(1:end-4);
MEEG        = spm_eeg_load([Fdata fs subfiles{s}]);

trials      = [5 52 81];
chid        = [1 11 15 9 2 12 15 10 3 5 7 13 4 6 8 14 17 18 19];

for t = 1:length(trials)
    subplot(2, length(trials), t)
    for c = 1:size(MEEG,1)
        plot(squeeze(MEEG(chid(c),:,trials(t)))-c*100);
        hold on
        ylim([-2100 200]);
        yvals(c)   = -c*100;
    end
end

subplot(2,length(trials),1)
chlabs = chanlabels(MEEG);
```

```
set(gca, 'YTick', flip(yvals), 'YTickLabel', flip(chlabs(chid)));


MEEG        = spm_eeg_load([Fdata fs 'M' subfiles{s}]);

subplot(2, length(trials), [1:length(trials)]+length(trials))

for t = 1:length(trials)
    plot(squeeze(MEEG(1,:,trials(t))) - t*100); hold on
end
```

A.6.2.6 nae_peb

```
% nae_peb
%==========================================================================
===
% This routine loads the inverted individual time window DCMs and
performs
% parametric empirical Bayesian analyiss

clear all
close all

% Housekeeping
%==========================================================================
===
D           = nae_housekeeping;
fs          = filesep;
Fbase       = D.Fbase;
Fdata       = D.Fdata;
Fscripts    = D.Fscripts;
Fdcm        = D.Fdcm;

clear D

% PEB Analysis
%==========================================================================
===
% Make second level model space
%--------------------------------------------------------------------------
---
subfiles = cellstr(spm_select('List', Fdata, '^N.*\.mat$'));

for s = 1:length(subfiles)

sub         = subfiles{s}(1:end-4);
dcmfiles    = cellstr(spm_select('FPList', Fdcm, ['^DCM_' sub
'.*.mat$']));
conds       = [];
cols        = flip(cbrewer('qual','Paired', 6));

for d = 1:length(dcmfiles), conds{d} = dcmfiles{d}(end-4); end

X      = [];
Xnames = {'All', conds{:}};
X(:,1) = ones(length(conds),1);
```

```
for c = 1:length(conds)
    X(:,1+c) = zeros(1,length(conds));
    X(c,1+c) = 1;
end

% Run PEB
%-----------------------------------------------------------------------
---
FCM = spm_dcm_load(dcmfiles);

M.X         = X;
M.Xnames    = Xnames;
M.Q         = 'all';

% Time constant parameters
%-----------------------------------------------------------------------
---
% G(:,1)  ss -> ss (-ve self)  4    MOD
% G(:,2)  sp -> ss (-ve rec )  4    INH
% G(:,3)  ii -> ss (-ve rec )  4    INH
% G(:,4)  ii -> ii (-ve self)  4    MOD
% G(:,5)  ss -> ii (+ve rec )  4    EXC
% G(:,6)  dp -> ii (+ve rec )  2    EXC
% G(:,7)  sp -> sp (-ve self)  4    MOD
% G(:,8)  ss -> sp (+ve rec )  4    EXC
% G(:,9)  ii -> dp (-ve rec )  2    INH
% G(:,10) dp -> dp (-ve self)  1    MOD
%
% G Parameters: The order in the DCM structure is as follows
% j     = [7 2 3 4 5 6 8 9 10 1];
% i.e.     M I I M E E E I M  M
% new   =  1 2 3 4 5 6 7 8 9 10
%
% T Parameters: The order is as follows
% ss sp ii dp
%  1  2  3  4
%  E  I  E  I

% Model space by parameter type nae_spm_fx_cmc
%-----------------------------------------------------------------------
---
clear fields F labels
fields{1}   = {'T(1)', 'T(2)', 'T(3)', 'T(4)'};     % time constants
fields{2}   = {'G(2)', 'G(3)', 'G(8)'};             % inh connections
fields{3}   = {'G(5)', 'G(6)', 'G(7)'};             % exc connections
fields{4}   = {'G(1)', 'G(4)', 'G(9)', 'G(10)'};    % mod connections

labels  = { 't', 'g_i', 'g_e', 'g_m' };

saveit = 1;

% Run PEB across reduced second level model space
%=======================================================================
===

for f = 1:length(fields)

    [PEB, RCM]  = spm_dcm_peb(FCM, M, fields{f});
    F(f) = PEB.F;

    if saveit try load([Fdcm fs 'PEB']); catch P = []; end; end
```

```
    P(s,f).PEB    = PEB;
    P(s,f).fields = fields{f};
    P(s,f).F      = PEB.F;
    if saveit, save([Fdcm fs 'PEB'], 'P'); end

end
end

%% Identify overall winning PEB model
%==========================================================================
===
if saveit, load([Fdcm fs 'PEB']); end

clear Fs Fall
for p = 1:size(P,1)
for m = 1:size(P,2)
    Fs(p,m) = P(p,m).F;
end
end
Fall    = sum(Fs);

% Plot free energies and model posteriors spm_dcm_bmc
%--------------------------------------------------------------------------
---
subplot(3,1,1), bar(Fall - min(Fall));
subplot(3,1,2), plot(Fs' - min(Fs'));
subplot(3,1,3),
    [alpha, exp_r, xp] = spm_BMS(Fs, 1e6, 1, 0, 1);
    bar(xp); title('RFX Analysis');

set(gca, 'XTick', 1:length(Fall), 'XTickLabel', labels);

[v l] = max(Fall);

%% Bayesian model reduction over winning PEB (Time constants and
inhibitory)
%--------------------------------------------------------------------------
load([Fdcm fs 'PEB']);
for p = 1:size(P,1)
    clear Snames Sfixed sep macseps winseps
    Snames = P(p,l).PEB.Snames

    for s = 1:length(Snames)
        macseps     = find(P(p,l).PEB.Snames{s} == '/');
        winseps     = find(P(p,l).PEB.Snames{s} == '\');
        if length(winseps) > length(macseps), sep = winseps(end);
        else sep = macseps(end); end

        Sfixed{s} = [Fdcm fs Snames{s}(sep + 1:end)];
    end

    FCM         = spm_dcm_load(Sfixed);
    M.X         = P(p,l).PEB.M.X
    M.Xnames    = P(p,l).PEB.Xnames;
    M.Q         = 'all';
    [PEB RCM]   = spm_dcm_peb(FCM', M, fields{l});
    try PMA         = spm_dcm_peb_bmc(PEB); catch PMA = []; end

    FEB(p).PMA    = PMA;
    FEB(p).RCM    = RCM;
    FEB(p).PEB    = PEB;
```

```
end
save([Fdcm fs 'Full Empirical Bayes'], 'FEB');
```

A.7 Mismatch negativity under ketamine – DCM analysis scripts

The Matlab scripts shown here contain code that can be used to reproduce a dynamic causal modelling analysis for mismatch negativity and repetition suppression event related potentials measured with EEG in healthy probands under the influence of the NMDA receptor blocker ketamine. This code was used for the analysis presented in chapter 6 of this thesis.

Below is a short summary of the code (included in the README file for the online repository), followed with exerpts of the custom code written for analysis. The code can be downloaded and run in full from an online repository accessible here: https://github.com/roschkoenig/Ketamine_DCM.

The code runs on Mathworks Matlab (tested with 2016b) and requires the following freely available packages to run

- Statistical Parametric Mapping - This academic freeware implements the DCM analysis applied here

A.7.1 README description of code function

The repository includes a number of different routines to be run manually to reproduce the different analysis steps included in the manuscript above. Most of these will produce a visual output and are further explained below.

A.7.1.1 Perform sensor space analysis across the different conditions

`ket_sensorspace`

This routine performs the 'standard' sensor space ERP analysis based on the data provided (in the SPM-specific MEEG format, in the `~/SPM-ready Data/` folder) The figures it produces were the basis for *Fig 2* in the manuscript accompanying this code. The first section will identify time periods of significant difference between (a) the deviant and the last standard, and (b) between the first and the last standard, stringently corrected for multiple comparisons. All ERPs and periods of significant difference will be plotted as below.

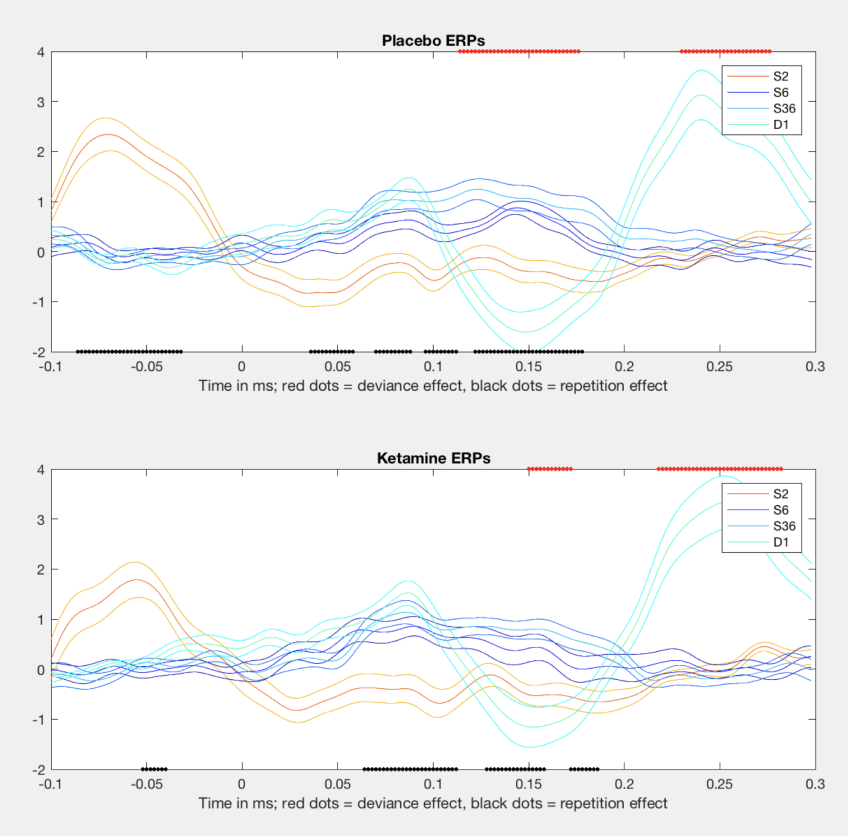

The second section will calculate the difference waveform between the first (i.e. deviant) and the last (i.e. standard 36) tone of the sequence (i.e. the mismatch negativity, *MMN*) and test for significant differences in peak amplitude. All testing up until this point is done at the *Fz* electrode, according to literature standards.

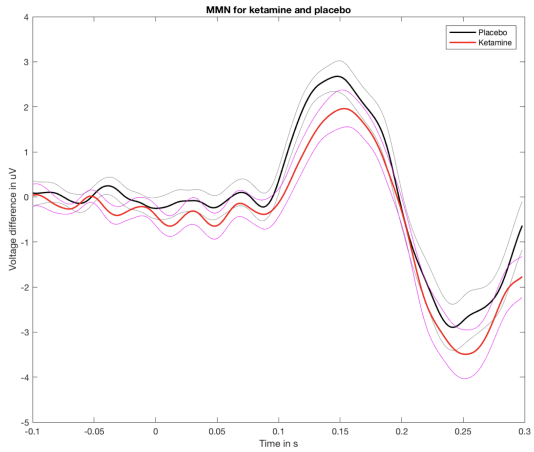

The last section will plot all EEG channels over time for the three standard - deviant difference waves (left to right: D1-S2, D1-S6, D1-S36); with placebo in the top row and ketamine in the bottom row. This illustrates an overall reduction of the ERPs caused by ketamine across the scalp and for all of the different conditions.

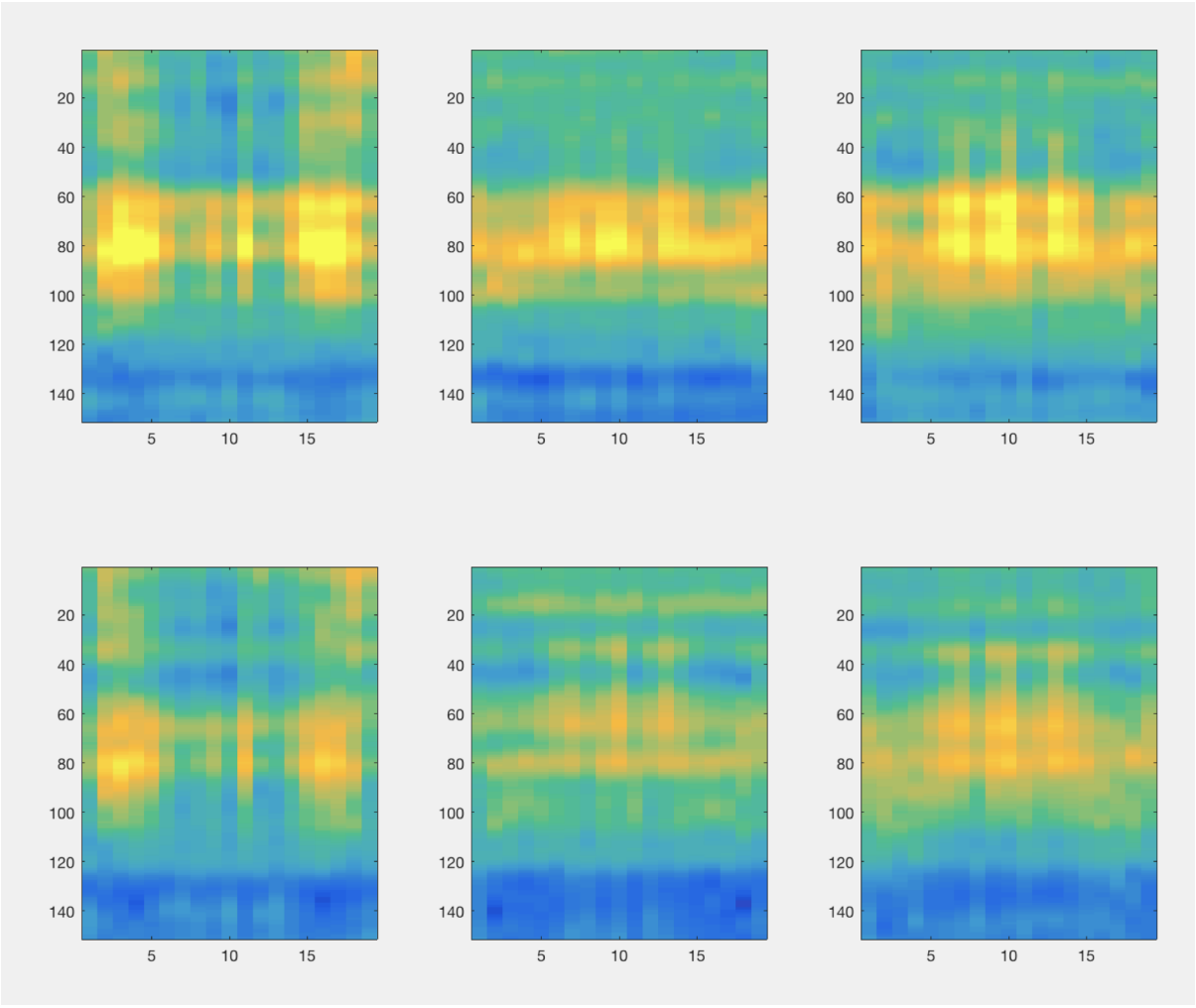

A.7.1.2 Invert Dynamic Causal Models (DCM) and perform Bayesian Model Reduction (BMR) to explain the effect of tone repetition

`ket_dcm`

This routine will perform a 2-stage DCM inversion for the data described in the section above: In the first instance, a single DCM will be inverted for the repetition effects across grand mean averages of the ERP. This grand mean inversion is saved and posterior estimates of the parameters are then used as priors for inverting individual subject DCMs. Each participant's ERPs will then be inverted in individual DCMs for the ketamine and the placebo condition separately. The inversion can take approximately ~30 minutes per subject and drug-condition and should produce the visual output seen below.

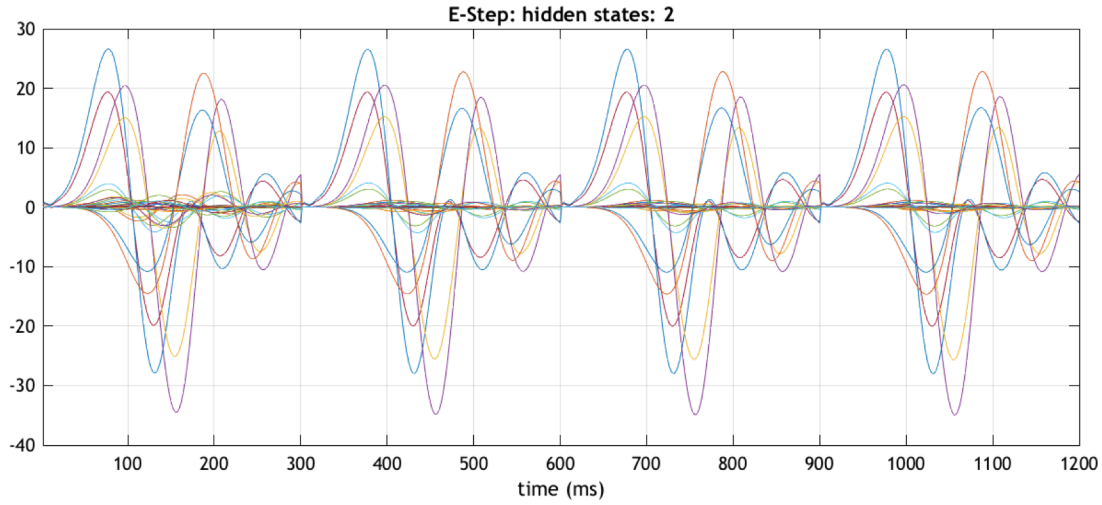
E-Step: hidden states: 2
30
20
10
0
-10
-20
-30
-40
100
200
300
400
500
600
700
800
900
1000
1100
1200
time (ms)

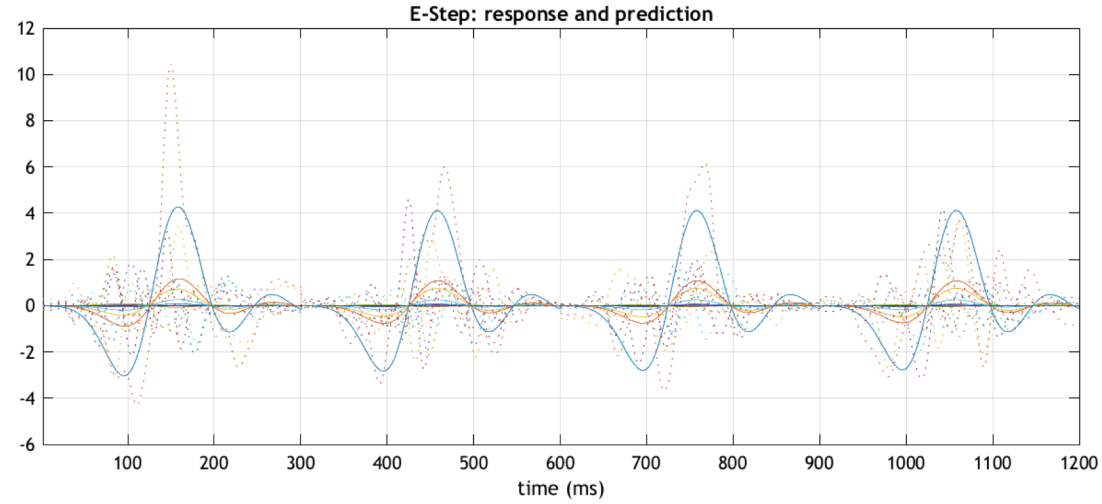
E-Step: response and prediction
12
10
8
6
4
2
0
-2
-4
-6
100
200
300
400
500
600
700
800
900
1000
1100
1200
time (ms)

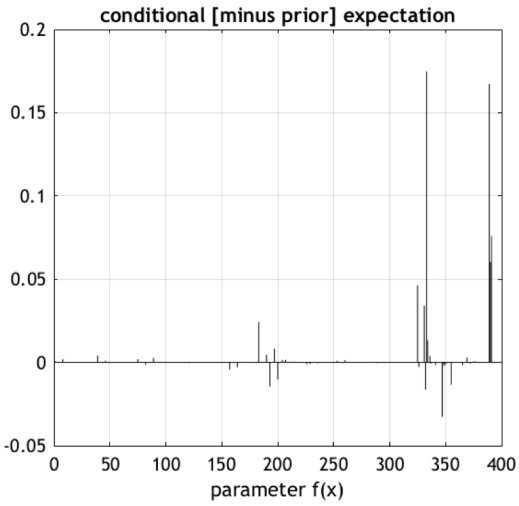
conditional [minus prior] expectation
0.2
0.15
0.1
0.05
0
-0.05
0
50
100
150
200
250
300
350
400
parameter f(x)

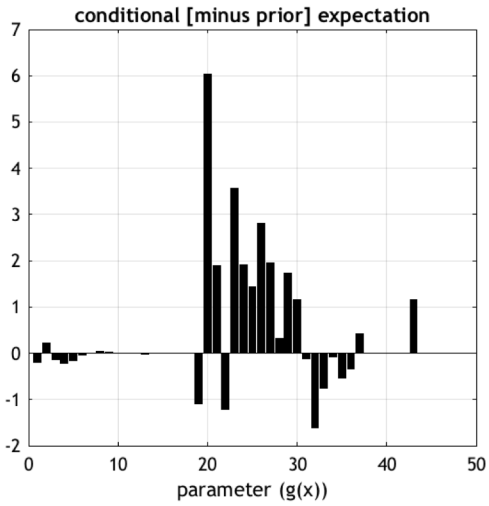
conditional [minus prior] expectation
7
6
5
4
3
2
1
0
-1
-2
0
10
20
30
40
50
parameter (g(x))

After all models have been inverted, the routine will also display the first principal eigenmodes of the model fits for each of the subjects, again separately for ketamine and placebo-controlled conditions. For best effects, this should be run with the publicly available 'cbrewer' package installed to show paired colour codes shown below and corresponding to the colours in the manuscript.

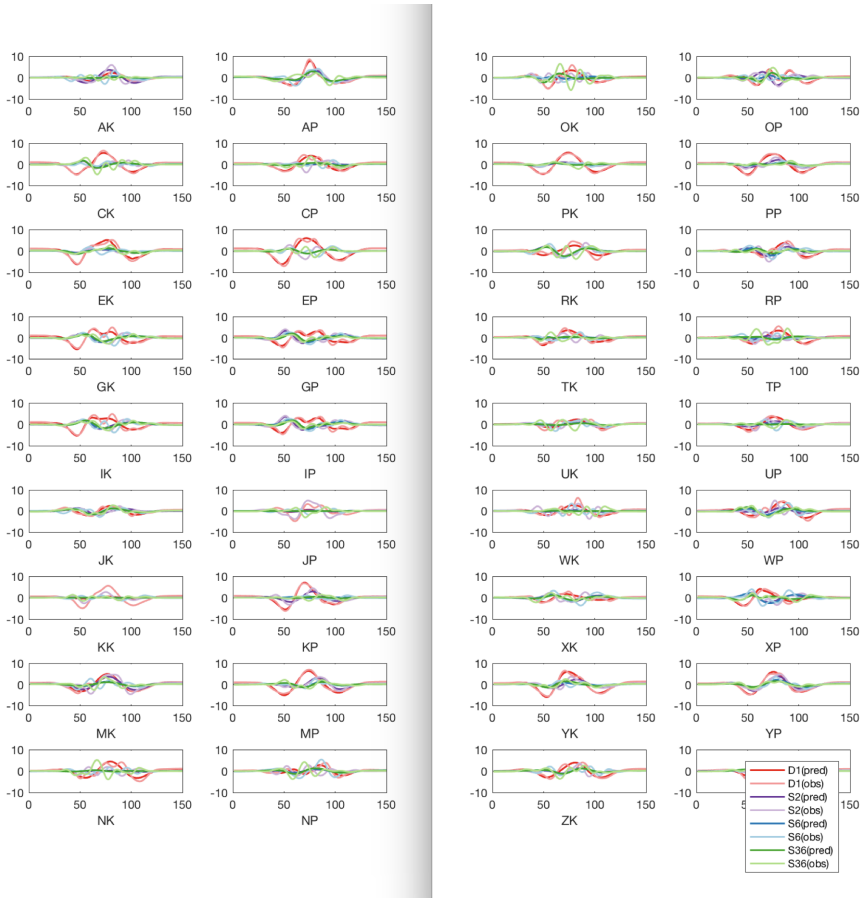

Based on the individually inverted (full) DCMs for the placebo condition, we then perform Bayesian model reduction, eliminating redundant model parameters and inferring which parameters are changed by repetition effects. The results will be shown in terms of free energy distribution over the model space, which consists of 3 sets of 8 models (i.e. combinations of the basis functions (3): monophasic decay, phasic response, or both; and synaptic parameters that are modulated (8): no extrinsic, forward, backward, or forward/backward modulations with and without intrinsic modulations). The winning model is that with the highest free energy, which is the full model (i.e. both basis functions, forward, backward and intrinsic effects).

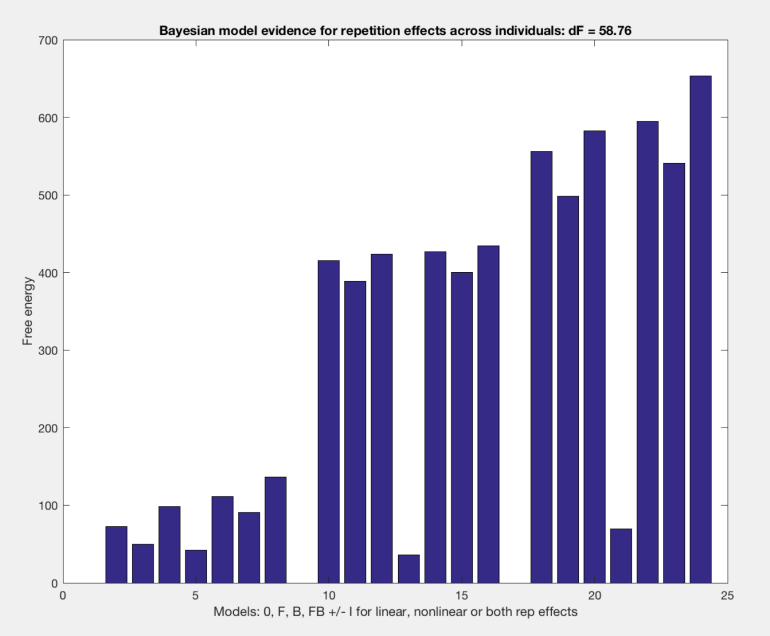

The estimated parameter values for the reduced model were then averaged across participants (using Bayesian parameter averaging) to show the repetition-dependent parameter changes.

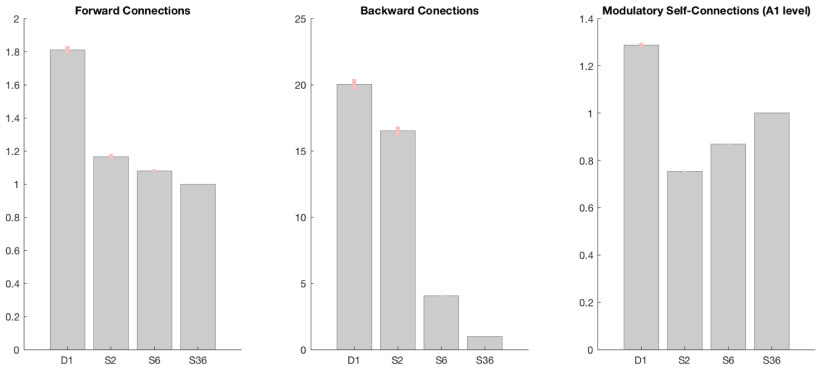

A.7.1.3 Run Parametric Empirical Bayesian (PEB) group analysis to explain the difference between ketamine and placebo

`ket_peb`

This routine takes the DCMs inverted at the first level (or the DCMs provided in this repository) and estimates shared group effects across individual DCMs using parametric empirical Bayes. These group effects represent the effect of ketamine in this study design, and are estimated using different combinations of free parameters: broadly this model space for the ketamine effect is divided into modulations of extrinsic (between-source) and

intrinsic (within-source) coupling parameters. The routine will run the different second level models, and display the free energy distribution over the model space (for Bayesian model comparison).

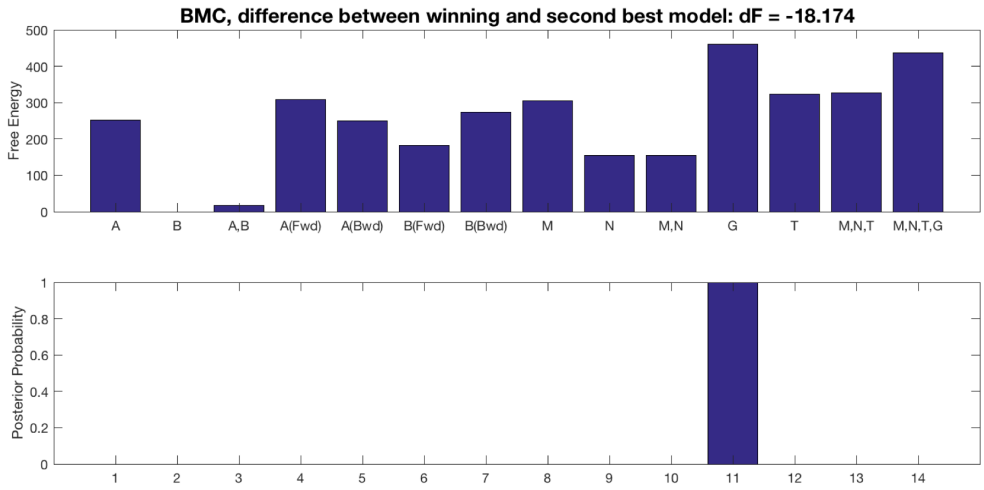

Selecting the winning model (one where only intrinsic connections are allowed to change depending on the drug condition), we then perform Bayesian model reduction to remove redundant model parameters and provide the best estimate for which connections are altered by ketamine across all subjects The standard SPM function will provide the following output.

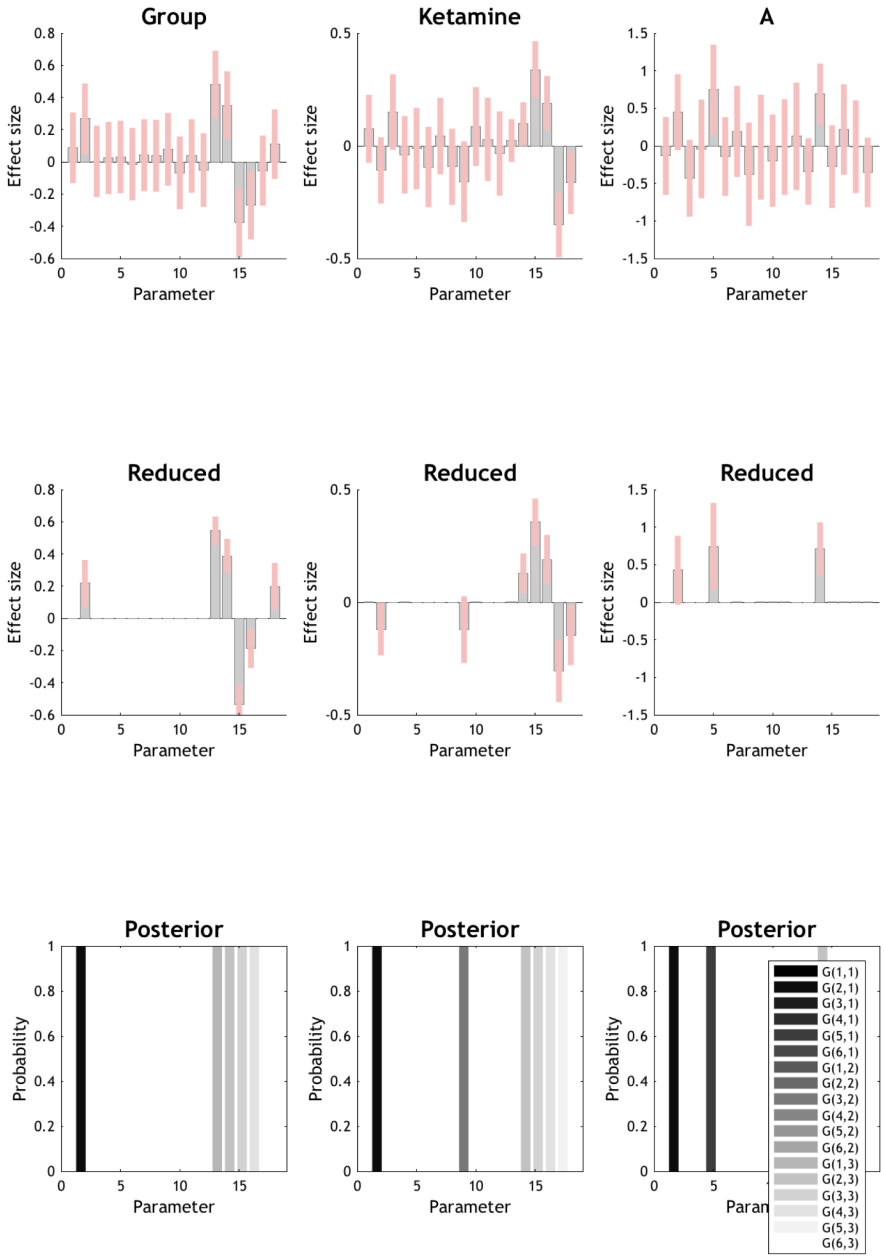

A.7.1.4 Simulate the ketamine effects on intrinsic connectivity parameters to visualise the resultant changes

`ket_simulate`

ln order to further explore the effect of the parameters identified on the PEB analysis we can simulate the model output for a range of parameter combinations. Here we take the grand mean model inversion as the starting pont and then push the STG and IFG

inhibitory parameters to the values estimated in the PEB - this shows that much of the measured effect can be reproduced by modulations of just these parameters.

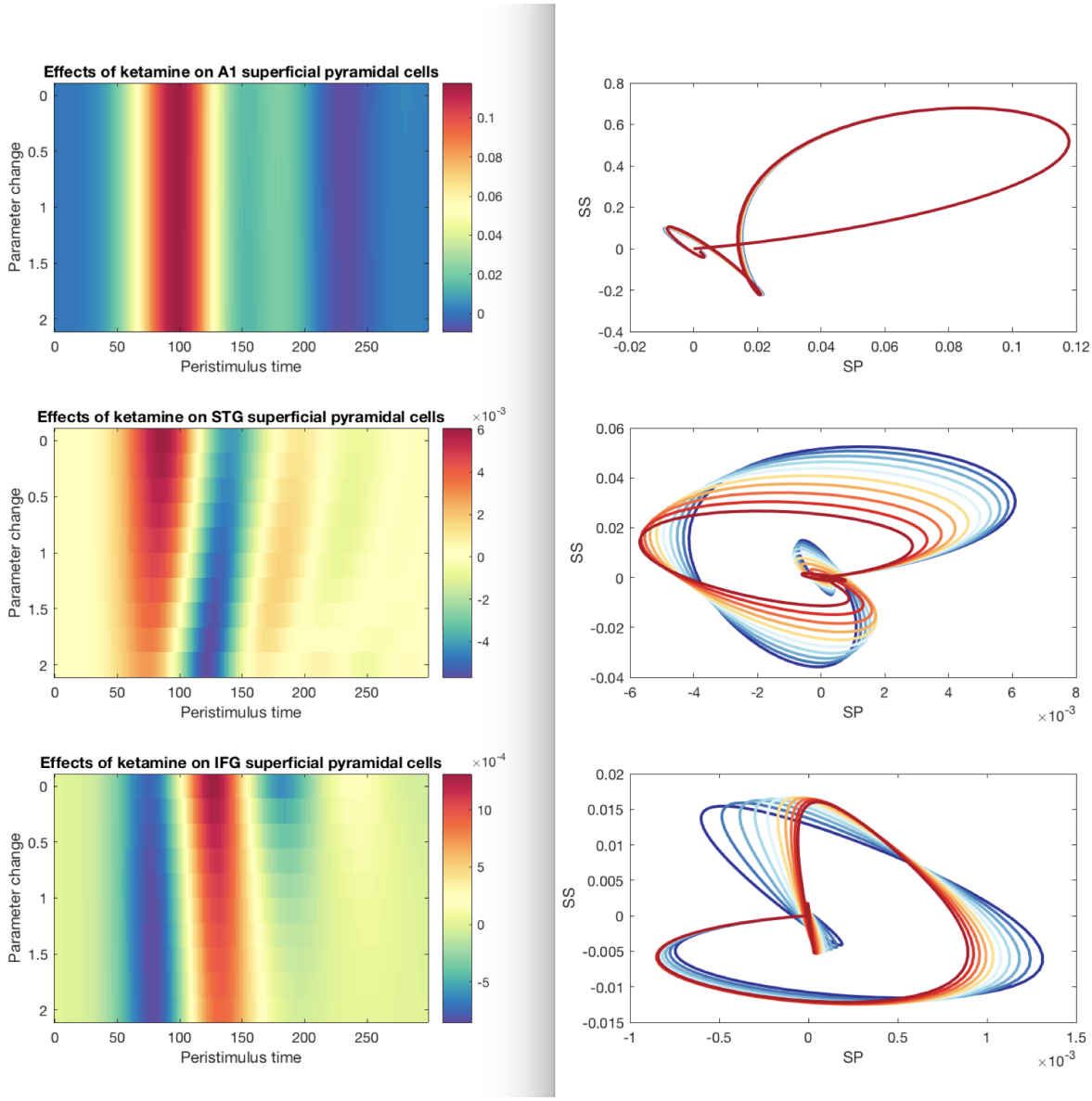

A.7.1.5 Other custom functions

- `ket_housekeeping` - this function defines the folder structures used for the analysis by all the ohter functions
- `ket_bmr_gen_model_space` - this function will generate the model space in terms of forward, backward and intrinsic connection used for DCM analysis at the first level (i.e. the effect of tone repetition)
- `ket_bmr_gen` - this function will generate the DCM structure required for Bayesian model reduction according to the model space in question (without inverting it)

- `ket_dcm_gm` - this function is used to invert a single DCM for the grand mean ERP wave forms - the posteriors of this inversion are subsequently used as the priors for the subject-specific analysis
- `ket_dcm_sgl` - this function will invert DCMs for single subjects, using the posteriors of the group inversion as priors

A.7.2 Custom Routines

A.7.2.1 ket_sensorspace

```
% Housekeeping
%=========================================================================
===
clear all
D = ket_housekeeping;

% Unpack housekeeping files
%-------------------------------------------------------------------------
---
Fbase       = D.Fbase;
Fspm        = D.Fspm;
Fdata       = D.Fdata;
Fanalysis   = D.Fanalysis;
Fbmr        = D.Fbmr;
GMFile      = D.GMFile;
sub         = D.sub;
fs          = filesep;

%% Load individual subject ERPs into single cell array
%=========================================================================
===
clist = {'S2P', 'S6P', 'S36P', 'D36P', 'S2K', 'S6K', 'S36K', 'D36K'};
clear D
for s = 1:length(sub)
    D{s}            = spm_eeg_load([Fdata fs 'm_meeg_' sub(s) '.mat']);
    currentconds    = condlist(D{s});
    currentchans    = chanlabels(D{s});
    cz              = find(strcmp(currentchans, 'CZ'));
    fz              = find(strcmp(currentchans, 'FZ'));

    for c = 1:length(clist)
        ci = find(strcmp(currentconds, clist{c}));
        C{c}.name           = clist{c};
        C{c}.data(s,:,:)    = D{s}(:,:,ci);
        C{c}.Fz(s,:)        = D{s}(fz,:,ci);
        C{c}.Cz(s,:)        = D{s}(cz,:,ci);
    end
end

%% Calculate ERP statistics
%=========================================================================
===
% Calculate standard errors around the mean
%-------------------------------------------------------------------------
---
for c = 1:length(C)
```

```
for t = 1:size(C{c}.Fz,2)
    C{c}.FzSE(t)    = std(C{c}.Fz(:,t)) / sqrt(size(C{c}.Fz,1));
end
C{c}.FzHI = mean(C{c}.Fz,1) + C{c}.FzSE;
C{c}.FzLO = mean(C{c}.Fz,1) - C{c}.FzSE;
end

% Calculate time points of significant difference
%-------------------------------------------------------------------------
---
for p = 1:2
for t = 1:size(C{1}.Fz,2)

    ci  = (p-1)*4;
    bonferroni      = 0.05 / size(C{1}.Fz,2);

    % Between S2 and S36 (i.e. repetition effect)
    %---------------------------------------------------------------------
---

    s2  = C{1+ci}.Fz(:,t);
    s36 = C{3+ci}.Fz(:,t);

    [H P CI]        = ttest(s2, s36);
    if P < bonferroni,  repfx(p,t) = 1;
    else                repfx(p,t) = 0; end

    % Between D1 and S36 (i.e. deviance effect)
    %---------------------------------------------------------------------
---
    d36  = C{4+ci}.Fz(:,t);
    s36 = C{3+ci}.Fz(:,t);

    [H P CI]        = ttest(d36, s36);
    if P < bonferroni,  devfx(p,t) = 1;
    else                devfx(p,t) = 0; end

end

repdur(p) = sum(repfx(p,50:end)) * 2;
devdur(p) = sum(devfx(p,50:end)) * 2;
end

% Plot ERPs and statistics
%=========================================================================
===
cols_unsort     = jet(10);          % standard color scheme
try cols_unsort = ccbrewer('qual', 'Paired', 10); end  % try nicer
colour scheme
figure

cols(1:2,:) = cols_unsort(9:10,:);  % cbrewer: purple
cols(3:4,:) = cols_unsort(1:2,:);   % cbrewer: blue
cols(5:6,:) = cols_unsort(3:4,:);   % cbrewer: green
cols(7:8,:) = cols_unsort(5:6,:);   % cbrewer: red

clear legid

for p = 1:2
for c = 1:4
```

```
    ci = 4*(p-1) + c;
    ti = time(D{1});

    subplot(2,1,p)

    % Plotting ERPs and SE intervals around
    %-------------------------------------------------------------------
---
    legid(c) = plot(ti,mean(C{ci}.Fz,1), 'Color', cols(2 + 2*(c-1),:));
hold on
    plot(ti,C{ci}.FzHI, 'Color', cols(1 + 2*(c-1),:));
    plot(ti,C{ci}.FzLO, 'Color', cols(1 + 2*(c-1),:));

    % The world's clumsiest way to illustrate the significant
intervals...
    %-------------------------------------------------------------------
---
    scatter(ti,repfx(p,:) * (-7) + 5, 50, 'k.');
    scatter(ti,devfx(p,:) * 7 - 3, 50, 'r.');

    % Set thresholds and axis definitions
    %-------------------------------------------------------------------
---
    ylim([-2 4]);
    xlim([-0.1 0.3]);
    legend(legid, {'S2', 'S6', 'S36', 'D1'});
    xlabel('Time in ms; red dots = deviance effect, black dots =
repetition effect');
end
end

subplot(2,1,1), title('Placebo ERPs');
subplot(2,1,2), title('Ketamine ERPs');


%% Calculate MMN statistics
%=====================================================================
===
% Calculate standard errors around the mean
%-------------------------------------------------------------------
---
MMN{1}.dat = C{3}.Fz - C{4}.Fz;
MMN{2}.dat = C{7}.Fz - C{8}.Fz;
ti = time(D{1});

for m = 1:length(MMN)
for t = 1:size(MMN{1}.dat,2)
    MMN{m}.SEM(t) = std(MMN{m}.dat(:,t)) / sqrt(size(MMN{m}.dat,1));
end
MMN{m}.HI = mean(MMN{m}.dat,1) + MMN{m}.SEM;
MMN{m}.LO = mean(MMN{m}.dat,1) - MMN{m}.SEM;
end

% Test for attenuation of MMN around 200ms, where rep effects are
strongest
%-------------------------------------------------------------------
---
p = MMN{1}.dat;
k = MMN{2}.dat;

ppeaks = max(p(:, 100:150)');   % note that time is indexed in 2ms steps
```

```
kpeaks = max(k(:, 100:150)');
[Hp Pp CIp Sp] = ttest(ppeaks, kpeaks, 'tail', 'right');

ptroughs = min(p(:, 150:200)');   % note that time is indexed in 2ms
steps
ktroughs = min(k(:, 150:200)');
[Ht Pt CIt St] = ttest(ptroughs, ktroughs, 'tail', 'left');

% Plot MMN for placebo and ketamine
%=========================================================================
===
figure
l(1) = plot(ti, mean(p,1), 'k', 'Linewidth', 1.5); hold on
plot(ti, MMN{1}.HI, 'Color', [0.5 0.5 0.5]);
plot(ti, MMN{1}.LO, 'Color', [0.5 0.5 0.5]);

l(2) = plot(ti, mean(k,1), 'r', 'Linewidth', 1.5); hold on
plot(ti, MMN{2}.HI, 'm');
plot(ti, MMN{2}.LO, 'm');

title('MMN for ketamine and placebo');
legend(l, {'Placebo', 'Ketamine'});
set(gcf, 'color', 'w');
ylabel('Voltage difference in uV');
xlabel('Time in s');


%% Plot MMN Scalp maps
%-------------------------------------------------------------------------
---
cols    = flip(cbrewer('div', 'RdYlBu', 100));
colormap parula
GM      = spm_eeg_load([Fdata fs 'gm_meeg_all']);
order =  {'F7', 'T3', 'T5', 'O1', 'P3', 'C3', 'F3', 'FP1', ...
          'CZ', 'FZ', 'PZ', ...
          'FP2', 'F4', 'C4', 'P4', 'O2', 'T6', 'T4', 'F8'};

for o = 1:length(order)
    clist       = chanlabels(GM);
    oldind(o)   = find(strcmp(clist, order{o}));
    data(o,:,:) = GM(oldind(o), :, :);
end

mmn_id{1} = [1 6;  7 12];
mmn_id{2} = [2 6;  8 12];
mmn_id{3} = [3 6;  9 12];

clear d
for m = 1:length(mmn_id)
    id      = mmn_id{m};
    d{1}    = data(:,:,id(1,1)) - data(o,:,id(1,2));
    d{2}    = data(:,:,id(2,1)) - data(o,:,id(2,2));

    subplot(2,3,m)
    imagesc(d{1}(:,50:end)', [-2 2]);
    subplot(2,3,m + 3)
    imagesc(d{2}(:,50:end)', [-2 2]);
end
```

A.7.2.2 ket_dcm

```
%% Ketamine DCM analysis using Parametric Empirical Bayes
%=========================================================================
===
% This code will run two functions, ket_dcm_gm - to invert the full
% model, and ket_dcm to invert separate placebo and ketamine models for
the
% individual subjects.

% Housekeeping
%=========================================================================
===
clear all
D = ket_housekeeping;

% Unpack housekeeping files
%-------------------------------------------------------------------------
---
Fbase       = D.Fbase;
Fspm        = D.Fspm;
Fdata       = D.Fdata;
Fanalysis   = D.Fanalysis;
Fbmr        = D.Fbmr;
GMFile      = D.GMFile;
sub         = D.sub;
fs          = filesep;

[rep_lin, rep_non] = ket_bmr_gen_model_space();

%% Invert DCMs
%=========================================================================
===
% This section will take a   !/*long*/!  time.
% A log of the model inversions is saved in the DCM folder that will
% document inversion steps taken for the individual models to invert.

% Invert DCM for grand mean
%-------------------------------------------------------------------------
---
diary([Fanalysis fs 'DCM_ALL_log']);
diary('on');

FCM = ket_dcm_gm(rep_lin{end}, rep_non{end}, Fanalysis, Fdata, Fspm);

% Invert individual subjects
%-------------------------------------------------------------------------
---
for s = 1:length(sub)
    SCM{s} = ket_dcm_sgl(sub(s), GMFile, rep_lin{end}, rep_non{end}, ...
                         [Fanalysis fs 'Individual'], Fdata, Fspm);
end

diary off

%% Plot example modes (first mode for each of the conditions)
%-------------------------------------------------------------------------
---
% This section loads the just inverted DCMs and plots the first
principal
% eigenmode of both observed ERPs and model predictions for each of the
```

```
% four conditions (D1, S2, S6, S36).

files = cellstr(spm_select('FPList', [Fanalysis fs 'Individual'],
'^*.mat'));

cols_unsort     = jet(10);          % standard color scheme
try cols_unsort = cbrewer('qual', 'Paired', 10); end  % try nicer colour
scheme

cols(1:2,:) = cols_unsort(5:6,:);   % cbrewer: red
cols(3:4,:) = cols_unsort(9:10,:);  % cbrewer: purple
cols(5:6,:) = cols_unsort(1:2,:);   % cbrewer: blue
cols(7:8,:) = cols_unsort(3:4,:);


for reps = 1:2
figure
for f = 1:18
    DCM = load(files{f+(reps-1)*18});
    DCM = DCM.DCM;

    subplot(9,2,f)
    for c = 1:4
        plot(DCM.H{c}(:,1), 'color', cols(c*2,:), 'Linewidth', 1.5);
hold on
        plot(DCM.H{c}(:,1) + DCM.R{c}(:,1), 'color', cols(c*2-1,:),
'Linewidth', 1.5);
        ylim([-10 10]);

        xlabel(DCM.name(end-9:end-8))
        set(gcf, 'color', 'w');
        set(gcf, 'Position', [100 + 400*(reps-1) 100 400 800]);
    end
end
end
legend({'D1(pred)', 'D1(obs)', 'S2(pred)', 'S2(obs)', 'S6(pred)',
'S6(obs)', 'S36(pred)', 'S36(obs)'});
```

A.7.2.3 ket_peb

```
%% Ketamine DCM analysis using Parametric Empirical Bayes
%=========================================================================
===
% This runs the second step of a two-level DCM analysis, modelling and
% parameter changes induced by katemine. It requires the full inversions
of
% the first level DCMs to be available

% Housekeeping
%=========================================================================
===
clear all
D = ket_housekeeping;

% Unpack housekeeping files
%-------------------------------------------------------------------------
---
Fbase       = D.Fbase;
```

```
Fspm        = D.Fspm;
Fdata       = D.Fdata;
Fanalysis   = D.Fanalysis;
Fbmr        = D.Fbmr;
GMFile      = D.GMFile;
sub         = D.sub;
fs          = filesep;

[rep_lin, rep_non] = ket_bmr_gen_model_space();


%% Run PEB Analysis
%=========================================================================
===
% This section sets up the between-DCM (2nd level) models, and runs PEB
% recursively over a model space specified in terms of which parameters
% contribute to explaining between-DCM variance.
% The winning model is then explored further by using Bayesian model
% reduction to identify parameter changes related to the main effect of
% ketamine (effect 2 here)
% This code will produce
%       1) Figure of Bayesian model comparison at the second level
%       2) The parameterised winning second level model (PEB{11})
%       3) A set of first level DCMs after second level inversion (RCM)
%       4) A Bayesian model average of the second level model after
%          exhaustive parameter seard (RMA)

clear DCM X M

% Load files into single cell array
%-------------------------------------------------------------------------
---
files = cellstr(spm_select('FPList', [Fanalysis fs 'Individual'],
'^*.mat'));
for f = 1:length(files)
    TCM = load(files{f});
    DCM{f} = TCM.DCM;
end

% Main Group Effect
%-------------------------------------------------------------------------
---
X(:,1)  = ones(1,length(DCM));


% Main Effect of Ketamine
%-------------------------------------------------------------------------
---
% This encodes the doses of ketamine: 0 = placebo, 1 = low, 2 = high
dose
%-------------------------------------------------------------------------
---
X(:,2)  = [2 0 2 0 2 0 1 0 1 0 2 0 1 0 1 0 1 0 1 0 1 0 1 0 1 0 1 0 1 0 2
0 2 0 1 0];


% Subject specific variation
%-------------------------------------------------------------------------
---
% This model component is used to model between-subhect variations as
% random effects of not interest
```

```
%-----------------------------------------------------------------------
---
subfx = zeros(length(DCM), length(sub));
for p = 1:length(sub)
    subfx([1:2] + 2*(p-1), p) = [1 1];
end
X   = [X, subfx];

M.X = X;
M.Xnames{1}     = 'Group';
M.Xnames{2}     = 'Ketamine';
for s = 1:length(sub)
    M.Xnames{2+s} = sub(s);
end

% Reduced models: Only extrinsic parameters
%-----------------------------------------------------------------------
---
C{1} = {'A'};   % All extrinsic
C{2} = {'B'};   % All extrinsic condition specific effects
C{3} = {'A', 'B'};  % All extrinsic and conditional
C{4} = {'A{1}(3,1)', 'A{1}(4,2)', 'A{1}(5,3)', 'A{1}(6,4)', 'A{2}(3,1)',
'A{2}(4,2)', 'A{2}(5,3)', 'A{2}(6,4)'}; % Forward
C{5} = {'A{3}(1,3)', 'A{3}(2,4)', 'A{3}(3,5)', 'A{3}(4,6)', 'A{4}(1,3)',
'A{4}(2,4)', 'A{4}(3,5)', 'A{4}(4,6)'}; % Backward
C{6} = {'B{1}(3,1)', 'B{1}(4,2)', 'B{1}(5,3)', 'B{1}(6,4)'};    %
Forward conditional
C{7} = {'B{1}(1,3)', 'B{1}(2,4)', 'B{1}(3,5)', 'B{1}(4,6)'};    %
Backward conditional

% Reduced models: Only intrinsic model parameters
%-----------------------------------------------------------------------
---
C{8} = {'M'};       % Modulatory
C{9} = {'N'};       % Modulatory conditional
C{10} = {'M', 'N'}; % Modulatory and condition specific effects
C{11} = {'G'};      % Intrinsic
C{12} = {'T'};      % Time constants
C{13} = {'M', 'N', 'G'};        % Intrinsic coupling
C{14} = {'M', 'N', 'G', 'T'};   % all intrinsic

labels = { 'A', 'B', 'A,B', 'A(Fwd)', 'A(Bwd)', 'B(Fwd)', 'B(Bwd)', ...
           'M', 'N', 'M,N', 'G', 'T', 'M,N,T', 'M,N,T,G', 'all' };
clear PEB F

%% Run PEB recursively over the set of reduced models defined in 'C'
%-----------------------------------------------------------------------
---
for c = 1:length(C)
    PEB{c} = spm_dcm_peb(DCM', M, C{c});
    F(c)   = PEB{c}.F;
end

%% Plot Bayesian model comparison between reduced second level models
%-----------------------------------------------------------------------
---
% Plot free energy difference (approx log(model evidence))
%-----------------------------------------------------------------------
---
subplot(2,1,1)
    bar(F-min(F));
```

```
    % Labels and Titles
    Franked = sort(F);
    df = Franked(1) - Franked(2);
    ylabel('Free Energy');
    title(['BMC, difference between winning and second best model: dF =
' num2str(df)], 'Fontsize', 15);

    % Plot settings
    set(gca, 'XTickLabels', labels);

% Plot posterior model probability
%-------------------------------------------------------------------------
---
subplot(2,1,2)
    title('Posterior Probability');
    bar(spm_softmax(F'))
    ylabel('Posterior Probability');

set(gcf, 'color', 'w');
set(gcf, 'Position', [100 500 900 400]);

%% Repeat PEB in the winning model (11) and run Baysian model reduction
%-------------------------------------------------------------------------
---
[REB, RCM]  = spm_dcm_peb(DCM',M,C{11});    % winning model from the
step above is M11
RMA         = spm_dcm_peb_bmc(REB);
```

A.7.2.4 ket_simulate

```
%% Simulating the effects of parameter changes on the grand mean
%=========================================================================
===
% Based on the PEB analysis specific parameter changes were identified
in
% the ii -> ss coupling. These are explored further by simulating data
% based on the grand mean model inversion with the added PEB-derived
% effects on ii -> ss coupling in STG and IFG. These are shown both in
time
% and in state space, illustrating that reduction in inhibitory
connections
% onto ss cells have impacts on superficial pyramidal cells and overall
% model output.

% Housekeeping
%=========================================================================
===
clear all
D = ket_housekeeping;

% Unpack housekeeping files
%-------------------------------------------------------------------------
---
Fbase       = D.Fbase;
Fspm        = D.Fspm;
Fdata       = D.Fdata;
Fanalysis   = D.Fanalysis;
Fbmr        = D.Fbmr;
GMFile      = D.GMFile;
sub         = D.sub;
```

```
fs          = filesep;

% Load and prepare DCM file
%-----------------------------------------------------------------------
---
DCM             = load(GMFile);
DCM             = DCM.DCM;
DCM.xY.Dfile    = [Fdata fs 'pgm_meeg_all'];
DCM             = spm_dcm_erp_dipfit(DCM,1);
DCM.name        = [Fanalysis fs 'Temp_DCM'];

% Simulate DCM outoput for different parameter combinations
%=======================================================================
===
% As identified from the PEB analysis, there are large opposing effects
on
% inhibitory interneuron connections on spiny stellate cells in IFG and
% STG. To explore these further, here we simulate the effects of sliding
% parameter changes of both IFG and STG ii -> ss inhibition.
% ** steps ** defines the resolution of the simulation
clear A1 STG IFG
steps       = 10;
G           = linspace(0, 2, steps);

for s = 1:steps

% Extract parameters and (symmetrically) change ii -> ss inhibition
%-----------------------------------------------------------------------
---
Sp        = DCM.Ep;
Sp.G(3,3) = Sp.G(3,3) + G(s);
Sp.G(4,3) = Sp.G(4,3) + G(s);
Sp.G(5,3) = Sp.G(5,3) - G(s);
Sp.G(6,3) = Sp.G(6,3) - G(s);

% Calculate model prediction based on the new parameterset
%-----------------------------------------------------------------------
---
y       = spm_gen_erp(Sp, DCM.M, DCM.xU);

% Extract population specific traces from regions
%-----------------------------------------------------------------------
---
pops    = {'II', 'SP', 'SS', 'DP'};

for p = 1:4
    pop = (p-1)*12;

    A1{p}(:,s) = y{1}(:,1 + pop);
    STG{p}(:,s) = y{1}(:,3 + pop);
    IFG{p}(:,s) = y{1}(:,5 + pop);

end

end

% Plot model predictions for increasing parameter changes - time
resolved
%-----------------------------------------------------------------------
---
figure
```

```
try     spectral = flip(cbrewer('div', 'Spectral', 100));
catch   spectral = jet(200);    end

colormap(spectral)
subplot(3,1,1)
    imagesc(DCM.xY.pst, G, A1{2}');
    title('Effects of ketamine on A1 superficial pyramidal cells',
'FontWeight', 'bold');
    xlabel('Peristimulus time');
    ylabel('Parameter change');
    colorbar
subplot(3,1,2)
    imagesc(DCM.xY.pst, G, STG{2}');
    title('Effects of ketamine on STG superficial pyramidal cells',
'FontWeight', 'bold');
    xlabel('Peristimulus time');
    ylabel('Parameter change');
    colorbar
subplot(3,1,3)
    imagesc(DCM.xY.pst, G, IFG{2}');
    title('Effects of ketamine on IFG superficial pyramidal cells',
'FontWeight', 'bold');
    xlabel('Peristimulus time');
    ylabel('Parameter change');
    colorbar

set(gcf, 'color', 'w');
set(gcf, 'Position', [100 100 400 800]);


% Plot model predictions for increasing parameter changes - state space
%-----------------------------------------------------------------------
---
figure
try     col50 = flip(cbrewer('div', 'RdYlBu', steps));
catch   col50 = jet(steps);    end

p1 = 2;     % Superficial pyramidal cells
p2 = 3;     % Spiny stellate interneurons

subplot(3,1,1)
for s = 1:size(A1{p1},2)
    plot(A1{p1}(:,s), A1{p2}(:,s), 'color', col50(s,:), 'Linewidth', 2);
hold on
    xlabel(pops{p1});
    ylabel(pops{p2});
end

subplot(3,1,2)
for s = 1:size(A1{p1},2)
    plot(STG{p1}(:,s), STG{p2}(:,s), 'color', col50(s,:), 'Linewidth',
2); hold on
    xlabel(pops{p1});
    ylabel(pops{p2});
end

subplot(3,1,3)
for s = 1:size(A1{p1},2)
    plot(IFG{p1}(:,s), IFG{p2}(:,s), 'color', col50(s,:), 'Linewidth',
2); hold on
    xlabel(pops{p1});
```

```
    ylabel(pops{p2});
end

set(gcf, 'color', 'w');
set(gcf, 'Position', [500 100 400 800]);
```